OPTIMIZATION OF ENGINEERED HEART VALVE TISSUE EXTRACELLULAR MATRIX

by

George Carl Engelmayr, Jr.

BS Chemical Engineering, The Pennsylvania State University, 1997

Master of Biotechnology, University of Pennsylvania, 2000

Submitted to the Graduate Faculty of

the School of Engineering in partial fulfillment

of the requirements for the degree of

Doctor of Philosophy

University of Pittsburgh

2005

UNIVERSITY OF PITTSBURGH

SCHOOL OF ENGINEERING

This dissertation was presented

by

George Carl Engelmayr, Jr.

It was defended on

November 21, 2005

and approved by

Jörg C. Gerlach, Professor, Department of Surgery

William S. Slaughter, Associate Professor, Department of Mechanical Engineering

George D. Stetten, Associate Professor, Department of Bioengineering

William R. Wagner, Associate Professor, Departments of Surgery and Bioengineering

Michael S. Sacks, W. K. Whiteford Professor, Department of Bioengineering
Dissertation Director

ABSTRACT

OPTIMIZATION OF ENGINEERED HEART VALVE TISSUE EXTRACELLULAR MATRIX

George Carl Engelmayr, Jr., PhD

University of Pittsburgh, 2005

Prosthetic heart valves, whether biologically-derived or mechanical, have improved the quality of life of millions of patients worldwide since their introduction in the 1960's. However, while currently available prosthetic valves perform sufficiently well in the short term, the side-effects of anticoagulation therapy (mechanical valves) and the structural degeneration of bioprosthetic and homograft valves represent significant drawbacks in the long-term. The limitations of these non-viable devices are especially pronounced in pediatric patients suffering from congenital valvular lesions, as none of the current prosthetic valves have the capacity to grow in tandem with the somatic growth of the patient.

Tissue engineered heart valves (TEHV) are conceptually appealing for use in the surgical repair of valvular lesions because they harbor a living cell population potentially capable of orchestrating tissue self-repair, growth, and resistance to infection. Since the mid-1990's, significant progress has been made toward the development of a functional TEHV, culminating in long-term implantation studies in sheep. In these previous studies, TEHV were constructed by seeding vascular-derived smooth muscle and endothelial cells, or bone marrow-derived mesenchymal stem cells (BMSC), onto bioresorbable polymer scaffolds. The resultant TEHV were subsequently cultivated in a pulsatile flow loop bioreactor in which TEHV could be exposed to graduated increases in mechanical stimulation prior to implantation.

Importantly, it was demonstrated through these previous studies that mechanical stimulation is critical to the development of a functional TEHV. In the absence of mechanical stimulation, TEHV exhibited significantly reduced extracellular matrix (ECM) formation, and thus upon scaffold degradation retained insufficient structural integrity for acute hemodynamic function. However, because the various mechanical stimuli (e.g., cyclic flexure, tension, and fluid flow) were coupled in the pulsatile flow loop bioreactor, it could not be deduced how the individual modes of mechanical stimulation contributed to the overall TEHV developmental response. Such information is essential, both for developing rationally designed mechanical conditioning regimens, and importantly for potential clinical applications, for quantifying the sensitivity of the tissue formation process to perturbations in these factors.

To establish biomechanical end-points for evaluating TEHV, in the current study mathematical models were developed to predict the effective stiffness of TEHV biomaterials from the properties and structure of the individual constituents. It was found that the effective stiffness of the nonwoven polymer scaffolds could accurately be predicted from the spring-like tensile properties and orientations of the scaffold fibers, and that the primary mechanical effect of ECM deposition was an increase in the number of fiber-fiber bond points. Toward quantifying the independent and coupled effects of mechanical stimulation on TEHV development, a novel flex-stretch-flow (FSF) bioreactor was developed in which multiple TEHV specimens could be subjected to well-defined combinations of mechanical stimuli. Finally, the FSF bioreactor was used to elucidate the independent and coupled effects of cyclic flexure and laminar flow on TEHV tissue formation by BMSC. The combination of flexure and flow was found to synergistically accelerate tissue formation and BMSC differentiation, thus paving the way toward rational designs for TEHV conditioning regimens utilizing novel cell sources.

TABLE OF CONTENTS

LIST OF TABLES

LIST OF FIGURES

PREFACE

It's tough work putting the past four and a half years into perspective. Let's leave it to say that they were both the most challenging and most rewarding years so far. First and foremost, I am gratefully indebted to Dr. Sacks and Dr. Borovetz for giving me the opportunity to study at University of Pittsburgh. I can honestly say that returning to academia, and in particular coming to the Engineered Tissue Mechanics Lab at University of Pittsburgh, was one of the best decisions I've made in my life. Dr. Sacks gave me a (sometimes daunting) degree of latitude in pursuing my doctoral research, and I will always credit those years of unbridled freedom to think and (loosely bridled) freedom to act for any future successes I have as an independent researcher. Just as valuable as the freedom was the guidance Dr. Sacks gave me, and in particular the help he gave me in focusing in the tumultuous sea of ideas the field of bioengineering tends to engender.

Coming back to school after industry was like a dream come true—literally like turning back that proverbial clock. I've made some of the best friends of my life in Pittsburgh, and I'm hopeful that we'll keep in touch throughout the years to come. If it were not for my family I would never have lasted this long. I want to thank Mom, Dad, and my sister Steph for always loving me and making me feel at home even when I'm not. And last, I am so thankful for meeting Shadow Huang in Pittsburgh. Through all the ups and downs you've always been there, and I know you'll always be there. I love you and thank you for making me happy all these years. And really last, a favorite line from one of my favorite artists:

> "Love's the only engine of survival"
>
> —Leonard Cohen, The Future

ACRONYMS

α-SMA	alpha smooth muscle actin
SMC	smooth muscle cell
EC	endothelial cell
VIC	valvular interstitial cell
VEC	valvular endothelial cell
BMSC	bone marrow-derived mesenchymal stem cell
RVE	representative volume element
WF	with-flexure
AF	against-flexure
PD	preferred fiber direction
XD	cross-preferred fiber direction
SALS	small angle light scattering
PGA	poly(glycolic acid)
PLLA	poly(L-lactic acid)
P4HB	poly(4-hydroxybutyrate)
APS	ammonium persulfate
TEMED	tetramethylethylenediamine
APTES	3-aminopropyltriethoxysilane
FSF	Flex-Stretch-Flow
VA-Type	vimentin-alpha smooth muscle actin positive cell type

NOMECLATURE

a_{eff}	fiber effective crimp amplitude
A_f	fiber cross-sectional area
a_o	fiber intrinsic crimp amplitude
b	representative volume element width
B_1	parameter used in calculating $(E_f)'$
B_2	parameter used in calculating $(E_f)'$
d_f	fiber diameter
$\Delta\kappa$	specimen change-in-curvature
E	specimen effective stiffness
E_f	fiber longitudinal stiffness
$(E_f)'$	fiber effective stiffness
EI	specimen flexural rigidity
I	specimen area moment of inertia
$I(\Phi)$	scattered light intensity distribution
$\bar{I}(\Phi)$	mean scattered light intensity distribution
κ_{eff}	fiber initial curvature of effective crimp geometry
λ	fiber weight / length
Λ	fiber intrinsic crimp wavelength
Λ_{eff}	fiber effective crimp wavelength
M	specimen bending moment
N_f	number of fibers / representative volume element

ρ_f	fiber density
$R(\Phi)$	fiber orientation distribution
σ	standard deviation parameter of $R(\Phi)$
t	specimen thickness
w	specimen width
ω	specimen weight / area
y_o	baseline parameter of $R(\Phi)$

1.0 INTRODUCTION

1.1 THE MAMMALIAN HEART AND ITS VALVES

A common anatomical feature of humans and other mammals is the four-chamber heart (**Figure 1**). While it is the function of the heart ventricles to pump blood to the lungs (deoxygenated; right ventricle) and the systemic circulation feeding the organs (oxygenated; left ventricle), it is the heart valves which serve to control blood flow through the heart [1].

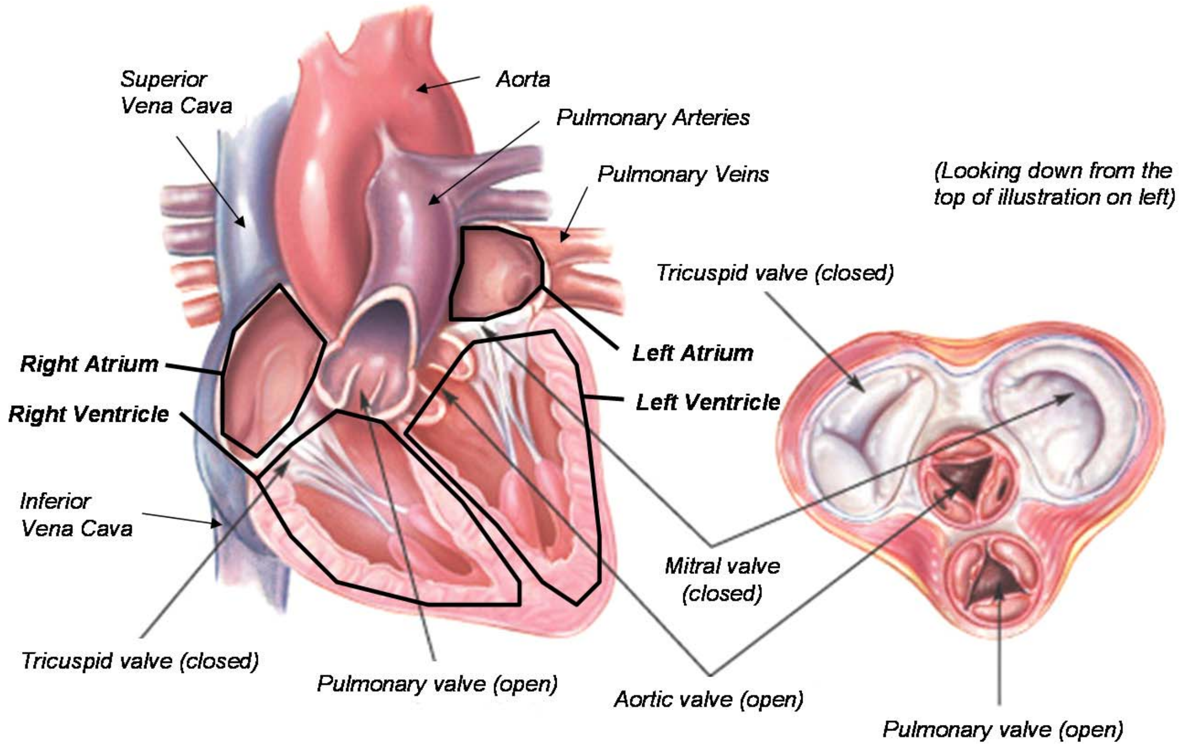

Figure 1 Gross anatomy of the four-chamber mammalian heart. Image adapted from Edwards Lifesciences, Irvine, CA (**www.edwards.com/PatientsAndFamilies/MyHeart/Anatomy/**).

During the cardiac cycle, blood depleted of oxygen by the metabolic demands of the bodily organs is returned to the right atrium of the heart via the inferior and superior Vena Cava. This deoxygenated blood is pumped into the right ventricle through the tricuspid valve, and subsequently pumped to the lungs via the pulmonary valve and pulmonary artery. Blood replenished with oxygen in the lungs returns to the left atrium of the heart via the pulmonary veins. Completing the cycle, the oxygenated blood is pumped into the left ventricle through the mitral valve, and subsequently pumped back to the systemic circulation and organs via the aortic valve and aorta. While healthy heart function is critically dependent on the efficient performance of each of the valves, the structures and functions of the semilunar valves (i.e., aortic, pulmonary) are both more simple, and more frequently subject to disease, than those of the muscularly-anchored atrio-ventricular valves (i.e, tricuspid and mitral valves). Thus, in the following sections the semilunar aortic and pulmonary valves will be primarily considered.

1.1.1 Organ-Level Structure of the Semilunar Valves

The aortic and pulmonary valves exhibit a unique tri-leaflet structure, with each of the individual leaflets exhibiting a semilunar (i.e., half-moon) shape (**Figure 2**). In light of the similarity of structure exhibited by the semilunar valves, only a detailed description of the aortic valve structure is presented here. The aortic valve consists of the three valve leaflets and the surrounding aortic root. The aortic valve is demarcated on the ventricular side by a semilunar line of attachment named the annulus fibrosis, and on the aortic side by a circular ridge of thickened tissue circumscribing the apices (i.e., commissures) of the semilunar leaflets referred to as the sinotubular junction [2]. The body of each leaflet spans from the annulus fibrosis to the free edge, forming a pocket-like cavity between the leaflet and its associated aortic root wall. During valve closure, these three pocket-like cavities fill with blood and ultimately press together in what is termed leaflet coaptation. The several millimeters of leaflet tissue that when coapted form a seal against retrograde blood flow are called the coapting surfaces or lunulas (**Figure 2**; area descending from the free edge to the dotted black line). At the center of each lunula is a small nodule of thickened tissue called the nodulus Arantii which supposedly reduces regurgitation. Because each of the leaflets is roughly equal in size, the circumferential angular distance from commissure to commissure is approximately 120 degrees. The triangular regions of aortic root descending from each of the three commissures and demarcated on either side by the semilunar lines of the annulus fibrosis are called the interleaflet triangles [2].

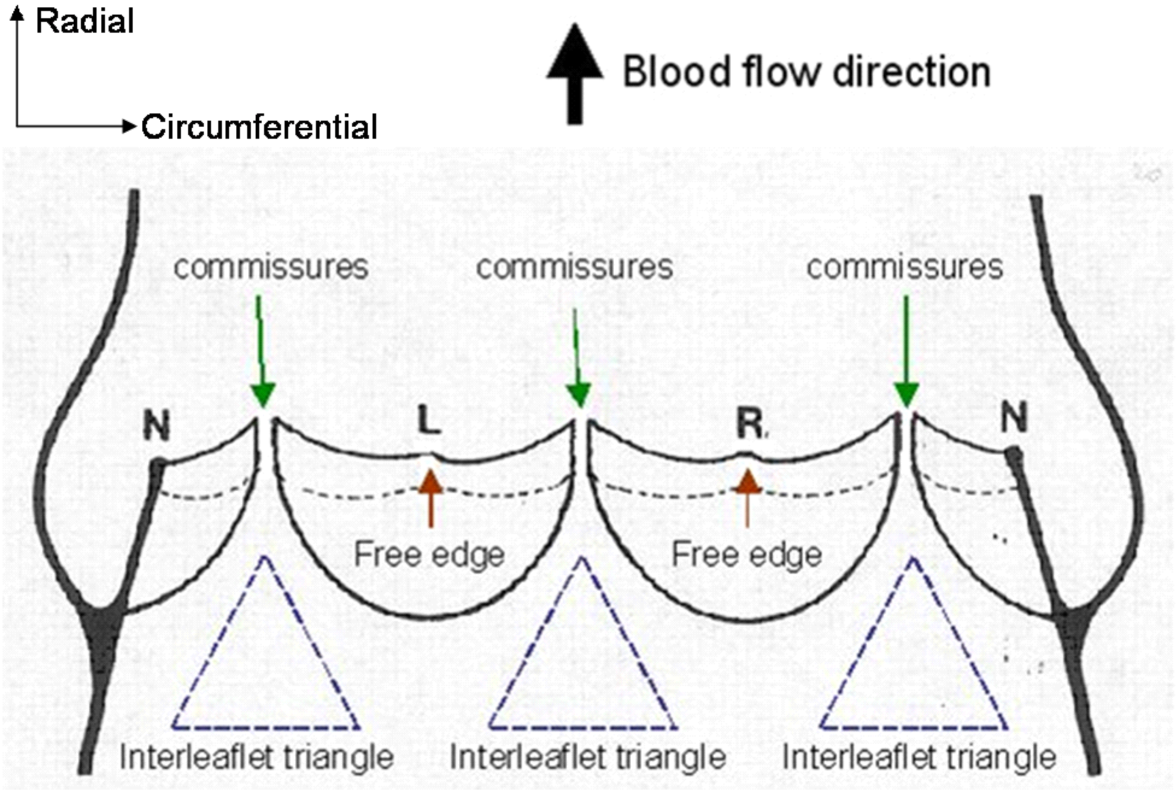

Figure 2 Surgical anatomy of a semilunar heart valve. Image courtesy of Thubrikar [3].

1.1.2 Tissue-Level Structure of the Semilunar Valve Leaflets

The tissue-level microstructure of the semilunar valve leaflet is uniquely adapted to withstand the repetitive loading of the cardiac cycle (**Figure 3**). As in the above description of the organ-level structure, the tissue level description here will focus on the aortic valve. The human aortic valve leaflet thickness ranges from approximately 700 microns at the annulus fibrosis to 200 microns at the free edge. Through the thickness, the leaflets exhibit a tri-layered structure, with the individual layers designated as the fibrosa (aortic side), spongiosa (central), and ventricularis (ventricle side). The fibrosa layer consists primarily of circumferentially-oriented type I collagen fibers, and provides the strength required to withstand the 80 mmHg transvalvular pressures experienced during aortic valve closure (diastole). In addition to the fiber level crimp intrinsic to type I collagen, the fibrosa also exhibits a macroscopic corrugated structure which is presumed to allow for radial leaflet expansion. On the opposite side of the leaflet, the ventricularis layer consists primarily of elastin, with some loosely arranged type I collagen fibers. First coined by Gross and Kugel [4], the ventricularis is thought to be important both in stabilizing the corrugated collagen structure of the fibrosa, and to provide a tensile pre-load in the leaflet. Situated between the fibrosa and ventricularis is the loosely organized, highly hydrated spongiosa layer, which consists primarily of water, proteoglycans, and glycosaminoglycans (GAG), with some small collagen fibers tethering the fibrosa to the ventricularis. GAG are long, negatively-charged polysaccharides that serve to imbibe water within the spongiosa, both in their free form, as well as when bound to a protein core (i.e., proteoglycan) [5]. While not completely understood, the spongiosa is thought to reduce shear stresses and buckling during leaflet flexion, thus contributing to leaflet durability [6, 7].

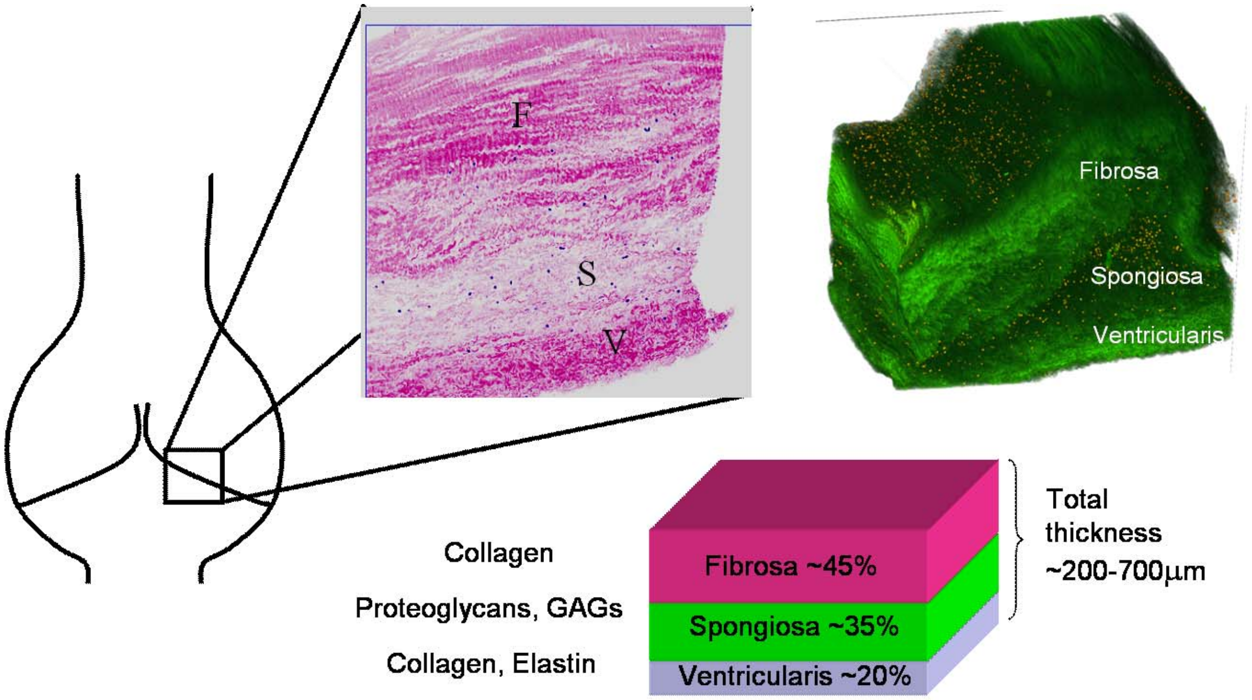

Figure 3 Tissue-level microstructure of a semilunar valve leaflet.

1.1.3 Cellular-level Structure of the Semilunar Valve Leaflet Tissue

The semilunar valve leaflets are populated by a mixed population of cells which are generally referred to as valvular interstitial cells (VIC). These VIC express a phenotype intermediate between smooth muscle cells (SMC) and fibroblasts, and have been characterized as VA-type myofibroblasts due to their dual expression of fibroblast markers such as vimentin and SMC markers such as alpha smooth muscle actin (α-SMA) [8-10]. While the quiescent state of the VIC appears to be more fibroblastic, under conditions of fetal development and/or active remodeling, such as during the Ross procedure (see Section 1.4), the VIC express a more SMC-like (i.e., α-SMA+) phenotype [11, 12]. Interestingly, recent studies have linked expression of the SMC-like phenotype to the contractile properties, leaflet stiffness, and mechanical environment of the valve [13, 14]. At the blood-leaflet interface, the leaflets are covered with a confluent lining of valvular endothelial cells (VEC). VEC, while similar in many respects to other vascular endothelial cells, the VEC express certain unique phenotypic and morphologic attributes [15, 16].

Collectively, the structures constituting the semilunar valves perform remarkably well, typically withstanding 3 x 10^9 cycles during an average human lifespan. Conversely, disruption of the complex arrangement of these tissue and organ-level structures, either by congenital malformation or acquired by disease, can lead to clinical symptoms mandating valve replacement.

1.2 HEART VALVE DISEASE AND CURRENT VALVE REPLACEMENTS

Prosthetic heart valves are implanted in ~ 275,000 patients each year [17]. Conditions warranting replacement of either the semilunar (i.e., aortic or pulmonary) or atrio-ventricular (i.e., mitral or tricuspid) valves can be generally characterized as either congenital or acquired. Congenital lesions in pediatric patients (e.g., pulmonary atresia, tetralogy of Fallot) often require complete reconstruction of the valvular outflow tract [18-20]. In older patients (i.e., 8th decade), senile degeneration of the valve leaflets is common, clinically manifesting as either stenosis (decreased valvular orifice area), insufficiency (regurgitant blood flow), or a combination thereof [21]. While mechanical, bioprosthetic, and homograft valve replacements have significantly improved the quality of life of many patients since their inception in the 1960's (**Figure 4**), currently available valve replacements continue to suffer from serious limitations [22].

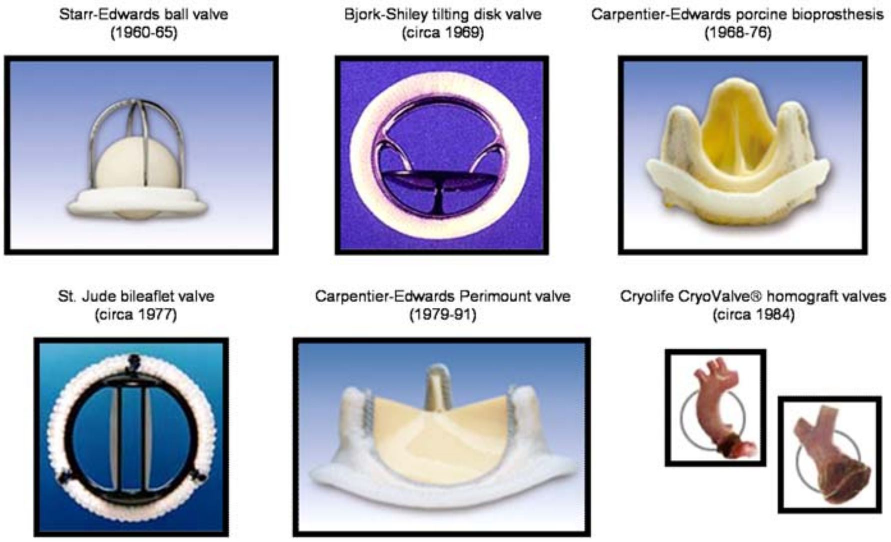

Figure 4 Overview of currently available replacement valves.

Mechanical valves offer superior long-term durability; essentially lasting the lifetime of the recipient; however they require chronic anticoagulation therapy to reduce the potential for thromboembolism and are susceptible to infection [23]. These drawbacks are of particular concern in women of child-bearing age, who carry an elevated risk of valve-related thrombosis and anticoagulant-related embryopathy during pregnancy [24, 25]. Bioprosthetic heart valves (BHV), fabricated from chemically-treated porcine valves or bovine pericardium, provide excellent hemodynamics, thereby avoiding the requirement of anticoagulation. Unfortunately BHV incur calcific and fatigue-related damage over a relatively short time frame of 10 to 15 years, resulting either in surgical intervention or mortality [22, 26, 27]. Homograft valves from human cadavers represent the gold-standard in terms of hemodynamics and functionality; however their use is restricted by donor scarcity. Efforts to improve the biocompatibility and durability of mechanical valves and BHV, respectively, will likely yield some degree of success in the future. Traditional valve designs, however, all lack living cells and thus do not possess the capacity for growth that is conceptually appealing in reconstructing pediatric valvular lesions.

1.3 RECONSTRUCTION OF VALVULAR LESIONS IN PEDIATRIC PATIENTS

Pediatric valvular lesions requiring reconstruction in early infancy are generally associated with severe cyanotic congenital heart diseases. In cyanotic congenital heart disease, the lesions allow for a mixture of oxygenated and deoxygenated blood to be pumped into the systemic circulation, thus resulting in a bluish coloration. The overall incidence of severe cyanotic congenital heart disease has been estimated at 1,391/million live births [28]. Based on the most recent (2003) official US Center for Disease Control (CDC) report of 4,089,950 live births [29], this translates to approximately 5689 new cases of severe cyanotic congenital heart disease per year in the US alone. Of these cases, the most common conditions potentially warranting repair or replacement of the pulmonary valve in early infancy are Truncus Arteriosus, Tetralogy of Fallot, and Pulmonary Atresia [30] (**Figure 5**). In Truncus Arteriosus, the normal ventricular septum (**Figure 5A**) separating the right and left ventricles is disrupted by a large ventricular septal defect resulting in the formation of a large, single great vessel (i.e., truncus) in which a mixture of oxygenated and deoxygenated blood is pumped to the lungs and systemic circulation (**Figure 5B**). In Pulmonary Atresia, the pulmonary valve is entirely absent, with blood flow diverted to the systemic circulation via a Patent Ductus Arteriosus (**Figure 5C**), and in Tetralogy of Fallot the pulmonary valve is stenotic (i.e., narrowed), in addition to a ventricular septal defect and other lesions (**Figure 5D**).

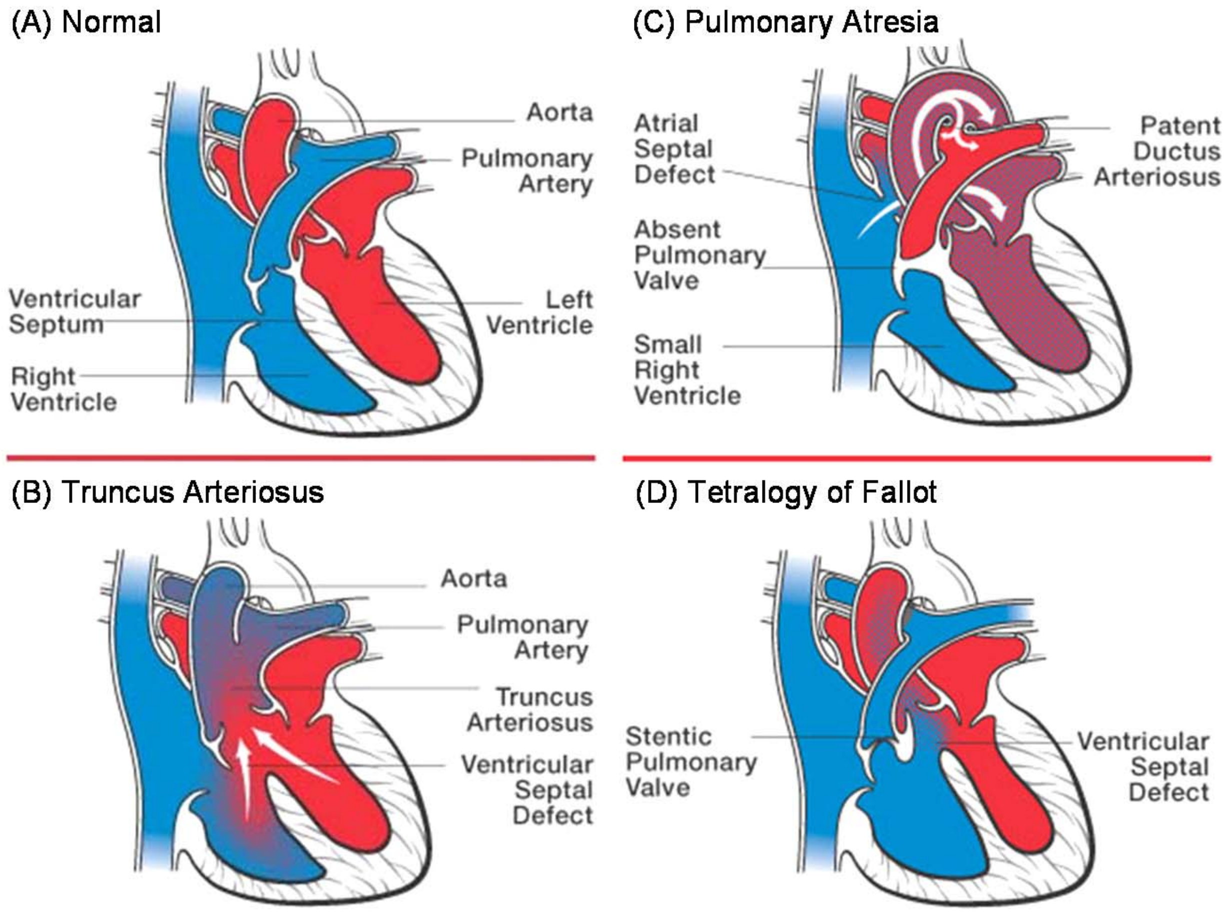

Figure 5 Common congenital valvular lesions. Adapted from the American Heart Association (www.americanheart.org).

Surgical inventions to correct these severe valvular lesions currently rely on the use of cryopreserved valved homografts derived from human cadavers. However, while current treatments are life-saving and perform well in the short-term, the cryopreserved valved homografts, while potentially retaining some degree of cellular viability, do not grow in tandem with the somatic growth of the neonate, and thus ultimately require reoperations and/or replacement [30]. The problem with size mismatch as a result of somatic growth is made clear in the following example. In a retrospective study by Perron et al. [30] at Children's Hospital Boston, at a mean operative age of 26 ± 28 days, the mean homograft size used was 9.0 ± 2 mm

(84 patients). At a mean time of 4.6 years, 37 patients (47%) had a reoperation, and the mean size of the new homografts was 17 ± 2 mm. The probability of freedom from reoperation was found to depend upon the size class of the graft, with time to reoperation being shortest for the smallest 6/7/8 mm class 1 grafts, and longest for the 12/14/15 mm class 3 grafts (p = 0.01; **Figure 6**).

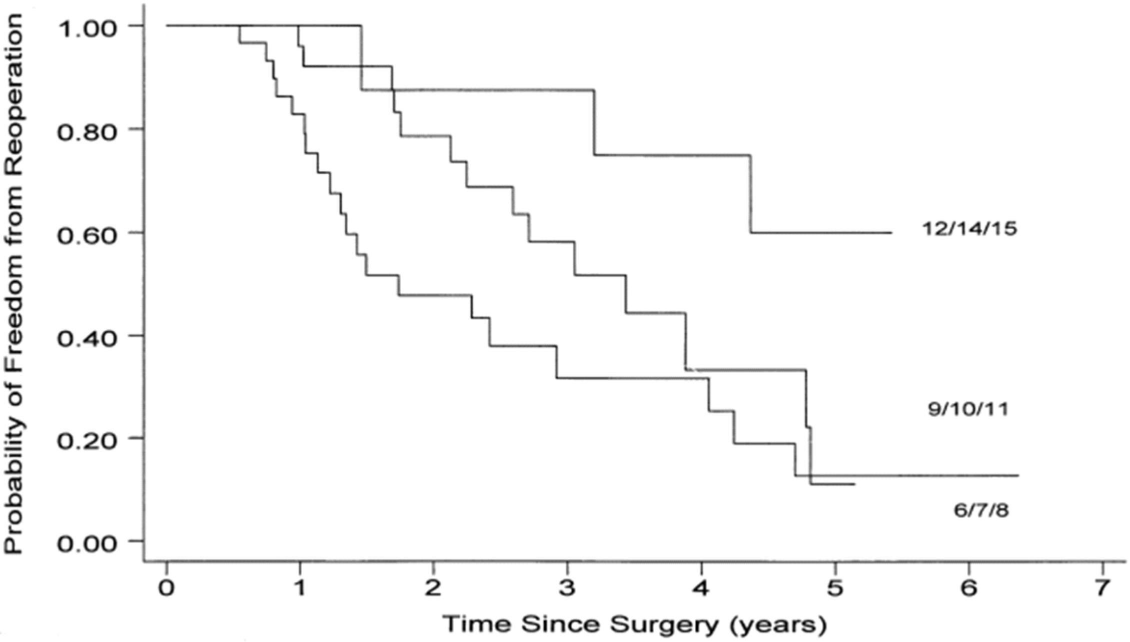

Figure 6 Probability of freedom from reoperation according to homograft size over time. Adapted from Perron et al. [30].

Thus for the pediatric population, in particular for neonates requiring small valved conduits, there is demonstrated clinical motivation for the development of a valved conduit that can grow with the patient, potentially mitigating the need for subsequent reoperations. One potential approach being investigated is the tissue engineered heart valve (TEHV).

1.4 TISSUE ENGINEERED HEART VALVES

In contrast to currently available replacement valves and valved conduits, tissue engineered heart valves (TEHV) are designed around a living cellular component. TEHV are typically constructed by seeding cells onto a porous, three-dimensional scaffold that resembles the anatomy of a native heart valve (**Figure 7**) [17, 31]. The majority of reports thus far have relied on vascular-derived cells, typically endothelial (EC) and smooth muscle cells (SMC) isolated from a section of carotid artery, aorta, or peripheral veins [32].

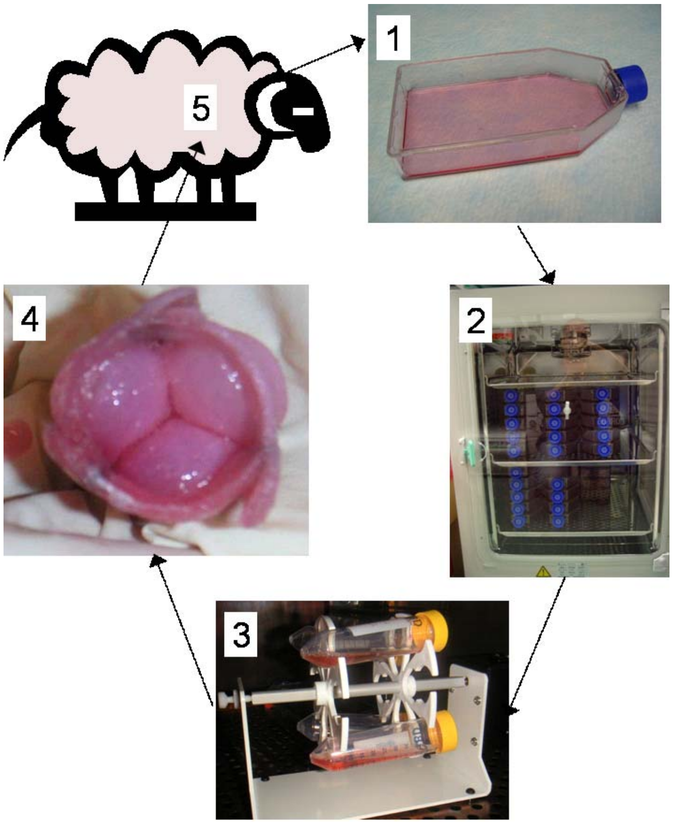

Figure 7 General steps in constructing a TEHV: isolate cells (1), expand cells (2), seed scaffold with cells (3), incubate cell-seeded scaffold (i.e., TEHV), and finally implant TEHV (5).

More recently, investigators have addressed the morbidity issues associated with such sources by constructing tissue engineered cardiovascular constructs based on bone marrow [33-35], cord blood [36], or peripheral blood-derived stem cells [37, 38]. The results of these new studies are encouraging; yielding similar results to that seen with vascular-derived cells; however the optimal cell source for TEHV has yet to be conclusively delineated. Likewise, there is a large degree of disparity in the types of materials used for the scaffold. Due to the acute mechanical strength criteria for valve replacements, the majority of TEHV developed thus far have relied on synthetic polymeric materials; such as polyglycolic acid (PGA) and poly-L-lactic acid (PLLA) [32, 33], or on biological materials, such as small intestinal submucosa (SIS) [39] and decellularized porcine valves [40].

Both TEHV design paradigms have demonstrated significant early achievements, including the successful demonstration of TEHV function in the pulmonary circulation of a growing lamb for 120 days (SMC + EC; PGA scaffold) by Hoerstrup et al. [32], and recently a 1 year follow-up on the first TEHV implanted in a human patient (EC; decellularized homograft) by Dohmen et al. [41]. More recently, Sutherland et al. [33] demonstrated that TEHV fabricated by seeding bone marrow-derived mesenchymal stem cells (BMSC) onto nonwoven 50:50 blend PGA/PLLA scaffolds could successfully function in the ovine pulmonary circulation for up to 240 days. However, while these results are encouraging, no study has demonstrated conclusively that TEHV have the capacity to grow in tandem with the somatic growth of the patient. In the study by Hoerstrup et al. [32], it was noted that the mild to moderate regurgitation observed at 16 and 20 weeks might have been a result of non-adaptation of the leaflets to the 4 mm growth in the pulmonary artery diameter over the 5 month period of the study. Indirect evidence for the growth potential of a living graft comes from studies involving the Ross procedure. First described by Donald N. Ross in 1967 [42], in the Ross procedure a diseased aortic valve is replaced with the patients own (i.e., autograft) pulmonary valve, while the pulmonary valve is typically replaced with a cryopreserved homograft valved conduit. In a recent study of pulmonary autograft explants, Rabkin-Aikawa et al. [12] demonstrated pathologic evidence for adaptive remodeling in the aortic site. Specifically, pulmonary autografts explanted after 3-6 years had retained their native tri-layed tissue morphology while exhibiting a thickness (0.9 ± 0.2 mm) similar to native aortic valves (0.7 ± 0.1 mm). Moreover, 3-6 year pulmonary autograft explants exhibited phenotypic characteristics similar to the native aortic valve, including expression of EphrinB2, a marker specific for arterial endothelium [43]. These morphologic and phenotypic adaptations corroborate other studies in which evidence for growth of the pulmonary autograft has been demonstrated indirectly in humans [44], and directly in a porcine animal model [45, 46]. Collectively, these studies provide evidence that autologous valved conduits have the capacity to grow, and support the possibility that TEHV may have the capacity to grow.

While the benefits of different cell sources, scaffold structures, and incubation conditions have been explored to an extent, little is known regarding the underlying mechanisms responsible for the development and maintenance of these engineered tissues. As such, a rational basis for the optimization and prediction of TEHV properties does not currently exist.

1.5 BIOMECHANICS AND FUNCTION OF NATIVE HEART VALVES

Mammalian semilunar heart valves are unique among tissues in that they passively undergo complex large deformations in response to the coupled effects of pulsatile blood pressure and flow (fluid shear stress) (**Figure 8**) [3].

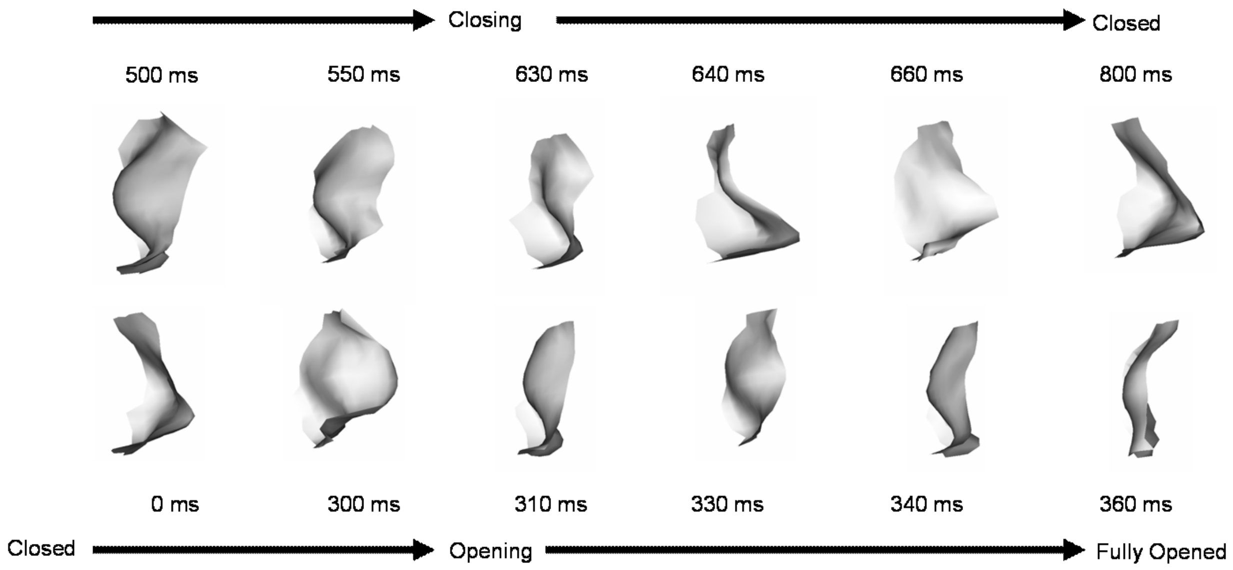

Figure 8 The passive deformation of a semilunar valve leaflet in response to blood flow is similar to the motion of a flag in the wind. The time series images were generated by surface meshing of data obtained by structured light projection upon a bioprosthetic heart valve leaflet in an *in vitro* pulsatile flow duplicator [47].

Their gross anatomical structure, extracellular matrix (ECM) microstructure, and concomitant mechanical properties appear to parallel physiological functional requirements (e.g., they exhibit a dense network of circumferentially oriented collagen fibers to support diastolic transvalvular pressure). Work by the Sacks group and others have quantified the relationships between collagen network structure and leaflet tissue mechanical behavior [48]. Moreover, recent studies suggest that mechanical forces are required during embryogenesis for normal semilunar valve development [49]. Finally, at least in the case of the mitral atrio-ventricular valve, altered leaflet stresses associated with papillary muscle ischemia have been demonstrated to result in an upregulation of type I collagen production *in vivo* [50, 51]. Together, observations of these structural features and biomechanical phenomena in native valves suggest a potential role for mechanical factors in the development of TEHV.

1.6 MECHANICAL CONDITIONING OF TEHV

It has been well documented that mechanical forces play a critical role in the homeostasis and remodeling of many load-bearing tissues and organs *in vivo* [52-54], as well as in the stimulation of native and engineered tissue biosynthesis and development *in vitro* [8, 55, 56]. As such, a number of investigators have developed systems to explore the role of mechanical stimulation in the context of their specific application [57, 58]. In order to prepare TEHV with sufficient mechanical strength for implantation, pulse duplicator bioreactors mimicking the *in vivo* mechanical environment have been developed [8, 32, 41, 59, 60]. The rational is that gradually increasing flow and pressure conditions will enhance and guide engineered tissue development, ultimately yielding mechanical properties suitable for suturing and acute hemodynamic function.

While the benefit of such pre-implantation conditioning compared to static incubation has been demonstrated (**Figure 9**), the underlying biomechanical phenomena have not been elucidated, nor the conditioning regimens optimized. In fact, pulse duplicator and flow loop bioreactors; while useful in developing three-dimensional, anatomical TEHV for implantation; have several drawbacks limiting their use in such biomechanical studies. Because these bioreactors aim to mimic the complex *in vivo* environment, the potential mechanical stimuli—such as shear stress, pressure, tension, and flexure—are inextricably coupled. As such, it would be difficult, if not impossible, to isolate the individual contribution of any particular mechanical factor in an intact TEHV.

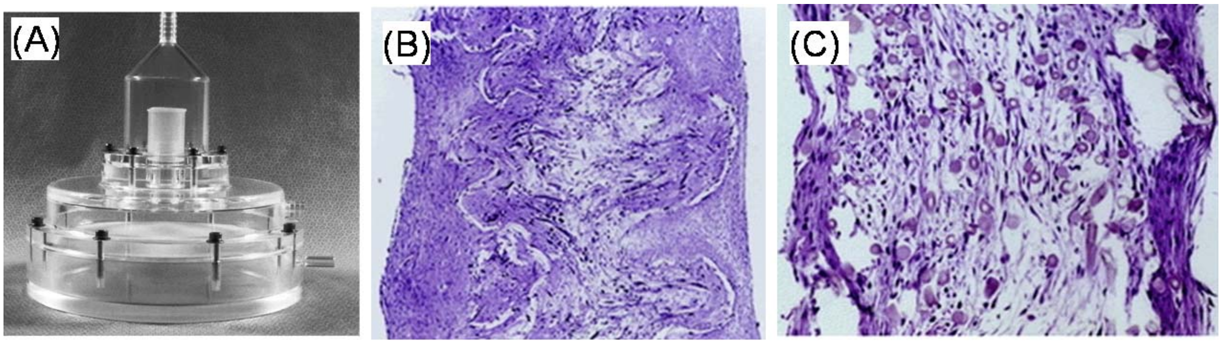

Figure 9 Pulse duplicator bioreactor (A) [59]. Representative H&E stained section of a TEHV cultivated for 14 days in a pulse duplicator bioreactor (B), and corresponding static control (C) [32]. Note the more robust tissue formation evident in the pulse duplicator TEHV.

Toward developing an understanding of the individual role of simple modes mechanical stimulation in TEHV development, bioreactors have recently been developed to provide fluid shear stress [61], cyclic flexure [62, 63], and tension [64] to TEHV biomaterials. The application of continuous laminar flow (fluid shear stress) *in vitro* was found to induce an approximately 1.5-fold increase in hydroxyproline concentration (a marker for collagen) in rectangular samples of TEHV by 14 days. In a recent study in our laboratory, cyclic flexure was demonstrated to induce quantitative and qualitative changes in the flexural behavior of two candidate TEHV scaffolds [62]. Moreover, cyclic flexure reproduced many of the aspects of development observed in TEHV incubated for 14 days in pulse duplicator bioreactors, including a nearly two-fold increase in collagen accumulation compared to static controls, and strong expression of the intermediate filament vimentin, a marker associated with native valve cell phenotype [63]. While these results have provided a substantial basis for the individual role of simple modes of mechanical stimulation in TEHV development, optimization of these phenomena requires an understanding of the underlying cellular mechanisms.

1.7 MECHANICAL STIMULATION OF CELLS

The first study to demonstrate that cyclic mechanical stretch can stimulate ECM synthesis *in vitro* was reported by Leung, Glagov, and Mathews [65]. In their seminal and innovative work, they developed a bioreactor in which rabbit aortic SMC were stretched on an elastin membrane derived from the media layer of bovine aorta (**Figure 10**). They demonstrated that the application of cyclic stretch at an amplitude of 10% and frequency of 1 Hz resulted in 3-5 fold increases in type I and type III collagen biosynthesis compared with static or agitated controls—all in the absence of any change in SMC proliferation.

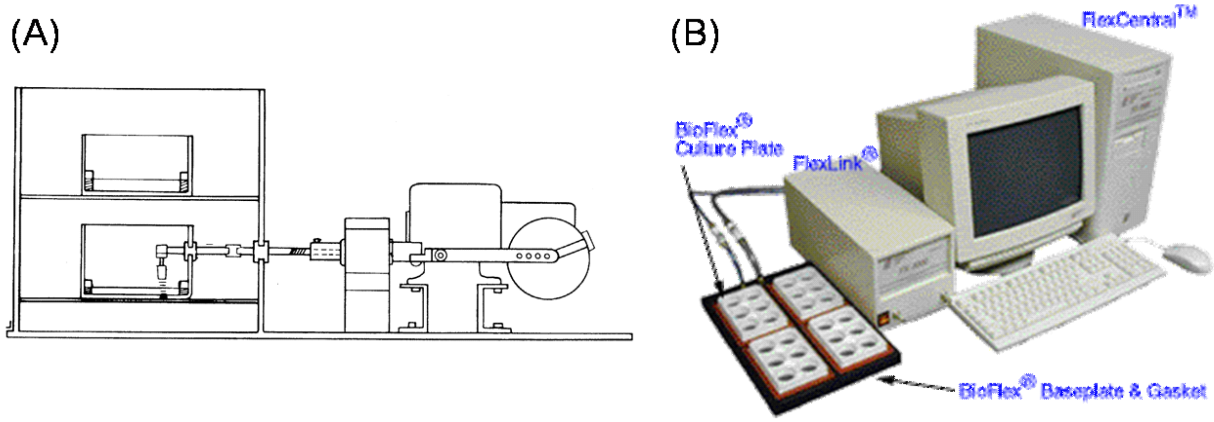

Figure 10 Examples of devices used to mechanically stimulate cells in 2-D tissue culture. The first device designed to mechanically stimulate cells was reported in 1976 and relied on an elliptical crank to stretch an elastin membrane (A). Image adapted from Leung et al. [65]. More recent devices have been marketed (e.g., Flexercell®) which incorporate robust computer control systems (B). Image courtesy of Dunn Labortechnik GmbH, Asbach, Germany (http://www.dunnlab.de).

In light of the role of SMC-mediated fibrosis in atherosclerosis; work in this area continued over the ensuing decades. Commercialization of the Flexercell® unit allowed researchers to focus on the biological aspects of cyclic mechanical stretch, without the difficulty of designing an experimental device [66]. A number of studies have investigated the effects of cyclic strain amplitude [65-70], frequency [71-73], and very recently, strain rate [74, 75], on cell phenotype, proliferation [76-78], apoptosis [79], and matrix synthesis in a two-dimensional (2D) cell culture setting. Moreover, in some cases the mechanism has been isolated to paracrine factors [78-80] or mechano-sensitive actuators, including integrins [71, 79], cadherins [81], gap junctions [82].

While use of the Flexercell® system has become ubiquitous across fields, recent interest in the field of tissue engineering has spurred a renewed interest in understanding the effects of cyclic mechanical loading on a three-dimensional (3D), cell-seeded scaffold. While the results of 2D studies appear to loosely parallel *in vivo* findings in native tissues, it is unclear if results established in 2D stretching systems can be directly scaled up to the 3D tissue engineering setting. While continuum mechanics and finite element methods can be applied to translate the macroscopic deformation of a 3D tissue engineering scaffold into microscale strains which the cells might experience [83], there are other factors associated with the 3D setting which need to be taken into consideration. First, the relative scale of the adhesive substrate to the cell may be considerably different in a tissue engineering scaffold (e.g., 10 μm diameter fiber) compared with in 2D culture (e.g., 185 cm^2 surface), potentially resulting in dramatic differences in cell shape, with concomitant effects on cell behavior [84]. Secondly, there are mass transport limitations associated with a 3D construct; and these limitations change with time as the cells secrete their ECM. Thirdly, the nature of the attachments to the substrate could be considerably different in a 3D case compared with 2D. For instance, in 2D the cells could become artificially polarized based on their attachments to the underlying, 2D substrate, whereas in 3D, the cells could potentially attached to ligands in all directions surrounding the cell, perhaps in a manner more consistent with that which occurs *in vivo* [85]. While these studies have demonstrated potentially useful relationships between cyclic stretch and cell behavior, the differences between the 2D cell culture and 3D tissue engineering settings highlight the need to investigate these phenomena in the 3D situation.

1.8 MICROSTRUCTURE AND MECHANOTRANSDUCTION IN TEHV

During seeding, cells attach to tissue engineering scaffolds through specific interactions between serum proteins adsorbed to the scaffold material and membrane-bound receptors [85]. As the majority of tissue engineering scaffolds are highly porous (greater than 90%), a large proportion of the seeded cells are initially adhered to themselves, rather than the scaffold (unpublished observations). Vascular smooth muscle cells, one of the most widely utilized cell types in cardiovascular tissue engineering applications, typically express T, R, and N-cadherin receptors through which they can undergo such homophilic cell-cell interactions [86]. Recently, studies on fibroblasts have demonstrated that N-cadherin can mediate intercellular signaling by stretch-sensitive calcium-permeable channels [81, 87]. Considering that the PGA and PLLA fibers of the most widely used TEHV scaffolds are not elastomeric, it is possible that mechanical forces are transduced to the cells through the local deformation of the cellular network.

As TEHV continue to develop *in vitro*, cells secrete and organize ECM, filling in the void space of the scaffold with tissue [8]. While standard histological methods have demonstrated the presence and gross organization of collagen, sulfated glycosaminoglycans (S-GAG), and elastin in TEHV, these methods provide little information regarding the three-dimensional attachment of the newly formed ECM to the scaffold. To reveal such intricate details, scanning (SEM) and transmission (TEM) electron microscopic techniques are traditionally employed. In one recent study, TEM of TEHV indicated the presence of actin/myosin filaments, collagen fibrils, and elastin fiber aggregates [35]. Furthermore, SEM demonstrated that TEHV incubated in a pulse duplicator bioreactor exhibited a confluent surface with cell orientation in the direction of flow [32]. Unfortunately, no TEHV study to date has performed the exhaustive electron microscopic analysis necessary to establish the interconnections between ECM components, cells, and scaffold. The lack of detailed information on the 3D microstructure of TEHV represents a significant gap in the literature.

1.9 MATHEMATICAL MODELING OF TEHV DEVELOPMENT

Theoretical models have been postulated to describe the mechanics of growth and remodeling in native and engineered tissues [88-92]. While these formulations are generally rigorous, they lack the detailed experimental data needed to validate their accuracy. Furthermore, none of these models can be directly applied to TEHV based on the most popular category of TEHV scaffolds—non-woven polymeric mesh scaffolds, such as PGA. In describing the mechanical behavior of a TEHV based on a non-woven PGA scaffold, the composite material could potentially be approximated as a discontinuous fiber reinforced composite [93]. While soft collagenous tissues generally exhibit non-linear, anisotropic mechanical properties, non-woven meshes of randomly oriented fibers can exhibit planar quasi-isotropy, depending upon the fabrication method [94]. Furthermore, studies in our laboratory have demonstrated that non-woven 50:50 blend PGA/PLLA scaffolds and cell-seeded constructs exhibit linear behavior in the low stress-strain regime of three-point flexure. Thus, it may be that simplified linear theories will be sufficient in describing the composite material behavior of these scaffold materials [95].

1.10MOTIVATION AND SPECIFIC AIMS OF THE PRESENT STUDY

Tissue engineered heart valves (TEHV) are being developed for the surgical repair of congenital valvular lesions in pediatric patients [31]. Because TEHV are populated with viable cells, they may possess a capacity for coordinating the growth and remodeling of the TEHV in tandem with the somatic growth of pediatric patients. Created by seeding vascular-derived cells onto synthetic scaffolds, TEHV exhibited enhanced extracellular matrix (ECM) development and improved mechanical properties when cultured under pulsatile flow and pressure conditions *in vitro* [32]. Moreover, native-like ECM microstructures [8] and mechanical properties [32] have been observed following 20 weeks implantation in the pulmonary circulation of sheep *in vivo*.

While the results of these studies are encouraging, much work remains to complete our understanding of the TEHV developmental process before clinical trials would be warranted [96]. First, the flow and pressure environments of pulsatile flow loop bioreactors are complex and inextricably coupled, precluding isolation of the independent effects of individual mechanical factors or inter-factor coupling. Such information is essential for the rational design of optimized TEHV conditioning regimens. Moreover, such information would represent a key component of our understanding of the engineered tissue formation process, and thus would help guide investigators in TEHV design. Ultimately, this information could help guide regulatory agencies in determining appropriate end-points for assessing TEHV structure and functional performance, as well as in delineating process validation requirements for bioreactors and conditioning protocols used in fabricating TEHV.

Secondly, considering the load-bearing function of the valve, of paramount importance is the development of methods to predict how the mechanical strength and stiffness of the TEHV evolve with *in vitro* incubation and subsequent *in vivo* implantation. TEHV are composite materials; prior to scaffold resorption, the effective mechanical properties will depend on the complex, time-varying interactions between the degrading scaffold and the ECM being deposited by the cells. Moreover, the structural-mechanics of the nonwoven fabrics used as TE scaffolds are complex themselves [97-99]. As such, prior to the work presented herein, no methods have been developed to predict the mechanical properties of nonwoven TE scaffolds from the properties of the constituent fibers, let alone the mechanical properties of the cell-seeded TEHV constructs. Again, this information represents another key component of our understanding of the engineered tissue formation process—specifically, the biomechanics of tissue deposition on nonwoven scaffolds—and could potentially lead to new scaffold biomaterials and designs.

Finally, the majority of studies to date have utilized vascular-derived SMC and EC in constructing TEHV. While these cell sources are acceptable for *in vitro* work and pre-clinical animal studies, one of the overall motivations behind tissue engineering is to circumvent the morbidity associated with the use of tissue autografts. Thus, the field has been compelled to develop novel cell sources that can be isolated relatively non-invasively from patients, and that exhibit the phenotypic plasticity required for creating a TEHV, despite the fact that they were not derived from a native valve.

Based on these three principal research areas, the specific aims of the present study were as follows:

1. **Quantify the effects of cyclic flexure on candidate TEHV scaffolds and on cell-seeded TEHV constructs.** We hypothesized that cyclic flexure; one of the primary modes of deformation experienced by native semilunar heart valves; would have independent effects on the TEHV developmental process, and potentially on the TE scaffolds themselves. To address these hypotheses, a cyclic flexure bioreactor was developed an implemented to investigate the effects of cyclic flexure on the structural-mechanical properties of nonwoven TE scaffolds, as well as on cell-seeded TEHV constructs *in vitro*.

2. **Develop a bioreactor to independently modulate the application of cyclic flexure, tension, and flow (fluid shear stress) to multiple TEHV samples.** We hypothesized that each of the mechanical stimuli experienced by TEHV in pulsatile flow loop bioreactors, cyclic flexure, stretch, and fluid flow, might synergistically effects TEHV development. To test this hypothesis, a novel flexure-stretch-flow (FSF) bioreactor was developed in which the individual FSF stimuli could be applied to multiple TEHV specimens independently or coupled.

3. **Quantify the independent and coupled effects of cyclic flexure and laminar flow on TEHV constructed using bone marrow-derived mesenchymal stem cells (BMSC).** BMSC represent a potentially attractive cell source for TEHV because they can be

isolated relatively non-invasively from a bone marrow biopsy, and because previous studies have demonstrated their remarkable pluripotency and phenotypic plasticity. To address the hypothesis that BMSC would differentiate differently in response to independent and combined modes of mechanical stimulation, we used the FSF bioreactor to investigate the independent and coupled effects of cyclic flexure and laminar flow on TEHV tissue formation by BMSC.

4. **Develop and experimentally validate structural-based models to predict the effective stiffness (E) of nonwoven TE scaffolds and cell-seeded TEHV constructs.** To fully characterize the mechanical properties of TEHV based on nonwoven scaffolds under physiologically-relevant loading modes, we first developed a structural model for the flexural mechanics of nonwoven TE scaffolds. We then developed additional experimental techniques for quantifying relevant structural features of TEHV (e.g., transmural collagen distribution), and implemented them in an extended structural model accounting for the composite properties of nonwoven nonwoven-ECM composites.

2.0 THE INDEPENDENT ROLE OF CYCLIC FLEXURE IN THE *IN VITRO* DEVELOPMENT OF AN ENGINEERED HEART VALVE TISSUE

As a first step toward a systematic investigation of mechanical stimulation in TEHV, we initially designed and implemented a bioreactor for the purpose of subjecting samples of TEHV to well-defined, simple modes of cyclic flexure [62, 63].

2.1 DESIGN AND QUALIFICATION OF A CYCLIC FLEXURE BIOREACTOR

As highlighted above in Section 1.6, bioreactors have previously been designed to apply complex pulsatile flow fields [32, 59], and more simple modes of mechanical loading such as cyclic tensile strain [64] and continuous laminar flow (fluid shear stress) [61] to TEHV. Cyclic flexure represents another important mode of deformation experienced by the semilunar heart valve leaflets during valve operation *in vivo*, and incubation in pulse duplicator bioreactors *in vitro*, and thus was hypothesized to have independent effects on TEHV development [62, 63].

The bioreactor was designed using Solidworks 3D CAD software (Solidworks Corp., Concord, MA), and the parts were fabricated by Apollo Precision, Inc. (Plymouth, MN). The structural elements of the device were machined from polysulfone. Neoprene gaskets were fitted between all joints to reduce the possibility of microbial contamination, and the bioreactor was assembled using 18-8 stainless steel screws (McMaster-Carr Supply Co., Cleveland, OH).

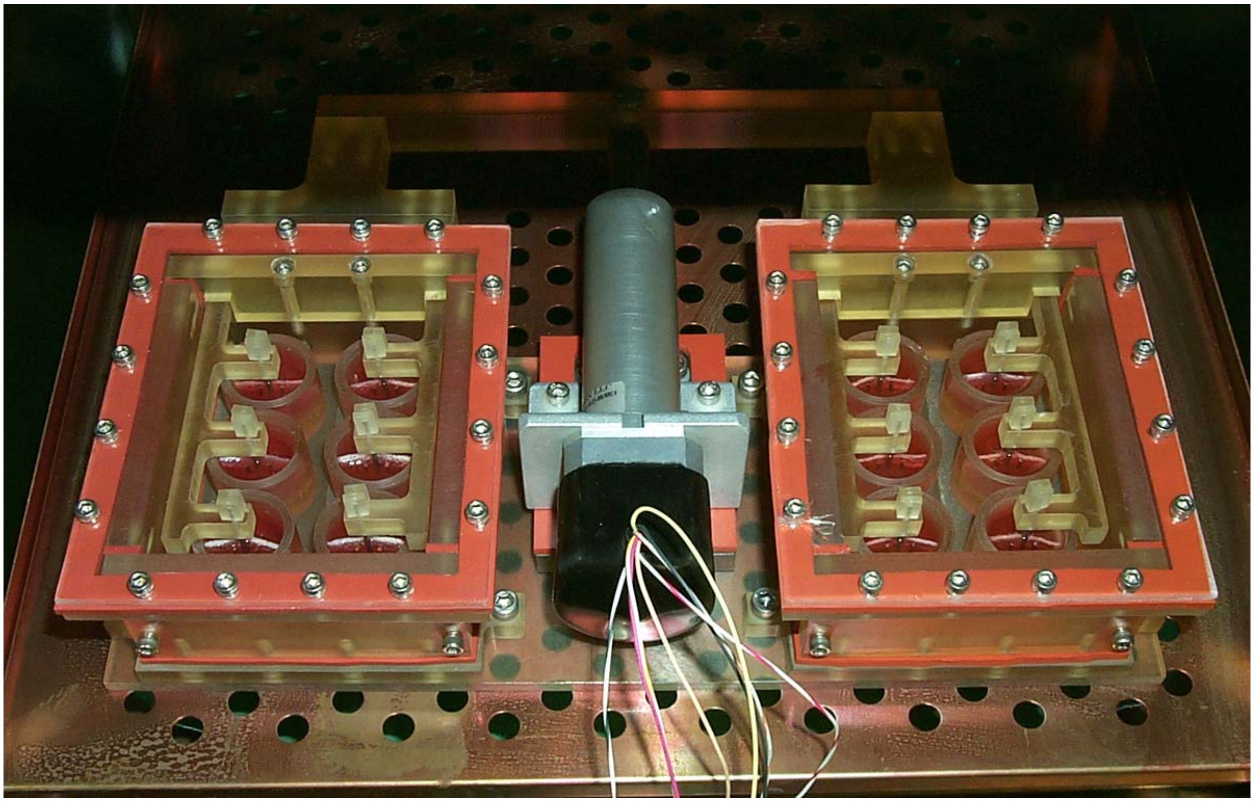

Figure 11 Photograph of the cyclic flexure bioreactor operating inside of a cell culture incubator.

The bioreactor consists of two identical chambers (127 mm x 101.6 mm), each containing 6 culture wells (25.4 mm diameter, 16 mm deep) (**Figure 11**). Situated within each well are four stainless steel "stationary posts" arranged orthogonally around a central channel in the floor of the culture well (1.9 mm deep). The device can thus accommodate a total of 12 rectangular samples (maximum dimensions approximately 25 mm x 7.5 mm x 2 mm), with each sample being positioned between the four stationary posts, orthogonal to the central channel (**Figure 12**). Cyclic flexural stimulation can be applied to each of the samples in the form of cyclic three-point flexure by an environmentally-sealed linear actuator (UltraMotion, Mattitick, NY). The piston of the actuator is rigidly coupled to a cross-arm in the form of a T-junction. Conversely, the cross-arm is rigidly coupled to the arm of each chamber. Each arm bifurcates and extends into a chamber (two penetrations per chamber). Both arms terminate in six fingers through which “flexure pins” can be inserted to bracket the rectangular samples in the middle. Therefore, each sample can be subjected to unidirectional or bi-directional three-point flexure. Frequency, amplitude, acceleration, and deceleration profiles can be developed using Windows-based Si Programmer software (Applied Motion Products, Watsonville, CA). The structural parts can be cold gas sterilized by ethylene oxide, and the bioreactor operates inside a humidified incubator.

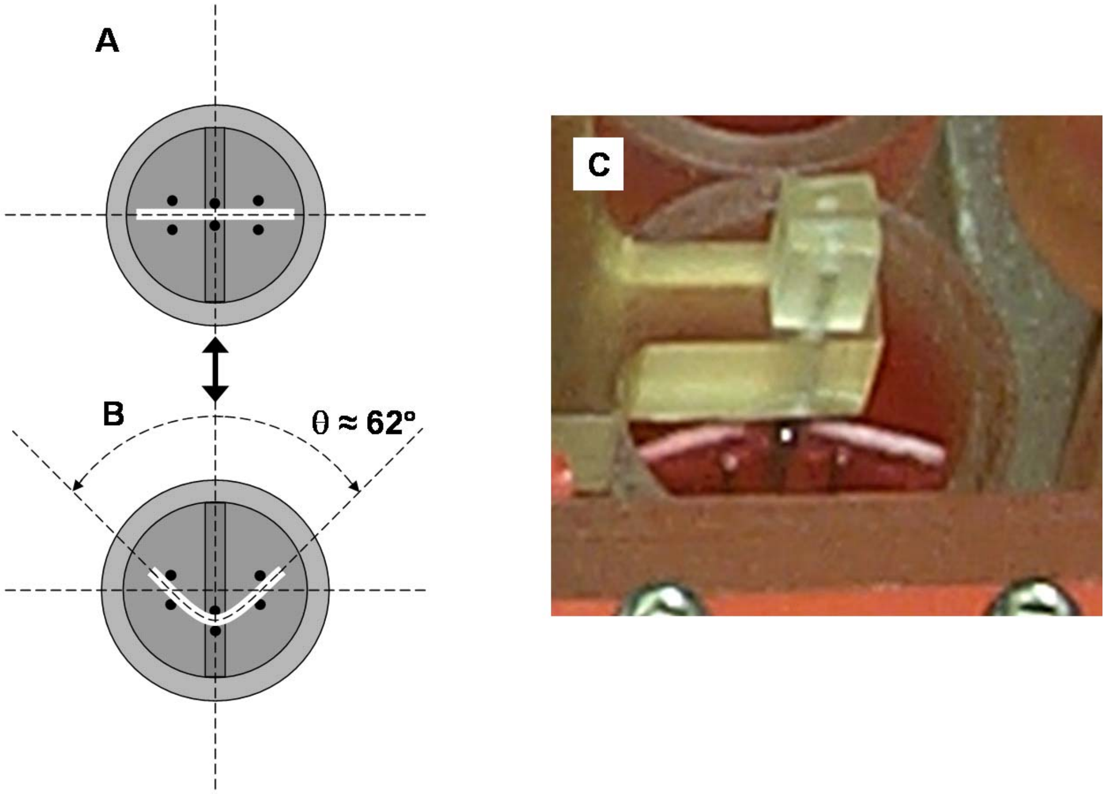

Figure 12 Schematic diagram of a representative culture well within the bioreactor. The scaffold sample (white bar) is situated between 4 stainless steel stationary posts (black dots), and bracketed from above by 2 centrally-positioned flexure pins (black dots). In the current study the linear actuator (not shown) cycled the flexure pins between the reference configuration (A) and the deformed configuration (B) at a frequency of 1 Hz and amplitude of 6.35 mm, corresponding with a flexure angle θ of approximately 62°. Photograph of an individual culture well (C).

2.2 THE EFFECTS OF CYCLIC FLEXURE ON TEHV SCAFFOLDS

2.2.1 Culture Medium

The culture medium used in these experiments was Dulbecco's Modified Eagle's Medium with 4.5 g/L glucose and L-glutamine supplemented with 10% fetal bovine serum (BioWhittaker, Walkersville, MD). Antibiotics were excluded in order to assess the sterility of the bioreactor.

2.2.2 Scaffolds

Scaffold materials consisted of a non-woven mesh of polyglycolic acid (PGA) fibers (Albany International Research, Mansfield, MA) dip-coated with poly-4-hydroxybutyrate (P4HB) (Tepha, Inc., Cambridge, MA), and a non-woven 50:50 blend mesh of PGA and poly-L-lactic acid (PLLA) fibers (Albany International Research, Mansfield, MA) dip-coated with P4HB. The PGA and PGA/PLLA scaffolds had an approximate fiber diameter of 0.012-0.015 mm and density of 69 mg/ml. Rectangular scaffold samples were cut to size (approximately 25 x 7.5 x 2 mm) and dipped briefly into a solution of P4HB in tetrahydrofuran (1% wt/vol), resulting in a P4HB coating following solvent evaporation. As described previously [32], P4HB is a bioresorbable thermoplastic that allows for scaffolds to be molded into any shape. Scaffolds were cold gas sterilized with ethylene oxide prior to use.

2.2.3 Flexure Experiments

A total of 60 scaffold samples were prepared for evaluation in this study (30 x PGA/P4HB, 30 x PGA/PLLA/P4HB). Two separate runs of the bioreactor were required to test all of the samples. In the first run, PGA/P4HB scaffold samples were loaded into the culture wells of the bioreactor under aseptic conditions (n=12). Control scaffold samples were loaded into identical culture wells maintained under static conditions inside a large Petri dish (n=12). In addition, samples of the virgin scaffold material (time = 0) were retained for flexure testing and scanning electron microscopy (n=6).

Approximately 6 ml of culture medium was added to each of the bioreactor and static control culture wells. The linear actuator was programmed to flex the scaffold samples at a rate of 1 cycle per second (1 Hz) in order to emulate the cardiac cycle. The center of each scaffold sample was displaced 6.35 mm in one direction, corresponding to a flexure angle of approximately 62º. The direction of flexure is referred to henceforth as "with-flexure" (WF), and the opposing direction is referred to as "against-flexure" (AF). After loading the bioreactor, the entire device was placed inside of a humidified incubator operating at 37 °C and 5% CO_2. The culture medium was not changed.

After 1 week (n=6) and 3 weeks (n=6) of cyclic flexure the scaffold samples were removed from the bioreactor under aseptic conditions to perform flexure testing and scanning electron microscopy. Corresponding control samples were removed from the static culture wells at each time point. In the second bioreactor run, PGA/PLLA/P4HB scaffold samples were loaded and incubated in the same manner as the PGA/P4HB scaffolds. After 3 weeks (n=6) and

5 weeks (n=6) of cyclic flexure the PGA/PLLA/P4HB scaffold samples were removed from the bioreactor, as well as the corresponding static control samples.

2.2.4 Bioreactor Operation and Sterility Results

The bioreactor demonstrated consistent operation throughout each of the two runs. Microscopic evaluation of the culture medium at each time point indicated that sterility was maintained throughout the course of each study (up to 5 weeks).

2.2.5 Effective Stiffness Measurement Methods

The device and methods used to measure the effective stiffness (E) of tissue samples have been described previously [62, 100]. Testing was performed in a bath of phosphate buffered saline at room temperature. In the case of cell-seeded scaffolds, testing was performed within 30 minutes post-culture. In brief, rectangular samples were marked with 5 to 10 black dots (~ 0.3 mm^2) on one long edge using a marker and subjected to three-point flexure by a calibrated flexure bar. The displacements of the sample markers, flexure bar marker, and a reference marker were recorded to video with a CCD camera and tracked using a custom C program (**Figure 13**-A, B). Based on the resolution, post coordinates, load, displacement, and marker coordinates, the program output the applied moment, M, and resulting change in curvature, $\Delta\kappa$ (**Figure 14**).

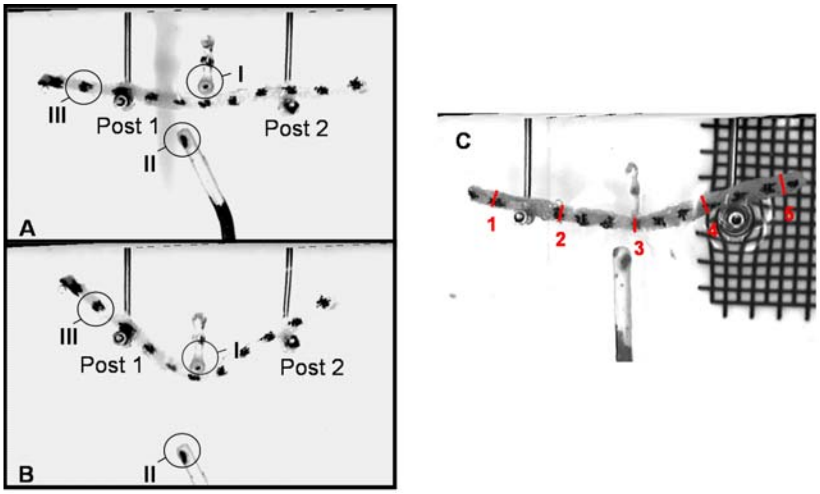

Figure 13 Effective stiffness testing video images. Recording starts with the sample in the horizontal, un-deformed reference state (A). During data analysis, the positions of the flexure bar (I), reference rod (II), and sample markers (III) are recorded throughout the entire breadth of the three-point flexure deformation (B). Representative thickness measurement image from SigmaScan Pro (SPSS, Inc., Chicago, IL) (C). Lines are traced across the thickness of the sample at five uniformly spaced locations along its length. The mean of the five line lengths was used as the thickness in the data analysis calculations.

The flexural rigidity, EI, was calculated by a least squares regression on M versus Δκ. Regression yields a linear relationship with a slope equal to EI, per the Bernoulli-Euler moment-curvature relationship [101]:

$$M = EI\Delta\kappa \tag{1}$$

The moment of inertia, I, was calculated from the following relation in which t and w are the thickness and width of the sample, respectively:

$$I = \frac{1}{12}wt^3 \tag{2}$$

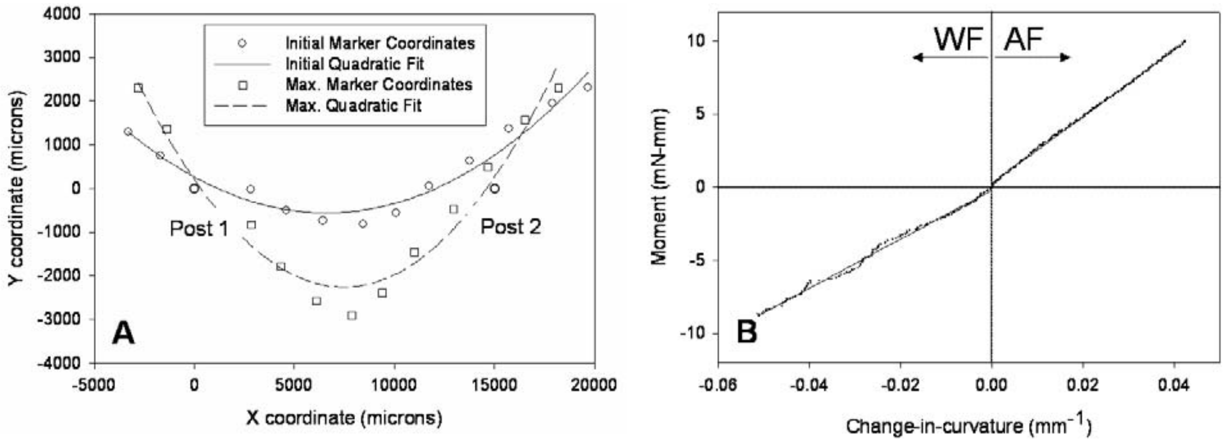

Figure 14 Representative marker position (A) and moment-curvature (B) plots output from the Matlab data analysis program.

Because non-woven PGA/PLLA scaffolds are highly compressible, t was measured using a calibrated digital image of each sample using SigmaScan Pro (SPSS, Inc., Chicago, IL) (**Figure 13**-C). The thickness, w, was measured using a slide caliper (accuracy ± 10 μm; The L.S. Starrett Co., Athol, MA), and E was calculated by dividing EI by I.

2.2.6 Scanning Electron Microscopy (SEM) Methods

One scaffold sample representing each flexed and static control time point (10 total) was prepared for scanning electron microscopy. Dry scaffold samples were attached to aluminum sample stubs and sputter coated with a thin layer of gold-palladium alloy (~3 nm thickness) in a Cressington 108auto sputter coater with a Cressington MTM-20 thickness controller (Cressington Scientific Instruments, Inc., Cranberry Twp., PA). Each scaffold sample was imaged at 40, 100, and 300-fold magnification at 5 kV on a JEOL JSM-6330F SEM (JEOL USA, Inc., Peabody, MA).

2.2.7 Effective Stiffness Results

E (mean ± SEM) of the virgin (time zero) PGA/P4HB scaffold samples was 844 ± 86 kPa (**Figure 15**). E values were observed to decrease over time for samples incubated under both flexed and static conditions. A significant decrease ($p < 0.01$) was observed in E between the virgin sample and the flexed sample at 1 week (-43%); no significant difference was observed between the virgin material and the static control sample at 1 week. Taken together, these data indicated that cyclic flexure has a significant effect on E compared to static incubation conditions at 1 week. Loss of stiffness was incurred by both static (-82%) and flexed (-91%) by 3 weeks, with a significant difference between groups ($p < 0.05$).

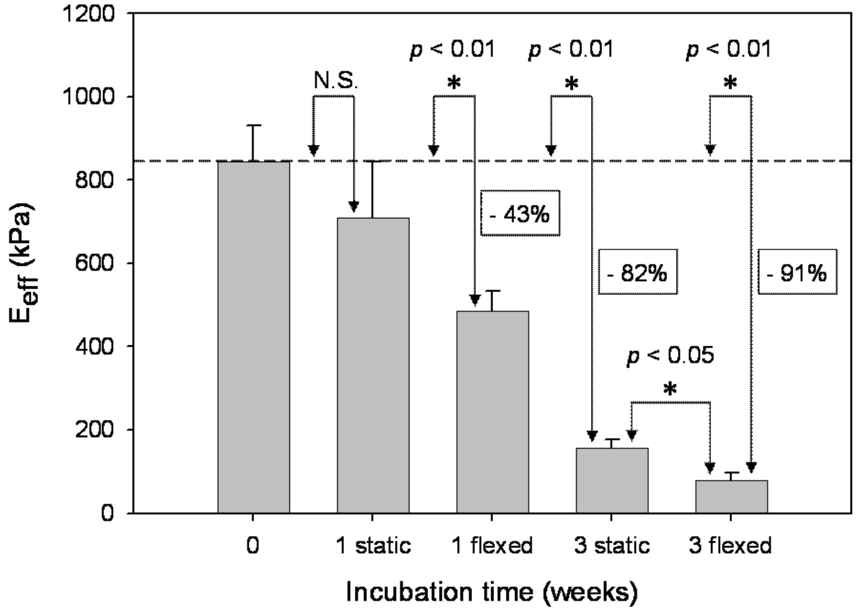

Figure 15 Effective stiffness (E) of PGA/P4HB scaffolds.

E of the virgin PGA/PLLA/P4HB scaffold samples was 1687 ± 151 kPa (**Figure 16**), about twice that of the PGA/P4HB. There was no significant difference in the static control samples between times 0, 3, and 5 weeks. There was a significant decrease in E between the flexed and static control samples at 3 weeks (-72%) and 5 weeks (-76%). There was not any significant difference in E between the flexed samples at 3 and 5 weeks.

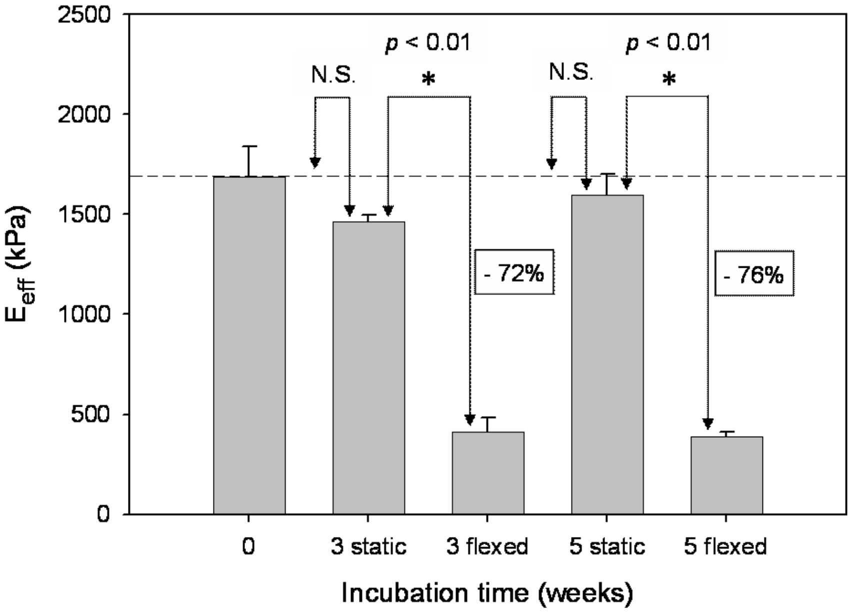

Figure 16 E of PGA/PLLA/P4HB scaffolds.

The effective stiffness ratio was calculated as the ratio of E measured in the "with-flexure" (WF) direction divided by that measured in the opposing "against-flexure" (AF) direction. An effective stiffness ratio of unity indicates isotropic flexural behavior, whereas any significant deviation from unity would suggest anisotropic flexural behavior. The effective stiffness ratio of the PGA/PLLA/P4HB scaffold samples is depicted in **Figure 17**.

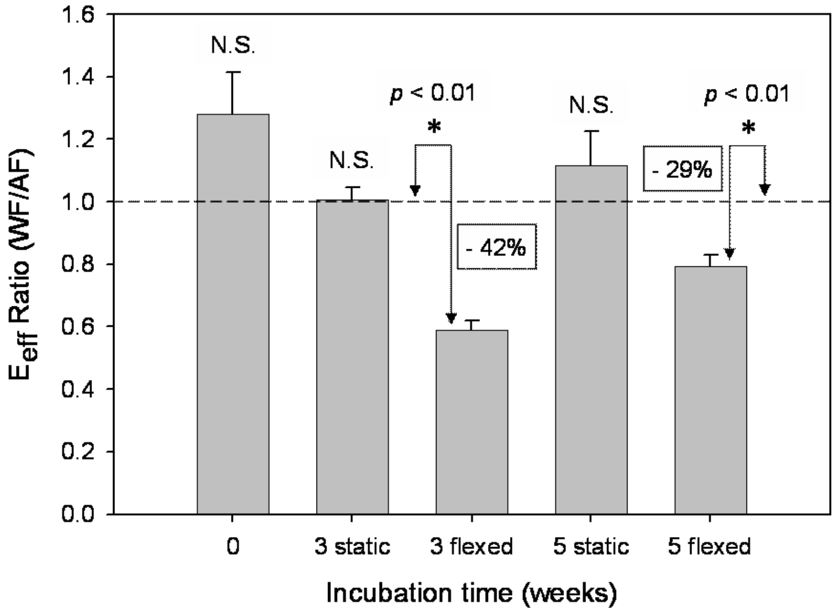

Figure 17 E ratio of PGA/PLLA/P4HB scaffolds.

Static control samples did not exhibit a statistically significant deviation from one, indicating that they exhibited isotropic flexural behavior. The effective stiffness ratio of flexed samples, however, exhibited a significant deviation from one (-42%) at 3 weeks and 5 weeks (-29%) ($p < 0.01$), indicating that these samples were stiffer when flexed in the "against-flexure" direction. The effective stiffness ratio of flexed and static PGA/P4HB samples did not deviate significantly from 1, indicating isotropic behavior.

2.2.8 SEM Results

Representative SEM images are depicted for comparison (**Figure 18**). The fiber architecture of the virgin scaffold materials appeared to be random within and across samples (data not shown), the P4HB coating did not appear to be uniform over the fiber structure, but rather appeared as sparsely distributed aggregates (**Figure 18**-A, D), fiber diameter did not appear to diminish over three weeks (PGA/P4HB) or five weeks (PGA/PLLA/P4HB), fibers appeared to fragment during incubation, and this fragmentation appeared to be more pronounced in the cyclically flexed PGA/P4HB samples (**Figure 18**-F).

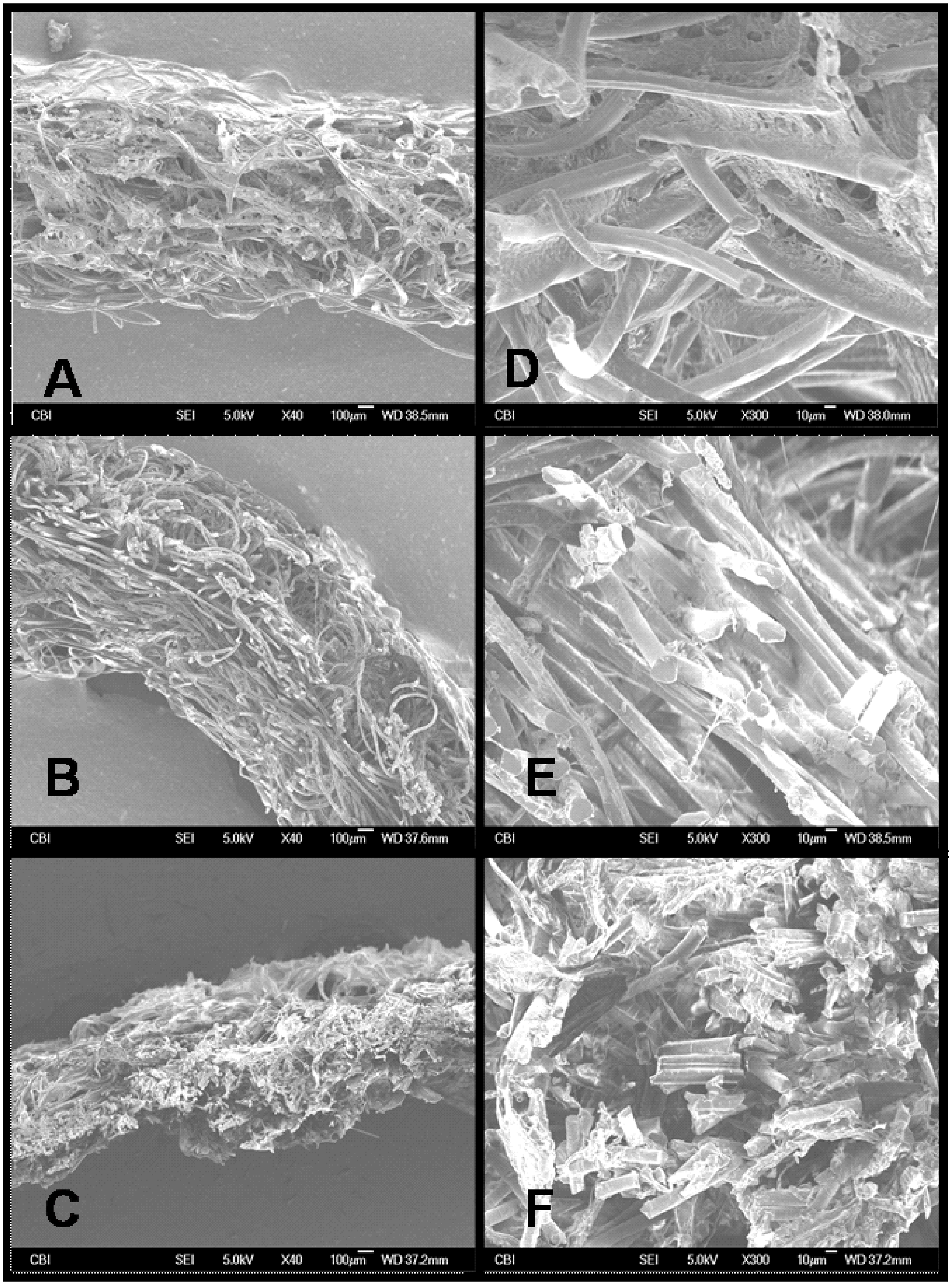

Figure 18 SEM images of scaffolds. Note the fragmentation of fibers in cyclic flexed PGA/P4HB (F).

2.3 DISCUSSION

In order to facilitate the systematic evaluation of candidate scaffolds and constructs, we developed a bioreactor for the incubation of biomaterial samples under conditions of cyclic 3-point flexure, a simple mode of flexural stimulation. While cyclic 3-point flexure is not identical to the mode of dynamic flexure exhibited by native heart valves *in vivo*, or by a TEHV in a pulse-duplicator, it allows us to isolate the effect of flexure from other potential modes of stimulation, such as pulsatile pressure or shear stress. To our knowledge, the bioreactor described herein is the first device aimed to study the independent effect of dynamic flexure on TEHV biomaterials. In these first experiments we have demonstrated the operation of the bioreactor and its ability to maintain sterility for at least 5 weeks in an incubator environment. In addition, we implemented the bioreactor to investigate the effect of dynamic flexure on the E of two different TEHV scaffold materials, PGA/P4HB and PGA/PLLA/P4HB.

PGA/P4HB and PGA/PLLA/P4HB were chosen primarily because they are currently being evaluated as candidate scaffolds for the fabrication of TEHV [32]. Based on recent studies which evaluated the effects of constant fluid flow [102] and dynamic compressive loading [103] on similar scaffold materials, we hypothesized that dynamic flexure in a non-flowing environment may augment the bulk degradation rate of the polymers or result in fatigue of the polymer fibers, with concomitant losses in effective stiffness. Moreover, because these non-woven fiber meshes scaffolds have been modified by P4HB dip-coating, we further hypothesized that they may be more susceptible to fatigue (e.g., disruption of dip-coating) under conditions of dynamic stimulation, potentially giving rise to unique mechanical properties.

In accordance with our hypotheses, incubation under dynamic flexure led to a trend of decreased E compared to static conditions in both scaffolds, and induced directional anisotropy ($p < 0.01$) in PGA/PLLA/P4HB samples at 3 and 5 weeks. SEM images of these samples hinted at some of the structural features and changes that may have been responsible for the E results. The heterogeneity observed in the virgin scaffold fiber structure, coupled with the observation that P4HB does not uniformly coat the samples, helps explain the variability in E measured for the virgin (time zero) replicates. Fragmentation of fibers, as opposed to diminishing fiber diameter and mass loss, appears to be a primary mechanism for loss of E in dynamically flexed PGA/P4HB samples. It is not clear from this study if dynamic flexure augmented the bulk degradation rate of the polymers, making them more susceptible to fracture. Interestingly, significant fragmentation of fibers was not observed in any of the PGA/PLLA/P4HB scaffolds, indicating that PLLA fibers may shield the PGA fibers from mechanical disruption.

Recent studies in our lab have demonstrated that uncoated PGA/PLLA scaffolds exhibit isotropic flexural behavior both at time zero, and after 3 weeks of static or dynamic flexural incubation (unpublished observations). Furthermore, the effective stiffnesses of these uncoated PGA/PLLA scaffolds, both at time zero, and after 3 weeks of static or dynamic flexural incubation, were approximately equal to those of the 3 week dynamically flexed PGA/PLLA/P4HB scaffolds in the present study. Collectively, these observations indicate that the contribution of the P4HB coating to the effective stiffness of the PGA/PLLA/P4HB scaffolds is removed by 3 weeks of dynamic flexural incubation. Disruption of the P4HB bonding between the fibers could potentially explain this behavior, however this could not be observed from the electron micrographs. These findings imply that P4HB dip-coating may be useful in modulating the response of non-woven PGA/PLLA scaffold flexural properties to dynamic flexure. Hypothetically, properties of an anatomical TEHV scaffold might be modified by P4HB dip-coating such that regions of the scaffold subjected to dynamic flexure (e.g., the leaflets) become more compliant, while regions of the scaffold not subjected to dynamic flexure (e.g., the aortic root) retain their stiffness. Further studies on anatomical TEHV scaffolds incubated in pulse duplicators would be necessary in order to conclusively demonstrate this behavior.

Non-woven PGA and PLLA scaffolds have been widely applied in cardiovascular, cartilage, and soft tissue engineering [61, 104-107]. As the structural integrity of a TEHV scaffold is critical for acute hemodynamic function, it is imperative to evaluate the mechanical properties of candidate TEHV scaffold materials under controlled deformation modes resembling those that manifest *in vivo*. Moreover, future advances in tissue engineering will likely stem from an improved understanding of the biomechanics of tissue growth and remodeling. Thus, the flexure bioreactor can be utilized to evaluate candidate TEHV scaffolds and constructs, as well as to investigate the underlying mechanisms by which mechanical loading influences tissue development.

2.4 EFFECTS OF CELL SEEDING ON CANDIDATE TEHV SCAFFOLDS

2.4.1 Scaffolds.

Scaffolds were a non-woven 50:50 blend of PGA and PLLA fibers (Albany International Research, Mansfield, MA). The PGA/PLLA scaffolds had an approximate fiber diameter of 0.012-0.015 mm and density of 61.75 mg/ml. Rectangular scaffold samples were cut to size (25 x 7.5 x 1 mm) and the initial (prior to sterilization) effective stiffness (E) of each sample was measured using a three-point flexure test (see Effective stiffness measurement). Scaffolds were then cold gas sterilized with ethylene oxide prior to use.

2.4.2 Culture Medium.

The culture medium was Dulbecco's Modified Eagle's Medium with 4.5 g/L glucose and L-glutamine (GIBCO™, Invitrogen Corporation, Grand Island, NY) with 10% fetal bovine serum (GIBCO™), 1% antibiotic-antimycotic (GIBCO™), and 2 ng/ml human recombinant basic fibroblast growth factor (bFGF; BD Biosciences, Bedford, MA). The medium was sterile filtered using a vacuum filtration unit (0.2 μm polyethersulfone (PES) membrane; Nalge-Nunc International, Rochester, NY).

2.4.3 Primary Cell Isolation.

Ovine vascular smooth muscle cells (SMC) were isolated and expanded as described previously [108, 109]. In brief, a 1 cm segment of carotid artery was harvested from an adult Dover sheep. The media was isolated by surgically clearing the adventitia, opening the segment longitudinally, and wiping the endothelium from the luminal surface with sterile gauze. The media was minced with scissors into small pieces (~ 1 mm^2) and placed into polystyrene tissue culture dishes (100 x 20 mm; BD Falcon™, BD Biosciences, Franklin Lakes, NJ) containing culture medium. After 7-10 days in a humidified cell culture incubator operating at 37°C and 5% CO_2, cells migrated from the minced tissue to form a confluent layer on the culture dish. SMC were characterized by immunohistochemical staining using a mouse monoclonal antibody to human SMC α-actin as the primary (Dako Corp., Carpinteria, CA), and a fluorescein isothiocyanate (FITC)-conjugated rabbit antibody to mouse IgG as the secondary (Dako Corp.).

2.4.4 Cell Expansion and Seeding.

The seeding apparatus and methods used in this study were adapted from Sutherland et al [108] and Nasseri et al [109]. One vial of SMC (approximately 7.5 x 10^6 cells, passage 9) cryo-preserved in culture medium supplemented with 5% dimethyl sulfoxide (DMSO; Sigma, St. Louis, MO) was thawed, resuspended in culture medium, and plated into three 185 cm^2 flasks (Nuclon™Δ SoLo flask; Nalgene Labware). After two 1:3 and one 1:2 serial passages (approximately 28 days), a total of 54 confluent 185 cm^2 flasks (passage 13) were ready for use. The flasks were trypsinized (0.25% trypsin, 1 mM EDTA; GIBCO™), and the SMC were resuspended to yield a seeding solution of approximately 8 x 10^6 cells/ml, as determined by cell counts with a hemacytometer (Hausser Scientific, Horsham, PA).

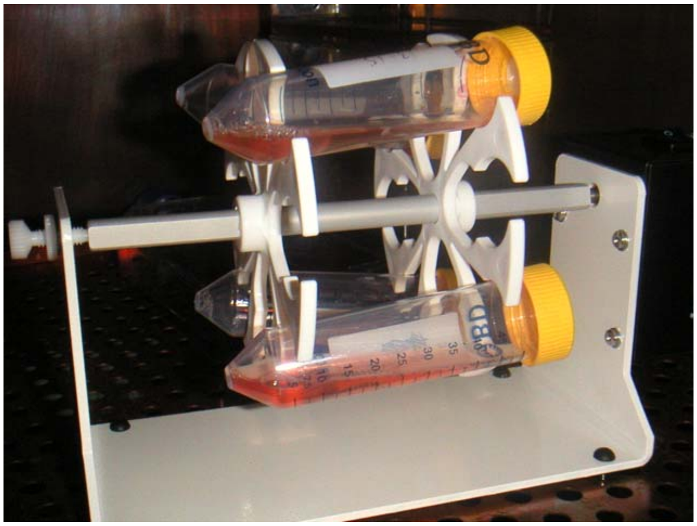

Figure 19 Photograph of the cell seeding apparatus.

Three scaffolds were placed into each of 4 seeding tubes. Each seeding tube consisted of a 50 cc centrifuge tube (Product # 91050; TPP, Trasadingen, Switzerland) fitted with a vent filter cap from a 50 cc tissue culture tube(Product # 91253; TPP), thereby allowing for gas exchange during seeding. Seeding solution (12 ml) was added to each tube to yield a seeding density of approximately 17 x 10^6 cells/cm^2. The tubes were rotated at 8 rpm (Labquake rotisserie rotator, Barnstead-Thermolyne, Dubuque, IA) inside an incubator operating at 37°C and 5% CO^2 for 30 hours, with the medium was changed every 6 hours due to the high cell density (**Figure 19**).

2.4.5 DNA Quantification Methods.

DNA was quantified by a technique adapted from Kim et al [110]. For each assay, thin samples (~ 25 x 1 x 1 mm) were cut from SMC-seeded scaffolds along their long axis and weighed (average wet weight 0.03 g) prior to extraction. Each sample was placed in a microcentrifuge tube and extracted in 1 ml of 0.125 mg/ml papain solution for 10 hours in a 60°C water bath. The 0.125 mg/ml papain solution was made immediately prior to use by adding L-cysteine dihydrochloride (Sigma) to a phosphate buffered EDTA solution (PBE) to a concentration of 10 mM, clarifying the solution using a syringe-driven filter (0.2 µm Millex®-LG PTFE membrane; Millipore, Bedford, MA), and adding papain (minimum 10 units/mg (P4762); Sigma) to a concentration of 0.125 mg/ml. The PBE solution was made beforehand by adding sodium phosphate dibasic (Sigma) and ethylenediaminetetraacetic acid (EDTA; Sigma) to deionized water at concentrations of 100 mM and 10 mM, respectively. The PBE solution was balanced to pH 6.5 with 0.5 N hydrochloric acid (Sigma) and sterile filtered using a vacuum filtration unit (0.2 µm PES membrane; Nalgene Labware). The extracts were assayed using the

PicoGreen dsDNA quantitation kit (Molecular Probes, Eugene, OR) per the manufacturer's instructions and using the blue channel of a TBS-380 Mini-Fluorometer (Turner Biosystems, Sunnyvale, CA).

2.4.6 Extracellular Matrix Analysis Methods.

Collagen, elastin, and sulfated glycosaminoglycans (S-GAG) were assayed by techniques adapted from Brown et al [105]. For each assay, thin samples (~ 25 x 1 x 1 mm) were cut from SMC-seeded scaffolds along their long axis and weighed (average wet weight 0.03 g) prior to extraction.

Total collagen was extracted from samples using a solution of 0.5 M acetic acid (Sigma) and pepsin (1 mg/ml Pepsin A (P-7000); Sigma). Each sample was placed in a microcentrifuge tube and incubated in 1 ml of extraction solution overnight (~ 16 hours) on a rocker (Orbitron Rotator I™; Boekel Scientific, Feasterville, PA) in a refrigerator at 2-8°C.

Elastin was extracted using a hot oxalic acid treatment. Samples were placed in 0.5 ml of 0.25 M oxalic acid (Sigma) in glass centrifuge tubes and incubated on a hot plate at approximately 85°C for 1 hour. Subsequently, the extracts were centrifuged at 3000 x g for 10 minutes at 4°C. The supernate was collected and the entire treatment was repeated two more times. The supernates from the three oxalic acid treatments were pooled, loaded onto Centricon RC/YM-3 centrifugal filters (Millipore, Bedford, MA), and centrifuged at 3000xg for an hour at room temperature. The concentrate was solublized in cold (< 5°C) Precipitating Reagent (Fastin™ assay kit, Biocolor Ltd., Newtownabbey, N. Ireland).

Proteoglycans and S-GAG were extracted using a solution of 4 M guanidine-HCl (Sigma) and 0.5 M sodium acetate (Sigma). To minimize proteolysis during the extraction, 100 μl of protease inhibitor cocktail stock solution was added to each extraction solution. The stock solution was prepared according to the manufacturer's recommendations by dissolving one Complete Mini Protease Inhibitor Tablet™ (Roche Diagnostics, Basel, Switzerland) in 1.5 ml of deionized water. Each sample was incubated in 1 ml of extraction solution overnight on a rocker table (Boekel Scientific) in a refrigerator at 2-8°C. Following the extraction steps, the collagen, elastin, and S-GAG extracts were assayed according to the guidelines provided with the Sircol™, Fastin™, and Blyscan™ assay kits, respectively (Biocolor Ltd., Newtownabbey, N. Ireland) using a Genesys 20 spectrophotometer (Thermo Spectronic, Rochester, NY).

2.4.7 DNA Quantification Results

The 30 hour seeding period yielded a DNA concentration of 536 ± 38 μg/g wet weight. Assuming a DNA content of 7.6 pg/cell [111], an average of $30 \pm 2 \times 10^6$ cells/scaffold were retained. Based on the theoretical seeding density of 17×10^6 cells/cm^2 determined from hemacytometer counts, these results suggest the seeding efficiency exceeded 90%.

2.4.8 Extracellular Matrix Quantification Results

Collagen was not detected biochemically at the 30 hour time point, while the S-GAG concentration was 1393 ± 145 μg/g wet weight. It is noteworthy that S-GAG concentration correlated strongly with DNA concentration within each group (data not shown). Elastin was not detected biochemically at the 30 hour or 3 week time points.

2.4.9 Effective Stiffness Measurement Results

E results for the unseeded scaffolds are summarized in **Figure 20**. The initial E (prior to sterilization) was 234 ± 27 kPa in the flex group and 249 ± 31 kPa in the static group (N.S.). Following 3 weeks of incubation, E of unseeded scaffolds was 249 ± 36 kPa in the flex group and 252 ± 20 kPa in the static group (N.S.). There were no significant differences in E between any of the unseeded scaffold sample groups. E results for the SMC-seeded scaffolds are summarized in **Figure 24**. The initial E (prior to sterilization) was 184 ± 22 kPa in the flex group and 164 ± 21 kPa in the static group (N.S.).

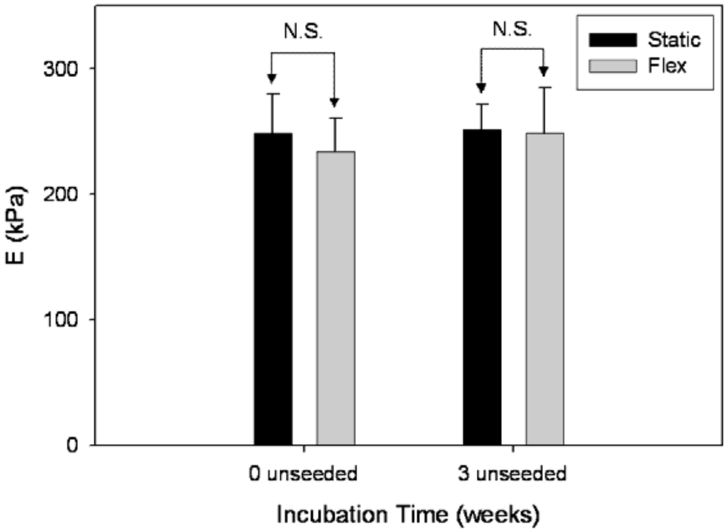

Figure 20 E results for unseeded scaffolds. Values presented are the mean of the measurements for 6 samples. Error bars indicate standard error. Insignificant comparisons are designated by "N.S.". Note that the non-woven 50:50 blend PGA/PLLA scaffolds exhibited no significant changes in E after 3 weeks of incubation under static or cyclic flexure conditions.

2.5 EFFECTS OF CYCLIC FLEXURE ON TEHV DEVELOPMENT

2.5.1 Cyclic Flexure Experiments

A total of 30 scaffolds were prepared for evaluation, and two separate cell expansions were conducted to generate the required number of SMC. With cells harvested from the first expansion, scaffolds (n=6) were seeded for 30 hours and immediately subjected to flexure testing and DNA and ECM quantification (see below), thus establishing a baseline for subsequent comparisons. With cells from the second expansion, scaffolds (n=12) were seeded as described previously while unseeded control scaffolds (n=12) were maintained under identical conditions in cell-free culture medium. Scaffolds were incubated under static conditions for 4 days in 6 ml of medium in 6-well plates (Costar Ultra Low Attachment; Corning, Corning, NY). Following this period, SMC-seeded scaffolds (n=6) and unseeded control scaffolds (n=6) were loaded into the bioreactor and subjected to unidirectional cyclic flexure at a frequency of 1 Hz and a central displacement of 6.35 mm (corresponding to a flexure angle of approximately 62□) for 3 weeks (flex group). The remaining SMC-seeded scaffolds (n=6) and unseeded control scaffolds (n=6) were maintained under static conditions for 3 weeks (static group). The bioreactor was removed from the incubator once daily (~ 30 minutes) to change the medium.

2.5.2 Histology and Immunohistochemistry Methods.

Histology was performed as described previously [8]. In brief, a thin sample of each SMC-seeded scaffold (~ 25 x 1 x 1 mm) was fixed in 10% formalin and embedded in paraffin. Serial sections (6 μm) were stained with hematoxylin and eosin (H&E) for morphology, and with a modified Movat pentachrome stain for ECM components. Immunohistochemical staining (Dako Corp.) was graded with respect to SMC α-actin and vimentin (- = no appreciable staining; + = weak staining < 50% of cells; ++ = strong in 10-50% of cells; and +++ = strong > 50% of cells).

2.5.3 Histology and Immunohistochemistry Results

H&E and Movat pentachrome stained sections revealed dense cellularity in the periphery (outermost 25%) of the scaffold thickness, with sparser cellularity in the central region (**Figure 21**). The flex group appeared to exhibit a more homogenous distribution of cells across the thickness compared with the static group, prompting quantification of the transmural cell distribution (see Transmural cell distribution analysis). Furthermore, the static group appeared to exhibit more cell necrosis than the flex group (data not shown). Movat pentachrome stained sections revealed the ECM to consist predominantly of proteoglycans (light blue), with sparse aggregates of collagen (yellow) (**Figure 21**). Elastin was not observed histologically. Immunohistochemical staining revealed a readily observable increase in vimentin expression in the flex group (+++; **Figure 22**D) compared with the static group (+; **Figure 22**C). SMC α-actin expression levels were comparable between groups (+++; **Figure 22**A, B).

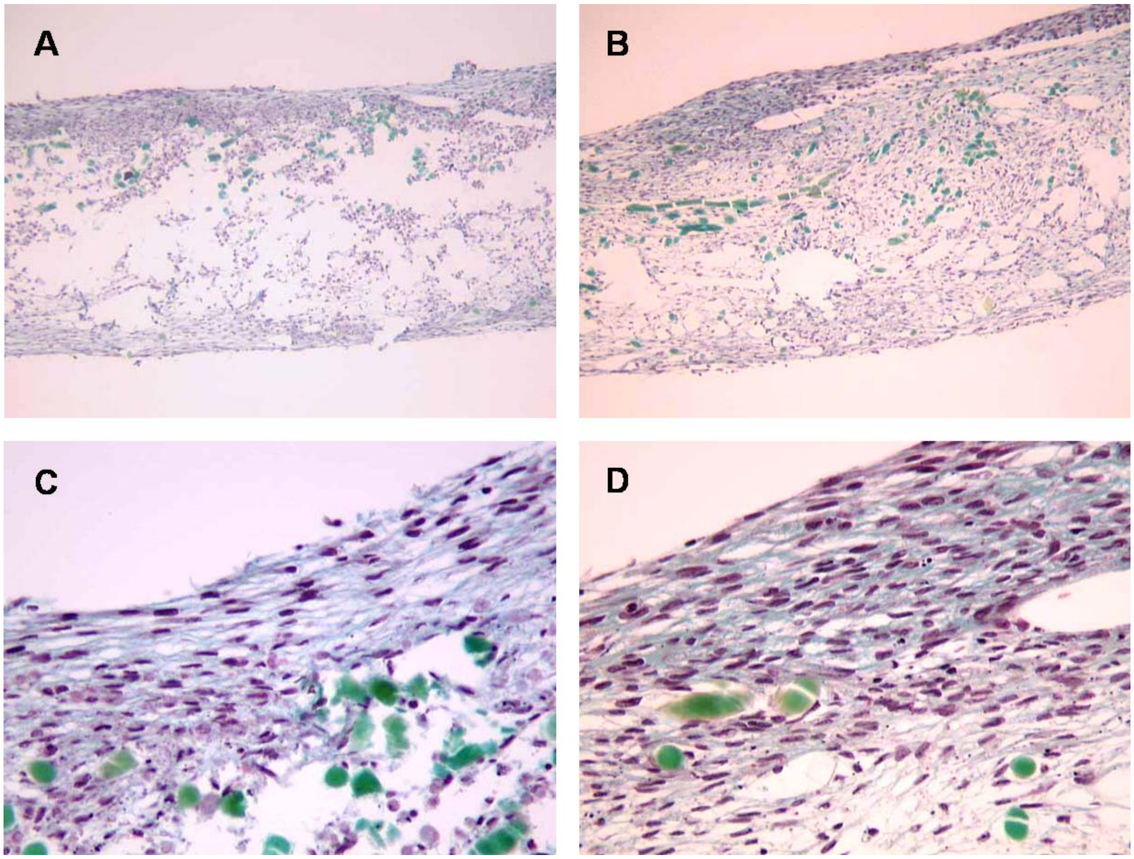

Figure 21 Modified Movat pentachrome stained sections of SMC-seeded scaffolds after 3 weeks of incubation (100x (A, B) and 400x (C, D) original magnification). The tissue consisted predominantly of cells (dark purple), proteoglycans (light blue), and collagen (yellow) (note that the green staining represents segments of scaffold fibers retained in the section). Tissue development in the periphery of the scaffold thickness (outermost 25%) was comparable between the static (A, C) and flex group (B, D). More tissue development was observed in the central region in the flex group (B) compared to the static group (A).

2.5.4 DNA Quantification Results

Following 3 weeks of incubation, the DNA concentration decreased 36% to 344 ± 5 μg/g wet weight in the flex group ($p < 0.01$) and decreased 42% to 307 ± 23 μg/g wet weight in the static group ($p < 0.01$), with no significant difference (N.S.) between the flex and static groups (**Figure 23**).

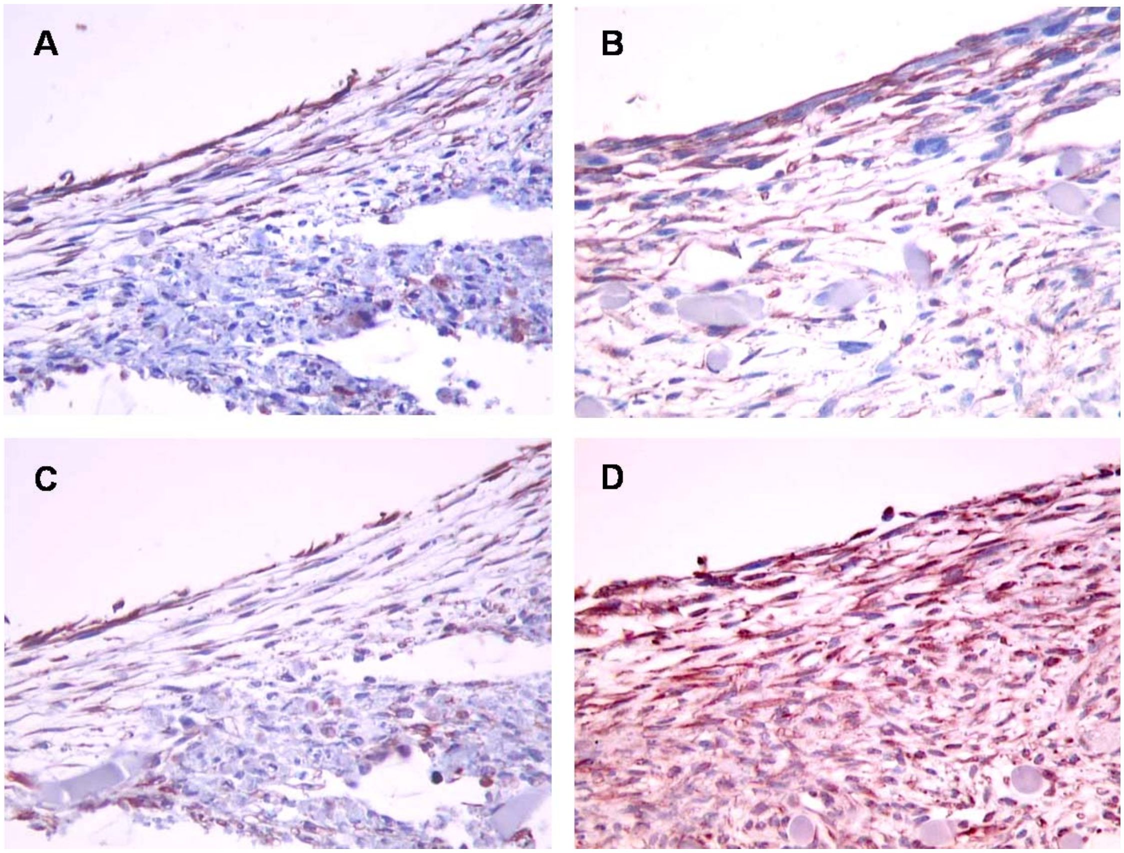

Figure 22 Histology and immunohistochemistry of TEHV. Note the more homogeneous transmural cell distribution and the dramatic upregulation of vimentin expression with cyclic flexure (D and F) compared to static (A and C), respectively.

2.5.5 Extracellular Matrix Quantification Results

By 3 weeks incubation, the collagen concentrations were 893 ± 133 and 546 ± 111 μg/g wet weight in the flex and static groups, respectively, indicating a 63% increase in collagen in the flex group compared to the static group ($p < 0.05$) (**Figure 23**). The S-GAG concentration decreased 45% to 769 ± 151 μg/g wet weight in the flex group ($p < 0.01$) and decreased 41% to 819 ± 93 μg/g wet weight in the static group ($p < 0.01$), with no significant difference between the flex and static groups (**Figure 23**). Elastin was not detected biochemically at any time point.

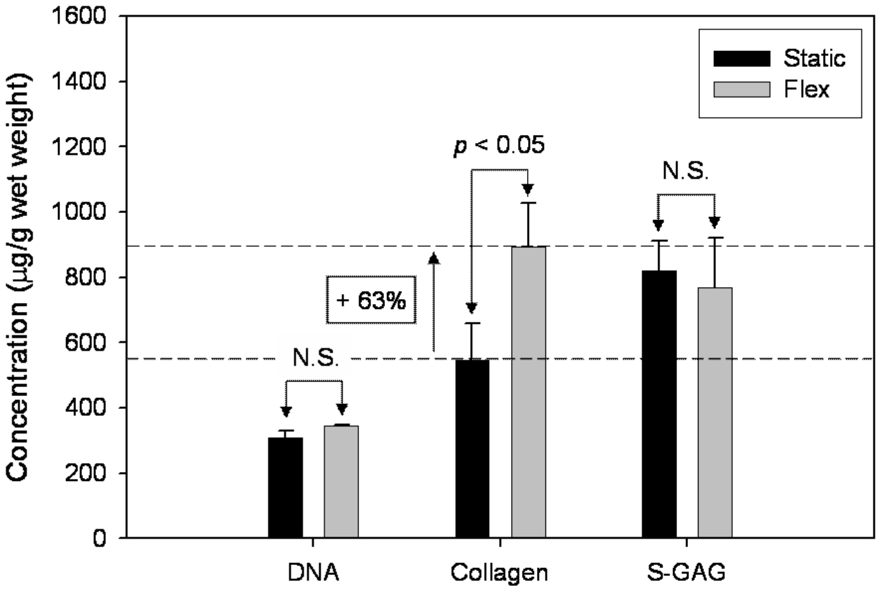

Figure 23 Composition of SMC-seeded scaffolds after 3 weeks of incubation. Values presented are the mean of the measurements for 6 samples. Error bars indicate standard error. Insignificant comparisons are designated by "N.S." The flex group exhibited a 63% increase in collagen compared to the static group ($p < 0.05$), with DNA and S-GAG concentrations comparable between groups. No elastin was detected at the 3 week time point.

2.5.6 Effective Stiffness Measurement Results

E results for the unseeded scaffolds are summarized in **Figure 20**. The initial E (prior to sterilization) was 234 ± 27 kPa in the flex group and 249 ± 31 kPa in the static group (N.S.). Following 3 weeks, E of unseeded scaffolds was 249 ± 36 kPa in the flex group and 252 ± 20 kPa in the static group (N.S.).

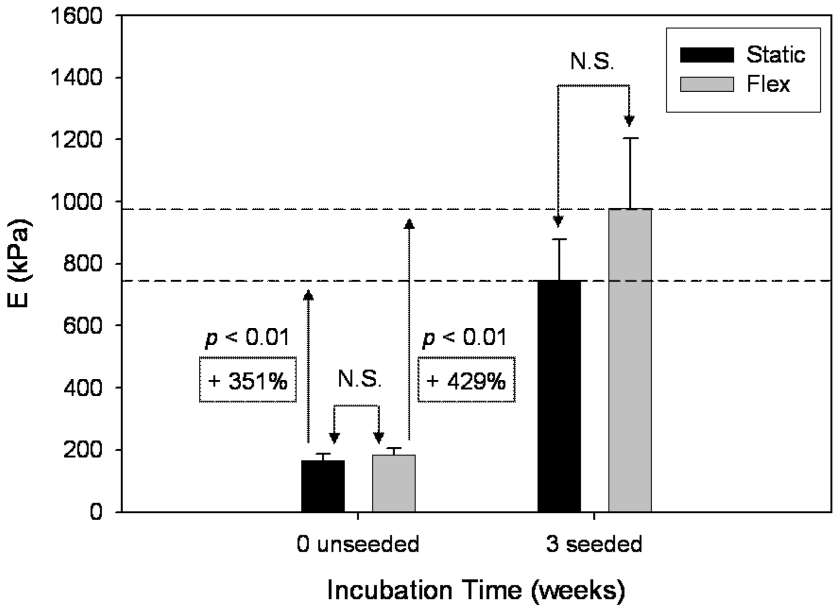

Figure 24 E results for SMC-seeded scaffolds. Values presented are the mean of the measurements for 6 samples. Error bars indicate standard error. Insignificant comparisons are designated by "N.S.". E of SMC-seeded scaffolds increased 429% in the flex group ($p < 0.01$) and 351% in the static group ($p < 0.01$), with a trend of increased E in the flex group (N.S.).

Following 3 weeks of incubation, E of SMC-seeded scaffolds increased 429% to 978 ± 228 kPa in the flex group ($p < 0.01$) and increased 351% to 748 ± 130 kPa in the static group ($p < 0.01$), with a trend of increased E in the flex group (N.S.) (**Figure 24**). It should be noted that there was no significant difference in the initial E (prior to sterilization) between the scaffolds that were ultimately seeded with SMC and the unseeded scaffolds.

The mean E was plotted versus mean collagen concentration across all sample groups, and a positive linear relationship was observed ($r^2 = 0.991$). To assess the generality of the relationship, data from a TEHV cultured for 9 weeks in a roller bottle was included in the regression, yielding an increase in the coefficient of determination ($r^2 = 0.996$) (**Figure 25**). Note the 9-week TEHV was made with non-woven PGA/PLLA, but with a different cell (ovine bone marrow stem cells) [34].

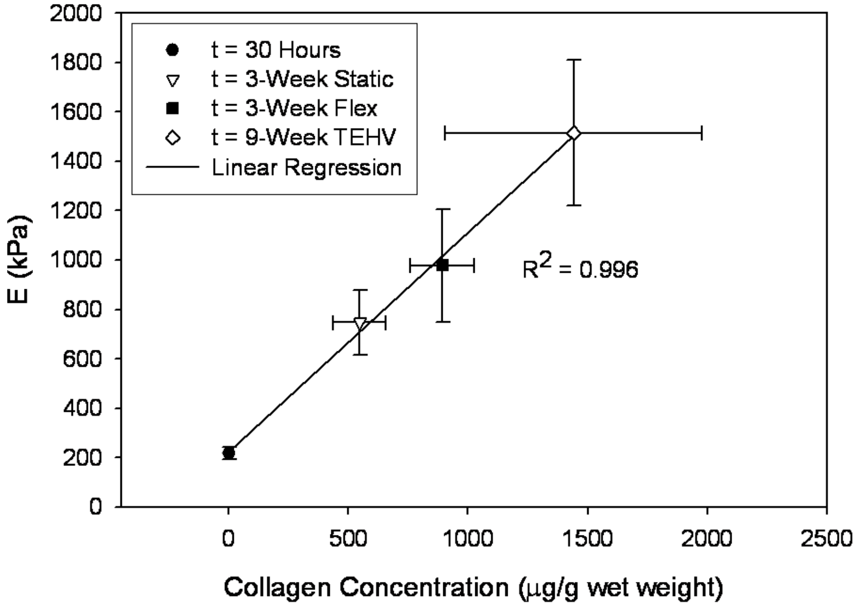

Figure 25 E results for SMC-seeded scaffolds plotted versus collagen concentration. Values presented are the mean of the measurements for 6 samples. Error bars indicate standard error. In order to assess the generality of the relationship between E and collagen concentration, supplementary results from a TEHV cultured for 9-weeks in a roller bottle were included in the regression. Note that the 9-week TEHV was constructed using the same PGA/PLLA scaffold used in the current study, but with a different cell type (bone marrow-derived stem cells). These results tentatively suggest that E depends primarily on the gross collagen concentration, and that given a comparable collagen output per cell, a variety of cell types may give rise to TEHV exhibiting similar mechanical properties.

2.5.7 Transmural Cell and ECM Distribution Analysis Methods.

High-magnification (400x) images were necessary to colorimetrically distinguish cell nuclei from the surrounding ECM. Panoramic images of transmural cross-sections were concatenating from ~ 15 digitized images of Movat-stained sections into a single image using Image Expert 2000 (Jasc Software, Inc., Eden Prairie, MN). Red-green-blue (RGB) color values corresponding with cell nuclei were determined using SigmaScan Pro (SPSS, Inc., Chicago, Il), and the images were analyzed using a program written in Matlab (The MathWorks, Natick, MA) to locate the coordinates of the cell nuclei with respect to the edges of the transmural cross-section. Each data set was analyzed by a histogram of normalized cell count versus normalized transmural thickness. The transmural thickness was normalized to itself (total normalized transmural thickness = 100%) and divided into twenty 5% increments. The normalized cell count was then calculated for each increment by dividing the number of cells located within that particular increment by the total number of cells counted over the entire transmural cross-section. One cross-section from the center of a 6 μm histological section was analyzed for each of 12 samples.

2.5.8 Transmural Cell and ECM Distribution Results.

A histogram of normalized cell count versus normalized transmural thickness is depicted in **Figure 26**. The total cells counted per transmural cross-section was 287 ± 35 cells in the flex group and 276 ± 31 cells in the static group (N.S.). Best-fits to the histograms were obtained with quadratic equations for the flex (r^2 = 0.223) and the static groups (r^2 = 0.896). The normalized cell count was significantly different between in 55% of the 20 transmural thickness increments, with the flex group exhibiting a lower count in the peripheral 25% of the thickness, and a higher count in the central 50%.

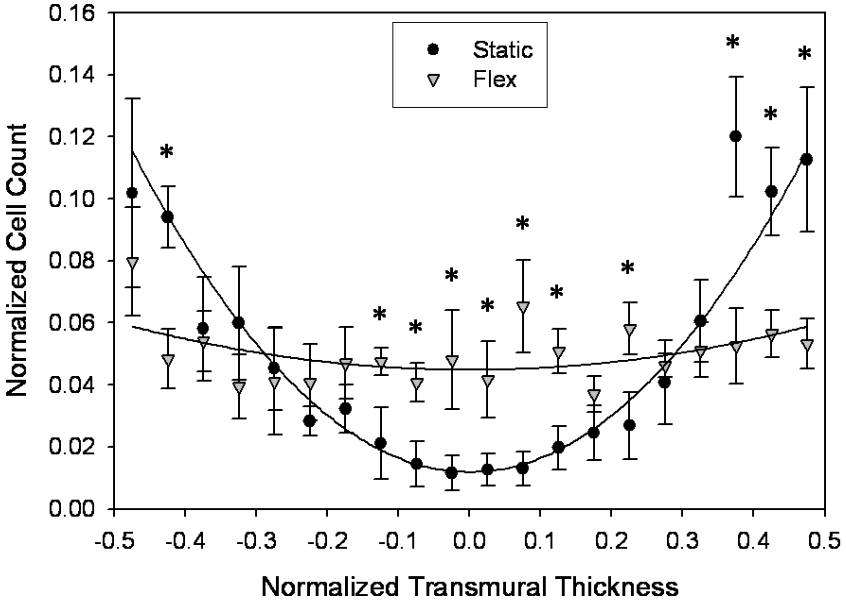

Figure 26 Histogram of normalized cell count versus normalized transmural thickness. Significant comparisons ($p < 0.05$) are indicated by asterisks. Note that the normalized cell count was significantly different between groups in 55% of the 5% transmural thickness divisions, with the flex group consistently exhibiting a lower normalized cell count in the peripheral 25% of the transmural thickness, and a higher normalized cell count in the central 50% of the transmural thickness.

2.6 DISCUSSION

The advent of a functional TEHV could represent a milestone in the treatment of valvular disease, in particular for women, who carry an elevated risk of valve-related thrombosis and anticoagulant-related embryopathy during pregnancy [24, 25], and for pediatric patients, in whom the growth potential of TEHV could mitigate the need for reoperations [19, 20, 30]. However, despite early experimental trials in humans [41, 112], questions outstand regarding the maturation and homeostasis of TEHV which must be addressed before further such trials are warranted [96].

BHV fabricated from glutaraldehyde-treated soft tissues are non-viable and susceptible to degeneration via calcification and fatigue [27, 113]. Living TEHV, in contrast, are hypothesized to have the capacity to actively remodel in response to *in vitro* and *in vivo* pulsatile flow conditions [8, 56, 59, 60]. This response is presumably due to the stimulatory effects of mechanical forces on the constituent cells; a phenomenon which has been documented in a variety of tissue culture and tissue engineering settings. Pulse duplicators, much like their native counterpart—the circulatory system—generate a complex milieu of coupled forces, any one of which may contribute independently or synergistically toward modulating TEHV development.

In the current study, the specific role of cyclic flexure was investigated by subjecting SMC-seeded scaffolds to cyclic three-point flexure at a physiological frequency and amplitude for 3 weeks. The argument for cyclic flexure is multifaceted. It represents a major mode of deformation in the native valve [47], generating a distribution of stresses and strains through the leaflet thickness which may potentially serve to transduce specific mechanical cues to the cells of the individual layers. Furthermore, from a practical standpoint, cyclic flexure is well-tolerated by non-woven scaffolds; the application of modest tensile strains of 2-10% induce permanent set, which complicates both the execution of such studies, and the interpretation of results [64, 114].

In a previous study we developed a bioreactor with the capacity to provide cyclic three-point flexure to up to 12 rectangular biomaterial samples [62]. Cyclic flexure of non-woven PGA and PGA/PLLA scaffolds modified with a P4HB dip-coating resulted in both qualitative and quantitative changes in E that were consistent with a physical disruption of the P4HB. In the current study we demonstrated that unmodified non-woven PGA/PLLA scaffolds incur no significant changes in E over 3 weeks of static or cyclic flexural incubation (**Figure 20**). Thus another advantage of this study was the ability to measure tissue-dependent changes in E in response to cyclic flexure, independent of changes in E due to scaffold degradation.

2.6.1 Cell Seeding Techniques

The seeding techniques used in this study were adapted from Sutherland et al [108] and Nasseri et al [109], with a few noteworthy modifications. We used a vented seeding tube in favor of a sealed tube, and thus were able to use the controlled gas environment of a cell culture incubator rather than requiring a manual gas exchange. Furthermore, the vented seeding tubes allowed for the use of an inexpensive rotisserie (~ \$300) rather than a hybridization oven (~ \$1500). In the case that larger scaffolds are required, such as for a TEHV, sterile vent filter caps are available for 35 x 150 mm Pyrex® hybridization tubes (Corning, Corning, N.Y.). Caution is advised, however, when combining caps with different tubes, as mismatched brands (TPP® cap to Falcon™ tube) were found to leak.

2.6.2 Tissue Development due to Cell Seeding

In order to establish a baseline for subsequent comparisons, E, DNA, and ECM content of SMC-seeded scaffolds was evaluated immediately after the 30 hour seeding period. A seeding efficiency exceeding 90% was achieved without pre-coating the non-woven PGA/PLLA scaffolds with supplementary cell adhesion proteins (e.g., collagen, poly-L-lysine) [61], suggesting that these relatively expensive—and potentially phenotype-altering [115]—factors may be unnecessary in this particular scaffold/cell system. The seeding efficiency observed here corresponded well the 93% seeding efficiency reported for similar PGA/P4HB scaffolds by Nasseri et al [109], albeit the 17-fold higher seeding density used in the current study. Secondly, a significant concentration of S-GAG (a measure of both free and proteoglycan-bound S-GAG) was detected biochemically, which correlated positively with DNA concentration ($r^2 = 0.698$) within the sample group (data not shown). In contrast, no collagen or elastin was detected biochemically at the 30 hour time point, suggesting that proteoglycan/S-GAG secretion precedes collagen and elastin secretion in TEHV development, potentially in a manner similar to that observed during fetal semilunar valve development [116]. Moreover, no significant change in E was measured after the 30 hour seeding period, suggesting that the attachment of cells to the scaffold fibers and subsequent accretion of proteoglycan/S-GAG was insufficient for increasing E at this early time point.

2.6.3 Tissue Development due to Cyclic Flexure

Following 3 weeks of incubation, E of SMC-seeded scaffolds increased 429% in the flex group ($p < 0.01$) and 351% in the static group ($p < 0.01$), with a trend of increased E and a significant 63% increase in collagen concentration ($p < 0.05$) in the flex group. DNA and S-GAG concentration were comparable between groups, and no elastin was detected biochemically. It should be noted that the increase in collagen concentration in the flex group remained significant when the collagen concentration was normalized to the DNA concentration (data not shown). Collectively, these results suggest that the collagen output per SMC was increased 63% in the flex group compared to the static group.

2.6.4 Cyclic Flexure versus other Mechanical Factors

In a recent study by Mol et al [64], the application of cyclic tensile strain (amplitude = 9%) to myofibroblast-seeded non-woven PGA/P4HB scaffolds resulted in a 71 ± 23% increase in hydroxyproline concentration (a surrogate marker for collagen) compared to static incubation by 3 weeks. A simultaneous increase of 112 ± 47% in DNA concentration was observed, suggesting that the increase in collagen concentration was due to the increased cellularity of the myofibroblast-seeded scaffold, and that the collagen output per cell was decreased. In another study by Jockenhoevel et al [61], the exposure of myofibroblast-seeded non-woven PGA scaffolds to continuous laminar flow for 2 weeks resulted in an increase of approximately 52% in hydroxyproline concentration. The DNA content was not quantified in that study, precluding estimation of the collagen output per cell. Most strikingly, in a pioneering study by Hoerstrup et al [32], incubation of SMC and endothelial cell (EC)-seeded PGA/P4HB scaffolds for 21 days in a pulse duplicator bioreactor resulted in an increase of approximately 1075% in hydroxyproline concentration compared with static incubation, with a simultaneous increase of 261% in DNA concentration. These data suggest that the collagen output per cell increased approximately 409%—roughly 6.5 times that observed in the current study under conditions of cyclic flexure alone.

Tentatively, these results suggest two potentially complementary hypotheses that warrant further investigation: i) that the stimulatory effects of cyclic flexure, cyclic tensile strain, and/or shear stress combine synergistically when coupled in a pulse duplicator bioreactor, and ii) that EC transduce mechanical signals present in pulse duplicator bioreactors (e.g., shear stress) in such as way as to augment the stimulatory effects observed in scaffolds seeded with only SMC or myofibroblasts.

2.6.5 E versus Collagen Concentration

In an effort to explain the increase in E in SMC-seeded scaffolds by 3 weeks, the mean E was plotted versus the mean DNA, S-GAG, or collagen concentration across all sample groups. While no significant correlations were found between the mean E and mean DNA or S-GAG concentration (data not shown), a positive linear relationship ($r^2 = 0.991$) was found between the mean E and mean collagen concentration. In order to assess the generality of the relationship, supplementary data from a TEHV incubated for 9 weeks in a roller bottle was included in the regression, yielding an increase in the coefficient of determination ($r^2 = 0.996$) (**Figure 25**) [108, 109]. These results may at first appear trivial—that the stiffness of a soft tissue is derived from its collagen content—however a review of the current literature suggests that this is the first study to demonstrate such a strong relationship in an engineered tissue constructed using a synthetic scaffold. Our ability to establish this relationship likely stemmed from the sensitivity of the three-point flexure test in evaluating E in a low stress-strain regime. Interestingly, the TEHV from which the supplementary data was derived was made using the same non-woven PGA/PLLA scaffold used in the current study, but with a different cell type (ovine bone marrow-derived stem cells) [117]. These data tentatively suggest that E depends primarily on the gross collagen content, and that given a comparable collagen output per cell, a variety of cell types may give rise to TEHV exhibiting similar mechanical properties. This finding could have important implications for the development of a clinically-feasible TEHV, as the majority of studies thus far have been conducted using cells derived from resected blood vessel segments.

2.6.6 Histology and Immunohistochemistry.

The quantitative analyses described above were corroborated by the histology, which revealed predominant proteoglycan and collagen accumulation consistent with a TEHV incubated for 14 days in a pulse duplicator bioreactor [8, 32], and suggested a more homogenous transmural cell and ECM distribution in the flex group (**Figure 21**). Interestingly, immunohistochemical staining demonstrated a significant increase in vimentin expression in the flex group (+++; **Figure 22D**) compared with the static group (+; **Figure 22C**), suggesting that cyclic flexure contributes to the maintenance of vimentin expression in TEHV, and possibly in the native ovine pulmonary valve (PV) [8]. These results are supported by previous reports in which the expression and organization of the intermediate filament vimentin has been correlated with *in vivo* hemodynamic parameters in endothelial cells [118], and with mechanical loading in chondrocytes [119]. In contrast to vimentin, SMC α-actin expression was elevated with respect to the native ovine PV (-; [8]) in both sample groups (+++; **Figure 22A, B**) [8]. Collectively, the immunohistochemical staining suggests that cyclic flexure induces a VA-type myofibroblast phenotype [120] consistent with the progression of TEHV development observed in a pulse duplicator bioreactor *in vitro*, and following implantation *in vivo*, yet independent of the additional mechanical factors (e.g., cyclic shear stress, pressure) generated by pulsatile flow [8].

2.6.7 Transmural Cell Distribution Analysis

The transmural cell distribution quantified by digital image analysis agreed well with microscopic observations, suggesting that cyclic flexure induces a more homogenous transmural cell distribution, with a lower fraction of nuclei localized in the peripheral 25% of the transmural thickness, and a greater fraction of nuclei localized in the central 50% of the transmural thickness compared with the static group. These results agreed with those of a recent study in which a similar homogenization of the transmural cell distribution was induced by cyclic uniaxial tensile loading of a gelatin sponge scaffold seeded with human heart cells [121]. It is unclear if this effect was due explicitly to the transmural distribution of tensile and compressive stresses and strains associated with flexure, or simply a result of increased convective mass transport induced by the cyclic flexure of the scaffold. It is noteworthy that no significant difference in thickness was measured between the flex and static groups (data not shown). Furthermore, while the transmural ECM distribution appeared to parallel the cell distribution, we were unable to establish this quantitatively, as the difference in the RGB color value of ECM components in digitized photomicrographs of Movat pentachrome stained sections was not sufficient for reliable thresholding.

2.6.8 Mechanotransduction in TEHV.

In the current study we demonstrated that cyclic flexure can independently yield many aspects of TEHV development observed in pulse duplicator bioreactors; however the mechanism by which mechanotransduction occurs remains unknown. In a study by Nikolovski and Mooney

[85], SMC adhesion to PGA was shown to occur via vitronectin and fibronectin adsorbed from the serum, suggesting that integrins $\alpha_v\beta_5$ and α_5, respectively may act as mediators of mechanotransduction. This conclusion is supported by a study in which integrin $\alpha_v\beta_3$-mediated mechanotransduction was quantified in SMC [71]. However, while SMC adhesion to ECM via integrins is predominant *in vivo*, tissue remodeling events in which the ECM is degraded induce increased cell-cell contacts via cadherins [86]. Moreover, cadherins have been demonstrated to mediate mechanotransduction in human gingival fibroblasts [81]. Thus, since SMC-seeded scaffolds are actively remodeling tissues, as evidenced by their elevated levels of SMC α-actin expression (**Figure 22A, B**), the potential role of cadherins in mediating mechanotransduction in TEHV warrants further investigation.

2.6.9 Summary

The current study is the first to demonstrate that cyclic flexure can independently influence the *in vitro* development of a TEHV. A trend of increased E, a 63% increase in collagen concentration ($p < 0.05$), increased vimentin expression, and a more homogenous transmural cell distribution were observed in SMC-seeded scaffolds subjected to 3 weeks of cyclic flexure compared to static incubation. The combination of a simple mode of deformation with a mechanically stable scaffold yielded a model system in which tissue-dependent changes in E could be measured independent of the confounding effects of scaffold degradation. Thus, the goal of this study was not to reproduce the material properties of native semilunar valve tissue, but rather to develop a fundamental understanding of how cyclic flexural loading affects the development of TEHV, in particular the development of ECM in TEHV, and, concomitantly, E.

A positive linear relationship (r^2 = 0.996) was found between the mean E and mean collagen concentration (**Figure 25**), to the best of our knowledge a first in the case of an engineered tissue based on a synthetic scaffold. The correlation depicted in **Figure 25** may be useful in predicting the mechanical properties of a TEHV based on a more rapidly degrading non-woven scaffold, as it provides a starting point for estimating E, given knowledge of the degradation profile of the unseeded scaffold. A comparison with previous studies on the effects of cyclic tensile strain, laminar flow (shear stress), and a pulse duplicator bioreactor tentatively suggests that the stimulatory effects of individual mechanical factors may combine synergistically in a coupled mechanical environment, and/or that EC may modulate the basal response of SMC-seeded TEHV to mechanical stimulation. Further *in vitro* studies, in which the coupled mechanical environment of a pulse duplicator bioreactor is reconstructed piecewise (e.g., independently combining flexure, flow, and tension), would be necessary in order to better understand and control the development of a TEHV, and may help illuminate the role of mechanical factors in the development and homeostasis of native and TEHV *in vivo*.

3.0 THE FLEX-STRETCH-FLOW BIOREACTOR

3.1 INTRODUCTION

While rudimentary aspects of TEHV development (e.g., cell proliferation, collagen secretion) can be stimulated *in vitro* by growth factors [122], higher level tissue morphogenesis (e.g., layer specialization in TEHV [8]) is seldom observed without mechanical stimulation. In contrast to growth factors, which generally interact with only one cell surface receptor, mechanical forces can be transduced through multiple cell surface receptors, deformation of intracellular cytoskeletal proteins, as well as deformation of the nucleus and its contents, and thus one mode of mechanical stimulation may initiate multiple signal transduction pathways. Moreover, the pleiotropic actions of mechanical stimulation can both accelerate the *de novo* synthesis of collagen [61, 63, 64], as well as guide its structural organization [123, 124]. For example, while DNA and collagen can approach native-like concentrations over 4 weeks static culture with basic fibroblast growth factor (bFGF) [122], it is only with 3-4 weeks bioreactor cultivation that layer stratification begins [32, 63], and not until several months *in vivo* that a tri-layered morphology reminiscent of a native semilunar valve develops [8, 33].

While it remains to be determined which morphological features of TEHV explants are due solely to hemodynamics and which to host cell infiltration and remodeling, mechanical forces are expected to play a significant role. As introduced in Section 1.5, previous studies have demonstrated that perturbation of the *in vivo* mechanical environment can influence embryonic valvulogenesis [49], and can lead to pathological remodeling of the native mitral valve [50, 51]. Moreover, while few long-term *in vitro* bioreactor studies have been reported, in at least one study reported by Kim et al. [115] it was observed that TE smooth muscle continues remodeling for at least 20 weeks in response to *in vitro* cyclic stretch, further suggesting that the coupled mechanical stimuli of pulsatile flow contribute to the *in vivo* development of TEHV.

Pulsatile flow loop bioreactors provide pressure and flow stimuli to native and engineered tissues targeted within the context of the tissue's ultimate physiomechanical function. [59]. More advanced designs incorporate control algorithms and regulators for independently modulating pressure and flow, thereby allowing for the simulation of sub to supra-physiologic hemodynamic conditions [125]. Thus, for the purpose of mechanically conditioning anatomically-shaped TEHV for implantation, pulsatile flow loop bioreactors are virtually indispensable. However, for developing a fundamental understanding of how individual modes of mechanical stimulation influence the tissue formation and remodeling process, a different bioreactor approach in which tissue deformations and strains are decoupled from flow and pressure stimuli is necessary. Toward this goal, we and others have designed bioreactors for investigating the independent effects of flexure [62, 63], tension [64], and fluid shear stress [61] on TEHV.

We previously demonstrated that cyclic flexure can independently stimulate many aspects of TEHV development observed in pulse duplicators, including increased collagen synthesis with concomitant increases in effective stiffness [63]. Interestingly, the increase in collagen output per cell observed under conditions of cyclic flexure (+ 63%) [63] was comparable to that observed by others under conditions of continuous laminar flow (+ 52%) [61] and significantly less that that observed in pulsatile flow loop bioreactor studies (+ 409%) [32].

Collectively, these findings suggested that the individual modes of mechanical stimulation may act synergistically to accelerate or amplify collagen synthesis. Accelerated collagen synthesis is critically important when using scaffolds based on rapidly degrading synthetic polymers such as poly(glycolic acid) (PGA), as the kinetics of scaffold degradation mandate a commensurate rate of tissue formation for the maintenance of structural integrity. If systematically quantified, the unique effects of individual mechanical stimuli could be recombined in novel ways to optimize *in vitro* TEHV development.

In the current paper we describe a novel bioreactor which will allow us to explore the independent and coupled effects of cyclic flexure, stretch, and flow (FSF) on TEHV tissue formation *in vitro*. Cyclic flexure and stretch can be applied via a linear actuator and novel "spiral-bound" tissue-gripping system. The FSF bioreactor generates flow via a magnetically-coupled paddlewheel rather than an external pump circuit, providing a closed system to help ensure sterility, while maintaining a compact footprint for placement inside a standard cell culture incubator. Toward qualifying the FSF bioreactor design for subsequent experiments using cell-seeded scaffolds, we report here on computational simulations assessing the response of flow and fluid shear stress profiles to changes in paddlewheel angular velocity, culture medium dynamic viscosity, and the spatial arrangement of specimens within the flow field. The CFD model was experimentally validated by particle image velocimetry (PIV).

3.2 METHODS

3.2.1 FSF bioreactor design.

The design methodology and materials of construction used in the FSF bioreactor was similar to that for our previous cyclic flexure bioreactor [62, 63]. The structural components of the FSF bioreactor were designed using Solidworks 3D CAD software (Solidworks, Corp., Concord, MA). Machined parts were fabricated from polycarbonate by Astro Automation, Inc. (Irwin, PA). Rubber bellows were custom ordered from Minor Rubber Company, Inc. (Bloomfield, NJ). The paddlewheel was fabricated by high resolution stereolithography (FineLine Prototyping, Inc., Raleigh, NC) using a Viper Si^{2}™ SLA® system (3D Systems Corp., Valencia, CA) and a high strength, water resistant resin (ProtoTherm 12120™; DSM Somos®, Newcastle, DE) (**Figure 29**). Two cylindrical (1/4 x 3/4 in.) nickel-coated, grade N38 neodymium (NdFeB) magnets (K&J Magnetics, Inc., Jamison, PA) were press-fit into prefabricated slots on one side of the paddlewheel. The magnets were oriented with their poles in the same direction. Synthetic sapphire ring jewel bearings (Bird Precision, Waltham, MA) were press-fit into either side of the paddlewheel to provide the low starting torque and friction characteristics necessary for effective magnetic torque transmission. All metallic components were made from 316 stainless steel. Platinum-cured silicone tubing will be used for culture medium perfusion.

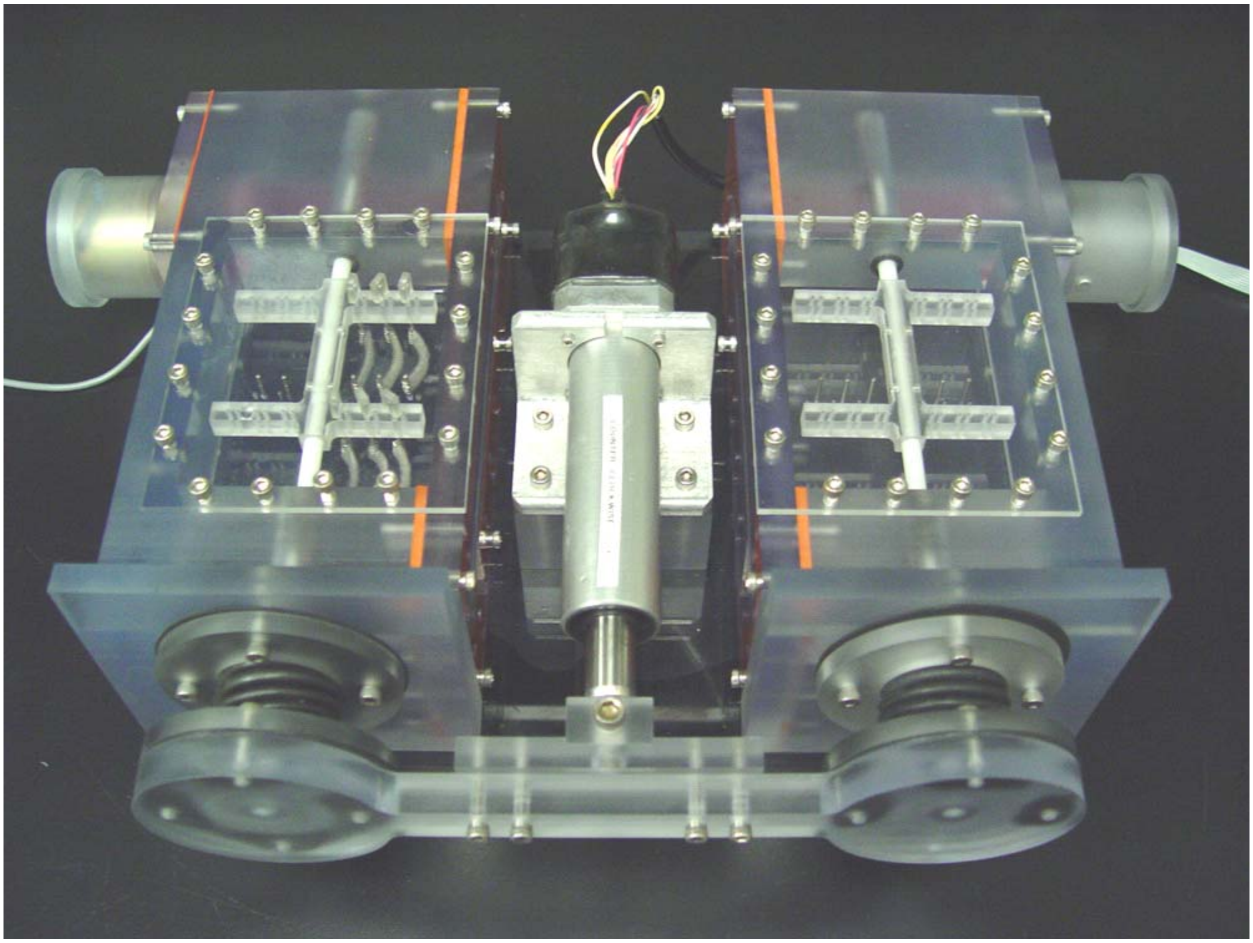

Figure 27	Photograph of the FSF bioreactor.

The bioreactor consists of two identical chambers, each containing 12 stainless steel "stationary posts" to which tissue specimens can be affixed (**Figure 27**). To attach specimens we developed an inexpensive yet high effective "spiral-bound" grip method. Spiral grips were fabricated by manually winding a length of stainless steel wire **(**316V, 0.009" diameter; Small Parts, Inc., Miami Lakes, FL) about a 2 mm diameter steel mandrel using a drill. Grips were cut to length and twisted onto both sides of specimens (**Figure 28A**). The device can thus accommodate a total of 24 rectangular samples (maximum dimensions approximately 25 mm x 7.5 mm x 2 mm). Cyclic flexure and/or stretch were applied by an environmentally-sealed linear actuator (UltraMotion, Mattitick, NY). The piston of the actuator is rigidly coupled to a cross-arm in the form of a T-junction. Conversely, the cross-arm is rigidly coupled to the arm of each chamber (**Figure 27**). Frequency, amplitude, acceleration, and deceleration profiles can be developed using Windows-based Si Programmer software (Applied Motion Products, Watsonville, CA). The structural elements of the device can be cold gas sterilized by ethylene oxide, and the entire device was designed to be operated inside of a standard humidified incubator.

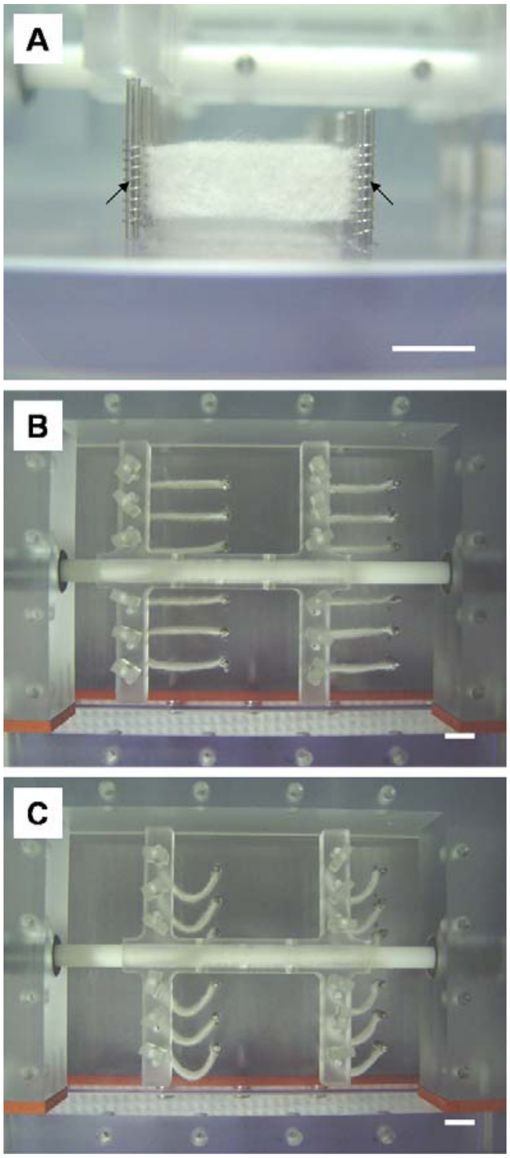

Figure 28 Photograph of a scaffold specimen “spiral-bound” between stationary and movable posts (A). Stainless steel wire (316V, 0.009” diameter; Small Parts, Inc., Miami Lakes, FL) was manually turned using a drill and mandrel (2 mm diameter) to form the spiral tissue binders. The binders were then wound through the scaffold specimens. Photograph of scaffold specimens in the neutral configuration (B). Scaffold specimens can be subjected to cyclic tensile loading by moving the movable posts to the left via the linear actuator (not shown). Photograph of scaffold specimens subjected to a tensile deformation (C). To ensure that all scaffold specimens bend in the same direction they are gently pushed in one particular direction using sterile forceps during after they are situated in the bioreactor. Scale bars = 1 cm.

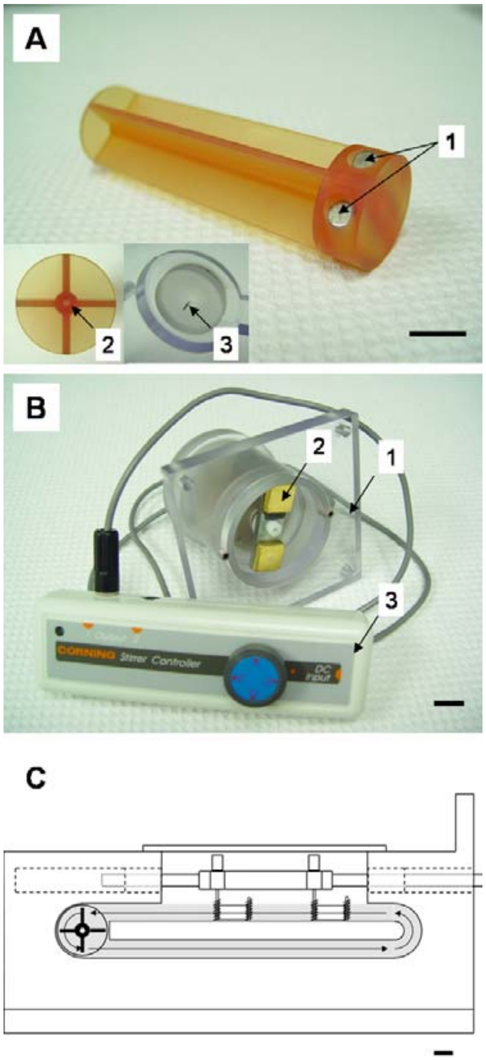

Figure 29 Overview of the paddlewheel flow system. Detail photograph of a single paddlewheel (A). Two neodymium magnets (1) are press-fit into holes in one side of the paddlewheel and are oriented with their poles in the same direction. Sapphire ring jewel bearings (2) are press-fit into holes on both sides of the paddlewheel and mate with stainless steel pivots (3) installed in the main chamber and opposite wall of the FSF. Detail photograph of a customized magnetic stirrer (B). The motor was installed in a custom housing (1) and the stock magnets were replaced with powerful neodymium magnets (2) to provide stronger torque coupling. The motor speed is controlled by a potentiometer (3). Overview photograph of the paddlewheel flow circuit (C). The magnetic stirrer (not shown) attaches to the FSF bioreactor chamber and mates with the paddlewheel. The fluid flow circuit is shaded gray and the direction of culture medium flow is indicated by black arrows. Scale bars = 1 cm.

3.2.2 Particle Image Velocimetry

The Particle image velocity (PIV) device used to experimentally quantify the flow field generated by the paddlewheel has been described previously [126]. In brief, the FSF bioreactor was filled with a solution of neutrally buoyant fluorescent polymer micro-spheres (35-6C, Duke Scientific, Palo Alto, CA) in 37°C water. The paddlewheel angular velocity was set to a predetermined value (350, 500, 1000, 1500, 2000) using a non-contact digital laser tachometer (ST6236B; Reed Instruments, Quebec, Canada). The FSF was then positioned for visualization by the PIV device (**Figure 30**). A Nd:YAG laser system (Solo PIV III 15 Hz, New wave Research Inc., Fremont, CA) emitting a 532 nm laser pulse was focused into a 2mm thick sheet using a cylindrical lens (Edmund Optics, Barrington, NJ), and was projected into the FSF from above (note that a temporary transparent lid was positioned directly atop the fluid to mimic the configuration of the 2-D CFD simulations). Particles were imaged through the transparent side of the FSF by a Kodak CCD camera (Megaplus ES 1.0, Eastman Kodak Company, San Diego, CA), a close-up lens (60 mm f2.8D AF Micro-Nikkor, Nikon, Japan), and XCAP-standard v.2.2 imaging software (EPIX Inc, Buffalo Grove, IL). Sets of two sequential images were captured within microseconds using the triggered double exposure mode of the camera, a frame grabber (PIXCI® D2X, EPIX Inc, Buffalo Grove, IL), and an eight analog output data acquisition card (NI-6713, National Instruments, Austin, TX). Images thus acquired were analyzed using custom software to extract the velocity profiles for subsequent comparison with CFD simulations.

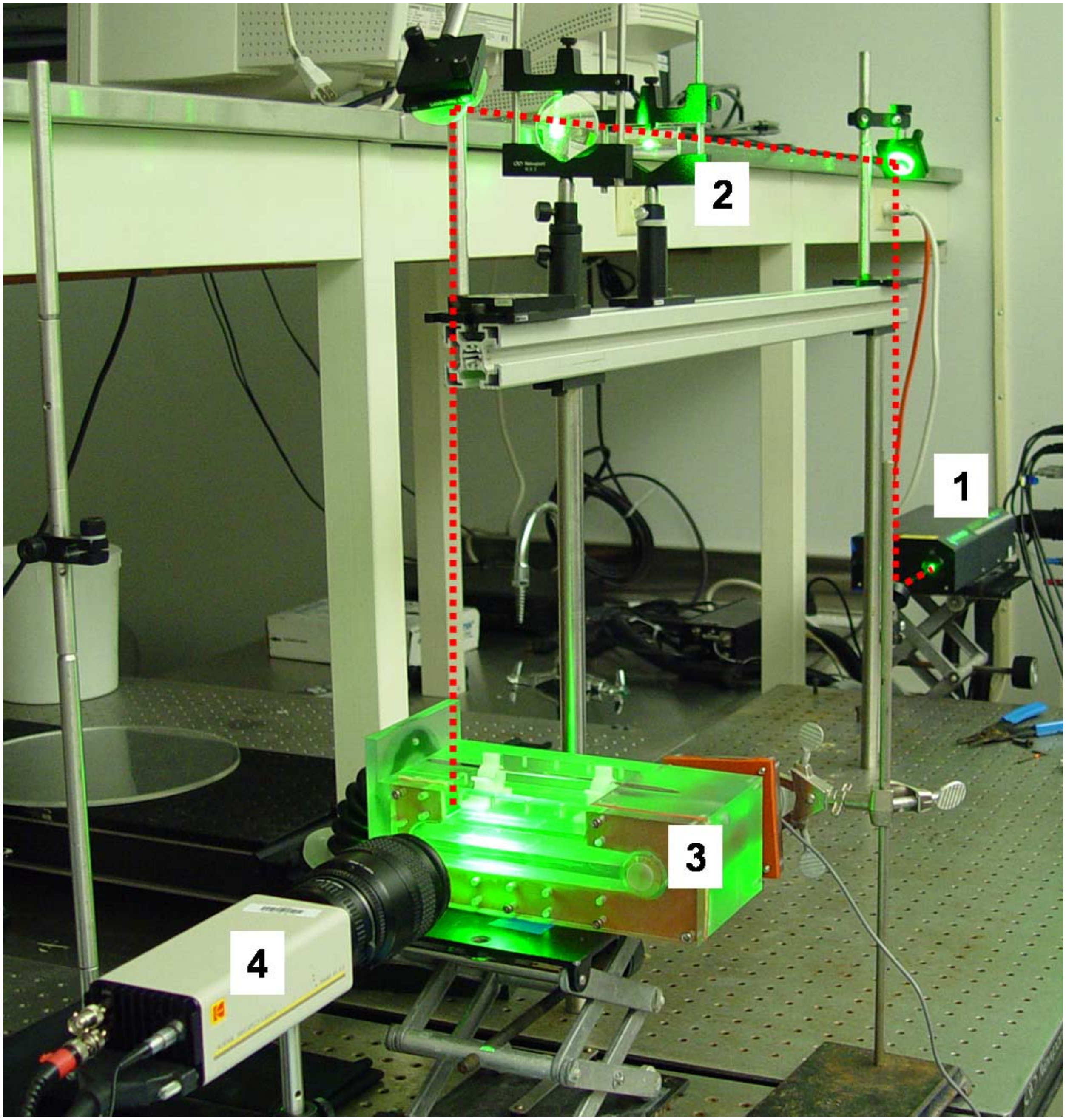

Figure 30 Particle image velocimetry (PIV) setup for experimental validation of the 2-D CFD models. The PIV device and experimental methods have been described previously by Budilarto et al. The pulsed laser sheet (1) was directed by a series of mirrors and lenses (2) into the top of the FSF bioreactor (3). The camera (4) imaged the laser-illuminated particles. The path of the laser sheet is highlighted by a red dashed line.

3.2.3 CFD Simulations

To validate the flow rate and fluid shear stress patterns generated by the novel paddlewheel flow system, we developed a computational fluid dynamics (CFD) model using GAMBIT® and FLUENT® (v6.2) software (Fluent, Inc., Lebanon, NH). The geometry of the paddlewheel and associated components of the FSF Bioreactor bath were exported from Solidworks® (Solidworks, Corp., Concord, MA) and reconstructed in the preprocessor GAMBIT. For simulating the relationship between paddlewheel rotational velocity and flow rate, a two-dimensional (2-D) model was developed in GAMBIT using a dynamic mesh of 50,000 triangular elements for the fluid phase (**Figure 31A**). The unsteady-state simulation was solved using FLUENT. Once the velocity profiles were solved using the 2-D model, velocity profiles were extruded into the third dimension and directly applied upstream of the tissue specimens in a local 3-D simulation to predict the wall shear stress profiles on the various specimens (**Figure 32**). Specimen-to-specimen variations in wall shear stress were not significant.

3.3 RESULTS

3.3.1 FSF bioreactor operation results

Operation of the bioreactor was straightforward and similar to our previously described cyclic flexure bioreactor [62, 63]. The culture medium capacity of each chamber was approximately 300 ml. Compared with the ~72 ml per chamber capacity of our previous cyclic flexure bioreactor, this allowed for a longer time between culture medium changes (generally every 3 days, versus everyday in the previous bioreactor). Loading scaffold specimens into the FSF was simplified by the spiral-bound gripping method (**Figure 28A**). Using sterile forceps, the stainless steel spiral grips could be positioned on the posts within the FSF with relative ease beneath a laminar flow hood.

3.3.2 2-D CFD simulation results

The 2-D simulations were run at 5 different paddlewheel rotational velocities for the standard culture medium dynamic viscosity (μ = 0.0076 dyne-s/cm^2), and at the lowest and highest velocities for two higher viscosity (μ = 0.0223 and μ = 0.037 dyne-s/cm^2) (**Figure 31**). The highest viscosity value corresponds with the viscosity of blood at a physiologic shear rate, and can potentially be simulated by adding the appropriate concentration of Dextran 40. The average velocities predicted using the 2-D model are summarized in **Table 1**. Results indicated that viscous energy loses along the length of the fluid flow circuit resulted in significantly decreased fluid velocities with increased fluid viscosity.

Table 1 Average culture medium velocities as a function of culture medium dynamic viscosity and paddlewheel rotational velocity.

Dynamic Viscosity (dyne-s/cm^2)	350 RPM	500 RPM	1000 RPM	1500 RPM	2000 RPM
0.0076	0.167 cm/s	0.392 cm/s	1.68 cm/s	3.73 cm/s	5.79 cm/s
0.0223	0.060 cm/s	n/a	n/a	n/a	2.15 cm/s
0.037	0.048 cm/s	n/a	n/a	n/a	1.34 cm/s

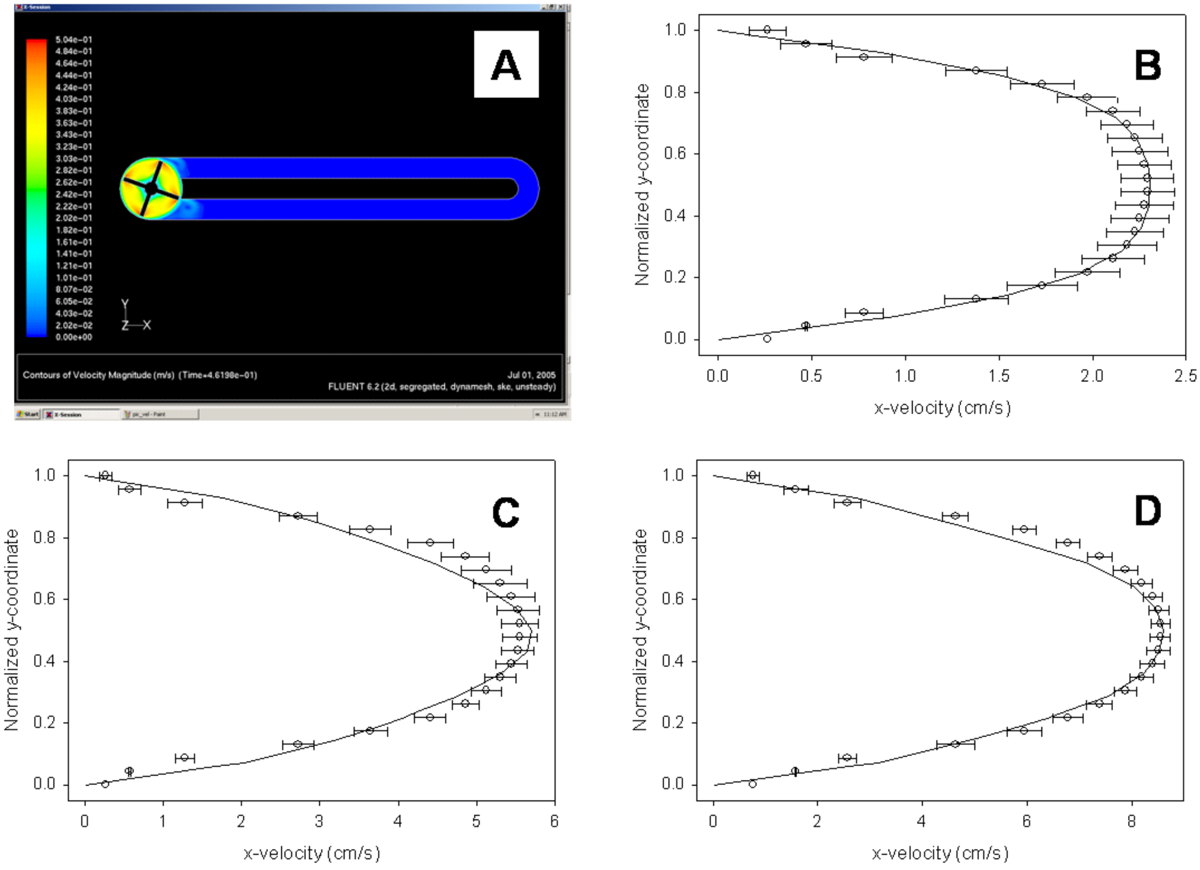

Figure 31 Two-dimensional CFD model and PIV experimental validation results. The 2-D model consisted of ~50,000 dynamic fluid elements (A). CFD predictions (solid lines) and PIV experimental measurements (open circles) of the x-component velocity profile for 1000 (B), 1500 (C), and 2000 (D) RPM paddlewheel rotational velocities. Similar agreement was found for velocity profiles at 350 and 500 RPM (data not shown). Depicted velocity profiles were taken at a dynamic viscosity (μ) of 0.0076 dyne-s/cm^2 corresponding with the viscosity of water (and culture medium) at 37°C. Y-component velocities were approximately three orders of magnitude less than x-component velocities and thus were not considered in the analysis.

3.3.3 3-D CFD simulation results

The 3-D simulations were run at 5 different paddlewheel rotational velocities for the standard culture medium dynamic viscosity (μ = 0.0076 dyne-s/cm^2), and at the lowest and highest velocities for two higher viscosity (μ = 0.0223 and μ = 0.037 dyne-s/cm^2). A minimal

FSF bioreactor bath geometry was constructed using GAMBIT (**Figure 32**). The upstream velocity and downstream pressure profiles obtained from the 2-D simulations were applied as boundary conditions at points 1 and 2, respectively. The Reynold's number and average shear stress per specimen was plotted as a function of paddlewheel rotational velocity (**Figure 33**). At the standard culture medium viscosity, the maximum predicted fluid shear stress was 1.145 ± 0.038 dyne/cm^2. Inter-specimen (**Table 2**) and intra-specimen (**Figure 34**) variations in shear stress were not significant.

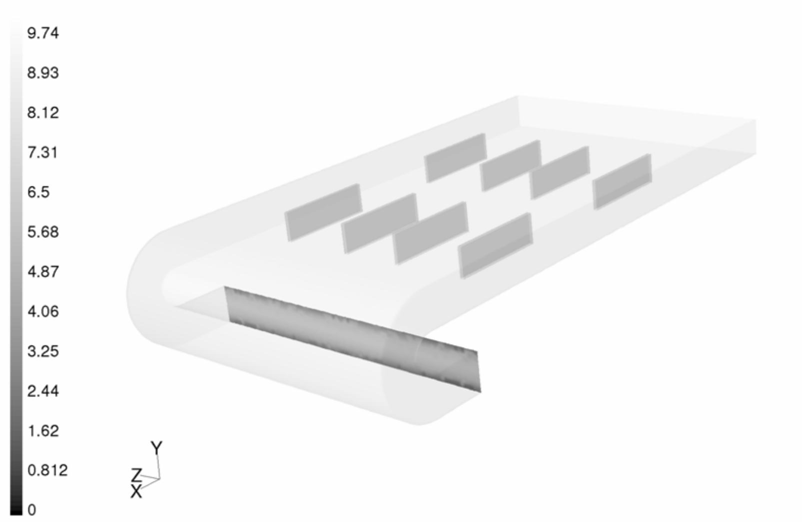

Figure 32 Specimen configurations within the three-dimensional CFD model. In the first specimen configuration analyzed, a total of 8 specimens (25 x 7.5 x 1 mm) were located in two rows of 4 (A). In the second specimen configuration (not shown), a total of 12 specimens were located in two rows of 6. Note that in the actual CFD simulations the 3-D model was partitioned along its symmetry plane to minimize processing time. The half-chamber 3-D model consisted of ~50,000 fluid elements.

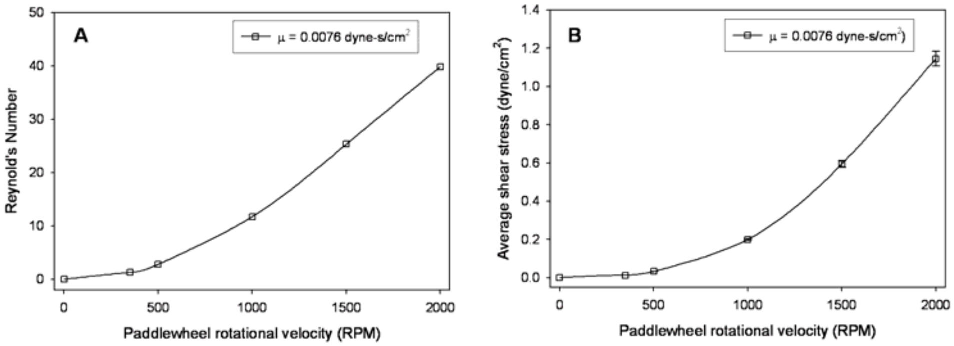

Figure 33 Three-dimensional CFD model results. The CFD predicted Reynold's number versus paddlewheel rotational velocity (A). Note that Reynold's number values were well within the laminar flow region (< 1000) within the vicinity of the specimens. The CFD predicted average fluid shear stress per specimen versus paddlewheel rotational velocity (B). The lowest dynamic viscosity simulated (m = 0.0076 dyne-s/cm2) corresponds to water (and culture medium) at 37°C, while the highest (m = 0.037 dyne-s/cm2) simulates the viscosity of blood at a physiologic shear rate. Experimentally, the culture medium viscosity can be augmented by the addition of appropriate concentrations of Dextran.

Table 2 Inter-specimen variation in fluid shear stress as a function of paddlewheel rotational velocity. Fluid shear stress (τ) values are reported in units of dyne/cm^2 with corresponding standard deviations (σ). Specimens were located symmetrically about the central axis of each FSF bioreactor chamber, and thus only 4 of the 8 specimens are presented below.

Specimen location	350 RPM		500 RPM		1000 RPM		1500 RPM		2000 RPM	
	τ	σ	τ	σ	τ	σ	τ	σ	τ	σ
inflow proximal	0.012	0.006	0.032	0.018	0.202	0.129	0.602	0.401	1.157	0.765
inflow distal	0.013	0.006	0.034	0.018	0.221	0.142	0.676	0.441	1.311	0.839
outflow proximal	0.012	0.006	0.031	0.016	0.186	0.102	0.541	0.296	1.020	0.552
outflow distal	0.013	0.006	0.032	0.016	0.194	0.103	0.579	0.311	1.114	0.590

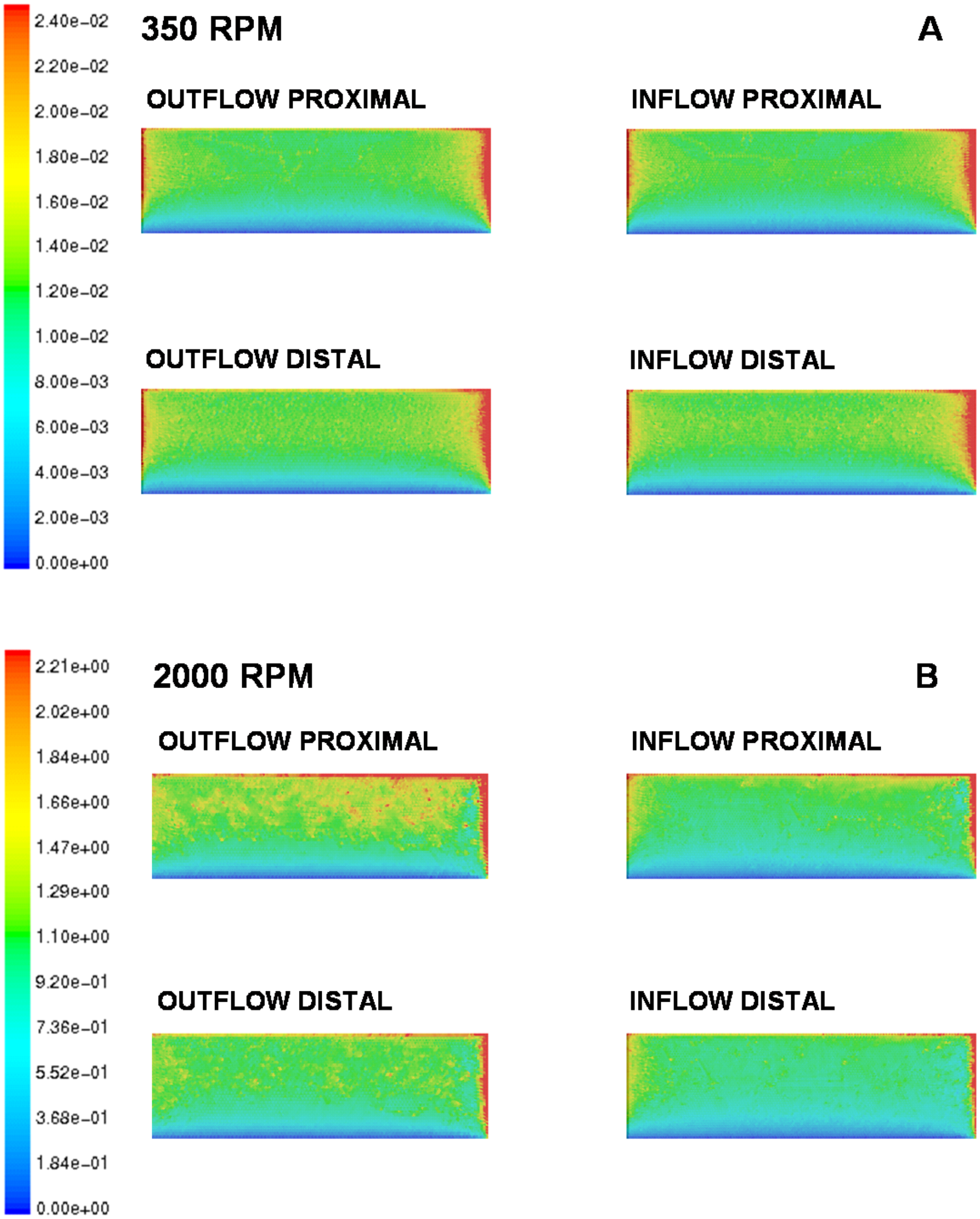

Figure 34 Intra-specimen variation in fluid shear stress at paddlewheel rotational velocities of 350 RPM (A) and 2000 RPM (B). Specimens designated as *proximal* were located nearest the wall of the FSF bioreactor chamber, and *distal* specimens were located toward the center of the chamber. Note that the highest fluid shear stress values (red) were predicted at the inflow (right hand) side of each specimen, and that the lowest values (blue) were predicted along the bottom edge of each specimen. Note that the color scale bar for 350 RPM ranges from 0 to 0.02 dyne/cm^2 (A), and that the color scale bar for 2000 RPM ranges from 0 to 2.21 dyne/cm^2 (B).

3.4 DISCUSSION

Semilunar heart valves are subjected to three major modes of mechanical loading due to pulsatile blood flow: tensile loading during valve closure (i.e., diastole), flexural loading during the opening and closing phases, and fluid shear stress during ventricular ejection (i.e., systole). In the native valve *in vivo*, and in a pulse duplicator bioreactor (i.e. pulsatile flow bioreactor) *in vitro*, the three major modes of mechanical loading are inextricably coupled (e.g., pressure-flow relationship), thus precluding isolation of the independent effects of any individual mechanical factor. In the flex-tension-flow (FSF) bioreactor these candidate modes of mechanical stimulation are decoupled, allowing for independent control of tensile, flexural, or fluid shear stress loading.

The reported speed range of the Corning 75mm immersible stirrer is 350-2000 RPM. Thus, using experimentally validated CFD models with a culture medium dynamic viscosity equal to that of water (0.0076 dyne-s/cm^2 at 37°C), the average shear stress range generated in the FSF bioreactor was predicted to be ~ 0.0125 – 1.1505 dyne/cm^2. While this range of shear stresses is much lower than the physiological shear stresses to which a native aortic valve is exposed to during systole (3-79 dyne/cm^2; Weston et al. [127]), studies have demonstrated that shear stresses in this relatively low range can effect collagen concentration in a TEHV similar to that under investigation in the current study (e.g., ~ 46% increase in hydroxyproline concentration upon 7 days exposure to ~ 0.066 dyne/cm^2, followed by a step change to ~0.13 dyne/cm^2 for an additional 7 days; Jockenhoevel et al. [61]). (Note that we estimated the shear stresses generated in the study by Jockenhoevel et al. from the dimensions of their laminar flow chamber using the equation $\tau_w = (6\mu Q)/(bh^2)$ [128], in which Q is the flow rate, b is the width of the rectangular flow chamber, and h is the height of the rectangular flow chamber).

We initially hypothesized that the shear stresses could be increased by increasing the viscosity of the culture medium to approximate the viscosity of blood at physiological shear rates (~ 0.037 dyne-s/cm^2 at 37°C). This can be accomplished by adding the appropriate amount of the polysaccharide Dextran-40 to the culture medium. We found, however, that the increased viscous loses along the length of the fluid flow circuit led to significant decreases in velocity that abrogated any effect of increased dynamic viscosity of fluid shear stress. Thus, the most feasible way of increased the fluid shear stress range of the FSF would be to incorporate a faster motor for spinning the paddlewheel.

4.0 INDEPENDENT AND COUPLED EFFECTS OF CYCLIC FLEXURE AND LAMINAR FLOW ON ENGINEERED HEART VALVE TISSUE FORMATION BY BONE MARROW-DERIVED MESENCHYMAL STEM CELLS

4.1 Introduction

As introduced in Section 1.1.3, the interstitium of native semilunar heart valve leaflets are populated by a mixed community of cells referred to as valvular interstitial cells (VIC). These VIC express a phenotype intermediate between smooth muscle cells (SMC) and fibroblasts, and have been characterized as VA-type myofibroblasts due to their dual expression of vimentin and alpha smooth muscle actin (α-SMA) [8]. At the blood-leaflet interface, the leaflets are covered with a confluent lining of valvular endothelial cells (VEC). VEC, while similar in many respects to other vascular endothelial cells, due express certain unique phenotypic and morphologic attributes [15, 16]. In designing a TEHV for potential future clinical applications, it is generally assumed that some other cell types will be utilized in lieu of the native VIC and VEC, which could only be isolated by highly invasive biopsy techniques. As introduced in Section 1.4, early attempts to develop a TEHV have successfully relied on carotid artery-derived vascular smooth muscle cells and endothelial cells [32]. In fact, TEHV explanted 20 weeks after implantation in the pulmonary circulation of sheep exhibited many of the phenotypic characteristics of the native ovine pulmonary valve, included prominent vimentin expression and diminished a-SMA expression that was localized primarily to the immediate sub-endothelial layer [8]. However, as the TEHV becomes more refined, the reality of potential future clinical applications has demanded the development of novel autologous cell sources that could be isolated relatively non-invasively from patients. In light of their potential to transdifferentiate toward a mesenchymal phenotype, peripheral blood-derived endothelial progenitor cells (EPC) have received much attention, as they could potentially be used as a single source for generated VIC-like and VEC-like cells for TEHV [15, 37, 129]. However, while the utility of EPC in developing a TEHV is still under investigation, preliminary functional assessment of EPC-seeded nonwoven scaffolds under mechanically active conditions suggest that EPC may require specialized culture medium/scaffold coating combinations in order to optimize EPC attachment and ECM synthesis. In tandem with EPC-based studies, investigators have also considered bone marrow-derived mesenchymal stem cells (BMSC) as a potential single cell source for TEHV [33-35, 130].

Bone marrow-derived mesenchymal stem cells (BMSC) represent a potentially attractive cell source for use in cardiovascular tissue engineering. BMSC can be isolated from adult patients relatively non-invasively, and BMSC have a pluripotent differentiation potential—previous studies have demonstrated their capacity to differentiate into bone, cartilage, tendon, fat, muscle, and early progenitors of neural cells. While the pluripotency of BMSC is potentially attractive, it also mandates stringent control over the differentiation process such that unwanted differentiation events are avoided.

Sutherland et al. [33] recently demonstrated that BMSC isolated from juvenile sheep can be used to fabricate TEHV, and that these TEHV can successfully function in the pulmonary outflow tract of sheet for at least 8 months. In this landmark study—the first long-term animal trial of a TEHV fabricated using non-invasively accessible adult stem cells—it was shown that BMSC-seeded scaffolds evolved a tri-layered morphology reminiscent of a native semilunar valve. Importantly, though BMSC-seeded TEHV stained negative for endothelial cell markers prior to implantation, 8 month explants exhibited a continuous von Willebrand factor (vWF) positive surface. It was not clear whether the endothelial cells were host derived, or whether they provided evidence of mesenchymal-to-endothelial transdifferentiation of the seeded BMSC, however previous 2-D tissue culture studies have shown that murine embryonic mesenchymal progenitors can undergo such transdifferentiation events in response to *in vitro* laminar flow [131]. Other studies have demonstrated that human BMSC can transdifferentiate into endothelial cells *in vitro* in response to low (2%) fetal calf serum and 50 ng/ml VEGF [132].

Toward developing optimized bioreactor conditioning regimens for BMSC-seeded TEHV, in the current study we investigated the independent and coupled effects of cyclic flexure and laminar flow on BMSC-seeded nonwoven scaffolds. BMSC were isolated from juvenile sheep, expanded *in vitro*, and seeded onto nonwoven 50:50 blend PGA/PLLA scaffolds. Following 4 days static culture, BMSC-seeded scaffolds were loaded into the FSF bioreactor and either maintained under static conditions (static group), or subjected to cyclic flexure (flex group), laminar flow (flow group), or combined cyclic flexure and laminar flow (flex-flow group) for 1 and 3 weeks. At each time point, specimens were characterized by DNA and ECM content, tissue effective stiffness (E), and by histology, immunohistochemistry, and scanning electron microscopy.

4.2 Methods

4.2.1 Bone marrow mesenchymal stem cell (BMSC) isolation

Bone marrow mesenchymal stem cells (BMSC) were isolated and characterized by Virna L. Sales, M.D. at Children's Hospital Boston as described previously by Sutherland et al [33]. Juvenile sheep (Dover/Suffolk cross) were sedated with ketamine at 25 mg/kg IM and xylazine at 0.05 mg/kg IM, intubated, and maintained on an inhaled 0.5% to 2% isoflurane/oxygen mixture. A stab incision was made over the mid part of the sternum and approached with an 11-gauge bone marrow biopsy needled (MDTech). Then, 15 ml of marrow was aspirated into a syringe containing 5 ml of 1000-IU/ml heparin sodium (Elkins-Sinn, Inc.). BMSC were obtained from ovine bone marrow using the method of Pittenger et al [133]. Medium was changed at 24, 48, and 72 hours, by which time colonies of spindle-shaped cells were observed. Cells were passaged at low density ($<10^4$ cells/cm^2) into successively larger tissue culture flasks and then into 1750 cm^2 polystyrene roller bottles (Corning, Inc.). The culture medium comprising DMEM supplemented with 10% FBS and 1% antibiotic/antimycotic solution (GIBCO). Air in the roller bottles was displaced with a 5% CO_2/air mixture, and bottles were rotated at 0.2 cycles per minute and 37°C. Cells were characterized by indirect immunofluorescence prior to use.

4.2.2 Indirect Immunofluorescence

BMSC were characterized by indirect immunofluorescence by Virna L. Sales, M.D. at Children's Hospital Boston as described previously by Sutherland et al. [33]. Cells were plated into 8-well chamber slides (Nalge Nunc International) for 24 hours before staining. Cells were washed with PBS and fixed with cold methanol. Slides were incubated for 1 hour at room temperature with mouse anti-human vimentin monoclonal antibody (Dako) at 1:300 dilution or anti-α-smooth muscle actin (SMA) monoclonal antibody (Sigma) at 1:1000 dilution. Cells were then washed in PBS and incubated with FITC-conjugated goat anti-mouse IgG as a secondary antibody (Vector) at 1:200 dilution. Cells were examined by fluorescence microscopy with a Nikon microscope and IP Laboratory imaging software. Characterized BMSC (passage 4) were cryopreserved in culture medium supplemented with 5% dimethyl sulfoxide (DMSO) and were shipped to University of Pittsburgh on dry ice.

4.2.3 Cell expansion and scaffold seeding

The general BMSC expansion and seeding techniques were the same as described above in Section 2.4.4 with the exception that twenty 500 cm^2 flasks (Nuclon™Δ TripleFlask; Nalgene Labware) were used in lieu of the 54 T185 flasks used previously. The culture medium was the same as described in Section 2.4.2, with the exception that bFGF was not added during BMSC expansion. The PGA/PLLA scaffolds were prepared the same as described above in Section 2.4.1, with the exception that scaffolds were "spiral-bound" by threading with stainless steel spiral wires as described above in Section 3.2.1 prior to ethylene oxide sterilization. Following

30 hours seeding, BMSC-seeded scaffolds were maintained in static culture for 4 days prior to loading into the FSF bioreactor.

4.2.4 Independent and coupled cyclic flexure and laminar flow bioreactor studies

A total of 48 BMSC-seeded scaffold specimens were prepared for evaluation in this study. Two separate runs of the bioreactor were required to test all of the specimens. In the first run, BMSC-seeded scaffolds were loaded into the bioreactor under aseptic conditions and incubated under static (n=12) or cyclic flexure (n=12) conditions. Cyclic flexure was applied at a frequency of 1 Hz and $\Delta\kappa$ of 0.554 mm^{-1}. In the second run, BMSC-seeded scaffolds were incubated under laminar flow (n=12) or laminar flow/cyclic flexure (n=12) conditions. Laminar flow was applied by setting the paddlewheel rotational velocity to the maximum value of 2000 RPM, which was shown above to yield an average fluid shear stress of 1.1505 $dyne/cm^2$. Specimens from each mechanical loading group were removed following 1 (n=6) and 3 (n=6) weeks. Following removal from the bioreactor, specimens were characterized as described above in Sections 2.2.5, 2.2.6, 2.4.5, 2.4.6, and 2.5.2.

4.2.5 Immunohistochemistry

In addition to the histology and immunohistochemistry described in Section 2.5.2, BMSC-seeded scaffolds were also evaluated for expression of collagen type I, collagen type III, fibronectin, CD31, and vWF.

4.3 RESULTS

4.3.1 DNA and ECM assay results

Following 1 week of incubation, the average DNA concentrations were 29.1 ± 3.8, 15.1 ± 1.3, 45.8 ± 3.6, and 59.8 ± 8.5 μg/g wet weight in the static, flex, flow, and flex-flow groups, respectively (**Figure 35**). By 3 weeks, the average DNA concentrations had decreased to 3.1 ± 0.5 (-89%; $p<0.001$), 3.8 ± 0.6 (-75%; $p<0.001$), 35.1 ± 1.8 (-23%; $p<0.05$), and 47.0 ± 4.8 (-21%; N.S.) μg/g wet weight in the static, flex, flow, and flex-flow groups, respectively. All DNA concentrations measured for BMSC-seeded constructs were significantly lower than values measured for ovine vascular SMC (Section 2.5.4) [63].

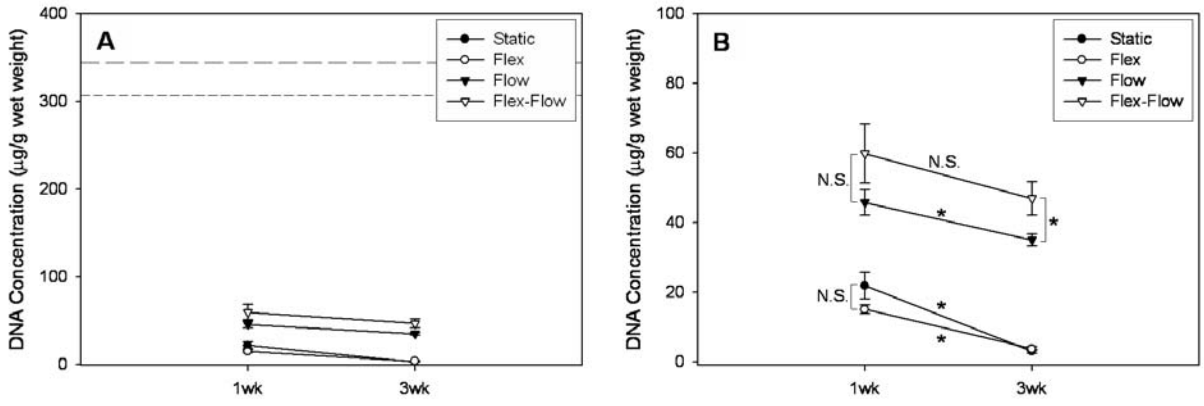

Figure 35 DNA assay results for BMSC-seeded 50:50 PGA/PLLA scaffolds. Note that the long and short dashed lines indicate the DNA concentration measured for SMC-seeded 50:50 PGA/PLLA scaffolds following either 3 weeks cyclic flexural or static incubation, respectively [63] (A). DNA results plotted on a reduced y-axis to facilitate visualization of the differences between experimental groups (B). Significant comparisons are indicated by asterisks (*).

4.3.2 S-GAG Assay Results

Following 1 week of incubation, the average S-GAG concentrations were 2997 ± 220, 2792 ± 189, 2237 ± 196, and 2482 ± 231 μg/g wet weight in the static, flex, flow, and flex-flow groups, respectively (**Figure 36**). By 3 weeks, the average S-GAG concentrations had increased to 3636 ± 345 (+21%; N.S.), 5637 ± 897 (+102%; $p<0.01$), and 2268 ± 67 (+1%; N.S.) μg/g wet weight in the static, flex, and flow groups, respectively, and had decreased to 1919 ± 54 (-23%; $p<0.05$) μg/g wet weight in the flex-flow group. All S-GAG concentrations measured for BMSC-seeded constructs were significantly higher than values measured for ovine vascular SMC (Section 2.5.4) [63].

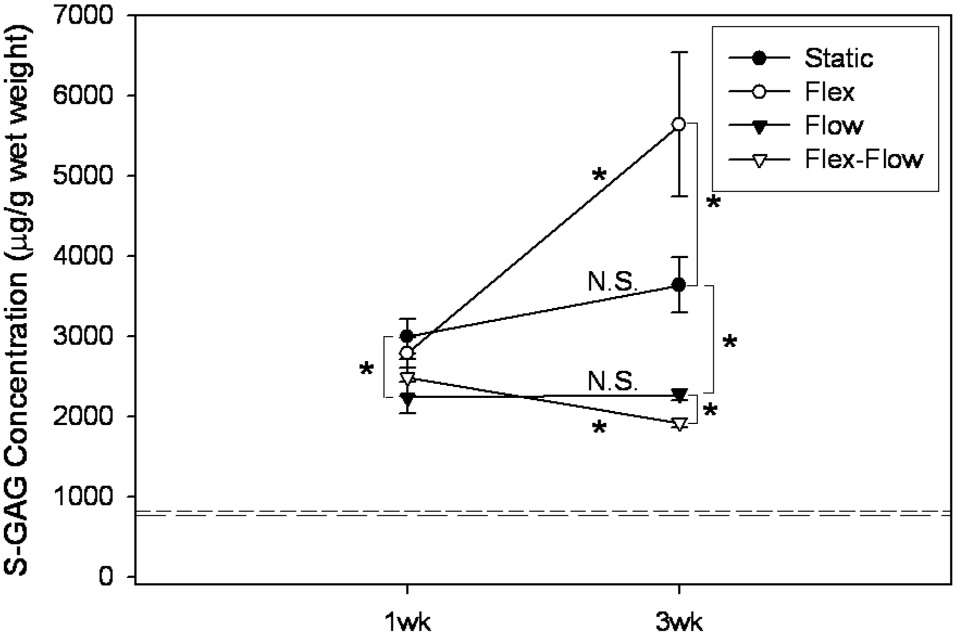

Figure 36 Sulfated glycosaminoglycan (S-GAG) assay results for BMSC-seeded 50:50 PGA/PLLA scaffolds. Note that the long and short dashed lines indicate the DNA concentration measured for SMC-seeded 50:50 PGA/PLLA scaffolds following either 3 weeks cyclic flexural or static incubation, respectively [63]. Significant comparisons are indicated by asterisks (*).

4.3.3 Collagen Assay Results

Following 1 week of incubation, collagen could not be detected biochemically in any of the test group specimens (**Figure 37**). By 3 weeks, the average collagen concentrations measured were 422 ± 98, 530 ± 106, 498 ± 95 and 844 ± 278 μg/g wet weight in the static, flex, flow, and flex-flow groups. The collagen concentrations measured for the static, flex, and flow groups were not significantly different from the value measured for SMC-seeded scaffolds incubated for 3 weeks under static conditions, and the collagen concentration measured for the flex-flow group was not significantly different from the value measured for SMC-seeded scaffolds incubated for 3 weeks under cyclic flexure conditions (Section 2.5.4) [63].

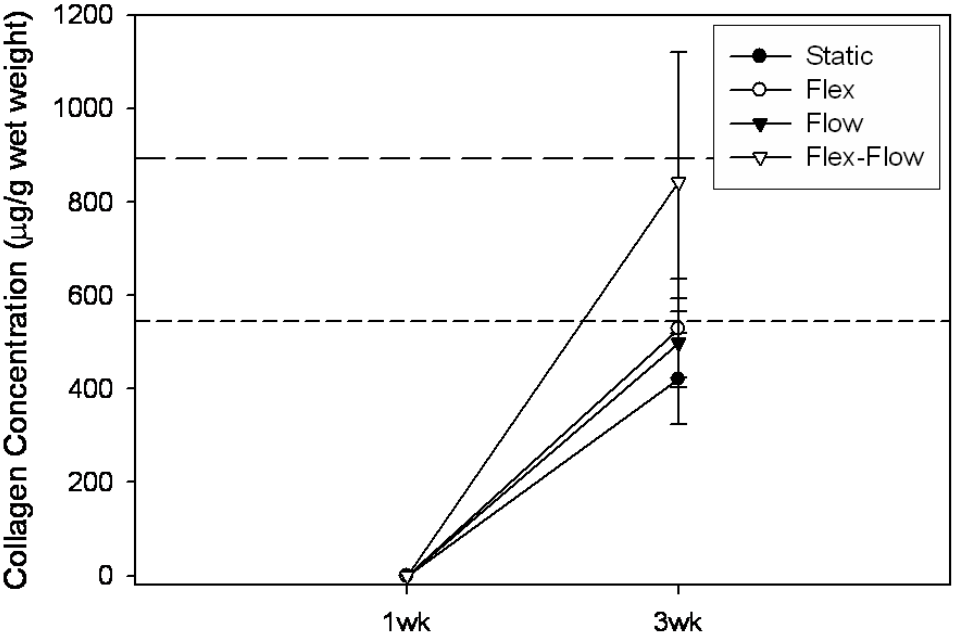

Figure 37 Collagen assay results for BMSC-seeded 50:50 PGA/PLLA scaffolds. Note that the long and short dashed lines indicate the DNA concentration measured for SMC-seeded 50:50 PGA/PLLA scaffolds following either 3 weeks cyclic flexural or static incubation, respectively [63]. Significant comparisons are indicated by asterisks (*).

4.3.4 Scanning electron microscopy (SEM) results

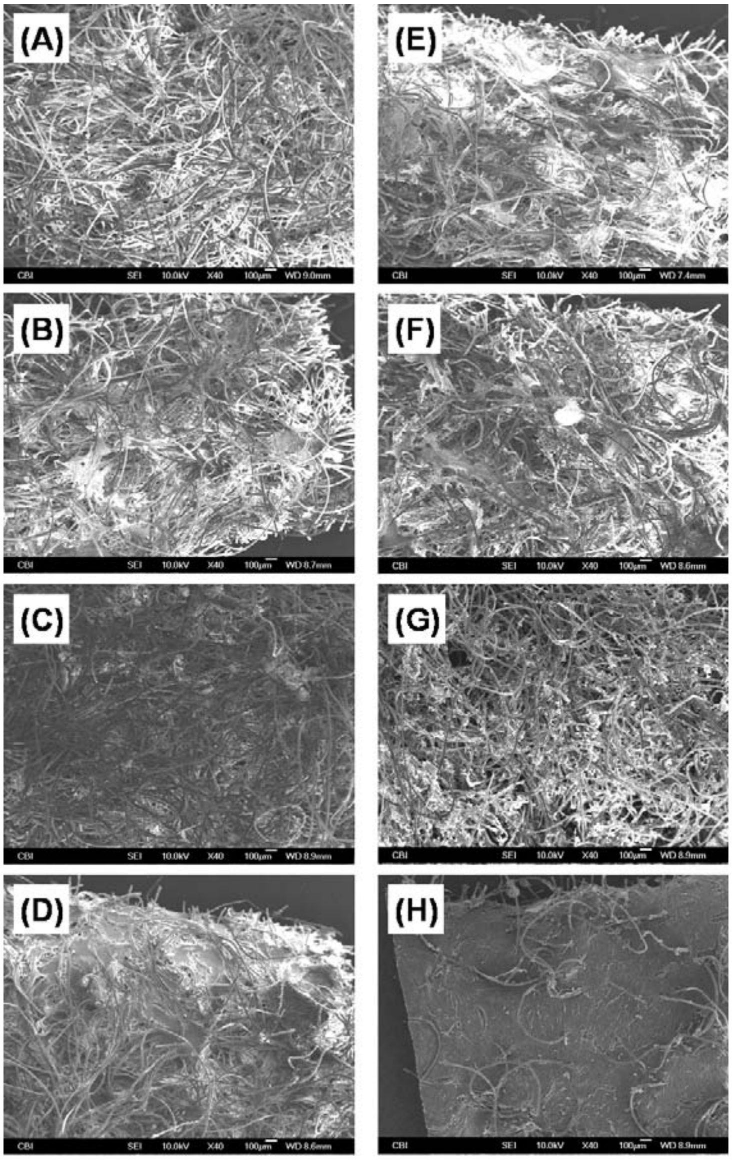

Figure 38 Scanning electron micrographs (SEM) of BMSC-seeded 50:50 PGA/PLLA scaffolds incubated under static (A, E), cyclic flexure (B, F), laminar flow (C, G) and cyclic flexure-laminar flow (D, H) culture conditions for 1 (A-D) and 3 (E-H) weeks in the FSF bioreactor. Note the dramatic increase in tissue formation exhibited by 1 and 3 weeks in the flex-flow specimens (D and H, respectively).

4.3.5 Histology Results

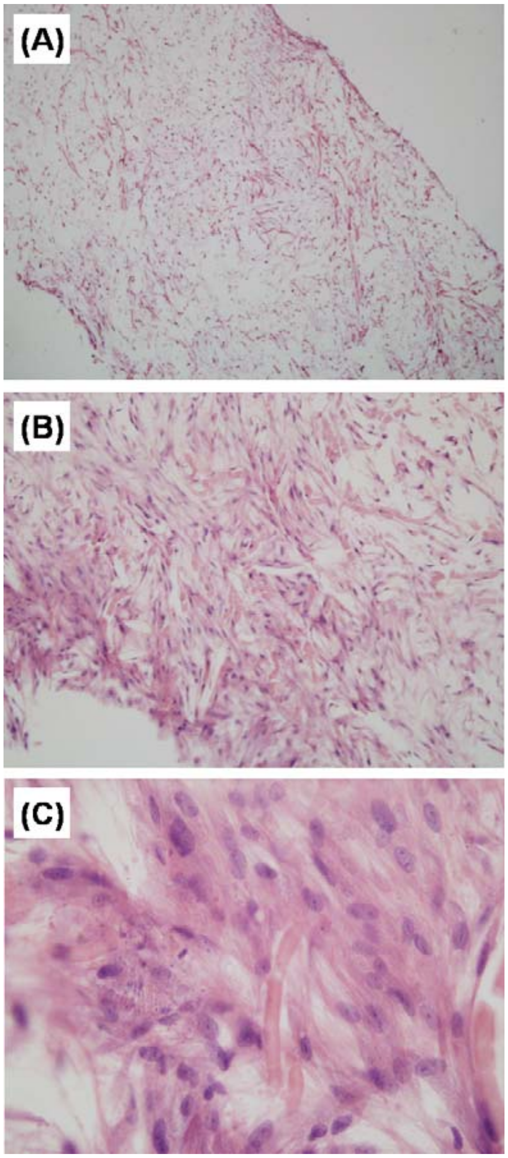

Figure 39 H&E stained sections of BMSC-seeded 50:50 PGA/PLLA incubated for 3 weeks under conditions of combined cyclic flexure and laminar flow (flex-flow) imaged at 40x (A), 100x (B), and 400x (C).

4.3.6 Immunohistochemistry Results

Within the 3-week flex-flow group, cells expressed α-SMA (**Figure 40A**, **C**), with qualitatively higher levels at the surface (**A**) versus the interstitium (**C**). While fibronectin and type I collagen were only weakly detected (data not shown), type III collagen was detected primarily at the surface (**B**) compared with the interstitium (**D**).

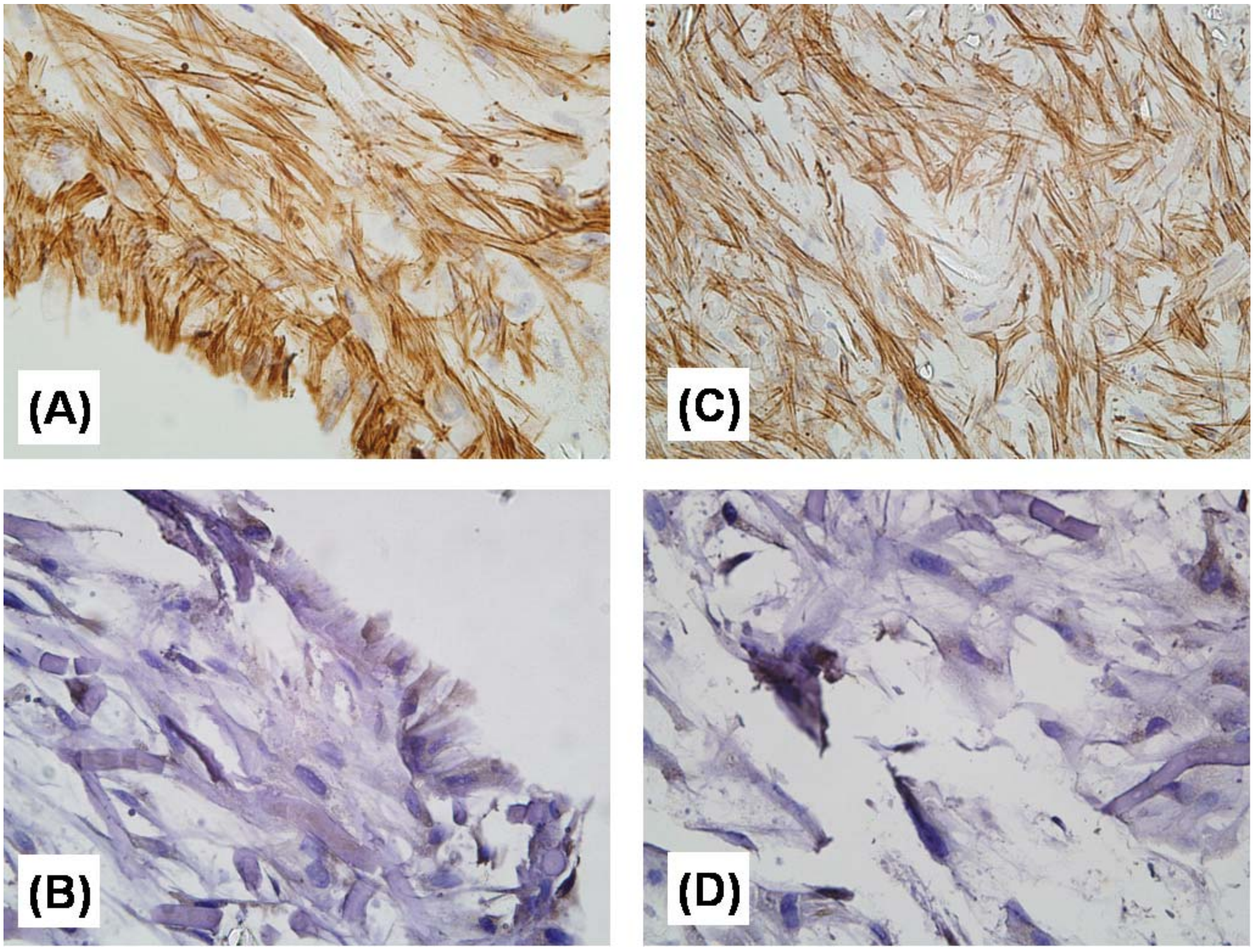

Figure 40 Immunohistochemistry results for a-SMA (A, C) and collagen type III (B, D) in 3-week flex-flow specimens (brown color indicates positive labeling).

Evidence for mesenchymal-to-endothelial transdifferentiation was found in the 3 week flex-flow group (**Figure 41**), with elevated expression of CD31 at the surface (**A**) compared with negligible expression in the interstitial region (**D**), elevated expression of vWF at the surface (**B**) compared with moderate expression in the interstitial region (**E**), and elevated expression of laminin at the surface (**C**), compared with negligible expression in the interstitium (**F**).

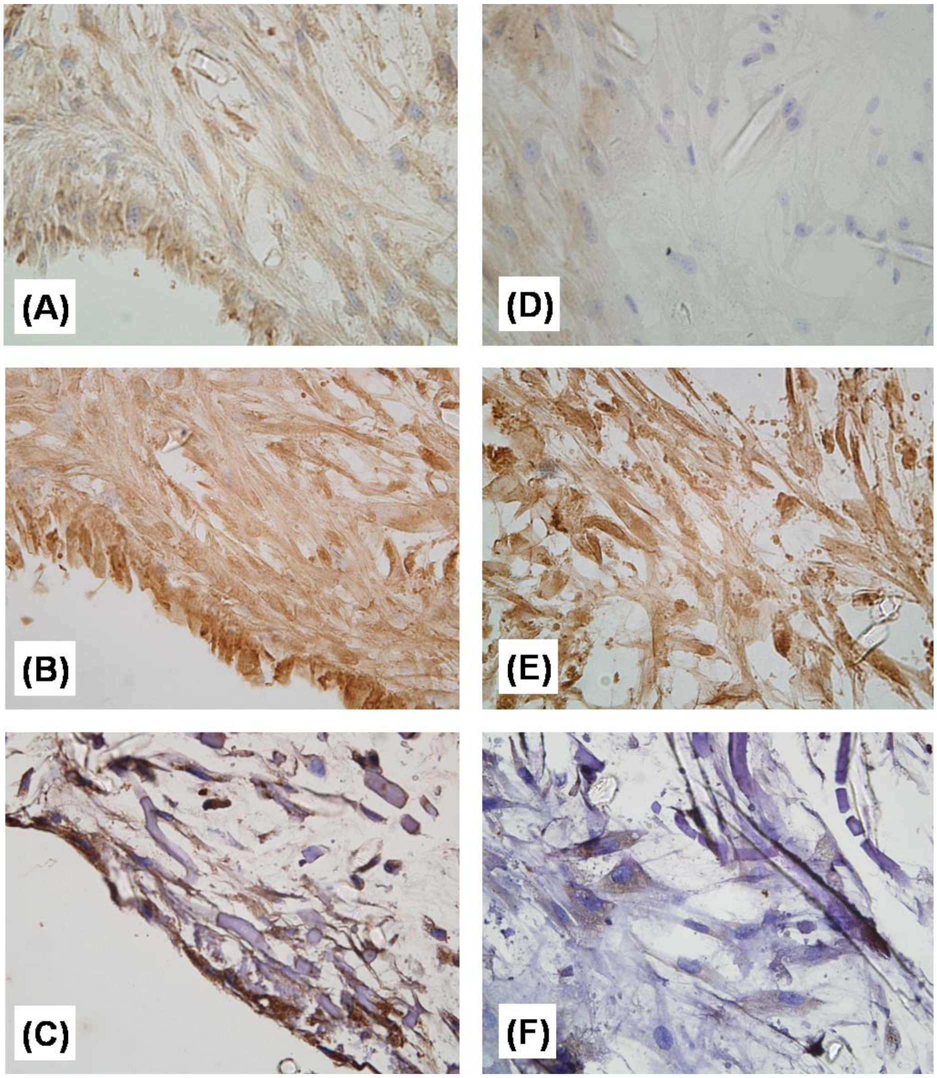

Figure 41 Immunohistochemistry for CD31 (A, D), vWF (B, E), and laminin (C, F) expressed at the surface (A-C) and in the interstitium (D-F) of 3-week flex-flow BMSC-seeded scaffolds (brown color indicates positive labeling).

4.3.7 Effective Stiffness Testing Results

Following 1 week of incubation, the average *E* values had increased from 206 ± 16 kPa (unseeded scaffold) to 226.76 ± 22.10 (+10%; N.S.), 235.83 ± 36.08 (+15%; N.S.), 252.63 ± 33.23 (+23%; N.S.), and 356.44 ± 42.93 kPa (+73%; $p<0.05$) in the static, flex, flow, and flex-flow groups, respectively (**Figure 42**). By 3 weeks, the average *E* values had increased further to 562.99 ± 143.97 (+148%; $p<0.01$), 677.31 ± 179.46 (+187%; $p<0.01$), 653.12 ± 185.60 (+159%; $p<0.01$), and 946.34 ± 232.57 (+166%; $p<0.05$) kPa in the static, flex, flow, and flex-flow groups, respectively. A trend of increased *E* was observed in the flex-flow specimens at 1 and 3 weeks.

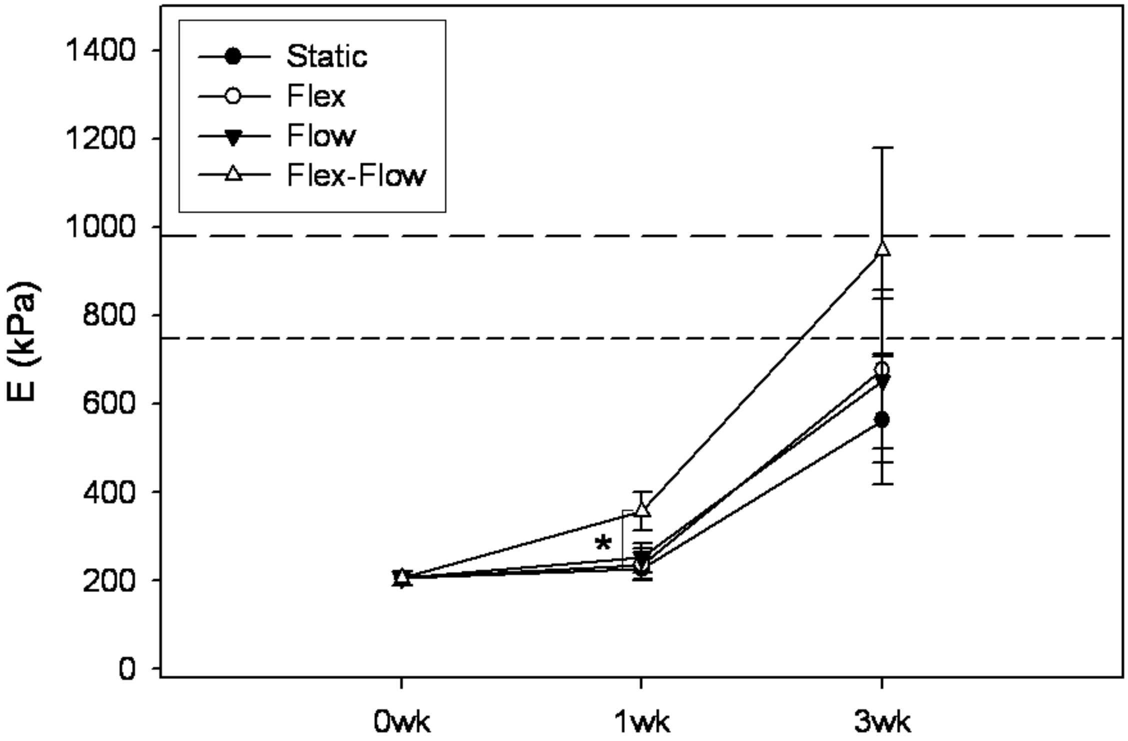

Figure 42 Effective stiffness (E) results for BMSC-seeded scaffolds.

4.4 DISCUSSION

In the current study we used the FSF bioreactor to investigate the independent and coupled effects of cyclic flexure and laminar flow on engineered heart valve tissue formation. The decision to shift from SMC to BMSC was motivated by the need to develop non-invasive cell sources for potential future clinical applications.

4.4.1 Implications of Proteoglycan / Sulfated-Glycosaminoglycan Results

In the current study we demonstrated that different modes of mechanical stimulation—cyclic flexure and laminar flow—had differential effects on the sulfated-glycosaminoglycan (S-GAG) concentration of BMSC-seeded scaffolds. As mentioned in Section 2.6.2, S-GAG concentration represents a measure of both free and proteoglycan-bound S-GAG. These previous results for SMC-seeded scaffolds demonstrated that proteoglycan/S-GAG secretion precedes collagen secretion in TEHV, with significant changes in S-GAG concentration occurring following 3 weeks bioreactor incubation [63]. Given that the initial ECM deposited within the scaffold consists predominantly of proteoglycans and S-GAG, it stands to reason that these molecules could have a significant impact on the phenotype and subsequent synthetic behavior of the constituent cells.

The role of small leucine-rich proteoglycans (SLRP) in modulating collagen fibrillogenesis has received much attention recently, as various gene knock-out models have demonstrated the important role of SLRP in several disease states. Some of the most actively studies SLRP are decorin, biglycan, fibromodulin, lumican. Each of these SLRP has demonstrated an important role in modulating the assembly of collagen molecules and fibers, and recently has been implicated in controlling the fate of BMSC [134]. Using a biglycan and decorin knock-out (*bgn/dcn-*) mouse, Bi et al. demonstrated that *bgn/dcn-* BMSC shift from growth to apoptosis in response to excess TGF-β signaling due to the lack of proper sequestration of TGF-β by biglycan and decorin.

5.0 A STRUCTURAL MODEL FOR THE FLEXURAL MECHANICS OF NONWOVEN TISSUE ENGINEERING SCAFFOLDS

5.1 INTRODUCTION

Nonwovens of bioresorbable aliphatic polyesters (e.g., polyglycolic acid (PGA), poly-L-lactic acid (PLLA)) represent one of the earliest, and to date, most ubiquitous biomaterials used as TE scaffolds [135]. Their commercial availability and amenability to tissue formation, however, belies their intricate microstructure [97] and mechanics [98, 99]. The complexity of mechanical interactions between the nonwoven scaffold, cells, and ECM has only begun to be addressed. For example, while we recently demonstrated a positive linear relationship between effective stiffness (*E*) and collagen concentration [63], determining the collagen's *specific stiffness* (i.e., stiffness/concentration) was compounded by concurrent variations in its transmural distribution. Thus, while the paradigm of seeding a nonwoven scaffold with cells has yielded promising results for applications as diverse as heart valves [32, 33], bladder [136], blood vessels [56], and cartilage [137], investigators still possess no basis for rational design; no experimentally validated framework for predicting the mechanical properties of cell-seeded nonwoven scaffolds, let alone their response to mechanical conditioning, currently exists.

To account for the strong sensitivity to fiber orientation, we have previously taken a structural approach toward describing the mechanical response of soft planar tissues under biaxial loading conditions [138]. Structural models provide a direct link between the intrinsic properties of individual tissue constituents, their microstructural arrangement, and gross tissue behavior, and thus lend themselves naturally to describing the interacting fiber populations (e.g., collagen, PGA, PLLA) within engineered tissues based on nonwoven scaffolds. While phenomenological models are useful in predicting the overall mechanical behavior of tissues, such as for bioprosthetic heart valve simulations [139], they generally cannot predict the internal mechanical environment experienced by the cells. Such information can only be predicted from a properly formulated structural model. A prerequisite for developing a structural model for a cell-seeded nonwoven scaffold, however, is an accurate model of the nonwoven scaffold itself.

Pioneering investigations into the structural mechanics of nonwoven textiles began in earnest with Backer and Petterson's [140] application of the fiber network theory proposed by Cox [141]. Later investigators refined this theory, quantifying and modeling the influence of fiber properties, bond properties [142], and fiber orientation [143] on the mechanical response of the fabric. Formally introduced as a TE scaffold by Freed et al. [135], needled nonwovens are a particular textile class characterized by discontinuous fibers and labile physical bonds [97]. The physical bonds are introduced by punching an array of barbed needles through a multi-layer fiber web, reorienting some fibers out of the horizontal plane into vertical loops about which neighboring fibers are entangled. Needling is an attractive bonding method for TE scaffolds because it yields a strong [144], highly interconnected porous structure from a single polymer, however fiber slippage results in limited elastic recovery under tensile loading [64, 114, 145]. In contrast, we recently demonstrated that nonwoven scaffolds can exhibit extended mechanical stability under cyclic flexural loading [63].

As discussed above in Section 3, cyclic flexure is a major mode of deformation experienced by native and tissue engineered heart valves (TEHV) during the opening and closing phases of normal valve function. We recently developed a bioreactor [62] and a sensitive three-point bending test [62, 100] to investigate the effects of cyclic flexural loading on TEHV biomaterials. While 50:50 PGA/PLLA nonwoven scaffolds dip-coated with poly-4-hydroxybutyrate (P4HB) incurred significant decreases in *E* with cyclic flexure [62], the unmodified 50:50 PGA/PLLA scaffold was found to be mechanically stable over a period of at least 3 weeks [63]. In smooth muscle cell (SMC)-seeded scaffolds [63], this property recently allowed us to demonstrate several-fold increases in *E* with the accretion of relatively small quantities of collagen *independent* of measurable changes in scaffold mechanical properties.

As a key step toward predicting the contribution of ECM formation on *E* of a cell-seeded nonwoven scaffold, in this section we developed a structural model for *E* of a nonwoven scaffold in bending. The model was formulated based on Freeston and Platt's "no freedom" of relative fiber motion model [146], with new assumptions introduced to describe the unique flexural mechanics of needled nonwovens. Specifically, the spring-like behavior of the crimped fibers was accounted for by calculating effective fiber stiffnesses using a model proposed by Lee and Argon [147]. Structural and mechanical properties of PGA and PLLA fibers and PGA, PLLA, and 50:50 PGA/PLLA scaffolds were measured and input into the model. The predicted values of *E* were compared with experimental measurements for scaffold specimens oriented in both the preferred (PD) and cross-preferred (XD) fiber directions. To assess the general predictive capability of the model, the predicted dependence of *E* on fiber diameter was compared with experimental measurements. Furthermore, to explore the utility of the model in nonwoven scaffold design, a sensitivity analysis was conducted on the key model parameters.

5.2 MATHEMATICAL FRAMEWORK

5.2.1 Structure of Needled Nonwoven TE Scaffolds

An accurate mathematical representation of a needled nonwoven TE scaffold first requires consideration of the fiber and fabric structures. These structures are introduced by an essentially three-step fabrication process [135]. First, the multifilament PGA or PLLA yarn is crimped and cut into 40 mm long segments. The crimping process imparts an intrinsic sinusoidal curvature to the individual fibers that can be observed by light microscopy (**Figure 43**A), and which we will later show is essential to the fiber and fabric mechanics. Secondly, the crimped yarn segments are carded (i.e., mechanically brushed) into a multi-layer fiber web exhibiting distinct PD and orthogonal XD fiber directions (**Figure 43**B). As mentioned previously, in the final fabrication step the oriented fiber web is physically bonded by needling. Needling discretizes the fiber web into a regular array of fibrous cubes demarcated at each corner by a physical bond of vertically-oriented fiber loops (**Figure 43**C). In the subsequent mathematical treatment, these cubes are considered as the representative volume elements (RVE).

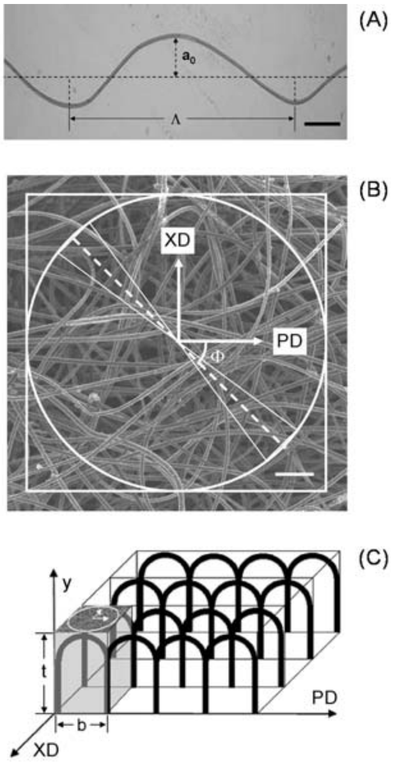

Figure 43 Representative photomicrograph of a crimped PGA fiber teased from a nonwoven PGA scaffold (40x original magnification, Scale bar = 100 μm) (A). The image was calibrated to the fiber diameter and the intrinsic crimp wavelength Λ and amplitude ao were measured using the Trace Measurement Mode of SigmaScan Pro (SPSS, Inc.). SEM image depicting the planar microstructure of a 50:50 PGA/PLLA scaffold (100x original magnification, Scale bar = 100 μm) (B). The angular orientation of the preferred fiber direction (PD) was arbitrarily designated as Φ = 0 degrees, with the orthogonal cross-preferred direction (XD) at Φ = ± 90 degrees. Schematic illustrating how the planar microstructure depicted in panel (B) relates to the three-dimensional structure of the needled nonwoven scaffold (C). The distance between the vertically-oriented loops of fibers introduced by needling provides an intuitive basis for the RVE width b. The angular and numerical distribution of fibers throughout the RVE thickness t was assumed to be equal.

5.2.2 Theoretical Bounds on the Effective Stiffness of a Nonwoven

Consider a rectangular specimen (i.e., beam) of nonwoven fabric. The flexure of a beam can be expressed by the well-known Bernoulli-Euler moment-curvature relation [101]:

$$M = EI\Delta\kappa \tag{3}$$

in which M is the applied bending moment, E is the effective stiffness, I is the area moment of inertia (i.e., $I = wt^3/12$ where w and t are the specimen width and thickness, respectively), and $\Delta\kappa$ is the resultant change in curvature. To model the flexural rigidity EI of idealized nonwoven fabrics consisting of straight (i.e., not crimped) fibers, Freeston and Platt [146] made simplifying assumptions regarding the fibers and fabric (Appendix A).

In their seminal work, Freeston and Platt derived analytical models to calculate EI for two extreme cases of fiber interaction: 1) "complete freedom" of relative fiber motion (i.e., no interaction), and 2) "no freedom" (i.e., fibers rigidly bonded at each cross-over point).

In the case of "complete freedom," EI per RVE can be expressed as (Appendix B):

$$(EI)_{RVE} = N_f E_f I_f \int_{-\pi/2}^{\pi/2} R(\Phi)\cos^4 \Phi d\Phi \tag{4}$$

where N_f is the number of fibers per RVE

$$N_f = \frac{\omega b}{\lambda} \tag{5}$$

in terms of the fabric weight per unit area ω, the RVE width b, and the fiber weight per unit length λ [148]. The longitudinal fiber stiffness E_f can be measured from uniaxial tensile tests of individual fibers (e.g., ASTM D 3379) and I_f is the fiber area moment of inertia (i.e., $I_f = \pi d_f^4/64$ where d_f is the fiber diameter). The fiber orientation distribution $R(\Phi)$ can be expressed according to:

$$R(\Phi)=\frac{N_f(\Phi)}{\sum_{-\pi/2}^{\pi/2} N_f(\Phi)\Delta\Phi} \qquad \lim_{\Delta\Phi\to 0} R(\Phi)=\frac{1}{N_f}\frac{dN_f(\Phi)}{d\Phi} \qquad \int_{-\pi/2}^{\pi/2} R(\Phi)d\Phi = 1 \tag{6}$$

where $N_f(\Phi)$ is the number of fibers oriented within an angular increment $\pm\Delta\Phi/2$ of a particular angle Φ. In the current study $R(\Phi)$ was quantified by a small angle light scattering (SALS) technique (see *Fiber orientation distribution analysis*).

In the case of “no freedom,” *EI* per RVE can be expressed as (Appendix C):

$$(EI)_{RVE} = \tfrac{1}{12} N_f E_f A_f t^2 \int_{-\pi/2}^{\pi/2} R(\Phi)\cos^4\Phi d\Phi \tag{7}$$

where A_f is the fiber cross-sectional area (i.e., $A_f = \pi d_f^2/4$).

Multiplication of either Eq. (4) or (7) by the number of RVE per width (i.e., *w*/*b*) of a particular experimental specimen of nonwoven yields lower or upper bounds on the experimentally measured value of *EI*, respectively. Division of this result by the appropriate value of *I* yields lower or upper bounds on *E*.

5.2.3 New Assumptions for Modeling Needled Nonwoven TE Scaffolds

To the best of our knowledge, the current study is the first to model the mechanics of a needled nonwoven TE scaffold. While Eq. (4) and (7) provide theoretical bounds on *EI* of idealized nonwovens consisting of straight fibers, the unique structure of needled nonwovens [97] suggests an intermediate behavior. For example, in a needled nonwoven the fibers *are physically bonded* at the sites of needling (i.e., *EI* > “complete freedom”), however the fibers *are* *not bonded* at each fiber-fiber cross-over point (i.e., EI < "no freedom"). Moreover, segments of the crimped fibers spanning between cross-over points are often highly curved, suggesting that the effective fiber behavior within the needled nonwoven is more like a spring than a rod.

Using Eq. (7) as a basis, we introduced the following new assumptions for modeling the flexural mechanics of a needled nonwoven scaffold:

1. *Representative volume element (RVE) dimensions depend on needling density*. Needling introduces an array of bonds across the horizontal plane of the fiber web (Fig. 1B), thus rendering the inter-bond distance an intuitive choice for the width b of the RVE. This basis for b is supported by Hearle and Purdy [98], who demonstrated a positive correlation between the initial tensile stiffness of a needled nonwoven and needling density. In the current study the needling density was ~ 155 penetrations/cm^2 (Dr. John Gray, personal communication), yielding an inter-bond distance of ~ 0.92 mm. For convenience, we set $b = 1$ mm (i.e., RVE width ≡ unit width).
2. *Fiber slippage is negligible in bending*. Per Hearle and Purdy [98], in the 0-20 % stress-strain regime needled nonwovens deform by straightening of fiber crimp, with little slippage of frictionally-bonded fibers. This is supported the finding that nonwoven 50:50 PGA/PLLA does not incur measurable changes in E with 3 weeks cyclic flexure [63].
3. *Vertically-oriented fibers do not contribute directly to EI*. While the loops of vertically-oriented fibers introduced during needling lend the nonwoven scaffold structural integrity [97], their direct contribution to EI was assumed to be negligible. This assumption is supported by Termonia [149], who using a numerical model demonstrated that the contribution of out-of-plane fibers to EI is negligible compared to the in-plane fibers.

4. *Fiber effective stiffness is governed by fiber crimp*. To account for the crimped fibers in the needled nonwoven we adapted a model proposed by Lee and Argon [147]. Crimped fibers were assumed to be sinusoidal in the undeformed state with an *effective crimp* amplitude a_{eff} and wavelength Λ_{eff} (i.e., $y = a_{eff}\sin(2\pi x / \Lambda_{eff})$). By *effective crimp* we refer specifically to the curved geometry of fiber segments spanning between rigidly bonded fiber-fiber cross-over points [147], and not to the *intrinsic crimp* imparted to the fibers during scaffold fabrication [135]. The longitudinal fiber stiffness E_f in Eq. (7) was thus replaced by an effective fiber stiffness, $(E_f)'$ (Appendix D):

$$(E_f)' = \frac{E_f}{64\left(a_{eff} / d_f\right)B_1 + 4B_2} \tag{8}$$

with parameters B_1 and B_2 given by the expressions:

$$B_1 = \sqrt{1+\left(\frac{2\pi a_{eff}}{\Lambda_{eff}}\right)\frac{1}{2\pi}\int_0^{2\pi}\sin^2 z\sqrt{1-\kappa_{eff}^2\sin^2 z}\,dz} \qquad B_2 = \frac{1/2\pi}{\sqrt{1+\left(\frac{2\pi a_{eff}}{\Lambda_{eff}}\right)^2}}\int_0^{2\pi}\frac{dz}{\sqrt{1-\kappa_{eff}^2\sin^2 z}} \tag{9}$$

and where κ_{eff} is the initial effective curvature of the fiber segment, given by the relation:

$$\kappa_{eff}^2 = \frac{\left(2\pi a_{eff} / \Lambda_{eff}\right)^2}{1+\left(\frac{2\pi a_{eff}}{\Lambda_{eff}}\right)} \tag{10}$$

5.3 MATERIALS AND METHODS

5.3.1 Nonwoven Scaffolds and Fibers

The scaffolds were needled nonwoven PGA, PLLA, and a 50:50 blend of PGA and PLLA fibers (Albany International Research, Mansfield, MA). A complete description of the scaffold manufacturing process was reported by Freed et al. [135], with the exception that the scaffolds used in the current study were bonded only by needling (i.e., scaffolds were not further bonded by pressing between heated metal plates as described previously [135]). The key properties of these scaffolds relevant to formulating the structural model were quantified in the current study (Table 1-4). Multifilament PGA and PLLA yarns (US Surgical, Norwalk, CT) were kindly provided by Dr. John Gray (Biomedical Structures, Inc., Slatersville, RI). The individual PGA and PLLA fibers in the yarn were 2.2 denier (Dr. John Gray, personal communication). The yarns were washed for 20 minutes in isopropyl alcohol in order to remove the spin finish and allowed to dry overnight beneath a laminar flow hood prior to use. The washed and dried yarns were separated into individual fibers prior to mechanical testing.

5.3.2 Uniaxial Testing of Single PGA and PLLA Fibers

Single PGA and PLLA fibers were tested per the guidelines provided in ASTM D 3379. Single fibers were center-line mounted on a slotted tab made of 60 grit sandpaper (Gatorgrit® multi-purpose sandpaper; Ali Industries, Inc., Fairborn, OH), and were subsequently bonded to the tab using Surebonder® All Purpose Mini Glue Sticks (FPC Corporation, Wauconda, IL) and the high temperature (165°C) setting of a Surebonder® Mini Glue Gun (FPC Corporation, Wauconda, IL). As per ASTM D 3379, a gage length at least 2000 times the diameter of the fiber (i.e., 30 mm) was used for all tests. Fiber diameters were measured from calibrated scanning electron micrographs of individual PGA and PLLA fibers (see *Scanning electron microscopy*). Fiber diameter was measured at 5 points along the length of the fiber using the Trace Measurement Mode of SigmaScan Pro (SPSS, Inc., Chicago, IL). The mean fiber diameter was used in the calculation of the fiber cross-sectional area. Tabs were mounted in the grips of an MTS Tytron™ 250 test system (MTS Systems Corporation, Eden Prairie, MN) and strained to failure at a rate of 1 mm/min. Force was recorded using the standard 500 N capacity load cell (accuracy ± 5%) and engineering stress was calculated by dividing the force by the mean initial cross-sectional area of the fiber. Engineering strain was calculated by dividing the change in fiber length by the original gage length. The fiber longitudinal stiffness was taken as the slope of the stress versus strain curve in the initial elastic region prior to yielding (i.e., ~ 0.6% strain). The tensile strength and strain-to-failure were recorded as the stress and strain at failure, respectively.

5.3.3 Effective Stiffness Measurement

The device and methods used to measure *E* have been described previously [62, 100]. In the current study testing was performed both on dry and 1x phosphate buffered saline (PBS)-bathed scaffolds. Rectangular specimens were cut to size (25 x 7.5 x 1 mm) with the long axis oriented in either the PD or XD (see *Fiber orientation distribution analysis*), were marked with 5 to 10 small black dots (~ 0.3 mm^2) along one long edge using a permanent marker, and were subjected to three-point bending by a calibrated bending bar of known stiffness. The displacements of the specimen markers, the bending bar marker, and a reference marker were recorded to video using a high-resolution CCD camera and tracked using a custom C program. Based on the resolution, post coordinates, load, displacement, and marker coordinates, the program calculated M and the resulting $\Delta\kappa$ of each specimen. The thickness t was measured using a calibrated digital image of each specimen using SigmaScan Pro (SPSS, Inc., Chicago, IL) with a resolution of ~30 μm. The width w was measured using a digital slide caliper (resolution ± 10 μm; The L.S. Starrett Co., Athol, MA). Finally, E was calculated via a linear regression using Eq. (3) and the value of I calculated using t and w.

5.3.4 Scanning Electron Microscopy

The methods used for scanning electron microscopy (SEM) of nonwoven scaffolds have been described previously [62]. In brief, specimens of PGA, PLLA, and 50:50 PGA/PLLA scaffold material and individual PGA and PLLA fibers were prepared for SEM. Dry specimens were attached to aluminum specimen stubs and sputter coated with a thin layer of gold-palladium alloy (~3 nm thickness) in a 108auto sputter coater with a MTM-20 thickness controller (Cressington Scientific Instruments, Inc., Cranberry Twp., PA). Specimens were imaged at 1800x for fiber diameter measurements and 100x for effective crimp quantification at 5 kV on a JEOL JSM-6330F field emission scanning electron microscope (JEOL USA, Inc., Peabody, MA).

5.3.5 Intrinsic and Effective Crimp Quantification

During the nonwoven scaffold manufacturing process, the multifilament PGA or PLLA yarn is crimped prior to cutting the yarn into 40 mm long fibers [135]. In order to quantify this *intrinsic crimp*, fibers were gently teased from the scaffolds and imaged under low power (40x) magnification (**Figure 43**A). Six images (1 fiber/image) were calibrated to the fiber diameter and the intrinsic crimp Λ and a_0 were measured using the Trace Measurement Mode of SigmaScan Pro (SPSS, Inc.). As introduced above in *New assumptions for modeling needled nonwoven scaffolds*, the *effective crimp* in determining $(E_f)'$ in Eq. (8) was assumed to be due to the curved geometry of fiber segments spanning between rigidly bonded fiber-fiber cross-over points [147]. The effective crimp amplitude a_{eff} and wavelength Λ_{eff} were measured for individual fiber segments in SEM images based on an idealized crimp structure that we proposed (**Figure 44**A). Because rigidly bonded fiber-fiber cross-over points cannot be discriminated from labile cross-over points via SEM, potential values for a_{eff} and Λ_{eff} were measured for fiber segments spanning each intervening cross-over point along the length of a particular fiber (**Figure 44**B).

Specifically, fibers (n = 6) were selected in SEM images of the PGA, PLLA, and 50:50 PGA/PLLA scaffolds, and the length of the straight line segment connecting one end of the fiber to the furthest observable fiber-fiber cross-over point was recorded as a potential value for 0.5 Λ_{eff}. The corresponding value of a_{eff} was recorded as the orthogonal distance from the midpoint of the 0.5 Λ_{eff} line segment to the midpoint of the curved fiber segment. This procedure was then repeated for each intervening cross-over point, yielding a set of approximately six potential values for Λ_{eff} and a_{eff} for each fiber measured.

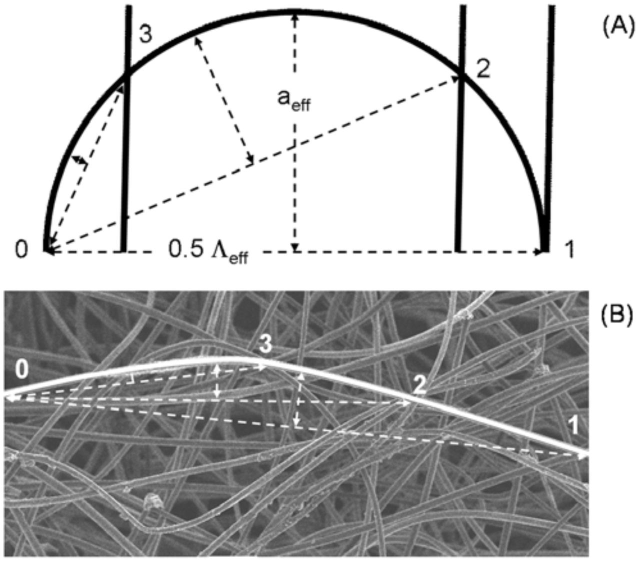

Figure 44 Schematic depicting the idealized structure used in quantifying the *effective crimp* (A). For each intervening fiber-fiber cross-over point (e.g., 1, 2, 3), a potential value for the effective crimp wavelength Λ_{eff} and amplitude a_{eff} were determined from the lengths of the dashed line segments. Schematic showing how the idealized structure (A) was implemented to quantify Λ_{eff} and a_{eff} in the SEM images (B).

5.3.6 Fiber Orientation Distribution Analysis

Small angle light scattering (SALS) was used to quantify $R(\Phi)$. A detailed description of SALS [150], and its application to fibrous PGA scaffolds [151], have been published. In brief, PGA, PLLA, and 50:50 PGA/PLLA scaffolds (10 x 10 mm) were scanned every 1 mm using a 1 mm diameter Helium-Neon laser beam. The resultant scattered light intensity distribution, $I(\Phi)$, recorded at ~ 60 random points within each specimen was averaged and the mean intensity distribution, $\overline{I}(\Phi)$, was used to obtain $R(\Phi)$ by using Eq. (6) with $\overline{I}(\Phi)$ analogous to $N(\Phi)$ and an angular increment $\Delta\Phi$ of 1 degree. $R(\Phi)$ was fit to the following normalized Gaussian distribution using Mathcad 11 (Mathsoft Engineering & Education, Inc., Cambridge, MA).

$$R(\Phi)=\frac{\dfrac{\sigma}{y_0}+\dfrac{1}{\sigma\sqrt{2\pi}}\exp\left(-\dfrac{\Phi^2}{2\sigma^2}\right)}{\int_{-\pi/2}^{\pi/2}\left[\dfrac{\sigma}{y_0}+\dfrac{1}{\sigma\sqrt{2\pi}}\exp\left(-\dfrac{\Phi^2}{2\sigma^2}\right)\right]d\Phi} \tag{11}$$

The constant y_0 was fit to yield distribution shapes suitable for modeling the experimentally measured fiber orientation distribution data. The normalized Gaussian distribution thus permitted simulation of the entire spectrum of possible fiber orientation distributions via perturbation of only the standard deviation parameter σ.

5.3.7 Calculating the Number of Fibers per RVE

To calculate N_f of each scaffold, Eq. (5) was used with b = 1 mm. The values for ω in Eq. (5) were calculated by multiplying the scaffold density reported by Albany International (Table 2) by the mean value of the measured scaffold thickness (Table 2) and are summarized in Table 3. The values for λ in Eq. (5) were calculated by multiplying the fiber density ρ_f by A_f (Table 3). The mean value of the reported density range for PGA (1.57 mg/mm^3 [135]) was used for the PGA fiber density and the mean value of the reported density of amorphous and 100% crystalline PLLA (1.269 mg/mm^3 [152]) was used for the PLLA fiber density. The values of A_f were calculated from the mean values of the measured fiber diameters (Table 1) using $A_f=\pi d_f^2/4$. For the 50:50 PGA/PLLA, ρ_f, A_f, and λ were taken as the average of the PGA and PLLA values.

5.3.8 Effective Stiffness Modeling

Each potential set of a_{eff} and Λ_{eff} values was used to calculate a corresponding value of $(E_f)'$ (Eq. (8)) and E (Eq. (7)), and the best-fitting set of a_{eff} and Λ_{eff} values (i.e., the set which yielded the closest agreement between the measured and predicted value of E) was determined for each of the six fibers imaged. The mean value of $(E_f)'$ was then calculated from the best-fitting Λ_{eff} and a_{eff} values, and EI of a RVE of PGA, PLLA, and 50:50 PGA/PLLA nonwoven scaffold was predicted using the structural model (Eq. (7) and (8)) and divided by the appropriate value of I to yield E. Lower and upper bounds on EI were calculated using the "complete freedom" and "no freedom" models (Eq. (4) and (7), respectively), and likewise divided by I to yield lower and upper bounds on E. In order to calculate the values of E for XD specimens, cosine was substituted for sine in Eq. (4) and (7). The values of the parameters used in the calculations are summarized in Tables 1-4. All equations were solved using MathCad 11.

5.3.9 Assessment of General Predictive Capability

To assess the general predictive capability of the structural model we chose to perturb the fiber diameter d_f. Because of the spring-like effective fiber behavior, the structural model (Eq. (7) and (8)) predicted that E would be highly sensitive to perturbations in d_f via a cumulative fourth-order dependence. To generate nonwoven PGA scaffolds with reduced fiber diameters, we relied on techniques described by Gao et al [107]. Nonwoven PGA scaffolds were incubated in 1M NaOH (Sigma) in PBS for 1, 3, and 5 minutes and then characterized by three-point bending to measure E and by SEM to measure d_f. For each measured value of d_f, the corresponding predicted value of $(E_f)'$ was calculated using Eq. (8) and the mean values of Λ_{eff} and a_{eff} for PGA (Table 4). The predicted values of E were then calculated using Eq. (7) with E_f replaced by $(E_f)'$ and A_f calculated using the measured d_f.

5.3.10 Sensitivity Analysis

To assess model sensitivity to key measured parameters, the ratio $(E_f)'/E_f$ was computed for a range of a_{eff} and Λ_{eff} values. The range considered for a_{eff} spanned from 0 (i.e., straight fibers) to 0.2 (the intrinsic crimp amplitude a_0 was measured to be 0.195 mm). The range considered for Λ_{eff} spanned from 0.4 (assuming a minimum value for the average inter-fiber distance to be 0.2 mm) to 2 (the intrinsic crimp wavelength Λ was measured to be 1.774 mm). The minimum value for the average inter-fiber distance was estimated by first calculating the number of fibers per hypothetical layer of the nonwoven (i.e., $N_f/(t/d_f)$), and then calculating the average inter-fiber distance, assuming that all of the fibers in a hypothetical layer are oriented orthogonal to the PD and XD directions in a ratio of 3 to 1. To assess model sensitivity to variations in $R(\Phi)$, model predictions for E of the 50:50 PGA/PLLA specimens oriented in the PD and XD were calculated for values of σ ranging from 1 to 120 degrees.

5.3.11 Statistics

Data were expressed as mean ± standard error (SEM). Groups were compared using unpaired, two-tail student t-tests. Differences were considered significant when $p < 0.05$.

5.4 RESULTS

5.4.1 Uniaxial Tensile Tests of PGA and PLLA Fibers

Representative stress versus strain curves for PGA and PLLA fibers are depicted in **Figure 45** and their mechanical properties (mean ± SEM) are listed in **Table 3**. The PGA fibers exhibited a significantly higher stiffness (+80%) and tensile strength (+51%) than the PLLA fibers ($p < 0.05$), while the PLLA fibers exhibited a significantly higher strain-to-failure (+41%) than the PGA fibers ($p < 0.05$). The general behavior of the PGA fibers tested in the current study compared favorably with a previous report by Slivka et al. [153].

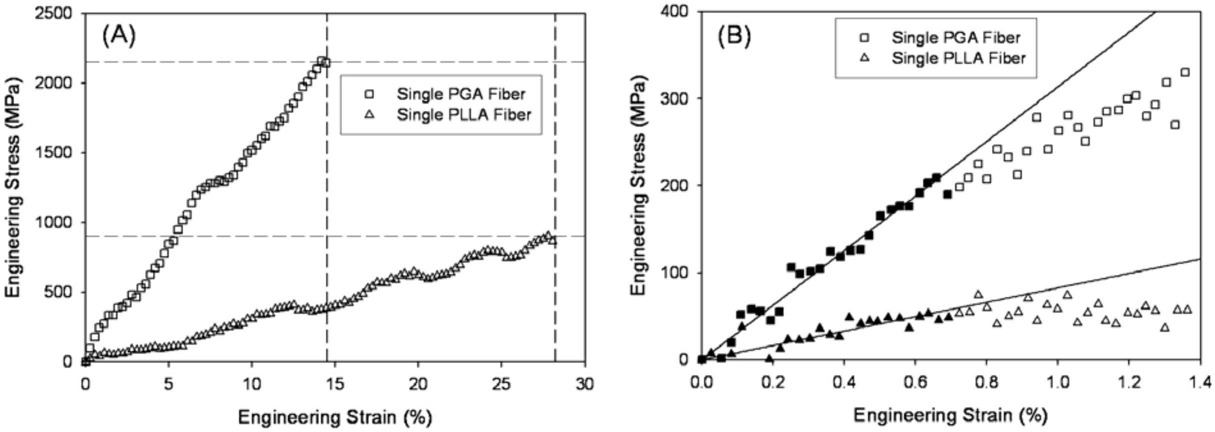

Figure 45 Representative uniaxial stress-strain curves for single PGA (□) and PLLA (△) fibers (A). The longitudinal fiber stiffness was taken as the slope of the initial linear region of the stress-strain curve prior to yielding (B). The PGA fibers exhibited a higher stiffness ($p < 0.05$) and tensile strength ($p < 0.05$) than the PLLA fibers. The PLLA fibers exhibited a higher strain-to-failure ($p < 0.05$) than the PGA fibers.

Table 3 Measured mechanical properties of individual PGA and PLLA fibers (US Surgical). All properties were measured for dry fibers at room temperature. Values represent mean ± SEM (n=6 fibers).

Material	Diameter (μm)	Longitudinal Stiffness (GPa)	Tensile Strength (MPa)	Strain to Failure (%)
PGA	12.95 ± 0.02	18.78 ± 3.43	1311.60 ± 203.33	17.29 ± 1.20
PLLA	16.36 ± 0.02	10.42 ± 1.39	869.85 ± 53.14	24.29 ± 2.25

Table 4 Structural properties of PGA, PLLA, and 50:50 PGA/PLLA scaffolds.

Material	Thickness (μm)	Bulk Density (mg/cm^3)	Mean Fiber Orientation Distribution, $R(\Phi)$ Normalized Gaussian Model ($\mu = 0$)		
			σ (degrees)	y_o	R^2
PGA	948 ± 28	69.0	31.66	25000	0.9951
PLLA	1153 ± 37	61.9	33.79	20000	0.9986
50:50	889 ± 6	61.75	32.97	15000	0.9987

5.4.2 Intrinsic and Effective Crimp

The mean values of the intrinsic crimp wavelength Λ and amplitude a_0 were 1.774 ± 0.101 mm and 0.195 ± 0.020 mm. The best-fitting of the potential effective crimp parameters Λ_{eff} and a_{eff} (**Table 5**) were lower, suggesting that the intrinsic crimp imparted to the yarn represents an upper limit on the effective crimp parameters and the concomitant values of $(E_f)'$.

Table 5 Best-fitting effective crimp wavelengths Λ_{eff} and amplitudes a_{eff} and calculated effective fiber stiffnesses $(E_f)'$ for the structural model. The effective fiber stiffnesses were calculated from Eq. (8) and the mean value was used in subsequent modeling calculations using Eq. (7).

Material	Λ_{eff} (mm)	a_{eff} (mm)	$(E_f)'$ (kPa)
PGA	1.197549	0.09296	7606
	1.703836	0.069814	12940
	1.419725	0.07763	10610
	1.102133	0.067197	14250
	1.736596	0.092093	7525
	1.518951	0.063095	15850
mean ± SEM	1.446465 ± 0.105973	0.077132 ± 0.005241	11464 ± 1418
PLLA	1.36339	0.109491	4872
	1.87314	0.127396	3543
	1.557829	0.081312	8536
	1.310796	0.101381	5660
	1.035789	0.090791	7154
	1.632403	0.096241	6140
mean ± SEM	1.462225 ± 0.118532	0.101102 ± 0.006541	5984 ± 712
50:50	1.23679	0.086656	8171
	0.823824	0.125644	4336
	0.896858	0.071466	12160
	1.080097	0.062754	15355
	1.1924	0.106574	5542
	1.080133	0.08935	7813
mean ± SEM	1.051684 ± 0.066225	0.090407 ± 0.009384	8896 ± 1694

5.4.3 Experimental effective stiffness

Mean three-point bending test results are presented for comparison in terms of load-deflection (**Figure 46**A-C) and moment-curvature (**Figure 46**D-F). Measured values of *E* for the dry PGA, PLLA, and 50:50 PGA/PLLA scaffolds (**Table 6**) were always higher than for the 1x PBS wetted scaffolds (data not shown), however the difference was not statistically significant. In contrast, significant differences were found for each material between *E* of the scaffolds cut in the PD versus XD directions ($p < 0.001$). For the dry scaffolds, the ratios of E in the XD to PD were 0.31, 0.35, and 0.38 for PGA, PLLA, and 50:50 PGA/PLLA, respectively. E results for the 50:50 PGA/PLLA scaffolds in the PD were comparable to our previously published results [63].

Table 6 Measured and predicted E of PGA, PLLA, and 50:50 PGA/PLLA scaffolds. Measured E values represent mean ± SEM (n=6 measurements). Predicted E values for the structural model were calculated using Eq. (7) with $(E_f)'$ given by Eq. (8). Lower and upper E bounds were predicted using Eq. (4) and (7).

Material	Material Direction	E Measured (kPa)	E Predicted (kPa)	E Lower Bound (kPa)	E Upper Bound (kPa)
PGA	PD	**284 ± 34**	**306**	70	501,000
	XD	**88 ± 7**	**81**	18	132,100
	Random*	N/A	189	43	309,500
PLLA	PD	**171 ± 14**	**168**	44	292,500
	XD	**60 ± 6**	**54**	14	94,280
	Random*	N/A	109	29	190,600
50:50 PGA/PLLA	PD	**206 ± 16**	**222**	80	366,000
	XD	**78 ± 5**	**76**	27	124,200
	Random*	N/A	147	53	240,800

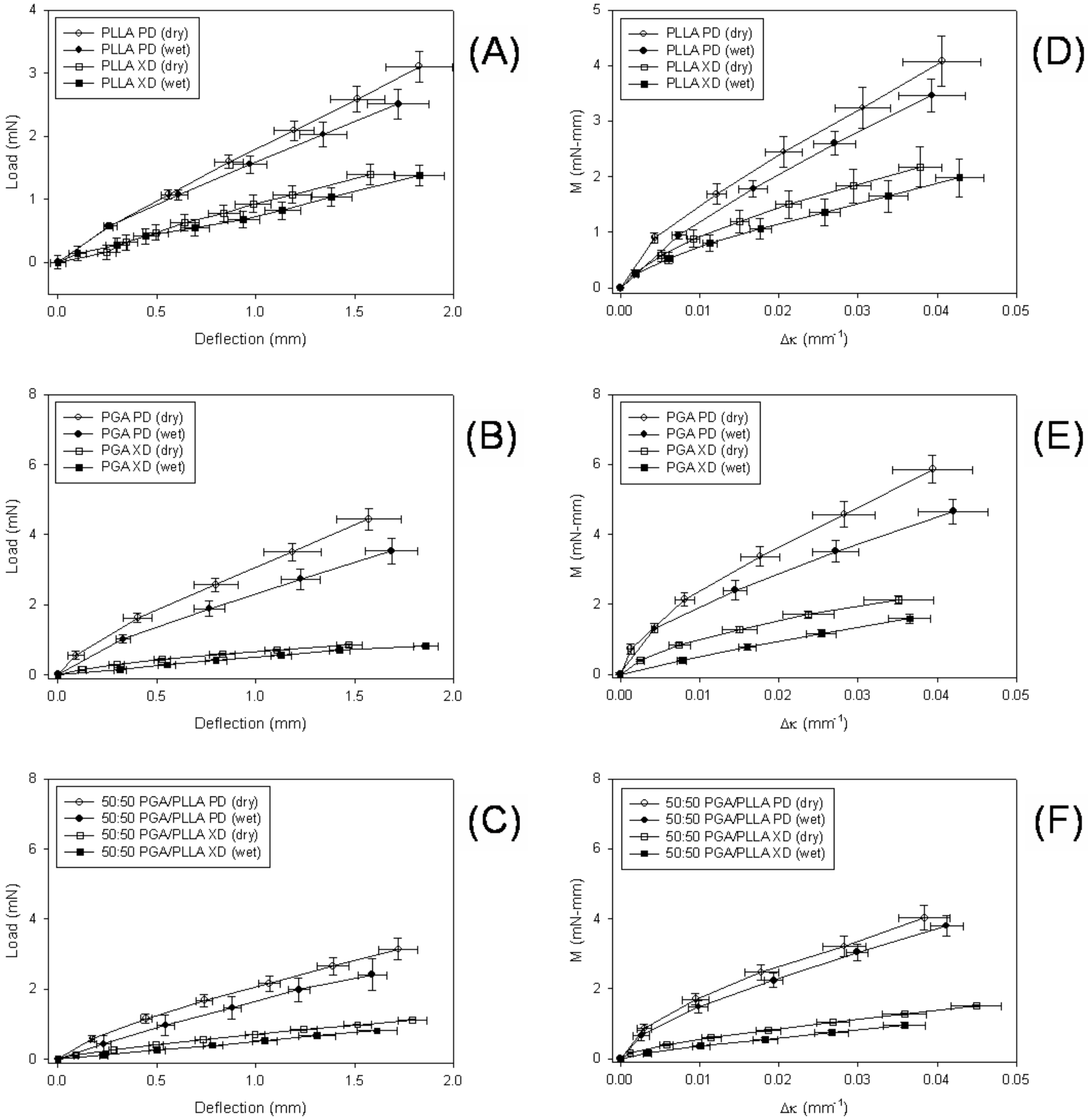

Figure 46 Mean load-deflection curves measured by three-point bending for both dry and wet PLLA (A), PGA (B), and 50:50 PGA/PLLA (C) scaffolds (n=6). Mean moment-curvature curves measured by three-point bending for both dry and wet PLLA (D), PGA (E), and 50:50 PGA/PLLA (F) scaffolds (n=6). *E* was calculated for each scaffold specimen via the Bernoulli-Euler moment-curvature relationship (Eq. (3)) and then averaged to yield the mean value of *E* (Table 5). Differences between dry and wet scaffolds were not statistically significant.

5.4.4 Fiber Orientation Distribution Analysis

A normalized Gaussian equation with a mean of zero (Eq. (11)) was found to fit the mean experimentally measured orientation distribution (**Figure 47**) very well, with coefficients of determination exceeding 0.99 for PGA, PLLA, and 50:50 PGA/PLLA (**Table 4**).

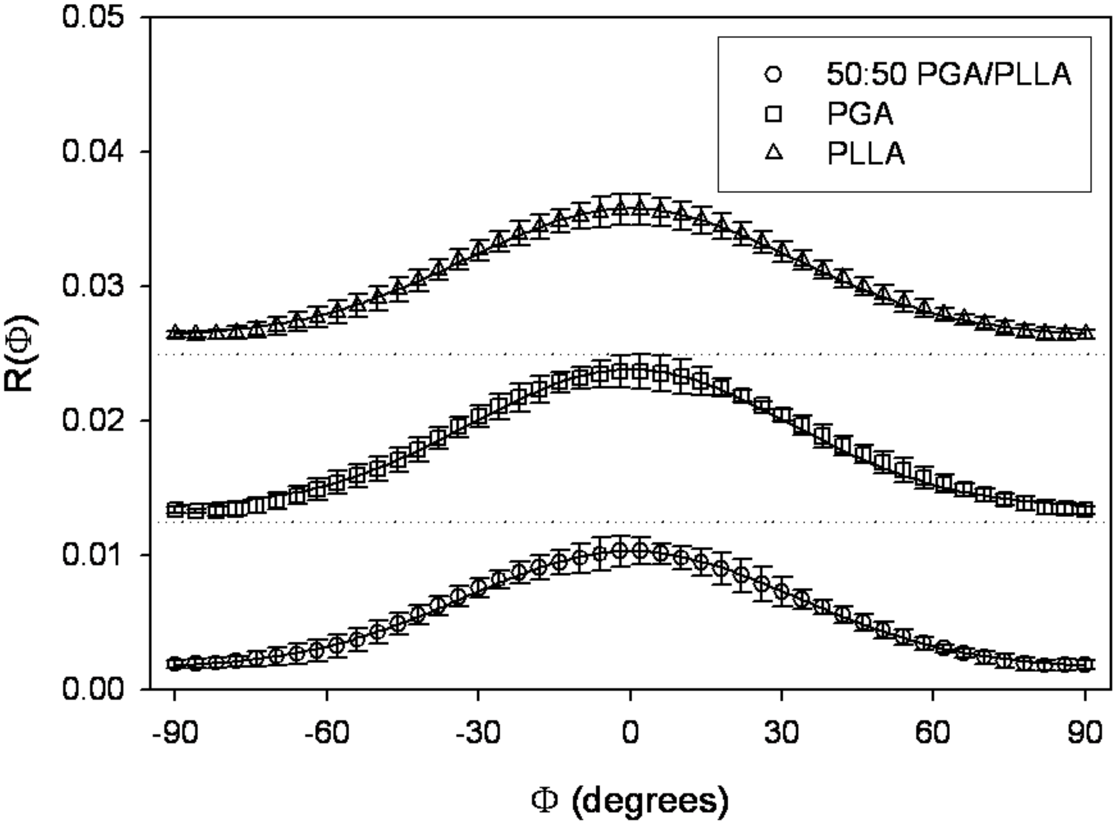

Figure 47 The fiber orientation distribution (mean ± SEM) for PGA (□), PLLA (△), and 50:50 PGA/PLLA (○) as measured by SALS. The distributions were modeling using a normalized Gaussian distribution (Eq. (11)) with the mean μ constrained to zero. Note that the distributions depicted for PGA and PLLA were scaled for presentation purposes (baseline indicated by dotted line), and that the integral from Φ = -90 to 90 degrees was exactly equal to 1 for each distribution.

5.4.5 Predicted Effective Stiffness Results

The values of *E* predicted by the structural model closely approximated the values measured experimentally using the three-point bending test (**Table 6**). Representative M-$\Delta\kappa$ plots are depicted for the PD (**Figure 48**A) and XD (**Figure 48**B) specimens. Using the mean values of $(E_f)'$ (Table 4), the model estimates were on average within ± 6% of the experimental results for the PD specimens and within ± 7% of the experimental results for the XD specimens. The predicted ratios of *E* in the XD to PD were 0.26, 0.32, and 0.34 for PGA, PLLA, and 50:50 PGA/PLLA, respectively. The "complete freedom" model underestimated *E*, yielding a lower bound on average 75% lower than the experimentally measured values for the dry scaffolds. In the other extreme case, the "no freedom" model severely overestimated *E*, yielding upper bounds ~ 3 orders of magnitude higher than the experimentally measured values for the dry scaffolds.

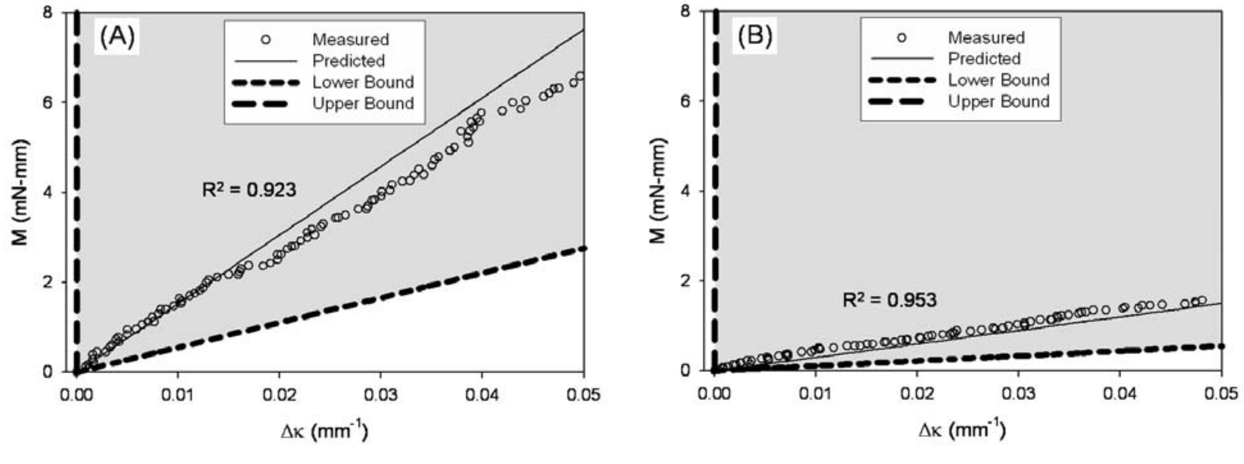

Figure 48 Representative experimental moment-curvature plots for PD (A) and XD (B) specimens of 50:50 PGA/PLLA scaffold (○). The experimental curves were bracketed by the lower and upper bounds calculated using Eq. (4) and (7). The structural model (Eq. (7) and (8)) closely matched the experimental data.

5.4.6 Assessment of General Predictive Capability

The rate of NaOH-mediated fiber surface hydrolysis observed in the current study (1.1 μm/min) compared favorably with that reported by Gao et al. [107] (0.65 μm/min) (data not shown). Using the same Λ_{eff} and a_{eff} values determined previously for the unmodified PGA scaffold (**Table 5**), the structural model simulated the experimentally-measured dependence of E on d_f with a coefficient of determination of 0.987 (**Figure 49**).

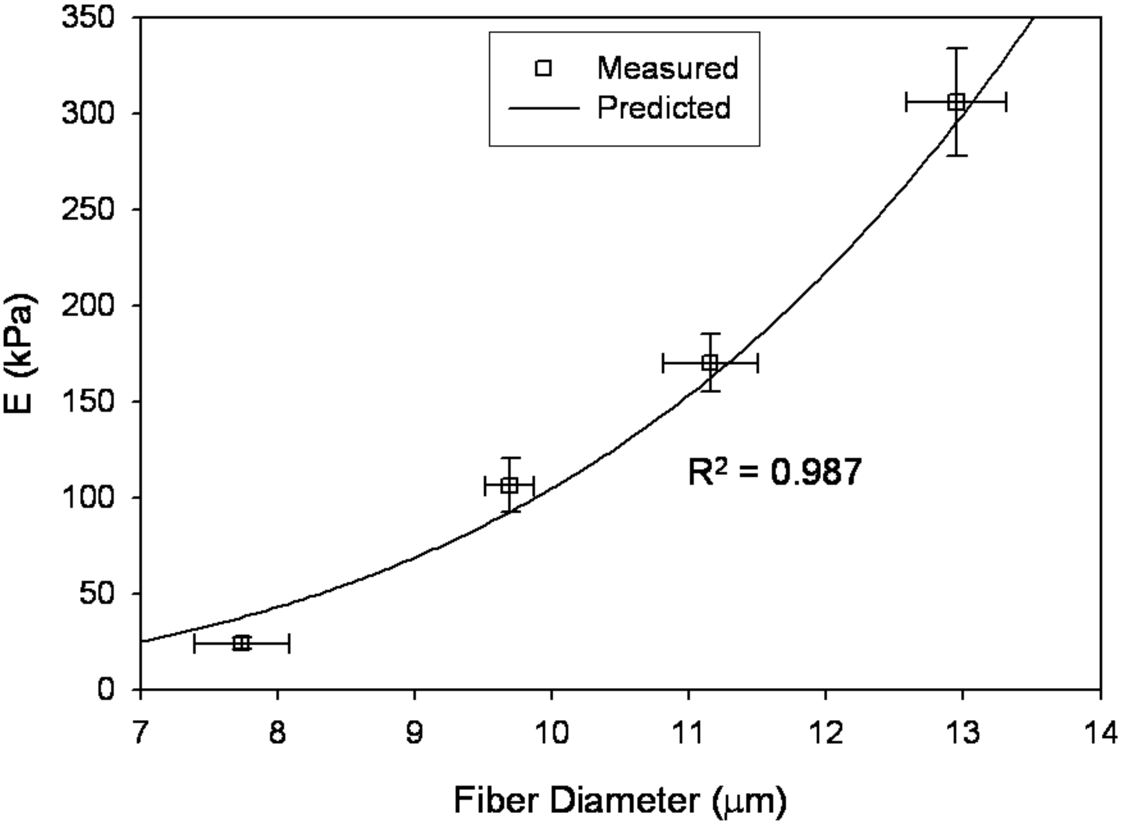

Figure 49 E versus d_f (mean ± SEM) measured for PD specimens of PGA scaffold subjected to surface hydrolysis in 1N NaOH solution. The model predictions were strikingly similar to the experimental results, thus providing additional verification of the predictive capacity of the model.

5.4.7 Sensitivity Analysis

The predicted dependence of the ratio $(E_f)'/E_f$ calculated using Eq. (8) demonstrated a much higher sensitivity to a_{eff} than Λ_{eff} (**Figure 50**A). For straight fibers (i.e., $a_{eff} = 0$) Eq. (8) correctly predicts a ratio $(E_f)'/E_f$ equal to 1. The normalized Gaussian distribution shifted from a peak at small values of σ (e.g., 10°) to nearly a constant at large values of σ (e.g., 50°), thus permitting simulation of the entire spectrum of possible fiber orientation distributions (**Figure 50**B). The values of *E* predicted for the PD and XD specimens converged to within 5% of the value predicted for a random distribution at a σ value of ~ 90°. In the σ range of 30° to 40°, the dependence of *E* on σ is practically linear, with slopes of -3.4 kPa/degree and 2.7 kPa/degree in the case of the PD and XD specimens, respectively ($R^2 > 0.995$).

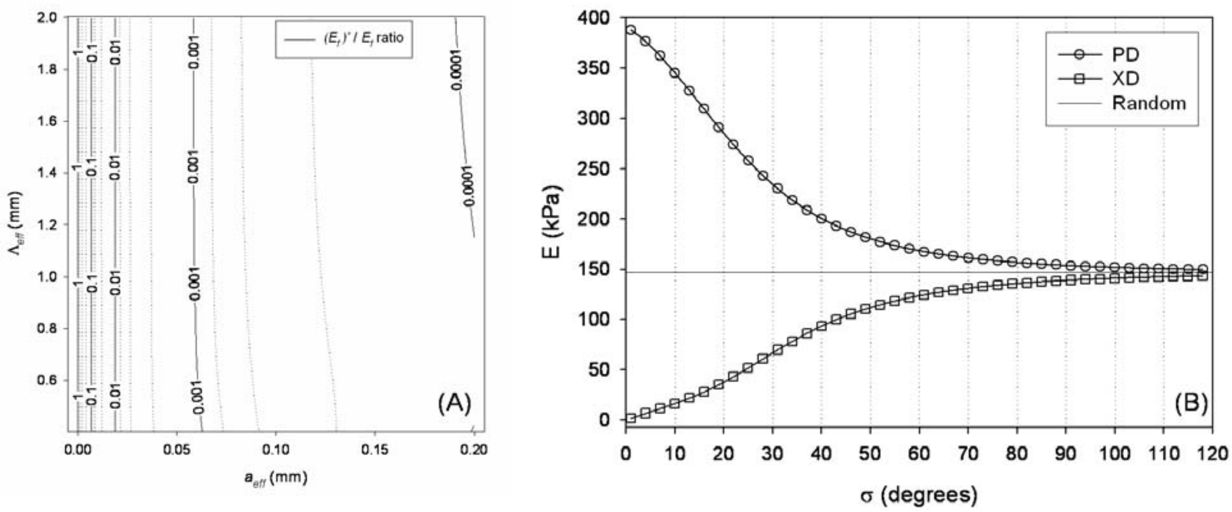

Figure 50 Predicted dependency of the $(E_f)'/E_f$ ratio (logarithmic scale) on the values of a_{eff} and Λ_{eff} (A). Note that in the limit a_{eff} goes to zero (i.e., straight fibers), Eq. (8) correctly predicts an $(E_f)'/E_f$ ratio of 1. Predicted dependency of *E* on the σ parameter of the fiber orientation distribution for 50:50 PGA/PLLA scaffolds (B).

5.5 DISCUSSION

Ever since the seminal work of Freed et al. [135], in which bovine articular chondrocytes were seeded onto a nonwoven PGA scaffold, the combining of cells with bioresorbable nonwovens has yielded valuable insight into the basic science of engineered tissue development. While investigators continue to introduce new types of scaffolds, some of which possessing potentially attractive properties such as elasticity [154], needled nonwovens continue to serve an important role in TE, both as a benchmark for evaluating novel biomaterials, and importantly for their own unique capacity to promote tissue formation; the merit of pursuing the application of these scaffolds clinically is substantiated by the promising results of several animal studies [32, 33, 56, 136].

However, while the outcomes of these ongoing experiments are encouraging, the underlying mechanisms governing the successful development of a functional tissue are not well understood. From a biomechanics perspective, perhaps the most fundamental issue yet to be addressed is the lack of information concerning the mechanics of the nonwoven scaffold itself. In the current study we focused on this issue, with the caveat that a mathematical model describing the scaffold is only the first step toward developing an accurate representation of the generally heterogeneous cell-seeded nonwoven scaffold.

In the current study we developed a structural model to predict E of a nonwoven TE scaffold from the fiber properties and the nonwoven structure. To the best of our knowledge, the current study is the first to model the mechanics of a needled nonwoven TE scaffold. For comparison, models developed by Freeston and Platt [146] for the extreme cases of “complete freedom” (lower bound) and “no freedom” (upper bound) of relative fiber motion were considered as well.

5.5.1 Predictive Capability of the Structural Constitutive Model

Overall, the value of E predicted by the model compared favorably with the experimental results, both for the PD and XD specimens. As reported in the results, the PD predictions (± 6%) were slightly better than the XD predictions (± 7%). There are several possible sources of error which may have contributed to these small deviations between the predicted and experimental results. First, it should be noted that in most cases the structural model slightly overestimated E in the PD and slightly underestimated E in the XD. This deviation could possibly be explained in two ways. In the SALS method, the scattered light intensity distribution $I(\Phi)$ represents the average angular orientation of fibers dispersed through the specimen thickness. This measure is thus consistent with the assumption of equal angular distribution through the RVE thickness made by Freeston and Platt in deriving their models [146], and also invoked in our structural model. However, based on the complex effects of needling on the vertical and horizontal alignment of fibers in needled nonwovens [97], it is possible that the angular orientation varies to some degree through the thickness. Thus, if $R(\Phi)$ was broader than that measured by SALS, then the values of E predicted for the PD specimens would have been lower and the values for the XD specimens higher (see *Sensitivity analysis* results). Recent improvements in the spatial resolution of x-ray microtomography have allowed for the quantification of through-thickness variations in the fiber structure of nonwovens [155], and thus this method may be useful in obtaining a more complete characterization of the three-dimensional fiber structure.

A second possible source of deviation might be that the effective crimp parameters are a function of the angle Φ. Such a dependence has previously been observed by Hearle and Stevenson [143], with fibers in the PD less curved (i.e., effectively stiffer) than fibers in the XD.

In the current study we did not account for the orientation of the fibers in measuring the crimp parameters. However, it is unlikely that this effect would help explain the data in the current study, as a decrease in fiber curvature in the PD direction and increase in the XD direction would produce the opposite effect; the value of E predicted for the PD would be higher and the value for the XD lower, thus resulting in an even larger deviation.

5.5.2 Implications of the General Predictive Capability

The model predictions were strikingly similar to the experimentally measured values of E (**Figure 49**), providing evidence that the structural model can be used to prepare a scaffold exhibiting a desired E. In the study by Gao et al. [107], a linear relationship was found between the decrease in d_f and hydrolysis time (0.65 μm/min). Furthermore, they demonstrated that the bulk properties of the fibers (e.g, molecular weight, crystallinity) had not changed significantly, suggesting that the fiber stiffness remained constant. In the current study, the values of Λ_{eff} and a_{eff} determined for the virgin scaffold continued to provide reasonable estimates for $(E_f)'$ following NaOH-mediated surface hydrolysis, suggesting that the reduction in d_f had little effect on the integrity of the physical bonds generated during the needling process. These results may prove useful in TEHV design, as the initially high stiffness of TEHV relative to native valvular tissue could potentially result in poor opening characteristics or undesirable transvalvular pressure gradients during the early phase of implantation prior to scaffold resorption [32, 33]. Moreover, in contrast to $R(\Phi)$, the fiber diameter d_f (and thus E) can be readily adjusted in the lab by surface hydrolysis following procurement of the scaffold. Interestingly, in a recent study by Prabhakar et al. [156], TE arteries created by seeding SMC onto NaOH surface hydrolyzed nonwoven PGA exhibited enhanced mechanical and phenotypic properties compared with untreated, heat-treated, or γ-irradiated PGA scaffolds, suggesting that the increased SMC adhesion [107] and decreased effective fiber stiffness may be a beneficial combination.

5.5.3 Small Strain versus Large Strain Behavior of Needled Nonwovens

Development of the structural model described herein was motivated by our ongoing research in the area of TEHV. Because cyclic flexure is the primary mode of TEHV deformation at early time points prior to scaffold degradation [62, 63], in the current study we focused on developing a model to predict *E* measured in bending. In our three-point bending test the tissue strains are typically less than ±7% [157], and thus within the initial stress-strain regime (0-20 %) [98] dictated by straightening of crimped fibers [145]. For a material whose tensile and compressive stiffnesses are equal, the value of *E* measured in bending should be equivalent to the initial stiffness measured in uniaxial tension. Such a one-to-one correspondence has previously been demonstrated for a wide variety of nonwoven materials [158], suggesting that the mechanism of initial deformation is similar in tension and compression. While previous studies have demonstrated that the out-of-plane compressive stiffness of nonwoven PGA scaffolds is relatively low (6.7 ± 0.5 kPa [159]), the good correspondence between *E* measured in bending and initial stiffness (gage length > average fiber length; unpublished observations) suggest that the in-plane compressive stiffness of the nonwoven scaffold is closer to the in-plane tensile stiffness. In contrast to the small strain behavior, the large deformation behavior of needled nonwovens is many-fold more complex.

It was demonstrated early on by Hearle and Sultan [145] that the uniaxial stress-strain behavior of needled nonwovens is highly nonlinear, exhibiting a sigmoidal shape qualitatively resembling that of a typical soft tissue [138]. They proposed that the stiffening observed at large strains was due to fiber reorientation and locking, with intermittent fiber slippage. In a later study, Hearle and Sultan [144] proposed initial theoretical models to describe the tensile response of needled nonwovens. While they stressed that the complexity of the needled nonwoven structure precluded an exact analysis, they discussed the factors influencing the tensile behavior qualitatively and developed a simplified model. Hearle and Purdy later explained that this initial model was inaccurate, owing to the physical implausibility of the proposed mechanism of inter-fiber friction development, and developed a more robust model to account for slippage effects based on a "capstan" equation [99]. Interestingly, for nonwoven 50:50 PGA/PLLA scaffolds, the peak tangent stiffness exhibited at larger strains (unpublished observations) is comparable to the value of E measured following reinforcement by *de novo* synthesized collagen [63].

5.5.4 The Effects of Needling Density

One parameter whose variation was not explored in the current study was needling density. As the needling density is directly related to the inter-bond distance, the effective crimp parameters would be expected to depend on the needling density. The needling density used to fabricate the PGA, PLLA, and 50:50 PGA/PLLA scaffolds was ~ 1,000 penetrations/in^2 (i.e., ~ 155 penetrations/cm^2; Dr. John Gray, personal communication). Studies by Hearle and Purdy [98] and Hearle et al. [160] have demonstrated an approximately linear increase in initial stiffness (equivalent to *E*) with increased needling density up to ~ 1000 pentrations/in^2, with a gradual decrease at higher needling densities attributed to fiber breakage. Thus, the needling density used for the nonwoven TE scaffolds is likely near the optimal level for maximizing *E*. Studies investigating needled nonwovens generated at different needling densities and different bulk densities would be necessary in order to conclusively demonstrate this phenomenon.

5.5.5 Reinforcement Effects in Needled Nonwoven Scaffolds

In a recent study we investigated the effects of cyclic flexural loading on the mechanical and structural properties of PGA and 50:50 PGA/PLLA scaffolds dip-coated with the biologically-derived thermoplastic poly-4-hydrobutyrate (P4HB) [62]. After dip-coating, *E* of the 50:50 PGA/PLLA scaffold was 1687 ± 151 kPa (compared with 206 ± 16 for the unmodified 50:50 PGA/PLLA (Table 5)). A comparison with the upper bound predicted using the "no freedom" model (Eq. (7)) suggests that dip-coating did not result in a switch from spring to rod-like fiber behavior, as this would suggest an *E* value of 366,000 kPa (Table 5). Kim and Mooney [114] have also demonstrated experimentally that even under extreme cases of fiber bonding, in which the mass of a PLLA binder was 200% of the initial mass of the PGA scaffold, the maximum initial stiffness achieved was only ~ 55,000 kPa.

In another study we demonstrated a strong positive linear relation between *E* and collagen concentration in a TEHV (**Figure 51**A) [63]. TEHV constructs were fabricated by dynamically seeding ovine vascular SMC onto nonwoven 50:50 PGA/PLLA scaffolds at a density of 17 x 10^6 SMC/cm^2. Immediately following the 30 hour seeding period, at which point no collagen could be detected biochemically, no increase in *E* was detected despite the dense cellularity (536 ± 38 μg DNA/g wet weight) and substantial accretion of sulfated glycosaminoglycans (S-GAG) (1393 ± 145 μg S-GAG/g wet weight). In identically fabricated constructs incubated under static or cyclic flexural loading conditions for 3 weeks, 351% (static) and 429% (cyclic flexure) increases in *E* were observed to correlate strongly with collagen concentration.

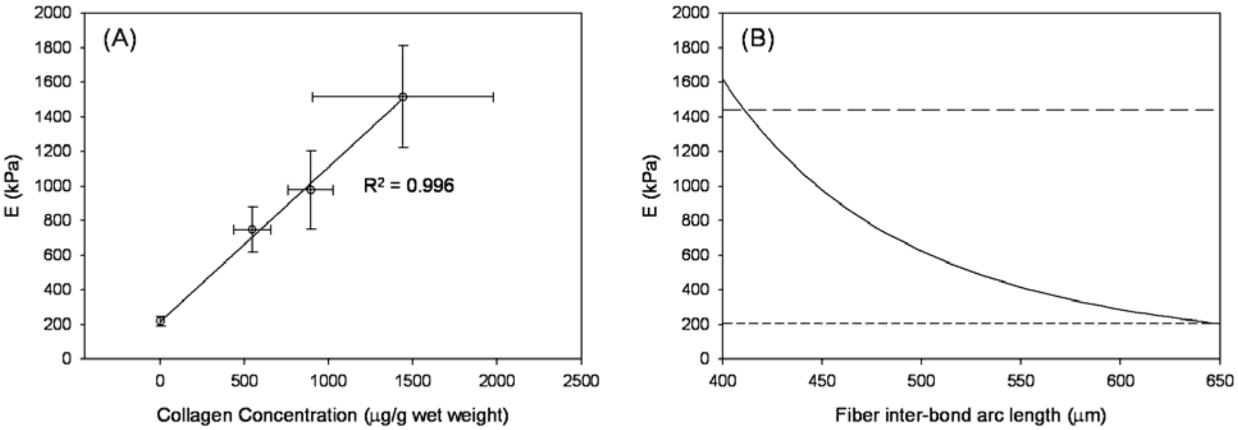

Figure 51 *E* results for cell-seeded nonwoven 50:50 PGA/PLLA scaffolds plotted versus collagen concentration (mean ± SEM, n=6) (A). Adapted from Engelmayr et al. [63] with permission by Elsevier Inc. Structural model predicted dependence of *E* on the fiber inter-bond arc length (B). Note that as the number of rigidly bonded fiber-fiber cross-over points increases (such as with P4HB dip-coating or collagen accretion), the fiber inter-bond arc length decreases and the fiber effective stiffness $(E_f)'$ increases. Values of *E* for unseeded (short dashed line) and 9-week mesenchymal stem cell-seeded (long dashed line) nonwoven 50:50 PGA/PLLA scaffolds are indicated for comparison.

Toward explaining these large increases in E, we initially attempted to estimate E of the cell-seeded nonwoven scaffolds using a simple rule-of-mixtures (ROM)

$$E = (E_f)' v_f + E_m v_m \tag{12}$$

in which E is the effective stiffness of the nonwoven nonwoven-ECM composite, and $(E_f)'$, E_m, v_f, and v_m are the effective stiffnesses and volume fractions of the scaffold and ECM phases, respectively [93]. Equation (12) assumes that all of the scaffold fibers are oriented parallel to the loading direction (i.e., overestimates the scaffold contribution to E), and thus given a measured value of E should provide a lower bound on E_m. It is evident, however, that higher order reinforcement mechanisms must be acting within the nonwoven nonwoven-ECM composite that are not predicted by Eq. (12). For example, assuming an upper bound on v_m of 0.96 and a constant $(E_f)'$ value of 8896 kPa (**Table 5**), Eq. (12) predicts lower bounds on E_m of 648 kPa and 410 kPa for the cyclic flexure and static specimens, respectively. Given the relatively low collagen content of these specimens, however, even these lower bounds on E_m appear unrealistically high. For example, in similarly fabricated TEHV based on rapidly degrading nonwoven PGA scaffolds, the initial stiffness measured in uniaxial tension following 20 weeks *in vivo* maturation and complete scaffold degradation (i.e., $E \equiv E_m$) was only ~ 160 kPa [32]. Based on the needled nonwoven TE scaffold structural-mechanics elucidated herein, a more reasonable explanation is that $(E_f)'$ is not a constant, but rather depends on E_m.

Figure 51B illustrates quantitatively the contribution of rigidly bonded fiber-fiber cross-over points (**Figure 44**) to E, with variations in a_{eff} and Λ_{eff} expressed in terms of a single arc length parameter. The fiber inter-bond arc length was calculated using the average values of a_{eff} and Λ_{eff} measured for the 50:50 PGA/PLLA scaffold (**Table 5**). Physically, Fig. 10B suggests that one of the principal reinforcement mechanisms acting in nonwoven nonwoven-ECM composites is an increase in the number of rigidly bonded fiber-fiber cross-over points, with a concomitant decrease in the arc length of the curved fiber segments spanning between these bond points, and thus effectively stiffer fibers. This unique reinforcement mechanism is dependent on both the spring-like tensile response of the crimped fibers, as well as on the splayed distribution of fiber orientations (i.e., availability of fiber-fiber cross-over points), and thus would not be expected to manifest in traditional unidirectional or straight fiber-reinforced composites [93]. Indeed, a thorough literature search suggests that this is the first study to report on this unique reinforcement mechanism, and the first to explain the large increases in *E* observed in nonwoven 50:50 PGA/PLLA scaffolds with tissue formation [63].

It must be noted, however, that the sharp increase in *E* predicted with decreased fiber inter-bond arc length (**Figure 51**B) must inevitably saturate as the fiber inter-bond arc length approaches the minimum inter-fiber distance. The minimum inter-fiber distance is a function of the scaffold bulk density (**Table 4**), and for the 50:50 PGA/PLLA scaffolds considered in the current study was estimated to be ~ 200 μm (see *Sensitivity analysis* methods). In support of this saturation behavior, the structural model predicts an *E* value of 36,200 kPa for a nonwoven PGA scaffold with a fiber inter-bond arc length of 200 μm. This approaches the maximum *E* value of ~ 55,000 kPa mentioned above for PLLA bonded PGA scaffolds [114].

In addition to the nonwoven nonwoven-ECM coupling described above, another factor which must be accounted for in predicting *E* of a cell-seeded nonwoven scaffold is the transmural distribution of cell and ECM constituents. As mentioned previously, it remains unclear if the quality or organization of the collagen deposited in response to cyclic flexure is fundamentally different than that deposited under static conditions, as concurrent changes were observed in the transmural cell and ECM distribution [63]. Equation (37) (see Appendix C) shows how the bending moment of a fiber M_f depends on the distance y the fiber lies from the neutral axis. In Eq. (37) the fiber stiffness E_f (or $(E_f)'$) is considered a constant, however in the case of a heterogeneous transmural distribution of collagen, the value of $(E_f)'$ accounting for the reinforcement mechanism described above would also be expected to vary with y. Thus, these results suggest that an accurate model for E of cell-seeded nonwoven scaffolds will need to account for both: (a) the unique coupling between $(E_f)'$ and E_m and (b) the transmural variation of collagen concentration (i.e., $E_m(y)$).

5.5.6 Implications for Cellular and ECM Deformation

The results of the current study demonstrate that the extension of curved fiber segments is fundamental to the deformation of needled nonwoven TE scaffolds. Thus, it would be expected that extension of these curved fiber segments will play an important role in determining the micro-scale strains imparted to the cells embedded in their ECM. Akbarov and coworkers [161] have developed rigorous analytical and numerical solutions for the stress distribution in the matrix phase surrounding sinusoidal curved fibers in composite engineering materials. Tentatively, these results leave open the possibility for significant cell and ECM strain amplification, with small longitudinal extensions yielding large transverse deflections in the curved fiber segments. If conclusively demonstrated, such a strain amplification phenomenon would have important ramifications for mechanotransduction in cell-seeded nonwoven scaffolds, and thus warrants further investigation.

5.5.7 Summary

In the current study we developed and experimentally verified a structural model to predict *E* of a nonwoven TE scaffold in bending. To the best of our knowledge this is the first study to report the following key findings:

- Needled nonwoven scaffolds are not isotropic, but rather exhibit distinct PD and XD fiber directions with an *E* ratio (PD/XD) of ~ 3-to-1.
- The crimped PGA and PLLA fibers behave like springs rather than straight rods, with effective stiffnesses $(E_f)'$ that can be calculated using the sinusoidal fiber shapes.
- The structural model can predict *E* of the surface hydrolyzed scaffolds described by Gao et al. [107], and thus can be used to design scaffolds with *E* similar to native soft tissues.
- The primary effect of collagen reinforcement in nonwoven nonwoven-ECM composites (i.e., cell-seeded scaffolds) is an increase in the number of rigidly bonded fiber-fiber cross-over points with concomitant increases in $(E_f)'$. This higher order reinforcement mechanism is dependent on the unique combination of the spring-like fibers and their angular dispersion, and precludes the use of simple rule-of-mixtures theory.

The structural model provides a rigorous, tractable mathematical foundation for developing a composite model of an engineered tissue based on a needled nonwoven scaffold. Toward this goal, concurrent studies are underway in our laboratory to quantify and model the interactions between the scaffold and the ECM.

6.0 MULTI-SCALE COMPOSITE MODELS FOR PREDICTING THE EFFECTIVE STIFFNESS OF ENGINEERED TISSUES BASED ON NONWOVEN SCAFFOLDS

6.1 INTRODUCTION

Tissue engineered heart valves (TEHV) constructed by seeding cells onto porous biodegradable scaffolds (e.g., nonwoven polyglycolic acid (PGA)) inherently begin development as composite materials. Prior to scaffold resorption, the effective mechanical properties of these constructs will include contributions from both the scaffold and tissue constituents (e.g., collagen) [162]. While the ultimate goal following implantation is the development of a mechanical stable tissue devoid of scaffold [17], the endpoint of our current *in vitro* conditioning regimens is a construct possessing sufficient extracellular matrix (ECM) and concomitant mechanical integrity to support acute hemodynamic function and subsequent *in vivo* remodeling [8, 32]. Thus, during both the *in vitro* and early *in vivo* phases of development, mechanical interactions between the scaffold and ECM will not only determine the strength and mechanical performance of the TEHV, but also the local mechanical environment experienced by the cells.

As demonstrated above in Section 2.5.8, TEHV specimens incubated under static and cyclic flexure conditions exhibit distinct transmural cell and ECM distributions (**Figure 52**). In Section 5.5.5 we demonstrated how the bending moment of a scaffold fiber depends on its distance from the neutral axis, and suggested that an accurate composite model of a cell-seeded nonwoven scaffold would need to account for the transmural cell and ECM distribution. Moreover, we demonstrated that a simple rule of mixtures approach does not apply to needled nonwoven scaffolds. This was due to the higher order reinforcement mechanism of increased fiber-fiber bonding with increased matrix stiffness, and suggested that more complex models would be needed to accurate reflect this behavior. In the following sections we describe two approaches toward modeling the composite mechanical properties of cell-seeded nonwoven scaffolds. In the first approach, we develop a meso-scale model that accounts for both the transmural distribution of collagen, as well as the unique nonwoven-ECM coupling exhibited in needled nonwovens. For this first approach, the transmural collagen concentration distribution is quantified by fluorescence image analysis of picro-sirius stained sections, and the nonwoven-ECM coupling behavior is quantified empirically using physical models of the ECM and the nonwoven-ECM composite. These data are used to retrospectively analyze the static and cyclic flexure specimens from our previous study [63]. In the second approach, we develop a micro-scale model in which we attempt to predict the change in fiber effective stiffness with ECM deposition from static equilibrium and strain energy considerations.

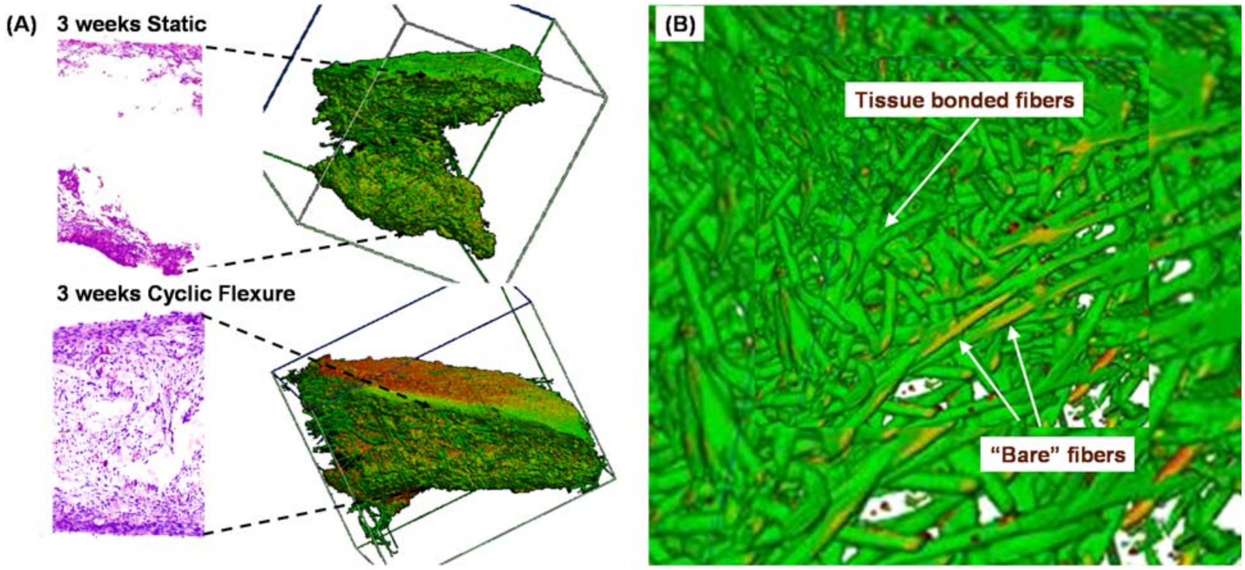

Figure 52 TEHV specimens cultivated for 3 weeks under static and cyclic flexure conditions reconstructed using digital volumetric imaging (RESview™, Resolution Sciences Corp., Corte Madera, CA) (A). Magnified view demonstrating bonded and "bare" fibers (B).

6.2 MESO-SCALE MODEL FOR NONWOVEN-ECM COMPOSITES

6.2.1 Mathematical Framework

One of our primary goals in the current study was to quantify the effective stiffness of the *de novo* synthesized ECM deposited within the scaffold—E_{ECM}. Quantification of E_{ECM} requires accounting for both nonwoven-ECM coupling, as well the transmural distribution of collagenous ECM. Assuming linear elastic, homogeneous, isotropic (LEHI) material behavior, *EI* of a composite beam exhibiting a transmural effective stiffness distribution *E(y)* can be expressed in the following integral form [163]:

$$EI = \int_{0}^{w} \int_{-t/2}^{t/2} E(y) y^2 dy dx \tag{13}$$

Note that Eq. (13) also assumes *E(y)* is symmetric about the geometric centerline of the beam cross section. In the case of the TEHV investigated in the current study this assumption has proved reasonable. As demonstrated previously in Section 5.5.5, a standard rule-of-mixtures accounting for the volume fractions and stiffnesses of individual composite constituents is inadequate to described nonwoven-ECM composites. Thus, based on the linear relationship we observed previously between *E* and collagen concentration (**Figure 25**), we initially chose to model *E(y)* by a simple linear model:

$$E(y) = R \cdot E_{ECM}(y) + E_s \tag{14}$$

where R is an empirically-determined nonwoven-ECM coupling parameter, $E_{ECM}(y)$ is the ECM effective stiffness at a particular distance y from the geometric center of the beam cross section, and E_s is the effective stiffness of the unseeded scaffold. Based again on the linear relationship between E and collagen concentration (**Figure 25**), $E_{ECM}(y)$ was expressed by the following relationship:

$$E_{ECM}(y) = C(y) \cdot B_c \cdot \overline{E}_c \tag{15}$$

where $C(y)$ is the normalized transmural collagen concentration distribution, B_c is the bulk collagen concentration, $\overline{E}_c$ is the collagen specific stiffness in units of kPa/(µg/g wet weight collagen). Collectively, these terms yield the governing equation:

$$EI = \int_0^w \int_{-t/2}^{t/2} \left[R\left(C(y) \cdot B_c \cdot \overline{E}_c \right) + E_s \right] y^2 dy dx \tag{16}$$

The parameters EI, R, $C(y)$, B_c, and E_s are each measured experimentally, yielding one equation and one unknown, $\overline{E}_c$. The experimental methods used in our laboratory to measure EI and E_s are described above in Section 2.2.5, and the methods used to measure B_c are described above in Section 2.4.6. The experimental methods used to measure R and $C(y)$ are detailed below. The value of $\overline{E}_c$ was found via nonlinear regression using the Levenberg-Marquardt method.

The value of the nonwoven-ECM coupling parameter R was found by analyzing physical models of the engineered tissue. The physical models were constructed as described below in

Section 6.2.4 by infiltrating scaffold specimens with polyacrylamide (Pam) gels (BioRad Laboratores, Hercules, CA) formulated at different acrylamide/bis concentrations. Both E of the Pam gel-infiltrated scaffold and E_{ECM} of the Pam gel were measured using our three-point bending test (Section 2.2.5). Finally, E was plotted versus E_{ECM} and R found by a linear regression on the initial linear region of the curve.

For each TEHV specimen to be analyzed, the effect of the potentially heterogeneous distribution of collagenous ECM needed to be accounted for. The transmural collagen concentration distribution $C(y)$ was quantified as described below in Sections 6.2.2 and 6.2.3 from image analysis of fluorescence micrographs of picro-sirius red stained tissue sections.

6.2.2 Fluorescence microscopy of picro-sirius red stained TEHV sections

Sections of TEHV were stained by the picro-sirius red method [164] as described previously [8]. In brief, samples of TEHV were fixed in 10% buffered formalin and embedded in paraffin. Serial sections (6 μm) were rinsed with distilled water and incubated with 0.1% (w/v) Sirius red F3BA (Polyscience, Inc., Warrington, PA) in saturated picric acid (Fisher Scientific) for 90 minutes. Sections were then rinsed twice with 0.01 M HCl for 1 minute and immersed in distilled water. After dehydration with ethanol for 30 seconds, sections were coverslipped.

In order to specifically detect collagen, picro-sirius red stained sections were observed via fluorescence microscopy [165, 166]. Sections were visualized at 100x magnification on a Nikon Eclipse E800 microscope. Epi-fluorescence mode was used with the Nikon TRITC HYQ filter set. 1600 x 1200 pixel grayscale images were captured using a Spot RT monochrome CCD camera with IR filter (model 2.1.1.1) via a 1x C mount coupler (HRD100-CMT) and Spot Imaging Software (Diagnostic Instruments, Inc., Sterling Heights, MI). An exposure time of 1 second was found to yield peak grayscale intensities of approximately 180 on a 0 to 255 scale, thereby avoiding saturation of the intensity scale and providing allowance for potentially higher collagen concentrations in future experiments.

6.2.3 Transmural collagen concentration distribution

A custom program was written in Matlab to analyze the grayscale images. Prior to image analysis, raw grayscale images were rotated and/or cropped such that the edges of the TEHV cross-section corresponded with the left and right edges of the image. Any residual fragments of scaffold appearing in the images were manually deleted. The pixel value of the dark background was set to zero by thresholding all pixels with intensity of 50 or less to zero (Corel Photo-Paint 10; Corel Corp.). A custom program was written in Matlab to compute the grayscale (0-255) intensity distribution across each row of the image (i.e., the tissue cross-section). The program then computes the mean grayscale intensity distribution, averages it and normalizes it to the thickness of the tissue cross-section.

6.2.4 Polyacrylamide Gels and Gel-infiltrated Scaffolds

50:50 blend nonwoven PGA/PLLA scaffolds described above in Section 2.4.1 were prepared for fabricating polyacrylamide gel infiltrated scaffolds. For each experiment, 10 ml of a particular concentration (**Table 7**) of acrylamide/bis solution was prepared per the manufacture's guidelines (Bio-Rad Laboratories, Hercules, CA). Note that the 1.5 M TRIS/HCL buffer, 10% sodium dodecyl sulfate (SDS), 30% acrylamide/bis, and tetramethylethylenediamine (TEMED) were all purchased pre-made from Bio-Rad. The 10% (w/v) ammonium persulfate (APS) solution was made fresh for each experiment by adding 0.5 g of APS to 5 ml of water. A Bio-Rad gel casting module was assembled using 1 mm spacer plates, and approximately 2.5 ml of the acrylamide/bis solution was pipetted in between the plates. Subsequently, nonwoven scaffold specimens (n=6) were immersed into the acrylamide/bis solution until saturated (< 30 sec.), and then slipped between the spacer plates using forceps such that they became immersed in the 2.5 ml of acrylamide solution already between the plates. After the scaffold specimens were situated between the spacer plates, the remaining volume of acrylamide/bis solution was pipetted on top of the scaffolds such that the scaffolds were entirely immersed. Finally, ~100 microliters of 1-butanol (Sigma) saturated with water (e.g., 1 ml of water mixed with 4.5. ml of 1-butanol) was pipetted on top of the acrylamide solution to aid in acrylamide polymerization, as it is inhibited by oxygen. Acrylamide/bis solutions were allowed to gel for 1 hour at room temperature prior to removal from the spacer plates (**Figure 53**). After gels were removed, gel-infiltrated scaffolds and gel specimens (25 x 7.5 x 1 mm) were cut from the gel using a razor and then prepared for three point bending testing as described above in Section 2.2.5.

Table 7 Quantities of chemicals used in preparing polyacrylamide gel solutions. All quantities are given in microliters. Note that APS stands for Ammonium Persulfate and TEMED for Tetramethylethylenediamine.

Material	5.0%	7.5%	10%	11.25%	12.5%	15%	17.5%	18.75%	20.7%
d$H_2$0	5670	4850	4200	3590	3180	2350	1520	1100	450
1.5 M Tris/HCL pH 8.8	2500	2500	2500	2500	2500	2500	2500	2500	2500
10% SDS	100	100	100	100	100	100	100	100	100
Acryl/Bis (30%)	1670	2500	3250	3750	4170	5000	5830	6250	6900
10% APS (fresh)	50	50	50	50	50	50	50	50	50
TEMED	5	5	5	5	5	5	5	5	5
Total	10000	10000	10000	10000	10000	10000	10000	10000	10000

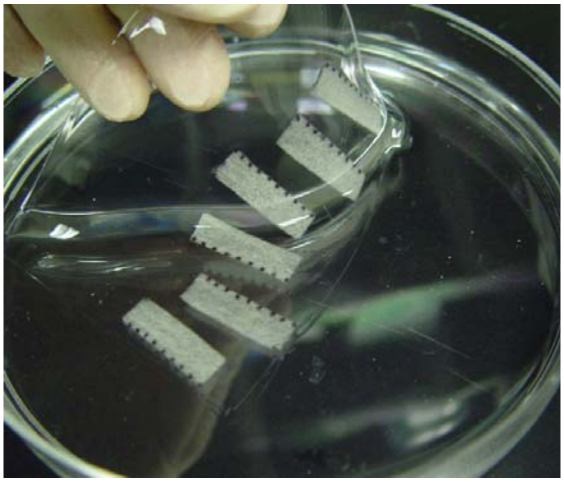

Figure 53 Photograph of polyacrylamide gel-infiltrated scaffold preparation.

6.3 Results

6.3.1 Fluorescence Microscopy Results

Fluorescent illumination of picro-sirius stained TEHV sections using the TRITC HYQ filter set yielded remarkably clear images of the collagen fibers (**Figure 54A**). As described previously, staining of the cell cytoplasm by the picric acid resulted in some background fluorescence; however the strongest fluorescence was associated with the fibrillar collagen network. Also, some scaffold remnants were found to fluoresce (**Figure 54A**, black arrow). These fluorescently labeled fibers were manually deleted from images prior to analysis. To demonstrate the equivalence between fluorescence intensity and the bulk biochemical collagen measurements, the mean normalized fluorescence intensity was plotted versus the bulk collagen concentration for each of the 12 specimens (n=6 static, n=6 cyclic flexure) from our previous study [63]. A strong positive linear relationship was found (R^2=0.915), indicating that the measured fluorescence intensities were indeed reflective of the collagen concentrations.

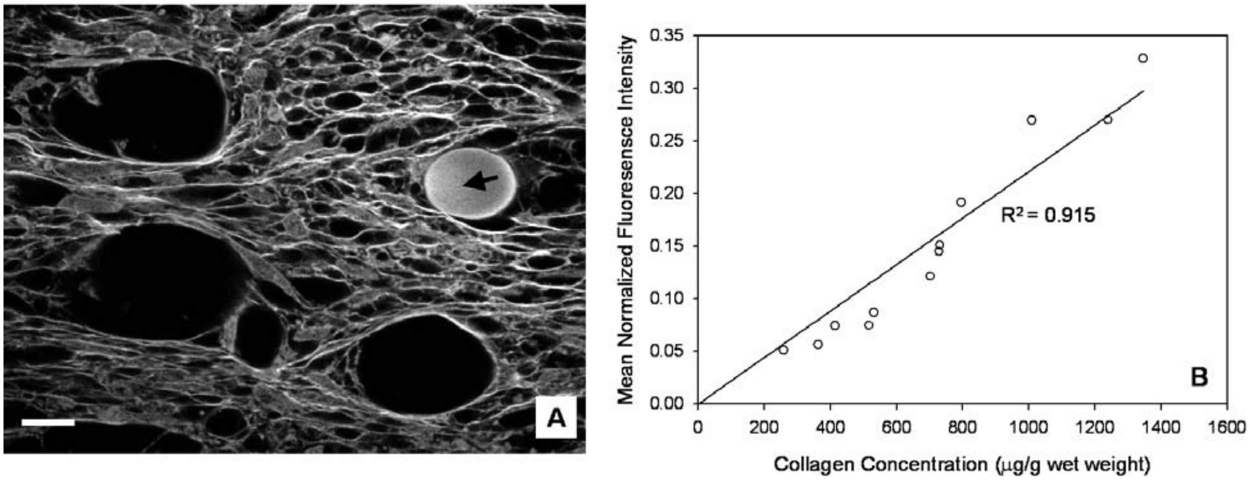

Figure 54 Fluorescence micrograph of a picro-sirius red stained TEHV section (A). The collagen fiber network fluoresced intensely compared with the background fluorescence of the cytoplasm. Scale bar = 10 µm.

6.3.2 Transmural Collagen Distribution Results

Fluorescent micrographs from 3 week flexed (**Figure 55A**) and static control (**Figure 55C**) specimens were analyzed by the custom Matlab program, yielding significantly different normalized transmural fluorescence intensity distributions (**Figure 55B** and **D**, respectively). The normalized fluorescence intensity distributions (i.e., *C(y)*, normalized collagen concentration distributions) for the flex (n=6) and static (n=6) groups were averaged for implementation in the meso-scale model (**Figure 56**), and fit to quadratic equations of the form $C(y) = ay^2 + c$ with coefficients a = 4.009 and c = 0.667 (R^2=0.9326; flex group) and a = 9.946 and c = 0.173 (R^2 = 0.9531; static group).

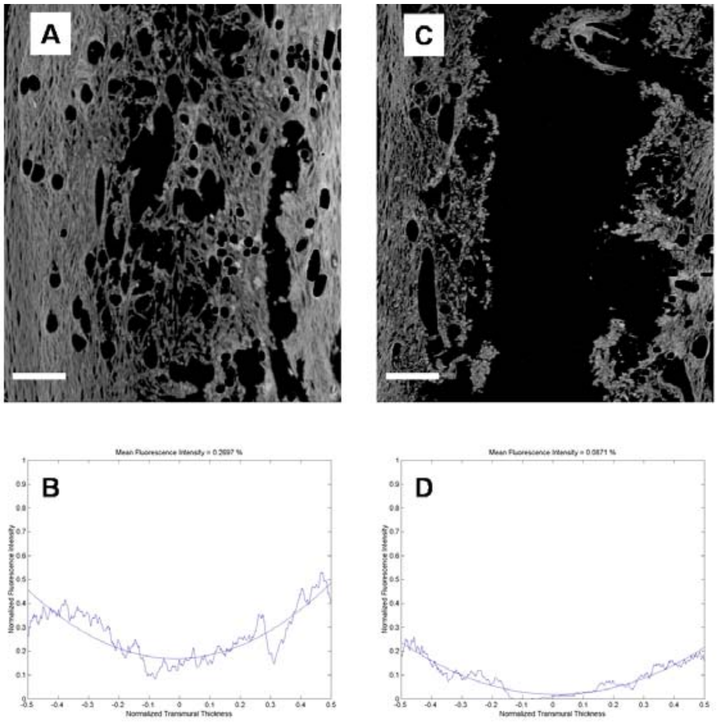

Figure 55 Representative fluorescent micrographs of picro-sirius red stained sections of cyclic flexure (A) and static (C) TEHV specimens. Scale bar = 100 μm. Normalized fluorescence intensity distributions output by the custom Matlab program (B and D, respectively). Normalized fluorescence intensity distributions for individual specimens were averaged for the static and cyclic flexure groups in the meso-scale model analysis.

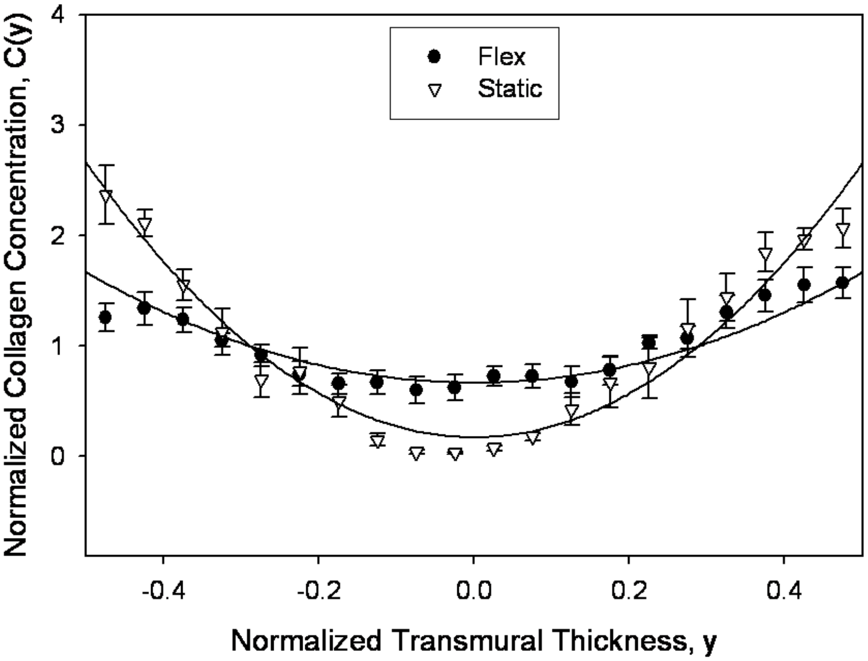

Figure 56 Average normalized collagen concentration distributions for the static and cyclic flexure groups.

6.3.3 Nonwoven-ECM Coupling Parameter Results

By varying the concentration of acrylamide/bis in fabricating the polyacrylamide gels, the effective stiffness of the polyacrylamide gels (i.e., E_{ECM}) was varied between 30 kPa (5% acryl/bis) and 665 kPa (20.7% acryl/bis) (**Figure 57A**). A plot of the effective stiffness of the gel-infiltrated scaffolds (E) versus E_{ECM} yielded a linear region within the range 0 kPa < E_{ECM} < 271 kPa. The nonwoven-ECM coupling parameter R was determined within this linear region by regression to be 7.444 kPa/kPa (**Figure 57B**).

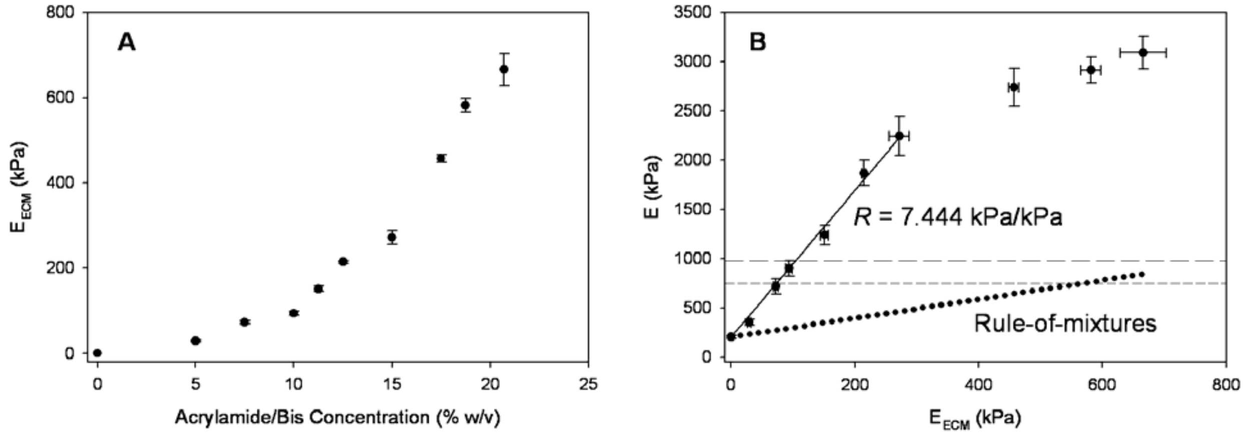

Figure 57 Effective stiffness of the polyacrylamide gel (i.e., E_{ECM}) as a function of percent (w/v) acrylamide monomer (A). The range of E_{ECM} values was ~30-665 kPa. E of the gel infiltrated nonwoven scaffolds (i.e., the TEHV analog) versus E_{ECM} (B). The nonwoven-ECM coupling parameter determined within the linear region was 7.444 kPa/kPa. For reference, the mean values of E from the flex (978 kPa; long dashed line) and static (748 kPa; short dashed line) groups are indicated [63]. The rule-of-mixtures did not fit the data (black dotted line).

6.3.4 Meso-Scale Model Results

The values of $C(y)$ and R (7.444 kPa/kPa) measured above in Sections 6.3.2 and 6.3.3, respectively were combined with the values of B_c, E_s (206 kPa), and E measured in our previous study [63] through the meso-scale model (Eq. (16)). The one unknown parameter, collagen specific stiffness $\bar{E}_c$, was solved for via a non-linear regression using the Levenberg-Marquardt method. There was a trend of increased $\bar{E}_c$ in the flex versus static group (**Table 8**), suggesting that while cyclic flexure primarily affects collagen content by 3 weeks, it may affect the structural-mechanical quality at later time points. Predicted values of $\bar{E}_c$ were then used to plot the transmural ECM effective stiffness distribution, $E_{ECM}(y)$ (**Figure 58**). Predicted values of $E_{ECM}(y)$ ranged from a minimum of 53.7 kPa (flex) and 7.5 kPa (static) in the center to a maximum of 134.4 kPa (flex) and 114.6 kPa (static) at the periphery.

Table 8 Summary of experimental group-specific parameters used and/or predicted by the meso-scale model. Note that E and B_c were obtained above in Sections 2.5.5 and 2.5.6 [63].

Experimental Group	E (kPa)	B_c (µg/g wet weight)	$C(y)=ay^2+c$ a	c	$\bar{E}_c$ (kPa/(µg/g wet weight)
Static	748 ± 130	893 ± 133	9.946	0.173	0.0789
Flex	978 ± 228	546 ± 111	4.009	0.667	0.0904

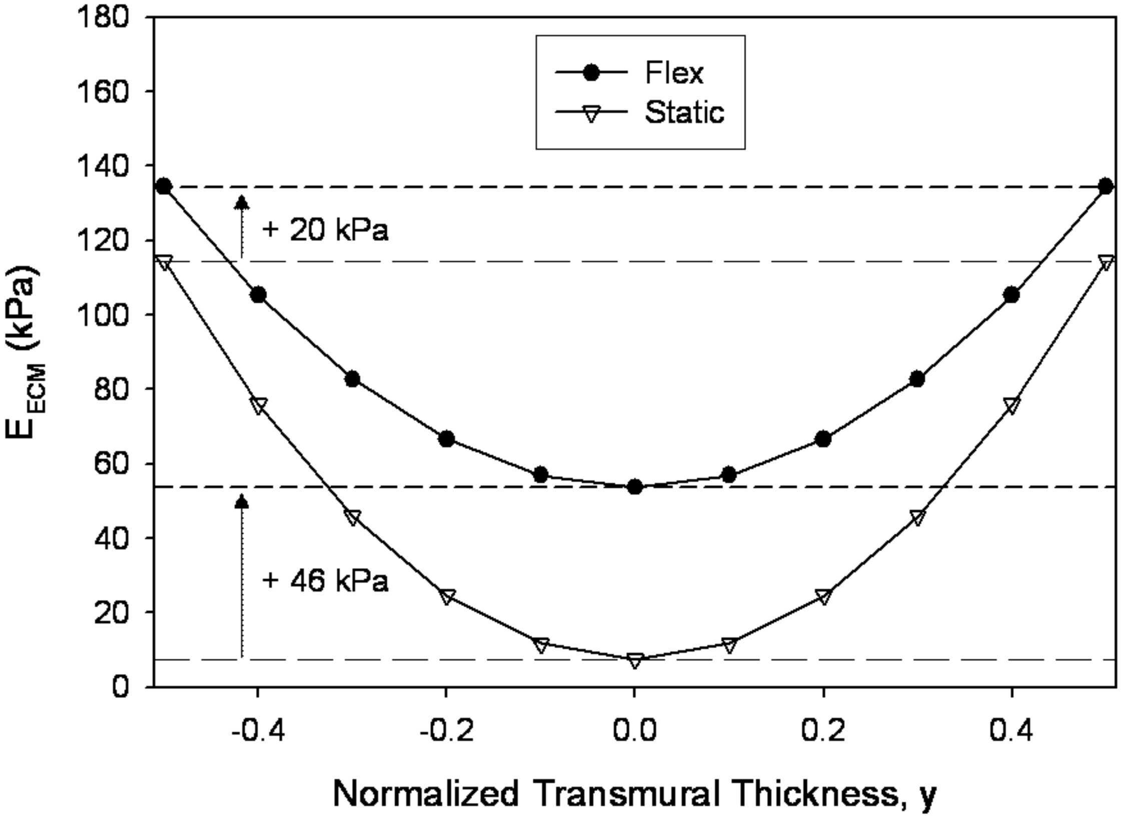

Figure 58 Transmural E_{ECM} distribution predicted using the meso-scale model (Eq. (16)).

6.4 MICRO-SCALE MODEL FOR NONWOVEN-ECM COMPOSITES

6.4.1 Mathematical Framework

While a fully non-linear approach for solving the problem of a curved fiber embedded in an elastic medium has been published by Akbarov and co-workers [167], previous approaches were limited to small deformations and only considered a single fiber orientation (i.e., parallel to the loading direction), and thus would not be directly applicable to the needled nonwoven-ECM composite, whose behavior was shown in Section 5.5.5 to be dominated by variations in fiber-fiber bonding at cross-over points. Toward developing a more fundamental understanding of the micro-mechanical interactions between needled nonwoven scaffolds and deposited ECM, in the current study we developed a simplified micro-scale model in which static equilibrium between the fiber and ECM phases, as well as the strain energy generated in the ECM phase in response to fiber curvature, were considered.

The governing equation assumed for the micro-scale model was static equilibrium between the needled nonwoven scaffold fibers and the ECM phase (e.g., ECM, polyacrylamide gel (ECM analog), expressed here in terms of the bending moments:

$$M_f = M_{ECM} \tag{17}$$

Substituting Eq. (39) for M_f and the Bernoulli-Euler moment-curvature relation (Eq. (1)) for the ECM phase, Eq. (17) can be re-expressed as:

$$\frac{N_f\left(E_f\right)' A_f t^2}{12\rho}\int_{-\pi/2}^{\pi/2} R(\Phi)\cos^4\Phi d\Phi = \frac{E_{ECM}I_{ECM}}{\rho} \tag{18}$$

However, while the right-hand term of Eq. (18) for the ECM phase would be appropriate for straight fibers, the actually bending moment generated in the ECM phase embedded with curved fibers would be expected to be much higher, given the contribution of strains in the transverse (e.g., z-axis) direction induced by straightening of the curved fibers in the longitudinal (e.g., x-axis) direction (**Figure 59**).

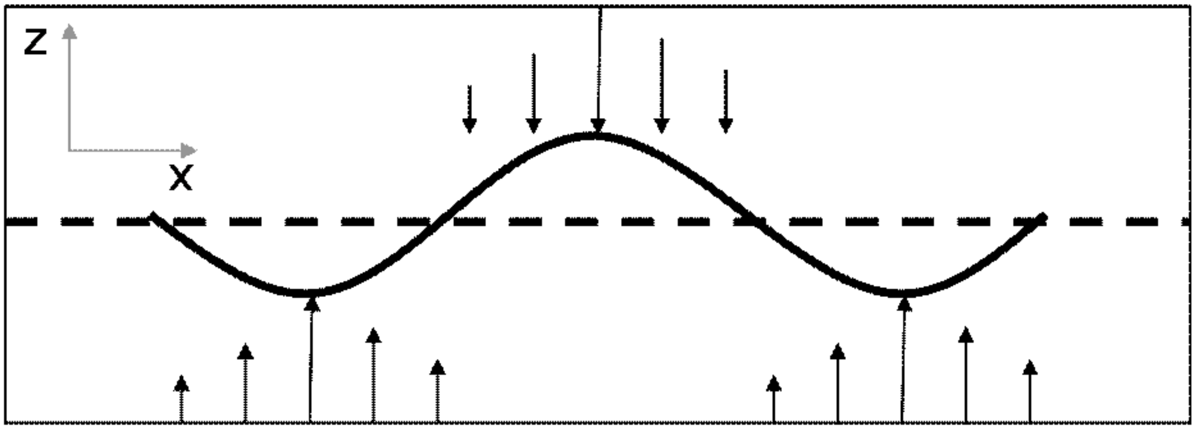

Figure 59 Schematic illustrating the transverse strains that would develop in the ECM phase (black arrows) in response to extension of a curved fiber (solid black curve) in the longitudinal direction to the straightened configuration (dashed black line). Transverse strains would be maximal at the maxima and minima of the curve.

Rather than focusing on the development of an exact solution for the transverse strains, whose solution is beyond the scope of this work, we estimated the ratio Υ of the strain energy generated in the ECM due to extension of a curved fiber, U_{ECM}^{curved}, to a straight fiber, $U_{ECM}^{straight}$, and used this ratio as a correction term in Eq. (18):

$$\frac{N_f \left(E_f\right)' A_f t^2}{12\rho} \int_{-\pi/2}^{\pi/2} R(\Phi)\cos^4 \Phi d\Phi = \Upsilon \frac{E_{ECM} I_{ECM}}{\rho} \tag{19}$$

By making appropriate substitutions for I_{ECM}, Eq. (19) reduces to:

$$\left(E_f\right)' = \frac{\Upsilon E_{ECM} A_{ECM}}{N_f A_f \int_{-\pi/2}^{\pi/2} R(\Phi)\cos^4 \Phi d\Phi} \tag{20}$$

In which $\left(E_f\right)'$ can be calculated using Eq. (8) from Section 5.2.3, and each of the terms on the right-hand side are known with the exception of Υ.

To estimate Υ we used the average effective crimp amplitude a_{eff} (0.090407 mm) and wavelength Λ_{eff} (1.051684 mm) values measured for the 50:50 PGA/PLLA scaffold (Section 5.4.2; **Table 5**) (Note: a_{eff} = 0.1 mm and Λ_{eff} = 1 mm were used for simplicity). The arc length of one wavelength was calculated by:

$$s = \int_{x=0}^{x=1} \sqrt{1 + \left(\frac{2\pi a_{eff}}{\Lambda_{eff}} \cos \frac{2\pi x}{\Lambda_{eff}} \right)^2} \tag{21}$$

And thus $U_{ECM}^{straight}$ was calculated by:

$$U_{ECM}^{straight} = U_x = \tfrac{1}{2} E_{ECM} \varepsilon_x^2 dV_x \tag{22}$$

where the fiber and ECM strain in the longitudinal (i.e., x-axis) direction is given by:

$$\varepsilon_x = \frac{s - \Lambda_{eff}}{\Lambda_{eff}} \tag{23}$$

and dV_{ECM} was calculated from:

$$dV_x = \Lambda_{eff} d_f \left(\delta a_{eff} \right) \tag{24}$$

where δ is some multiple of a_{eff} that reflects the range of influence of the curved fiber in the transverse direction. In the micro-scale model the parameter δ was fit, and the fitted value was compared with the average inter-fiber distance (see Section 5.3.10) to test for physical plausibility.

The strain energy for the curved fiber case was given as the sum of the strain energy generated by longitudinal strains (i.e., U_x) and 4 times the strain energy generated in the transverse direction for a one-quarter wavelength segment of fiber:

$$U_{ECM}^{curved} = U_x + 4U_y \tag{25}$$

where U_y was calculated from:

$$U_y = \sum \tfrac{1}{2} E_{ECM} \varepsilon_y^2 dV_y \tag{26}$$

where ε_y is a function of position x along the length of the one quarter wavelength, and is given by:

$$\varepsilon_y = \frac{y - y_o}{y_o} \tag{27}$$

where y_o is given by:

$$y_o = \left(\delta a_{eff}\right) - a_{eff} \sin\left(\frac{2\pi x}{\Lambda_{eff}}\right) \tag{28}$$

and y is simply given by δa_{eff}. The one quarter wavelength was discretized into twenty-six 0.01 mm-wide volume elements dV_y given by $0.01 d_f y_o$.

In fitting the micro-scale model to the polyacrylamide gel / gel-infiltrated scaffold results presented above for the meso-scale model (Section 6.2), the ratio Υ was calculated for both the PD and XD specimens by fitting individual values for the parameter δ. The value of δ, which is related to the average inter-fiber distance, was assumed to be different for the PD and XD directions due to the 3:1 ratio of fibers oriented in those directions, respectively.

6.4.2 Micro-scale model results

The values of δ were found to be 3.52 and 4.90 for the PD and XD specimens, respectively. Physically, δa_{eff} represents the effective height of the rectangular slab in which the curved fiber is embedded, and thus for an a_{eff} value of 0.1 mm, the inter-fiber distance for the PD specimens would range from a minimum of 152 microns to a maximum of 352 microns, depending on whether the fibers were aligned anti-phase or co-phase, respectively. In Section 5.3.10, the average inter-fiber distance for the PD specimens was estimated to be ~ 200 microns, which falls within the range predicted by the micro-scale model. For the XD specimens, the corresponding minimum and maximum inter-fiber distances would be 290 and 490 microns, respectively. That the inter-fiber distance is larger for the XD specimens makes sense intuitively, since there are fewer fibers oriented in the XD direction and thus the average distance between them should be greater than for the PD direction. The values of ϒ corresponding with these values of δ were found to be 7.35 and 4.10 for the PD and XD specimens, respectively. Physically, this means that the strain energy generated in the ECM by extension of a curved fiber in the PD direction is 7.35-fold the strain energy associated with extension of a straight fiber. This additional strain energy is due to the transverse strains associated with straightening of the curved fiber. The reason why ϒ is lower for the XD direction is due to the fact that more ECM is associated with each fiber, and thus the difference between extending a straight fiber and curved fiber is reduced.

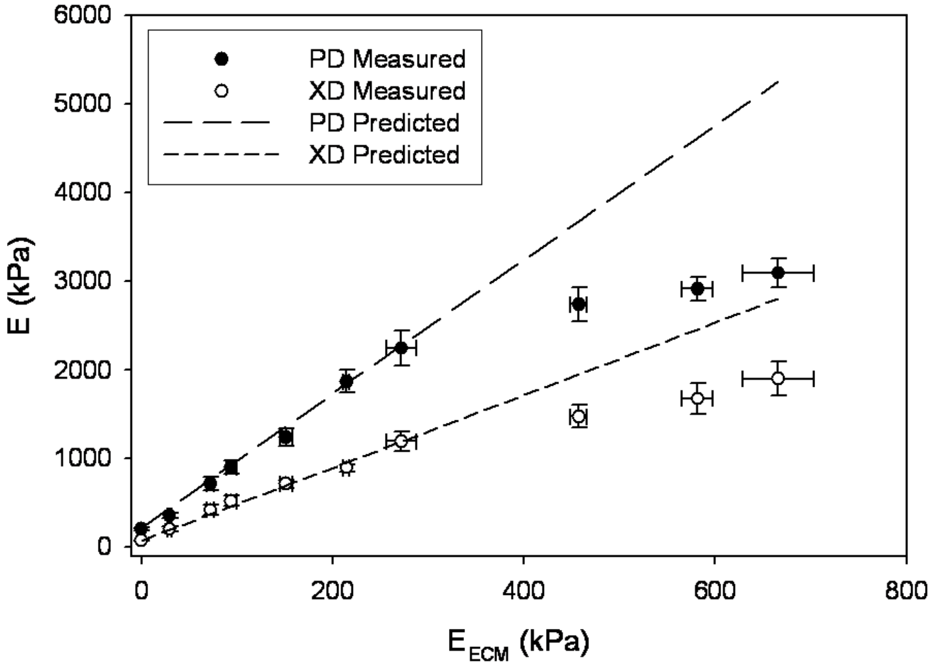

Figure 60 Micro-scale model results for preferred (PD) and cross-preferred (XD) fiber directions.

6.5 DISCUSSION

6.5.1 Transmural collagen concentration distribution

Martin et al. [168] previously reported on an imaging-based method for quantifying the transmural distribution of sulfated glycosaminoglycan (S-GAG) concentration in native and tissue engineered cartilage. They identified a pixel parameter (red intensity) that could be measured in digitized photomicrographs of Safranin-O stained histological sections and subsequently correlated with the biochemically measured S-GAG concentration. Their method was unique in that it allowed not only for binary segmentation of an image into S-GAG positive and negative regions, as had been done previously for S-GAG (refs), but also for correlation to the S-GAG concentration at a particular position. Their ability to establish such a strong correlation was due in part to the specific and stoichiometric binding of the cationic dye Safranin O to the negatively charged groups of chondroitin-6-sulfate or keratan sulfate.

In the current study we developed a similar method for quantifying the transmural distribution of collagen concentration. As opposed to previous studies, in which binary segmentation based on pixel intensity threshold was used to discriminate collagenous regions from non-collagenous regions, the method developed here relates pixel intensity to collagen concentration. As in the case of the study by Martin et al., our ability to establish this relation is due to the specificity and stoichiometric binding of Sirius red to fibrillar collagens. In a previous study by Junqueira et al. [169] it was demonstrated that collagen types I, II, and III each bind an average of 126 molecules of Sirius red per collagen molecule. Moreover, they demonstrated a linear relationship between the optical density at 540 nm (the absorption maxima of Sirius red) and collagen concentration. This is, in fact, the basis of the Sircol® collagen assay kit used in our biochemical assays of collagen concentration.

7.0 FUTURE DIRECTIONS

The field of heart valve tissue engineering, while no longer in its infancy *per se*, is still remarkably young. While the first mechanical and bioprosthetic valve replacements were introduced over 40 years ago [170], the first attempts to develop a TEHV began only a decade ago. While significant progress has been made, much work remains, both in delineating the functional requirements of a TEHV suitable for clinical evaluation, as well as developing the means to produce one. The following sections describe in detail future directions in heart valve tissue engineering that may help lead toward this ultimate goal.

7.1 GUIDANCE OF TEHV CELL AND COLLAGEN ORIENTATION

7.1.1 Introduction

The tensile mechanical properties of heart valve leaflets and other load-bearing soft tissues are exquisitely sensitive to collagen fiber orientation [48, 171]. In the case of valvular tissues, the geometric arrangement of the collagen fiber network is finely tuned to organ-level functional requirements [3], and can be remodeled by the resident cells in response to chronic shifts in physiological stresses [51]. In developing a functionally-equivalent tissue engineered heart valve (TEHV), a primary goal is to recapitulate the essential features of this native microstructure for ensuring both robust mechanical function and long-term durability [172].

However, while circumferentially-oriented collagen fibers have been observed in the fibrosa-like layer of 20 week explants, the cells and collagen of these TEHV based on bioresorbable nonwoven scaffolds do not exhibit a well organized structure during *in vitro* conditioning and at early time points *in vivo* [8].

Toward enhancing the *in vitro* stage of tissue formation, pulsatile flow loop bioreactors have been designed to develop optimized mechanical conditioning protocols for TEHV [32, 173]. We recently demonstrated that cyclic flexure, the major mode of TEHV deformation in a pulsatile flow loop, can independently enhance collagen synthesis with concomitant increases in tissue effective stiffness [62, 63]. However, while these and other studies [61, 64] have clarified the role of mechanical forces in stimulating TEHV collagen *synthesis*, investigators currently possess limited data regarding the evolution of TEHV collagen *orientation*. Specifically, the potential role of initial scaffold microstructure in guiding cell and collagen orientation remains unaddressed.

Numerous studies have demonstrated the capacity of micro-grooves and other structured surface topologies to guide cell and collagen orientation in monolayer tissue culture [174], however it is not clear to what degree guidance phenomenon may manifest, or explicitly be exploited, in the fully three-dimensional (3-D) tissue engineering (TE) setting. TE scaffolds differ significantly from micro-grooved substrates in that they consist of a 3-D open pore network in which multiple layers of cells and extracellular matrix (ECM) span and fill the void spaces between scaffold structural members. In the first study of its kind, we previously utilized a small angle light scattering (SALS) technique to quantify the collagen fiber orientation of the TE skin equivalent Dermagraft™ [151]. By scanning both cell-seeded and unseeded samples of the Vicryl® scaffold, it was possible to optically decouple the collagen fibers from the scaffold fibers via the principle of superposition, and thereby to establish the orientation of collagen fibers to be parallel to the major axis of the diamond-shaped pores.

In the current study we extended our previous work [151] by developing an *in vitro* model system in which large-scale (~ 200 μm) open pore structures of varying geometry could be rapid-prototyped and systematically evaluated for their cell and collagen orientating capacity. Non-degradable scaffolds exhibiting a grid of 200 μm wide rectangular pores (1:1, 2:1, 5:1, and 10:1 aspect ratios) and diamond-shaped pores (600 x 1000 μm) were fabricated from a transparent epoxy resin via high-resolution stereolithography. The scaffolds were surface modified to support cell adhesion by covalently grafting GRGDS peptides, sterilized, and seeded with neonatal rat skin fibroblasts. Following 4 weeks of static incubation, the resultant collagen orientation was assessed quantitatively by SALS, and cell orientation was evaluated by laser confocal and scanning electron microscopy.

7.1.2 Methods

7.1.2.1 Scaffold Fabrication

Non-degradable scaffolds with rectangular pores (1:1, 2:1, 5:1, and 10:1 aspect ratio) were fabricated by high-resolution stereolithography (FineLinePrototyping, Inc., Raleigh, NC) using a Viper Si^{2}™ SLA® system (3D Systems Corp., Valencia, CA) and a transparent resin (WaterClear™ 10120, DSM Somos®, Newcastle, DE). The struts of the scaffolds were approximately 100 μm wide, and the inside dimensions of a 1:1 aspect ratio pore were 200 x 200 μm (**Figure 61**). To compare results with our previous work [151], we fabricated scaffolds with a diamond-shaped pore structure similar to that of the Vicryl® scaffold used in manufacturing the TE skin equivalent Dermagraft™. The inside dimensions of the diamond-shaped pores were 600 x 1000 μm. The gross dimensions of each of scaffold were 20 x 20 x 0.75 mm. Scaffolds were surface modified to promote cell attachment by adapting a previously described method [175].

Scaffolds were rinsed in acetone (SIGMA®, Sigma-Aldrich Co., St. Louis, MO), ethanol (SIGMA), and deionized water and then immersed in a 4% (v/v) solution of 3-aminopropyltriethoxysilane (SIGMA) in acetone for 10 minutes. The scaffolds were then rinsed as above and immersed in a 6% (v/v) glutaraldehyde (SIGMA) in a 0.2M TRIS (SIGMA) solution for 10 minutes. The scaffolds were then rinsed in deionized water, placed into sterile 50 cc centrifuge tubes, and incubated for 16 hours at 8 rpm (Labquake rotisserie rotator, Barnstead-Thermolyne, Dubuque, IA) in a 0.1 mg/ml solution of GRDGS peptides (SIGMA) in phosphate buffered saline (PBS) (GIBCO™, Invitrogen Corporation, Grand Island, NY). Following the GRGDS incubation, scaffolds were rinsed in deionized water and incubated for 16 hours at 8 rpm (Labquake rotisserie rotator) in 0.1M ethanolamine (SIGMA) in PBS to quench any unreacted aldehyde groups. Scaffolds were sterilized in 70% isopropyl alcohol (LabChem, Inc., Pittsburgh, PA) for 30 minutes and rinsed three times with sterile PBS prior to cell seeding.

7.1.2.2 Cell Culture and Seeding

In order to compare our new *in vitro* model system to our previous structural investigations on the TE skin equivalent Dermagraft™ [151], in the current study 27FR neonatal rat skin fibroblasts (CRL-1213, ATCC, Manassas, VA) were utilized in lieu of the vascular-derived smooth muscle cells (VSMC) and other cell types typically used in TEHV fabrication [32]. Cells were expanded in Dulbecco's Modified Eagle's Medium with 4.5 g/L glucose and L-glutamine (GIBCO) supplemented with 10% fetal bovine serum (GIBCO) and 1% antibiotic-antimycotic (GIBCO). A total of 10 confluent 185 cm^2 flasks (Nuclon™Δ SoLo flask; Nalgene Labware) of cells (Passage 19) were trypsinized (0.25% trypsin, 1 mM EDTA; GIBCO) and resuspended in 300 ml of culture medium to yield a seeding solution of approximately 3 x 10^5 cells/ml, as determined by cell counts with a hemacytometer (Hausser Scientific, Horsham, PA).

The general seeding techniques have been described previously [63]. One scaffold was placed into each of 30 seeding tubes. Each seeding tube consisted of a 50 cc centrifuge tube (Product # 91050; TPP, Trasadingen, Switzerland) fitted with a vent filter cap from a 50 cc tissue culture tube (Product # 91253; TPP), thereby allowing for gas exchange during seeding. Seeding solution (10 ml) was added to each tube to yield a seeding density of approximately 7.5 x 10^5 cells/cm^2 (i.e., 3 x 10^6 cells / 4 cm^2 scaffold). The tubes were rotated at 8 rpm (Labquake rotisserie rotator) inside an incubator operating at 37°C and 5% CO_2 for 30 hours. Following seeding, scaffolds were incubated under static conditions for 28 days in 6 ml of medium in 6-well plates (Costar Ultra Low Attachment; Corning, Corning, NY). The culture medium was changed daily throughout the course of the study. Unmodified scaffolds (i.e., lacking the GRGDS surface modification) pre-incubated for 16 hours in culture medium served as controls.

7.1.2.3 Small Angle Light Scattering

Small angle light scattering (SALS) was used to quantify the orientation of the *de novo* synthesized collagen. A detailed description of the SALS device and analysis methods [150], as well as its application to fibrous PGA scaffolds [151], have been published previously. In brief, 1 scaffold sample (20 x 20 mm) was scanned at discrete intervals (1 mm) using a 1 mm diameter Helium-Neon laser beam. The resultant scattered light intensity distribution at each point was averaged and normalized for both unseeded and seeded scaffolds and the preferred fiber direction (distribution centroid) and orientation index (OI, a measure of the degree of orientation) were calculated. SALS data were expressed as mean ± standard error (SEM). Test groups were analyzed by ANOVA and Tukey HSD multiple comparison test using SYSTAT 10 (SPSS, Inc., Chicago, Il). Differences between test groups were considered statistically significant when $p < 0.05$.

7.1.2.4 Multiphoton Laser Scanning Confocal Microscopy.

To evaluate cellular orientation, one scaffold sample representing each pore aspect ratio was prepared for laser confocal microscopy by labeling for F-actin. In brief, scaffold samples were removed from culture, rinsed 3 times in PBS, and fixed for 2 hours in fresh 4% (w/v) paraformaldehyde (Fischer Chemicals, Fair Lawn, NJ)) in PBS. Fixed scaffolds were then washed 3 times in PBS, extracted for 3 minutes in 0.1% (v/v) Triton X-100 (Sigma) in PBS, washed 3 more times with PBS, pre-incubated in 1% (w/v) bovine serum albumin (Sigma) in PBS (BSA buffer) for 20 minutes, and then incubated for 1 hour in Alexa Fluor® 568-Phalloidin (2:150 (v/v) dilution; Molecular Probes). Following labeling, scaffold samples were washed 3 times in BSA buffer, 3 times in PBS, and then stored in PBS at 2-8°C prior to laser confocal imaging. Samples were imaged using a multiphoton laser scanning confocal microscope system comprising a titanium-sapphire ultrafast tunable laser system (Coherent Mira Model 900-F;

Coherent, Inc., Santa Clara, CA), Olympus Fluoview confocal scanning electronics (Olympus America, Inc., Melville, NY), an Olympus IX70 inverted system microscope, and custom built input-power attenuation and external photomultiplier detection systems. Z-axis image acquisition utilized two-photon excitation at 850nm with an Olympus water-immersion objective (40X UApo 1.15NA). Red fluorescence emission detection utilized a HQ610/75m emission filter (Chroma Technology Corp., Rockingham, VT). Individual images planes (1024x1024 pixel resolution) were acquired at 2μm z-axis intervals.

7.1.2.5 Scanning Electron Microscopy.

One scaffold sample representing each pore aspect ratio was prepared for scanning electron microscopy (SEM). Samples were fixed for 1 hour in 2.5% (v/v) glutaraldehyde (SIGMA), washed 3 times in 1x PBS (15 minutes each), fixed for 1 hour in 1% (w/v) Osmium Tetraoxide (SIGMA), washed 3 more times in 1x PBS, and then dehydrated by stepping through graded ethanol (SIGMA) solutions (30%, 50%, 70%, 90%, 100%) for 15 minutes each. The fixed and dehydrated samples were critical point dried using an EMscope critical point dryer 750 (EMscope Laboratories, Ashford, Kent, U.K.). Critical point dried samples were attached to aluminum sample stubs and were sputter coated with a thin layer of gold-palladium alloy (~3 nm thickness) in a Cressington 108auto sputter coater with a Cressington MTM-20 thickness controller (Cressington Scientific Instruments, Inc., Cranberry Twp., PA). Each scaffold sample was imaged at 5 kV on a JEOL JSM-6330F field emission scanning electron microscope (JEOL USA, Inc., Peabody, MA). To quantify intra-pore cellular orientation, SEM micrographs were converted to binary images by contrast enhancement and thresholding (Corel Photo-Paint 10;

Corel Corp., Ottawa, Canada) and the median of the cell major axis angular orientation was quantified using the fill measurement option of SigmaScan Pro (SPSS, Inc.).

7.1.3 Results

Scaffold fabrication via high-resolution stereolithography proved to be a simple, relatively inexpensive method for prototyping a variety of pore shapes (**Figure 62**A). Pre-incubation of unmodified scaffolds in serum-supplemented culture medium was insufficient to promote cellular attachment. In contrast, the GRGDS surface modification strategy employed herein was inexpensive and straight forward, allowing for robust cellular attachment with no observable toxicity. Periodic evaluation of the scaffolds by light microscopy revealed that the cells attached to the struts of the scaffolds and proceeded to span the pores in a generally circumferential pattern (**Figure 62B**). The majority of pores were completely spanned by a 30-50 μm thick tissue layer following 4 weeks incubation, as illustrated via light and laser confocal microscopy for a 1:1 aspect ratio pore (**Figure 63A** and **C**, respectively) and one half of a 2:1 aspect ratio pore (**Figure 63B** and **D**, respectively). No consistent variations in cellular orientation were detected through the 30-50 μm thickness of the tissue layers via examination of the individual 2 μm thick laser confocal planes (data not shown).

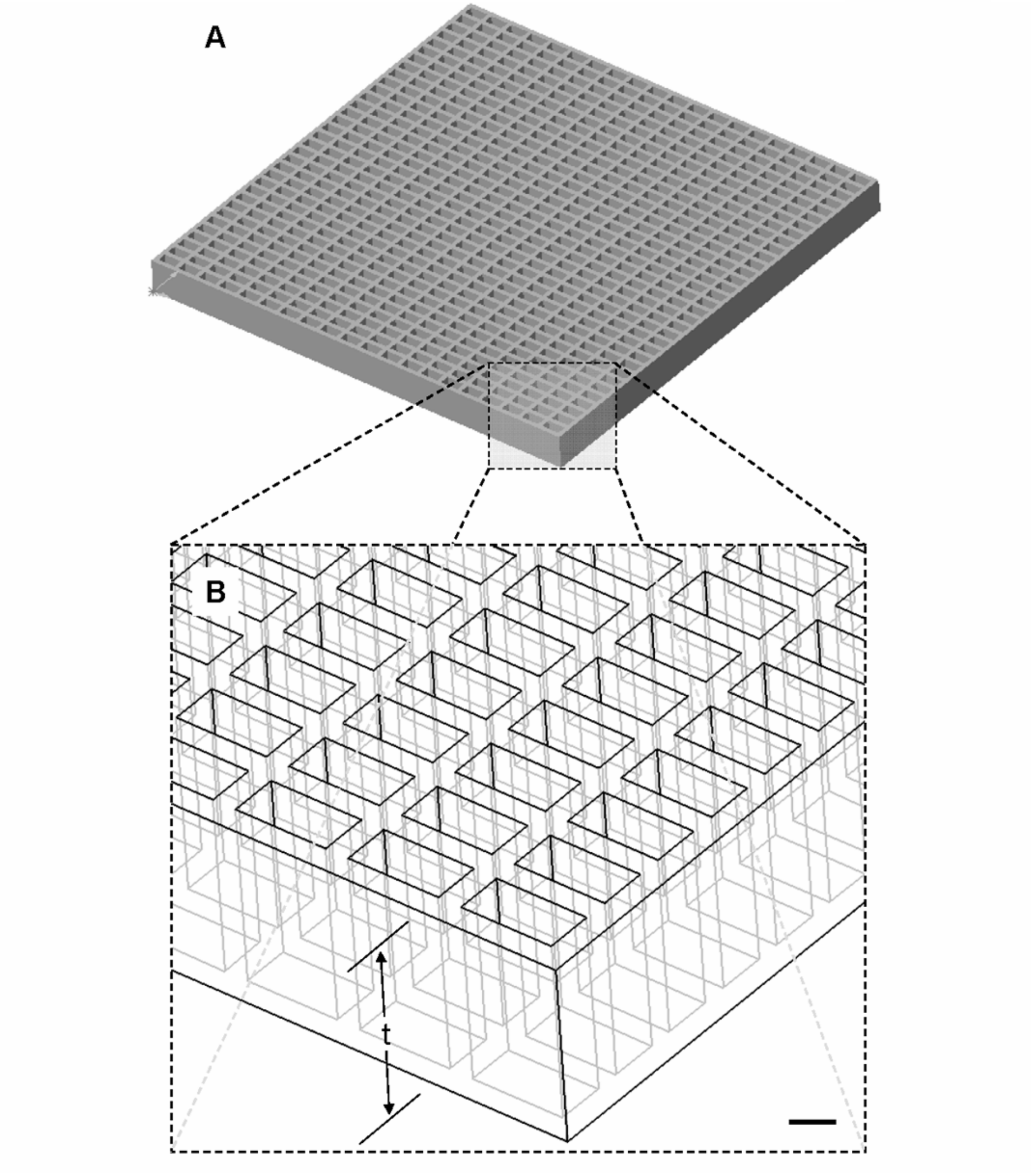

Figure 61 Schematic illustrating the three-dimensional macroscopic structure of one quarter of a 2:1 aspect ratio scaffold (A). The entire lateral area of each scaffold specimen was 2 x 2 cm^2. High magnification schematic depicting a small region of a 2:1 aspect ratio scaffold (B). The thickness t of each scaffold specimen was approximately 750 μm. The struts of the pores were 100 μm wide, and the 2:1 aspect ratio pores were completely open from the top to bottom surface of the scaffold with a lateral area of 200 x 400 μm (Scale bar = 200 μm).

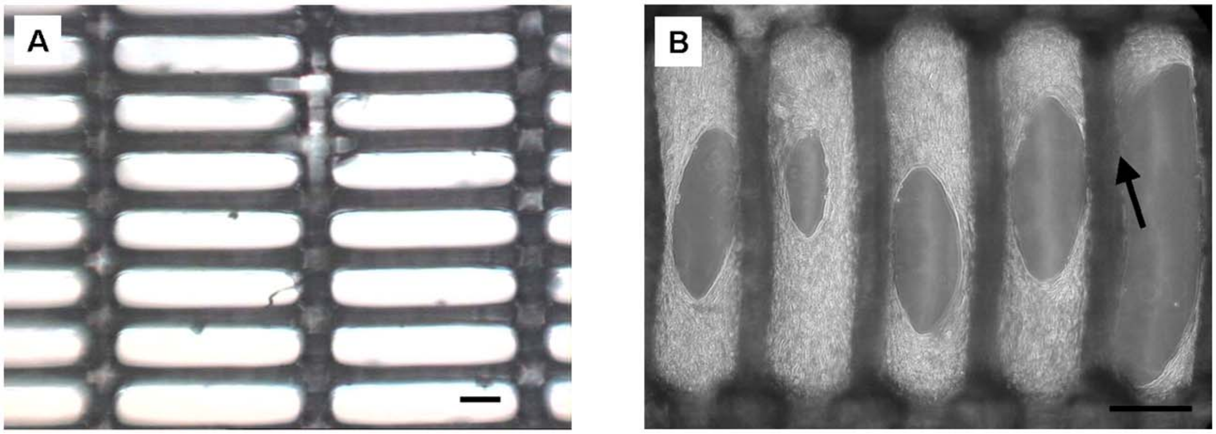

Figure 62 Light micrograph of an unseeded 5:1 aspect ratio scaffold (scale bar = 200 μm) (A). Light micrograph of a seeded 5:1 aspect ratio scaffold following 1 week incubation (scale bar = 200 μm) (B). While cells spanned the 1:1 aspect ratio pores in a generally circumferential pattern (not shown), the 5:1 aspect ratio pores (and the 2:1 and 10:1) were spanned in an elliptical pattern with the long axis of the ellipse aligned to the long strut axis. In some isolated pores, the cells did not attach uniformly around the perimeter of the pore during seeding and ultimately assumed a preferred orientation orthogonal to the long strut (black arrow).

SALS of unseeded scaffolds revealed the characteristic scattered light signatures of orthogonal two strut systems, with distinct peaks located ~90 degrees apart and the area under each peak proportional to the relative strut length oriented in that direction (**Figure 64A**). The preferred strut directions for the unseeded scaffolds (**Figure 64B**, black bars) did not differ significantly from their theoretical values calculated based on the additive contribution of each strut. SALS results for the seeded scaffolds demonstrated broader distributions (**Figure 64A**), with the median of the distribution shifted toward the angular orientation of the long-strut axis (**Figure 64B**, gray bars). Physically, this result suggests that the overall orientation achieved by the collagen fibers (and cells) within a high aspect ratio pore coincides with the long strut axis.

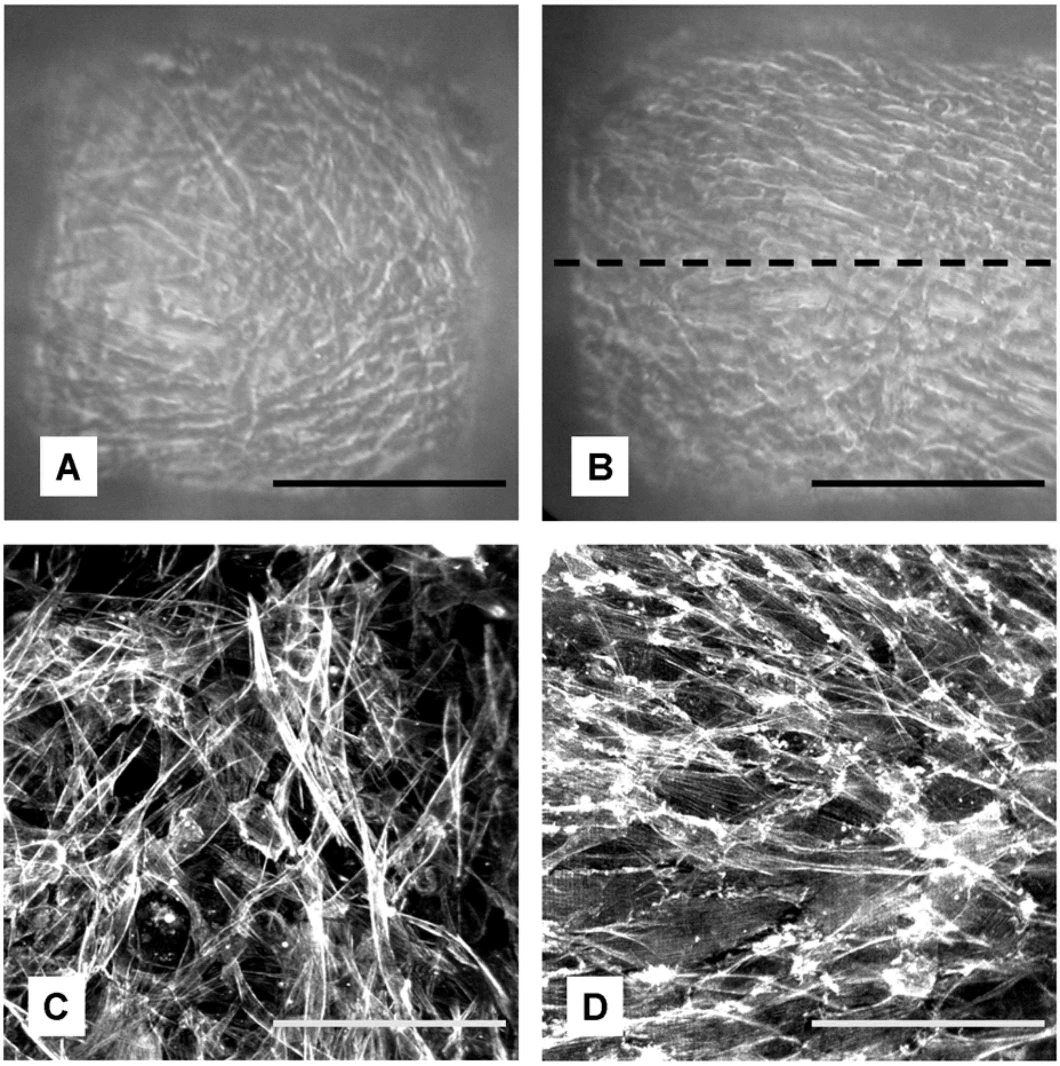

Figure 63 Light micrographs depicting a single 1:1 aspect ratio pore (A) and one half of a 2:1 (B) aspect ratio pore following 4 weeks incubation (scale bars = 100 μm). While the orientation of cells within the 1:1 aspect ratio pores was effectively random (A), 2:1 aspect ratio pores exhibited preferential cellular orientation along the long strut axis (black dashed line) (B). Laser scanning confocal microscopy conducted on scaffolds fluorescently labeled with Alexa Fluor® 568-Phalloidin (2:150 (v/v) dilution; Molecular Probes) for the intracellular filament F-actin (C, D) corroborated light microscopy observations (scale bars = 100 μm). The thicknesses of the tissue layers (measured using the confocal microscope) were typically 30 to 50 μm on both sides of the scaffold.

Orientation maps of the SALS scans revealed a heterogeneous spatial distribution of orientations (black vectors) and orientation index (OI) over the lateral surface of the 1:1 aspect ratio scaffolds, with decreased OI variability and magnitude with increasing aspect ratio up to 10:1 (**Figure 65**). This result suggests an improved alignment of the collagen fibers with increasing pore aspect ratio beyond the alignment contributions due to the pore geometry itself.

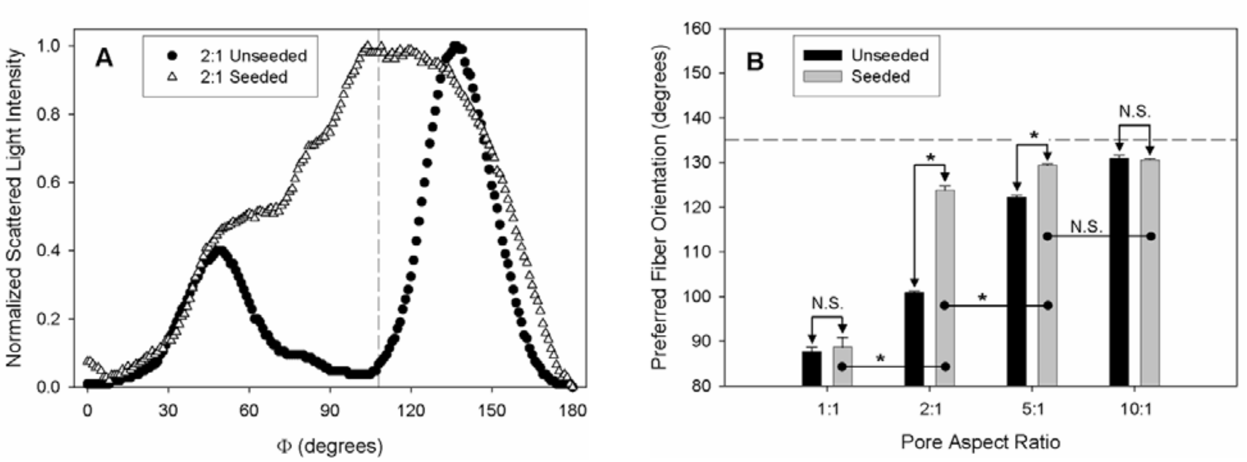

Figure 64 Representative SALS results for unseeded (●) and seeded (△) 2:1 aspect ratio scaffolds (A). Subtraction of the scaffold signal via the principal of optical superposition revealed that the preferred collagen fiber orientation was approximately 108 degrees for this particular sample (black dashed line). For the seeded scaffolds (white bars), the 2:1, 5:1, and 10:1 aspect ratio pores each demonstrated a marked capacity for guiding collagen fiber orientation (B). Preferred directions progressively aligned toward the 135 degree orientation of the long strut axis (black dashed line). Asterisks indicate statistically significant comparisons ($p < 0.05$) as found by the Tukey HSD test. N.S. indicates nonsignificant comparisons.

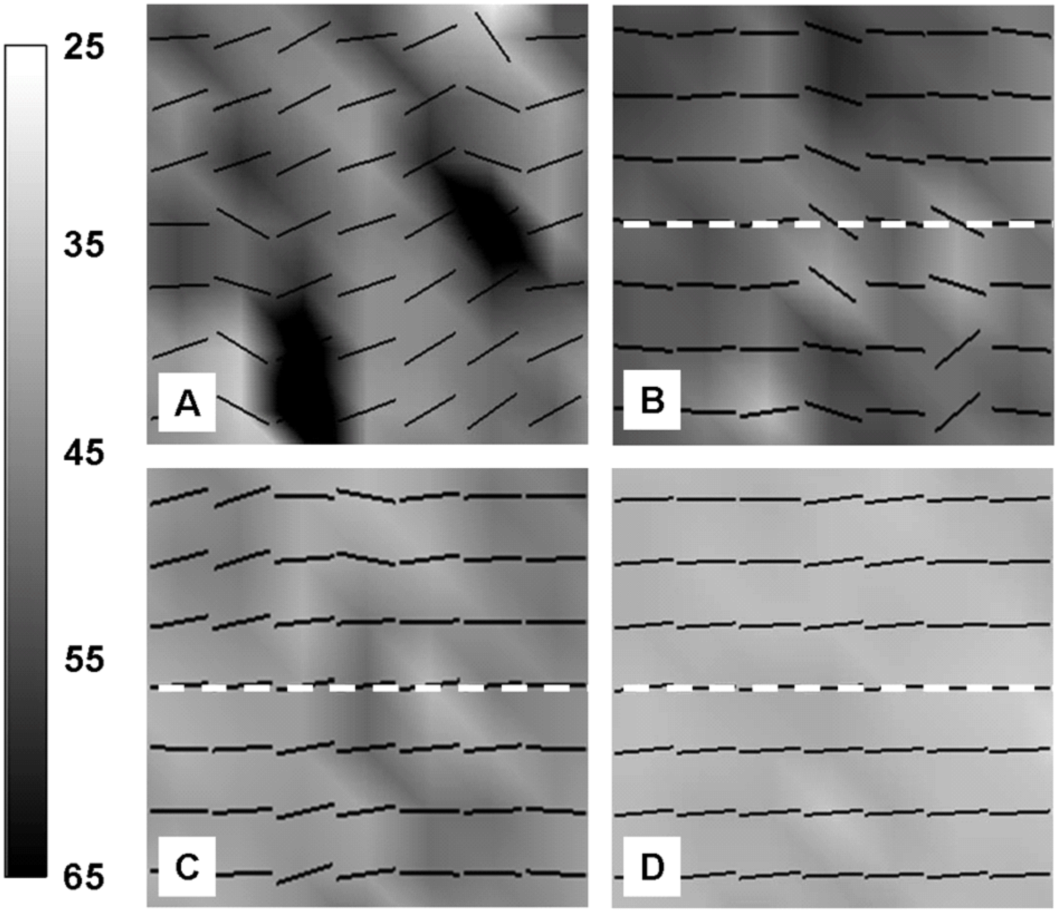

Figure 65 Representative SALS orientation maps for 1:1 (A), 2:1 (B), 5:1 (C), and 10:1 (D) aspect ratio scaffolds depicting the local preferred direction (black vectors) and the orientation of the long strut axis (white dashed line) overlaid upon the orientation index (OI). OI is a measure of the degree of orientation, with the lowest OI values (white) indicating the highest degree of orientation. Scaffolds exhibiting 1:1 aspect ratio pores (A) showed evidence of heterogeneous collagen orientation, with a high degree of spatial variability both in preferred direction and OI. A progressive decrease in OI variability and magnitude was observed with increasing pore aspect ratio (B, C, and D). Orientation maps for unseeded scaffolds were uniformly homogenous with low (> 30) OI values (data not shown).

Scanning electron micrographs for a representative 5:1 aspect ratio scaffold overall supported this observation (**Figure 66**), with intra-pore orientation of the cells parallel to the long strut axis (dashed black line) observed at low magnification (300x) (**Figure 66A**). At higher magnification (950x) individual cells and ECM could be discerned at the surface of the

30-50 μm thick tissue layer (**Figure 66B**). While the structure of the collagen embedded within the tissue layers could not be observed via SEM, in some cases where the tissue layer separated from the scaffold struts it was possible to observe collagen fibers (~ 100-300 nm diameter) spanning the gap (**Figure 66C**). It should be noted that the observed separation of the tissue layer from the scaffold struts is an artifact of critical point drying (**Figure 66C**).

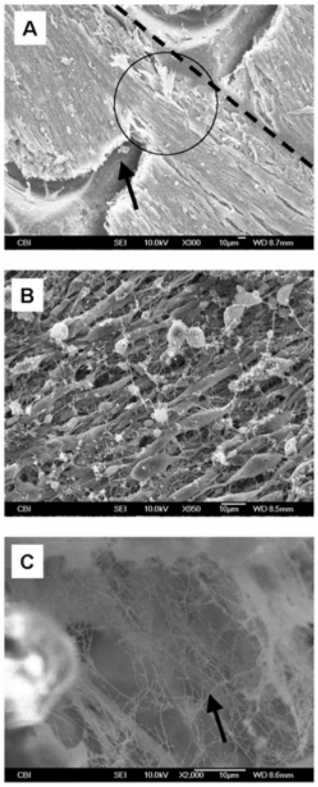

Figure 66 Scanning electron micrographs (SEM) from a representative 5:1 aspect ratio scaffold. At lower magnification (300x) it was possible to distinguish the orientation of cells parallel to the long strut axis (black dashed line) (A). Note that while the bulk of tissue deposition was confined within the pores, cells (inscribed by black circle) were often observed bridging the short struts (black arrow) between adjacent pores, generally retaining their bulk orientation. At higher magnification (950x) individual cells and collagen could be discerned at the surface of the 30-50 μm thick tissue layer (B). While the structure of the collagen embedded within the tissue layer could not be observed via SEM, in some cases where the tissue layer separated from the scaffold struts it was possible to observe collagen fibers (~ 100-300 nm diameter) spanning the gap (C).

To quantify the observed intra-pore cellular orientations, image analysis was conducted on SEM images. While cellular orientation results generally corroborated our SALS findings for collagen fiber orientation (data not shown), isolated pores were found to exhibit significant intra-pore variability in cellular orientation, as depicted for a 10:1 aspect ratio pore (**Figure 67**).

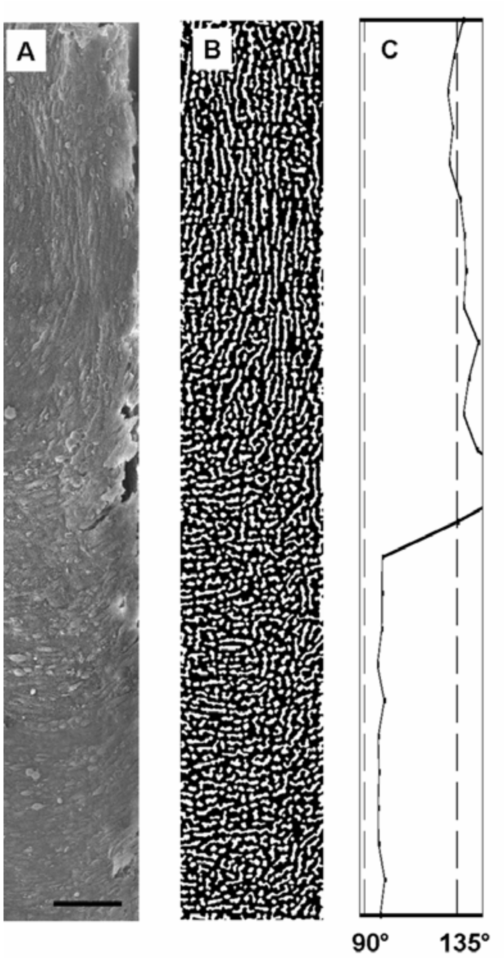

Figure 67 Panoramic scanning electron micrograph of a 10:1 aspect ratio pore (scale bar = 100 µm) (A). The image was reconstructed by concatenating several overlapping SEM images using Image Expert 2000 (Jasc Software, Inc., Eden Prairie, MN). Note the shifting orientation of the cells along the long axis, as highlighted in the contrast enhanced binary image (B). The median of the cell major axis angular orientation was quantified using the fill measurement option of SigmaScan Pro (SPSS, Inc.) (C). The left-most dashed line represents the angular orientation of the short strut (90 degrees) and the right-most dashed line represents the orientation of the long strut (135 degrees).

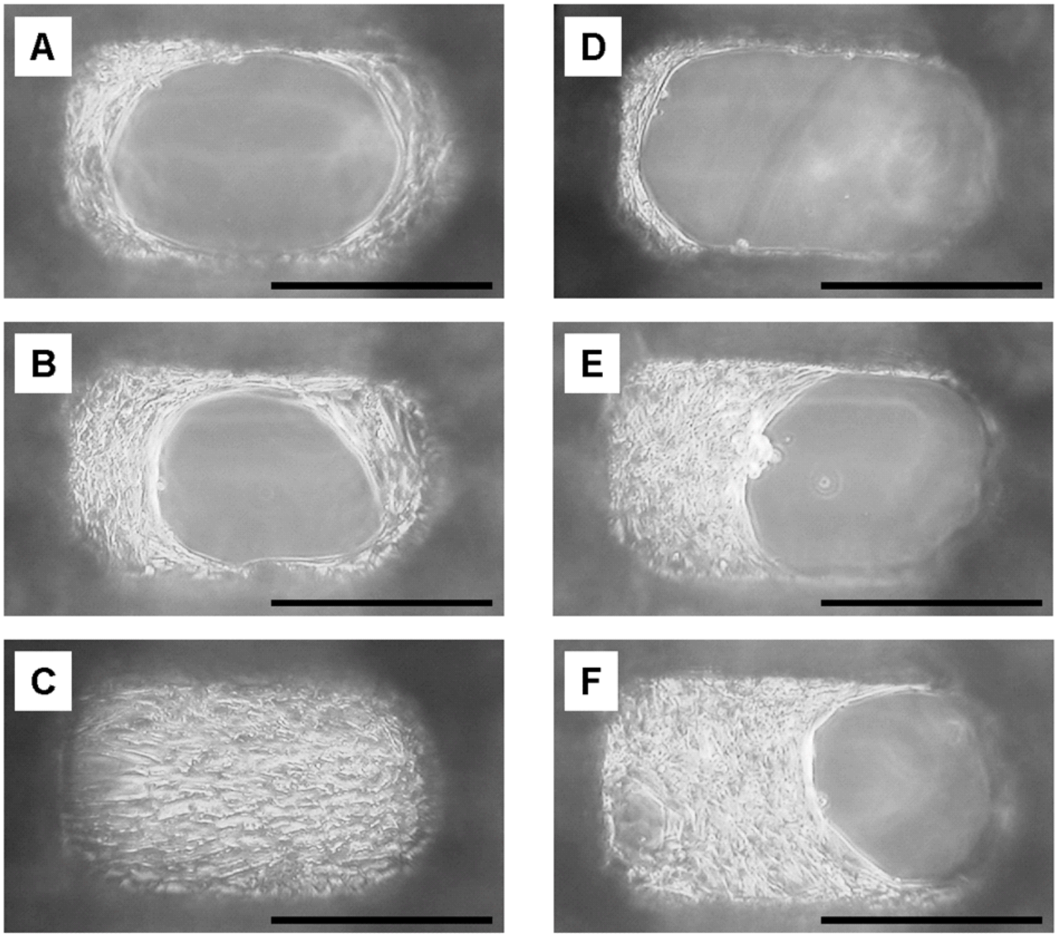

Figure 68 Light micrographs depicting the evolution of cellular orientation with time in 2:1 aspect ratio pores for cases of: uniform initial cell attachment around the pore perimeter (A-C), and non-uniform cell attachment (D-F). Cells typically attached uniformly around the pore perimeter (A), with successive growth fronts spanning the pore in a circumferential pattern (B), ultimately yielding preferential cellular alignment roughly parallel to the long strut axis (C). In isolated atypical pores, cells attached non-uniformly around the pore perimeter during seeding (D), with successive growth fronts spanning back-and-forth across the short strut axis (E), and ultimately yielding preferential cellular alignment roughly parallel to the short strut axis (F). Scale bars = 200 μm

By examining the evolution of cellular orientation over time in individual pores, it was found that the spatial uniformity of cellular attachment around each pore perimeter achieved during seeding significantly influenced the ultimate cellular orientation (**Figure 68**). In the case that cells initially attached uniformly around the pore perimeter (**Figure 68A**), cells proceeded to span the pore in the typical circumferential pattern via an elliptical growth front whose major axis was oriented roughly parallel to the long strut axis (**Figure 68B**), and ultimately yielded preferential cellular alignment parallel to the long strut axis (**Figure 68C**). In contrast, some isolated pores were observed in which initial cellular attachment following seeding was not uniform around the pore perimeter, but rather localized either to the strut intersections or the short struts (**Figure 68D**). In these isolated pores, cells proceeded to span the pore in an atypical back-and-forth pattern across the short strut axis (**Figure 68E**), ultimately yielding preferential cellular alignment orthogonal to the typical preferred direction (**Figure 68F**). We previously quantified the structure of diamond-shaped pores (**Figure 69A**) and the resultant preferred direction of the collagen fibers using SALS [176]. Scanning electron microscopy confirmed that the predominant orientation of cells is parallel to the major axis (black dashed line) of the diamond-shaped pores (**Figure 69B**). In contrast to rectangular pores, in isolated diamond-shaped pores where initial cellular attachment was not uniform around the pore perimeter, diamond-shaped pores were observed to maintain an elliptical growth front whose major axis (black arrow) was nearly parallel to the major axis of the pore (**Figure 69C**).

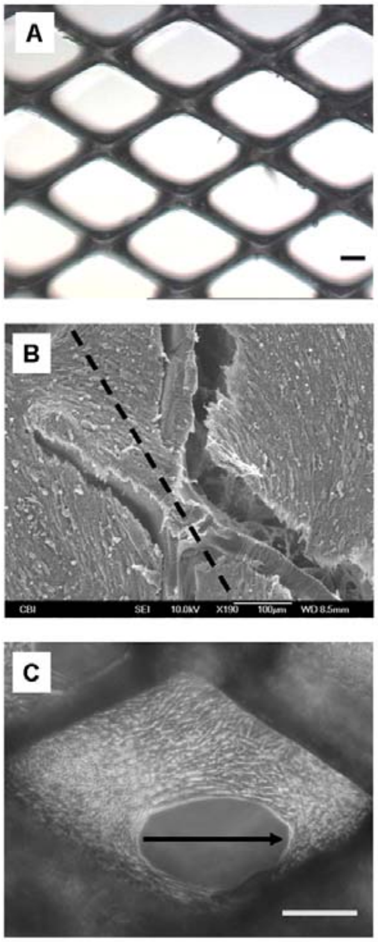

Figure 69 Light micrograph of a scaffold exhibiting a diamond-shaped pore structure similar to the Vicryl® scaffold used previously for manufacturing Dermagraft™ (scale bar = 200 µm) (A). Scanning electron micrograph (190X) of a cell seeded scaffold showing the intersection of four diamond-shaped pores (B). Note the predominant orientation of cells parallel to the major axis (black dashed line) of the diamond-shaped pores. Light micrograph of a single diamond-shaped pore following 1 week incubation (scale bar = 200 µm) (C). Note that despite an initially non-uniform distribution of cells around the pore perimeter, the diamond-shaped pore maintained the long axis of the growth front (black arrow) nearly parallel to the major axis of the pore.

7.1.4 Discussion

In developing a functionally-equivalent TEHV, the geometric arrangement attained by the collagen fiber network following both *in vitro* and *in vivo* remodeling is perhaps the single most important structural end-point to be matched to the native tissue. For the native aortic valve, we previously demonstrated that collagen fiber orientation dictates local and global tissue anisotropy [177]. Using a structural constitutive model, we demonstrated that the full spectrum of biaxial mechanical behavior, including axial coupling, could be accurately modeled and predicted by incorporating the experimentally measured collagen fiber orientation distribution [138]. However, while investigators recognize the critical importance of collagen fiber orientation in the mechanics and durability of load-bearing soft tissues, methods to guide the development of a functional collagen fiber network have yet to be delineated for engineered tissues based on synthetic scaffolds.

In the current study we investigated the ability of large-scale (200 μm) high aspect ratio open pore structures to guide engineered tissue cell and collagen orientation. Non-degradable scaffolds exhibiting a grid of 200 μm wide rectangular pores (1:1, 2:1, 5:1, and 10:1 aspect ratios) and diamond-shaped pores (600 x 1000 μm) were fabricated from a transparent epoxy resin via high-resolution stereolithography. Scaffolds were surface modified to support cell adhesion and evaluated for their capacity to promote the orientation of neonatal rat skin fibroblasts and their *de novo* synthesized collagen. In contrast to square pores, which yielded an effectively random cell and collagen orientation, preferential alignment parallel to the long strut axis and decreased spatial variability were observed to occur with increasing pore aspect ratio following 4 weeks of static incubation. Moreover, diamond-shaped pores exhibited an enhanced capacity to guide cellular orientation due to their relative insensitivity to the uniformity of initial cellular attachment around the pore perimeter.

7.1.4.1 Guidance of Collagen Orientation in Engineered Tissues

Depending upon the particular TE paradigm, distinct methods may be used to guide the development of an appropriate collagen fiber orientation. For example, in the case of collagen gel based TE constructs, collagen orientation and tissue anisotropy can be achieved by a variety of means, including magnetic forces [178], gel boundary conditions [123], substratum topology [179], and mechanical loading [180]. However, while the methods to guide collagen fiber orientation in these collagen gel based systems are well established, collagen gel based TE constructs continue to suffer from relatively low mechanical stiffness and strength. TE constructs based on synthetic bioresorbable scaffolds tend to offer improved mechanical performance over collagen gel based constructs; however it is less clear how to ensure the development of appropriately oriented cells and collagen fibers. While mechanical stimulation in the form of tension [64, 114], flexure [63], and flow [61] has been shown to enhance the synthesis of collagen on synthetic bioresorbable nonwoven scaffolds, the role of the scaffold microstructure in guiding the orientation of the deposited collagen has yet to be delineated. Of potential use in guiding cell and collagen orientation, the synthetic bioresorbable nonwoven scaffolds currently used to construct TEHV do exhibit a distinct preferred fiber direction that can be quantified by SALS, with an ~ 3-fold decrease in effective stiffness going from the preferred to the orthogonal cross-preferred fiber direction [181]. Nonwovens, however, are not the first choice for fundamental investigations of scaffold-mediated guidance due to spatial variations in effective pore size and shape.

7.1.4.2 Fabrication of Scaffolds with Well-Defined Microstructure.

Rapid-prototyping methods such as fused deposition modeling and stereolithography offer the possibility of fabricating geometrically well-defined scaffold microstructures [182]. While the spatial resolution of standard rapid-prototyping technologies is currently limited to about 50 μm [183], we have previously shown that the large scale (280 x 400 μm) diamond-shaped pores of a woven bioresorbable Vicryl® scaffold can significantly influence engineered tissue collagen fiber orientation [151]. For the purposes of evaluating candidate scaffold designs, the non-degradable epoxy resin scaffolds developed in the current study are advantageous because the intrinsic orienting capacity of the microstructure is decoupled from the potentially confounding effects of scaffold degradation. Moreover, because the epoxy resin scaffold does not intrinsically support cellular attachment, cell specificity and behavior can potentially be modulated via the surface modification. For example a recent study demonstrated significant differences in the physiology of neonatal cardiac myocytes when seeded on RGD versus YIGSR-modified substrates [184]. For ultimately translating the results of the current study to degradable polymers, as well as to create smaller feature sizes, a recently described microsyringe deposition technique may be useful [185]. Using the microsyringe technique, Vozzi et al. achieved spatial resolutions on the order of 10 μm using bioresorbable poly(DL-lactide-*co*-glycolide) (PLGA).

7.1.4.3 Mechanisms Governing Large-Scale Orientation.

In the current study, we demonstrated that scaffold pore structures over an order of magnitude larger than the cells could direct cell and collagen orientation. The mechanisms governing cellular and fiber alignment on these scaffolds are likely very distinct from the contact guidance phenomena observed on micro-grooved substrates. For example, while several mechanisms have been postulated to explain contact guidance on micro-grooved substrates, ranging from bending restrictions imposed on lamellipodia to selective protein adsorption due to differences in groove and ridge surface free energies [174], each of these mechanisms would invariably affect the orientation of individual cells. In contrast, the orienting capacity of large-scale open pore structures likely depends on the coordinated behavior of groups of hundreds of cells. Based on observations made on micro-grooved substrates [186], the orientation of collagen fibers within our system is likely concomitant to cellular orientation.

In light of the different mechanisms responsible for cellular and collagen orientation in large-scale open pores versus micro-grooves, it is not surprising that differences are observed in the orienting capacity. While micro-grooved substrates appear to ubiquitously align cells along their long axis, we observed here that the orienting capacity of open pore structures depends in part on the spatial uniformity of initial cellular attachment around the perimeter of the pores. For example, while the 10:1 aspect ratio pores were highly effective in guiding global collagen orientation, scanning electron microscopy revealed isolated pores in which cells switched orientation by nearly 90 degrees over the pore length (**Figure 67**). Such intra-pore variations in orientation were observed to depend on the uniformity of initial cellular attachment around the pore perimeter, with uniform cellular attachment leading to the typically observed preferential alignment parallel to the long strut axis, and non-uniform attachment resulting in the atypical orthogonal alignment (**Figure 68**). Because the cells did ultimately span the majority of the pores, observed cases of non-uniform initial cell attachment were likely a consequence of the *seeding process*, not the surface modification. Based on light microscopic observations made during the 4 weeks incubation period (**Figure 68**), we developed schematics illustrating the distinct patterns of cellular growth front propagation observed depending on the uniformity of initial cellular attachment around the pore perimeter (**Figure 70**). In the case that cells (small ellipses) were uniformly distributed around the perimeter of the pore (**Figure 70A**), successive growth fronts (gray ellipses) spanned the pore in an elliptical pattern with the major axis of the ellipse (black arrow) oriented parallel to the long strut axis. In the case of that cells attached non-uniformly around the pore perimeter, cells attached preferentially to the strut intersections with successive growth fronts (gray curves) spanning the pore back-and-forth across the short strut axis (black arrow) (**Figure 70B**).

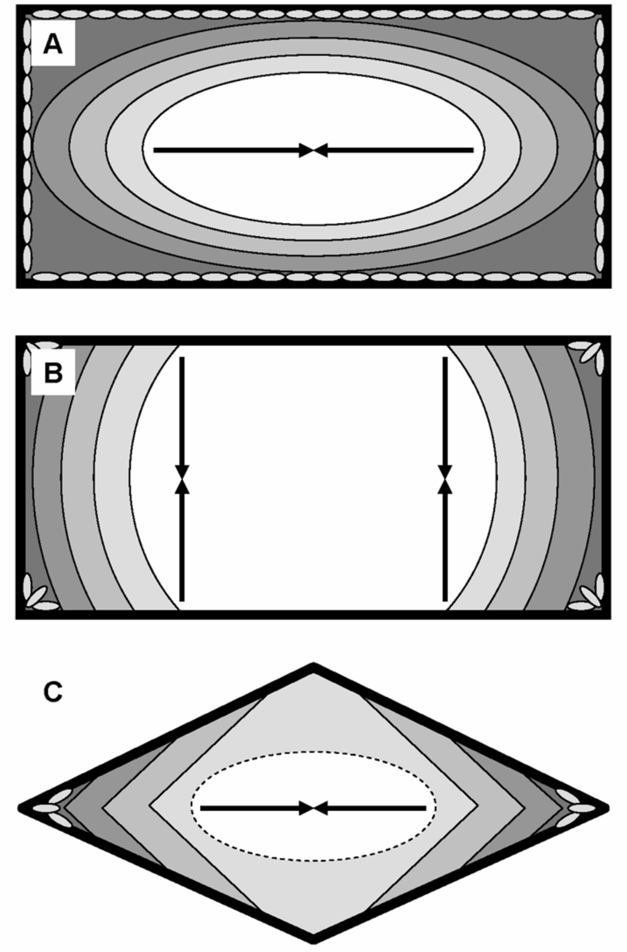

Figure 70 Schematic illustrating the distinct patterns of growth front propagation observed in 2:1 aspect ratio pores. In the case that cells (small ellipses) were initially distributed homogeneously around the perimeter of the pore (A), successive growth fronts (gray ellipses) filled the pore in an elliptical pattern with the major axis of the ellipse (black arrow) oriented parallel to the long strut axis (A). In the case that cells were initially distributed heterogeneously around the perimeter of the pore (B), cells were observed to attach preferentially to the strut intersections with successive growth fronts (gray curves) filling the pore back-and-forth across the short strut axis (black arrows) (B). In the case of heterogeneous cell attachment to a 2:1 aspect ratio diamond-shaped pore (C), cells were observed to attach preferentially at the tight V-shaped strut intersections and successive growth fronts filled the pore back-and-forth across the minor axis direction. However, as opposed to the rectangular pore, the slope of the struts ultimately induced the formation of an elliptical growth front (dashed ellipse) oriented parallel to the major axis (black arrow) as the two growth fronts approached from either side of the pore.

Our findings thus far suggest that diamond-shaped pores may be less sensitive to the spatial uniformity of initial cellular attachment (**Figure 69**). In the case that cells initially attached non-uniformly around the perimeter of a 2:1 aspect ratio diamond-shaped pore (**Figure 69C**), cells attached preferentially at the tight V-shaped strut intersections with successive growth fronts initially spanning the pore back-and-forth across the minor axis direction. However, as opposed to the rectangular pore, the slope of the struts ultimately induced the formation of an elliptical growth front (dashed ellipse) oriented parallel to the major axis (black arrow) as the two growth fronts approximated the gap from either side of the pore (**Figure 70C**). Because cells tended to aggregate more prevalently at the strut intersections, the geometry of these intersections may play a key role in guiding subsequent cellular and collagen orientation.

7.1.4.4 Combinations of Large-Scale, Micro-Scale, and Mechanical Guidance.

It may be possible to develop scaffolds whose structural members (e.g., fibers, struts) possess an additional level of controlled surface topology to aid in the guidance of cellular and collagen orientation. In a previous study [187], multi-grooved substrates were fabricated exhibiting 90-degree V-shaped micro-grooves of 2 μm pitch and 1 μm depth and 50 μm wide by 25 μm deep macro-grooves. The micro-grooves were found to be sufficient for cellular orientation, while the macro-grooves appeared to promote collagen secretion and orientation. Hypothetically, a scaffold could be designed in which the struts of the open pore structure are micro-grooved to enhance the orientation of cells along a particular axis.

To combine mechanical with structural guidance, elastomeric scaffolds need to be fabricated. Recent studies on micro-grooved elastomeric substrates suggest a significant degree of coupling between cellular orientation and response to stretch [188]. Electrospinning elastomers such as poly(ester urethane)urea (PEUU) represents one possible method for generating elastomeric scaffolds with oriented nano-scale structures [189]. Recent studies have demonstrated that highly aligned poly-L-lactic acid fibers can be electrospun by optimizing the spinning conditions [190]. However, while the average fiber orientation can be controlled, local variations are inherent due to the stochastic nature of the electrospinning process. Larger scale oriented pore structures have recently been fabricated from PEUU by thermally-induced phase separation (TIPS) [191]. Thus using PEUU it may be possible to incorporate large-scale, micro-scale, and mechanical guidance in a scaffold design via the combination of electrospinning with TIPS.

7.1.4.5 Summary.

In the current study, we developed an *in vitro* model system in which arbitrary large-scale (~200 μm) open pore structures could be rapid-prototyped and systematically evaluated for their cell and collagen orientating capacity. Non-degrading scaffolds with high aspect ratio rectangular pores were fabricated by stereolithography and demonstrated a significant capacity to guide global cell and collagen fiber orientation compared with square pores. Preferential alignment parallel to the long strut axis and decreased spatial variability were observed to occur with increasing pore aspect ratio. The mechanisms governing cell and collagen orientation within these large-scale open pore structures likely depends on the coordinated behavior of large groups of cells and fibers, as opposed to the phenomenon of contact guidance on micro-grooved substrates which can affect individual cells. A comparison of cellular growth front propagation patterns in rectangular versus diamond-shaped pores suggest that diamond-shaped pores are less sensitive to the spatial uniformity of initial cellular attachment, and thus represent an attractive structural motif for mediating guidance in TE scaffold designs.

APPENDIX A

FREESTON AND PLATT'S GENERAL ASSUMPTIONS FOR MODELING NONWOVENS

The general assumptions invoked by Freeston and Platt [146] in their unit cell (i.e., RVE) representation are paraphrased below, with each assumption followed by a justification of its applicability to the materials considered in the current study.

1. *Fibers are linear elastic, homogenous, and isotropic.* At very small strains (~0.6%) the PGA and PLLA fibers investigated herein were linear elastic (**Figure 45**). While the fibers were melt extruded and likely transversely isotropic, we measured the longitudinal fiber stiffness, which is the stiffness governing the flexural behavior of the fibers.
2. *RVE boundaries are orthogonal to the direction of applied stress (i.e., no fabric shear).* Scaffold specimens were cut orthogonal to the PD and XD fiber directions, ensuring that the RVE boundaries were orthogonal to the direction of applied stress when tested in three-point bending. Moreover, the shear stiffness of needled nonwovens is relatively high and thus shear deformations would be expected to be negligible. In the case of a needled nonwoven PGA scaffold, the shear stiffness was reported by Shum et al. to be 763 kPa [192] (i.e., ~ 2.5-fold the measured value of *E* (**Table 6**)).

3. *Fiber diameter is small compared with fiber length (i.e., fiber shear is negligible)*. The fibers within the needled nonwoven were 40-50 mm long [135], compared with a fiber diameter of 0.01295 mm in the case of PGA and 0.01636 mm for PLLA (**Table 3**). Thus the fiber diameters were small (~ 3/10000) compared with the fiber length.
4. *Fiber cross-section is circular and fiber diameter does not vary along fiber length*. The fiber diameters were measured via an image analysis technique. The fiber diameter was measured at five points along the fiber length for each PGA (n=6) and PLLA (n=6) fiber with a standard error of 0.02 μm. Thus the fiber diameter did not vary significantly along the fiber length.
5. *Fiber diameter and fabric thickness are small compared to the radius of curvature*. The minimum radius of curvature achieved in the three point bending tests was approximately 10 mm. Therefore the fiber diameters (0.01295 for PGA and 0.01636 for PLLA) and the fabric thickness (~ 1mm) were each small relative to the minimum radius of curvature.
6. *Cross-sections initially plane and normal to the fiber centerline remain so after bending*. As stated above, the shear stiffness of needled nonwoven scaffolds is relatively high, and thus shear deformations within the scaffold would be expected to be small in bending.
7. *Fibers do not buckle*. In the case of straight fibers, the assumption of no fiber buckling is a necessary simplification in the absence of data regarding the strain criterion for fiber buckling within the nonwoven fabric. This assumption was thus invoked in calculating the lower and upper bounds on *E* (**Table 6**). However, in formulating the structural model for the needled nonwoven scaffold, fiber buckling is explicitly assumed; the effective longitudinal stiffness of the crimped fibers is assumed to be governed by the

bending and extension of their sinusoidal curved structure (see *New assumptions for modeling needled nonwoven scaffolds*).

8. *Fiber angular and numerical distribution is equal through the thickness of the RVE.* While it is possible that minor through-thickness variations in the angular distribution are generated during the needling process [97], structural model implementation of $R(\Phi)$ determined by our effectively 2D SALS technique yielded E predictions in close agreement with experimental measures for both PD and XD specimens (**Table 6**).

APPENDIX B

DERIVATION OF FREESTON AND PLATT'S "COMPLETE FREEDOM" MODEL

In Freeston and Platt's "complete freedom" model, individual fibers of the nonwoven are assumed to bend independently of one another. Thus the net moment required to bend this hypothetical fabric about an arbitrary axis (e.g., the $\vec{k}$-axis) is simply the sum of the individual fiber bending moments about this axis. The $\vec{k}$-component of the bending moment vector for a fiber initially oriented at an angle Φ to the orthogonal axis (e.g., the $\vec{i}$-axis) is given by:

$$M_f = E_f I_f \left(\vec{T} \times \vec{K}\right)_{\vec{k}} \tag{29}$$

in which $\vec{T}$ and $\vec{K}$ are the unit tangent and curvature vectors of the fiber, respectively. $\vec{T}$ and $\vec{K}$ can be calculated from the relations:

$$\vec{T} = \frac{d\vec{R}/d\theta}{\left|d\vec{R}/d\theta\right|} \tag{30}$$

$$\vec{K} = \frac{d\vec{T}/d\theta}{\left|d\vec{R}/d\theta\right|} \tag{31}$$

where the position vector, $\vec{R}$, to any point on the axis of a bent fiber is given by:

$$\vec{R} = \vec{i}\,(\rho\cos\theta) + \vec{j}(\rho\sin\theta) - \vec{k}(\rho\theta\tan\Phi) \tag{32}$$

where ρ is the radius of curvature (i.e., $1/\Delta\kappa$). Upon substitution of Eq. (32), (31), and (30) into Eq. (29) and simplification via the appropriate trigonometric identities, Eq. (29) reduces to:

$$M_f = \frac{E_f I_f}{\rho}\cos^3\Phi \tag{33}$$

The relative frequency of fibers parallel to the $\vec{i}$ -axis is $R(\Phi)\cos\Phi$ (Eq. (6)), and thus the net bending moment is given by:

$$M_{RVE} = \frac{N_f E_f I_f}{\rho}\int_{-\pi/2}^{\pi/2} R(\Phi)\cos^4\Phi d\Phi \tag{34}$$

Multiplication of Eq. (34) by ρ yields Eq. (4), the expression for *EI* per RVE.

APPENDIX C

DERIVATION OF FREESTON AND PLATT'S "NO FREEDOM" MODEL

Freeston and Platt's "no freedom" model is based on the assumption that the individual fibers are rigidly bonded at each cross-over point, thus giving rise to continuum plate behavior. The fabric strain along the $\vec{i}$ -axis direction is thus given by:

$$\varepsilon_{\vec{i}} = y / \rho \tag{35}$$

where y is the distance from the neutral axis of the fabric. Invoking small strain and first order approximations applied to nonwovens by Backer and Petterson [140], the fiber strain is given by

$$\varepsilon_f = \varepsilon_{\vec{i}} \cos^2 \Phi = \left(y \cos^2 \Phi \right) / \rho \tag{36}$$

Thus, the $\vec{k}$ -component of the bending moment of a fiber is given by

$$M_f = F_f y \cos \Phi = \left(E_f A_f y^2 \cos^3 \Phi \right) / \rho \tag{37}$$

where F_f is the force on a fiber. This equation is analogous to Eq. (33) in the “complete freedom” model described above. The relative frequency of fibers per unit cross-sectional area parallel to the $\vec{i}$ -axis is given by

$$P = \frac{R(\Phi)\cos\Phi}{bt} \tag{38}$$

Thus, the sum of all the moments about the $\vec{k}$ -axis is given by:

$$M_{RVE} = N_f \int_{-\pi/2}^{\pi/2} P \left\{ \int_{-t/2}^{t/2} \int_{-b/2}^{b/2} M_f \, dx dy \right\} d\Phi = \frac{N_f E_f A_f t^2}{12\rho} \int_{-\pi/2}^{\pi/2} R(\Phi) \cos^4 \Phi d\Phi \tag{39}$$

Multiplication of Eq. (39) by ρ yields Eq. (7), the expression for *EI* per RVE.

APPENDIX D

DERIVATION OF LEE AND ARGON'S EFFECTIVE FIBER STIFFNESS MODEL

To derive their effective fiber stiffness model, Lee and Argon considered a one wavelength-long segment of a sinusoidal shaped fiber (**Figure 43**A). Expressions were developed for the strain energy *U* due to axial tension and bending under an applied load *F* and applied bending moment *M*. The strain energy due to bending U_b can be expressed as:

$$U_b = \int_{-\Lambda_{eff}/4}^{3\Lambda_{eff}/4} \frac{\left\{ M - Fa_{eff}\left(1+\sin\frac{2\pi x}{\Lambda_{eff}}\right)\right\}^2}{2EI} \sqrt{1+\left(\frac{2\pi a_{eff}}{\Lambda_{eff}}\cos\frac{2\pi x}{\Lambda_{eff}}\right)} dx \qquad (40)$$

and the strain energy due to tension U_t can be expressed as:

$$U_t = \int_{-\Lambda_{eff}/4}^{3\Lambda_{eff}/4} \frac{A_f}{2E_f}\left[\frac{F}{A_f}\frac{1}{\sqrt{1+\left(\frac{2\pi a_{eff}}{\Lambda_{eff}}\cos\frac{2\pi x}{\Lambda_{eff}}\right)^2}}\right]\sqrt{1+\left(\frac{2\pi a_{eff}}{\Lambda_{eff}}\cos\frac{2\pi x}{\Lambda_{eff}}\right)^2} dx \qquad (41)$$

where the total strain energy is the arithmetic sum of tension and bending:

$$U = U_b + U_t \tag{42}$$

To facilitate subsequent derivations, Lee and Argon transformed the independent variable x to the dummy variable $z = (\pi/2\Lambda_{eff})\, x + \pi/8$ and also utilized Eq. (10) to describe the initial effective curvature of the fiber segment. The moment M could then be found from the condition of no end rotation (i.e., $dU/dM = 0$) as $M = Fa_{eff}$. The displacement δ of the fiber end could then be found from Castigliano's second theorem:

$$\delta = \frac{dU}{dF} = F\left(\frac{4a_{eff}^{\ 2}}{E_f I_f}\Lambda_{eff} B_1 + \frac{4\Lambda_{eff}}{A_f E_f} B_2\right) \tag{43}$$

where the parameters B_1 and B_2 are given by Eq. (9). Finally, the effective fiber stiffness $(E_f)'$ is found by the relationship:

$$(E_f)' = \frac{F}{A_f(\delta/\Lambda_{eff})} = \frac{E_f}{\frac{4A_f}{I_f} a_{eff}^{\ 2} B_1 + 4B_2} \tag{44}$$

which reduces to Eq. (8) upon substituting the appropriate values for I_f and A_f.

BIBLIOGRAPHY

1. Hurst, J.W., R.B. Logue, C.E. Rackley, R.C. Schlant, E.H. Sonnenblick, A.G. Wallace, and N.K. Wenger, *The Heart*. 6th ed. 1986, New York: McGraw Hill.

2. Sutton, J.P., 3rd, S.Y. Ho, and R.H. Anderson, *The forgotten interleaflet triangles: a review of the surgical anatomy of the aortic valve.* Ann Thorac Surg, 1995. **59**(2): p. 419-27.

3. Thubrikar, M., *The Aortic Valve*. 1990, Boca Raton: CRC. 221.

4. Gross, L. and M. Kugel, *Topographic anatomy and histology of the valves in the human heart.* American Journal of Pathology, 1931. **7**: p. 445-456.

5. Lovekamp, J.J., D.T. Simionescu, J.J. Mercuri, B. Zubiate, M.S. Sacks, and N.R. Vyavahare, *Stability and function of glycosaminoglycans in porcine bioprosthetic heart valves.* Biomaterials, 2005.

6. Talman, E.A. and D.R. Boughner, *Effect of altered hydration on the internal shear properties of porcine aortic valve cusps.* Ann Thorac Surg, 2001. **71**(5 Suppl): p. S375-8.

7. Vyavahare, N., M. Ogle, F.J. Schoen, R. Zand, D.C. Gloeckner, M. Sacks, and R.J. Levy, *Mechanisms of bioprosthetic heart valve failure: fatigue causes collagen denaturation and glycosaminoglycan loss.* J Biomed Mater Res, 1999. **46**(1): p. 44-50.

8. Rabkin, E., S.P. Hoerstrup, M. Aikawa, J.E. Mayer, Jr., and F.J. Schoen, *Evolution of cell phenotype and extracellular matrix in tissue-engineered heart valves during in-vitro maturation and in-vivo remodeling.* Journal of Heart Valve Disease, 2002. **11**(3): p. 308-14; discussion 314.

9. Filip, D.A., A. Radu, and M. Simionescu, *Interstitial cells of the heart valves possess characteristics similar to smooth muscle cells.* Circ Res, 1986. **59**(3): p. 310-20.

10. Messier, R.H., Jr., B.L. Bass, H.M. Aly, J.L. Jones, P.W. Domkowski, R.B. Wallace, and R.A. Hopkins, *Dual structural and functional phenotypes of the porcine aortic valve interstitial population: characteristics of the leaflet myofibroblast.* Journal of Surgical Research, 1994. **57**(1): p. 1-21.

11. Rabkin-Aikawa, E., M. Farber, M. Aikawa, and F.J. Schoen, *Dynamic and reversible changes of interstitial cell phenotype during remodeling of cardiac valves.* J Heart Valve Dis, 2004. **13**(5): p. 841-7.

12. Rabkin-Aikawa, E., M. Aikawa, M. Farber, J.R. Kratz, G. Garcia-Cardena, N.T. Kouchoukos, M.B. Mitchell, R.A. Jonas, and F.J. Schoen, *Clinical pulmonary autograft*

valves: pathologic evidence of adaptive remodeling in the aortic site. J Thorac Cardiovasc Surg, 2004. **128**(4): p. 552-61.

13. Merryman, W.D., I. Youn, H.D. Lukoff, P.M. Krueger, F. Guilak, R.A. Hopkins, and M.S. Sacks, *Correlation between heart valve interstitial cell stiffness and transvalvular pressure: Implications for collagen biosynthesis.* Am J Physiol Heart Circ Physiol, 2005.

14. Merryman, W.D., H.Y.S. Huang, F.J. Schoen, and M.S. Sacks, *The effects of cellular contraction on aortic valve leaflet flexural stiffness.* Journal of Biomechanics, In press.

15. Dvorin, E.L., J. Wylie-Sears, S. Kaushal, D.P. Martin, and J. Bischoff, *Quantitative evaluation of endothelial progenitors and cardiac valve endothelial cells: proliferation and differentiation on poly-glycolic acid/poly-4-hydroxybutyrate scaffold in response to vascular endothelial growth factor and transforming growth factor beta1.* Tissue Eng, 2003. **9**(3): p. 487-93.

16. Paranya, G., S. Vineberg, E. Dvorin, S. Kaushal, S.J. Roth, E. Rabkin, F.J. Schoen, and J. Bischoff, *Aortic valve endothelial cells undergo transforming growth factor-beta-mediated and non-transforming growth factor-beta-mediated transdifferentiation in vitro.* Am J Pathol, 2001. **159**(4): p. 1335-43.

17. Rabkin, E. and F.J. Schoen, *Cardiovascular tissue engineering.* Cardiovasc Pathol, 2002. **11**(6): p. 305-17.

18. Stark, J., *The use of valved conduits in pediatric cardiac surgery.* Pediatr Cardiol, 1998. **19**(4): p. 282-8.

19. Mayer, J.E., Jr., *Uses of homograft conduits for right ventricle to pulmonary artery connections in the neonatal period.* Semin Thorac Cardiovasc Surg, 1995. **7**(3): p. 130-2.

20. Allen, B.S., C. El-Zein, B. Cuneo, J.P. Cava, M.J. Barth, and M.N. Ilbawi, *Pericardial tissue valves and Gore-Tex conduits as an alternative for right ventricular outflow tract replacement in children.* Ann Thorac Surg, 2002. **74**(3): p. 771-7.

21. Cheitlin, M.D., *Pathophysiology of valvular aortic stenosis in the elderly.* Am J Geriatr Cardiol, 2003. **12**(3): p. 173-7.

22. Schoen, F. and R. Levy, *Tissue heart valves: Current challenges and future research perspectives.* Journal of Biomedical Materials Research, 1999. **47**: p. 439-465.

23. Cannegieter, S., F. Rosendaal, and E. Briet, *Thromboembolic and bleeding complications in patients with mechanical heart valve prostheses.* Circulation, 1994. **89**: p. 635-641.

24. Leyh, R.T., S. Fischer, A. Ruhparwar, and A. Haverich, *Anticoagulant therapy in pregnant women with mechanical heart valves.* Arch Gynecol Obstet, 2003. **268**(1): p. 1-4.

25. Chan, W.S., S. Anand, and J.S. Ginsberg, *Anticoagulation of pregnant women with mechanical heart valves: a systematic review of the literature.* Arch Intern Med, 2000. **160**(2): p. 191-6.

26. Schoen, F. and R. Levy, *Pathology of Substitute Heart Valves.* Journal of Cardiac Surgery, 1994. **9**: p. 222-227.

27. Sacks, M.S. and F.J. Schoen, *Collagen fiber disruption occurs independent of calcification in clinically explanted bioprosthetic heart valves.* J Biomed Mater Res, 2002. **62**(3): p. 359-71.

28. Hoffman, J.I. and S. Kaplan, *The incidence of congenital heart disease.* J Am Coll Cardiol, 2002. **39**(12): p. 1890-900.

29. Martin, J.A., B.E. Hamilton, P.D. Sutton, S.J. Ventura, F. Menacker, and M.L. Munson, *Births: final data for 2003.* Natl Vital Stat Rep, 2005. **54**(2): p. 1-116.

30. Perron, J., A.M. Moran, K. Gauvreau, P.J. del Nido, J.E. Mayer, Jr., and R.A. Jonas, *Valved homograft conduit repair of the right heart in early infancy.* Ann Thorac Surg, 1999. **68**(2): p. 542-8.

31. Stock, U.A., J.P. Vacanti, J.E. Mayer Jr, and T. Wahlers, *Tissue engineering of heart valves -- current aspects.* Thorac Cardiovasc Surg, 2002. **50**(3): p. 184-93.

32. Hoerstrup, S.P., R. Sodian, S. Daebritz, J. Wang, E.A. Bacha, D.P. Martin, A.M. Moran, K.J. Guleserian, J.S. Sperling, S. Kaushal, J.P. Vacanti, F.J. Schoen, and J.E. Mayer, Jr., *Functional living trileaflet heart valves grown In vitro.* Circulation, 2000. **102**(19 Suppl 3): p. III44-9.

33. Sutherland, F.W., T.E. Perry, Y. Yu, M.C. Sherwood, E. Rabkin, Y. Masuda, G.A. Garcia, D.L. McLellan, G.C. Engelmayr, Jr., M.S. Sacks, F.J. Schoen, and J.E. Mayer, Jr., *From stem cells to viable autologous semilunar heart valve.* Circulation, 2005. **111**(21): p. 2783-91.

34. Perry, T.E., S. Kaushal, F.W. Sutherland, K.J. Guleserian, J. Bischoff, M. Sacks, and J.E. Mayer, *Thoracic Surgery Directors Association Award. Bone marrow as a cell source for tissue engineering heart valves.* Annals of Thoracic Surgery, 2003. **75**(3): p. 761-7; discussion 767.

35. Hoerstrup, S.P., A. Kadner, S. Melnitchouk, A. Trojan, K. Eid, J. Tracy, R. Sodian, J.F. Visjager, S.A. Kolb, J. Grunenfelder, G. Zund, and M.I. Turina, *Tissue engineering of functional trileaflet heart valves from human marrow stromal cells.* Circulation, 2002. **106**(12 Suppl 1): p. I143-50.

36. Kadner, A., S.P. Hoerstrup, J. Tracy, C. Breymann, C.F. Maurus, S. Melnitchouk, G. Kadner, G. Zund, and M. Turina, *Human umbilical cord cells: a new cell source for cardiovascular tissue engineering.* Ann Thorac Surg, 2002. **74**(4): p. S1422-8.

37. Kaushal, S., G.E. Amiel, K.J. Guleserian, O.M. Shapira, T. Perry, F.W. Sutherland, E. Rabkin, A.M. Moran, F.J. Schoen, A. Atala, S. Soker, J. Bischoff, and J.E. Mayer, Jr., *Functional small-diameter neovessels created using endothelial progenitor cells expanded ex vivo.* Nat Med, 2001. **7**(9): p. 1035-40.

38. Perry, T.E., S. Kaushal, B. Nasseri, F.W.H. Sutherland, J. Wang, K.J. Guleserian, J. Bischoff, J.P. Vacanti, M.S. Sacks, and J.E. Mayer, *Peripheral blood as a cell source for tissue engineering heart valves.* Surgical Forum, 2001. **LII**: p. 99-101.

39. Matheny, R.G., M.L. Hutchison, P.E. Dryden, M.D. Hiles, and C.J. Shaar, *Porcine small intestine submucosa as a pulmonary valve leaflet substitute.* J Heart Valve Dis, 2000. **9**(6): p. 769-74; discussion 774-5.

40. Zeltinger, J., L.K. Landeen, H.G. Alexander, I.D. Kidd, and B. Sibanda, *Development and characterization of tissue-engineered aortic valves.* Tissue Eng, 2001. **7**(1): p. 9-22.

41. Dohmen, P.M., A. Lembcke, H. Hotz, D. Kivelitz, and W.F. Konertz, *Ross operation with a tissue-engineered heart valve.* Ann Thorac Surg, 2002. **74**(5): p. 1438-42.

42. Ross, D.N., *Replacement of aortic and mitral valves with a pulmonary autograft.* Lancet, 1967. **2**(7523): p. 956-8.

43. Shin, D., G. Garcia-Cardena, S. Hayashi, S. Gerety, T. Asahara, G. Stavrakis, J. Isner, J. Folkman, M.A. Gimbrone, Jr., and D.J. Anderson, *Expression of ephrinB2 identifies a stable genetic difference between arterial and venous vascular smooth muscle as well as endothelial cells, and marks subsets of microvessels at sites of adult neovascularization.* Dev Biol, 2001. **230**(2): p. 139-50.

44. Simon, P., C. Aschauer, R. Moidl, M. Marx, F.P. Keznickl, E. Eigenbauer, E. Wolner, and G. Wollenek, *Growth of the pulmonary autograft after the Ross operation in childhood.* Eur J Cardiothorac Surg, 2001. **19**(2): p. 118-21.

45. Schoof, P.H., M.G. Hazekamp, G.K. van Wermeskerken, E. de Heer, J.A. Bruijn, A.C. Gittenberger-de Groot, and H.A. Huysmans, *Disproportionate enlargement of the pulmonary autograft in the aortic position in the growing pig.* J Thorac Cardiovasc Surg, 1998. **115**(6): p. 1264-72.

46. Schoof, P.H., A.C. Gittenberger-De Groot, E. De Heer, J.A. Bruijn, M.G. Hazekamp, and H.A. Huysmans, *Remodeling of the porcine pulmonary autograft wall in the aortic position.* J Thorac Cardiovasc Surg, 2000. **120**(1): p. 55-65.

47. Iyengar, A.K.S., H. Sugimoto, D.B. Smith, and M.S. Sacks, *Dynamic in vitro quantification of bioprosthetic heart valve leaflet motion using structured light projection.* Ann Biomed Eng, 2001. **29**(11): p. 963-73.

48. Sacks, M.S. and W. Sun, *Multiaxial Mechanical Behavior of Biological Materials.* Annu Rev Biomed Eng, 2003.

49. Hove, J.R., R.W. Koster, A.S. Forouhar, G. Acevedo-Bolton, S.E. Fraser, and M. Gharib, *Intracardiac fluid forces are an essential epigenetic factor for embryonic cardiogenesis.* Nature, 2003. **421**(6919): p. 172-7.

50. Kunzelman, K.S., D.W. Quick, and R.P. Cochran, *Altered collagen concentration in mitral valve leaflets: biochemical and finite element analysis.* Ann Thorac Surg, 1998. **66**(6 Suppl): p. S198-205.

51. Quick, D.W., K.S. Kunzelman, J.M. Kneebone, and R.P. Cochran, *Collagen synthesis is upregulated in mitral valves subjected to altered stress.* Asaio J, 1997. **43**(3): p. 181-6.

52. Huiskes, R., R. Ruimerman, G.H. van Lenthe, and J.D. Janssen, *Effects of mechanical forces on maintenance and adaptation of form in trabecular bone.* Nature, 2000. **405**(6787): p. 704-6.

53. Zou, Y., H. Takano, H. Akazawa, T. Nagai, M. Mizukami, and I. Komuro, *Molecular and cellular mechanisms of mechanical stress-induced cardiac hypertrophy.* Endocr J, 2002. **49**(1): p. 1-13.

54. Malaviya, P., D.L. Butler, G.P. Boivin, F.N. Smith, F.P. Barry, J.M. Murphy, and K.G. Vogel, *An in vivo model for load-modulated remodeling in the rabbit flexor tendon.* J Orthop Res, 2000. **18**(1): p. 116-25.

55. Weston, M.W. and A.P. Yoganathan, *Biosynthetic activity in heart valve leaflets in response to in vitro flow environments.* Annals of Biomedical Engineering, 2001. **29**(9): p. 752-63.

56. Niklason, L.E., J. Gao, W.M. Abbott, K.K. Hirschi, S. Houser, R. Marini, and R. Langer, *Functional arteries grown in vitro.* Science, 1999. **284**(5413): p. 489-93.

57. Mitchell, S.B., J.E. Sanders, J.L. Garbini, and P.K. Schuessler, *A device to apply user-specified strains to biomaterials in culture.* IEEE Trans Biomed Eng, 2001. **48**(2): p. 268-73.

58. Cacou, C., D. Palmer, D.A. Lee, D.L. Bader, and J.C. Shelton, *A system for monitoring the response of uniaxial strain on cell seeded collagen gels.* Med Eng Phys, 2000. **22**(5): p. 327-33.

59. Hoerstrup, S.P., R. Sodian, J.S. Sperling, J.P. Vacanti, and J.E. Mayer, Jr., *New pulsatile bioreactor for in vitro formation of tissue engineered heart valves.* Tissue Eng, 2000. **6**(1): p. 75-9.

60. Dumont, K., J. Yperman, E. Verbeken, P. Segers, B. Meuris, S. Vandenberghe, W. Flameng, and P.R. Verdonck, *Design of a new pulsatile bioreactor for tissue engineered aortic heart valve formation.* Artif Organs, 2002. **26**(8): p. 710-4.

61. Jockenhoevel, S., G. Zund, S.P. Hoerstrup, A. Schnell, and M. Turina, *Cardiovascular tissue engineering: a new laminar flow chamber for in vitro improvement of mechanical tissue properties.* Asaio J, 2002. **48**(1): p. 8-11.

62. Engelmayr, G.C., Jr., D.K. Hildebrand, F.W. Sutherland, J.E. Mayer, Jr., and M.S. Sacks, *A novel bioreactor for the dynamic flexural stimulation of tissue engineered heart valve biomaterials.* Biomaterials, 2003. **24**(14): p. 2523-32.

63. Engelmayr, G.C., Jr., E. Rabkin, F.W. Sutherland, F.J. Schoen, J.E. Mayer, Jr., and M.S. Sacks, *The independent role of cyclic flexure in the early in vitro development of an engineered heart valve tissue.* Biomaterials, 2005. **26**(2): p. 175-87.

64. Mol, A., C.V. Bouten, G. Zund, C.I. Gunter, J.F. Visjager, M.I. Turina, F.P. Baaijens, and S.P. Hoerstrup, *The relevance of large strains in functional tissue engineering of heart valves.* Thorac Cardiovasc Surg, 2003. **51**(2): p. 78-83.

65. Leung, D.Y., S. Glagov, and M.B. Mathews, *Cyclic stretching stimulates synthesis of matrix components by arterial smooth muscle cells in vitro.* Science, 1976. **191**(4226): p. 475-7.

66. Sumpio, B.E., A.J. Banes, W.G. Link, and G. Johnson, Jr., *Enhanced collagen production by smooth muscle cells during repetitive mechanical stretching.* Arch Surg, 1988. **123**(10): p. 1233-6.

67. Sumpio, B.E. and A.J. Banes, *Response of porcine aortic smooth muscle cells to cyclic tensional deformation in culture.* J Surg Res, 1988. **44**(6): p. 696-701.

68. Sumpio, B.E., A.J. Banes, G.W. Link, and T. Iba, *Modulation of endothelial cell phenotype by cyclic stretch: inhibition of collagen production.* J Surg Res, 1990. **48**(5): p. 415-20.

69. Hsieh, A.H., C.M. Tsai, Q.J. Ma, T. Lin, A.J. Banes, F.J. Villarreal, W.H. Akeson, and K.L. Sung, *Time-dependent increases in type-III collagen gene expression in medical collateral ligament fibroblasts under cyclic strains.* J Orthop Res, 2000. **18**(2): p. 220-7.

70. Matsumoto, T., M. Kawakami, K. Kuribayashi, T. Takenaka, and T. Tamaki, *Cyclic mechanical stretch stress increases the growth rate and collagen synthesis of nucleus pulposus cells in vitro.* Spine, 1999. **24**(4): p. 315-9.

71. Goldschmidt, M.E., K.J. McLeod, and W.R. Taylor, *Integrin-mediated mechanotransduction in vascular smooth muscle cells: frequency and force response characteristics.* Circ Res, 2001. **88**(7): p. 674-80.

72. Coplen, D.E., E.J. Macarak, and P.S. Howard, *Matrix Synthesis by Bladder Smooth Muscle Cells Is Modulated by Stretch Frequency.* In Vitro Cell Dev Biol Anim, 2003. **39**(3): p. 157-162.

73. Lavagnino, M., S.P. Arnoczky, T. Tian, and Z. Vaupel, *Effect of amplitude and frequency of cyclic tensile strain on the inhibition of MMP-1 mRNA expression in tendon cells: an in vitro study.* Connect Tissue Res, 2003. **44**(3-4): p. 181-7.

74. McKnight, N.L. and J.A. Frangos, *Strain rate mechanotransduction in aligned human vascular smooth muscle cells.* Ann Biomed Eng, 2003. **31**(3): p. 239-49.

75. Clark, C.B., N.L. McKnight, and J.A. Frangos, *Strain and strain rate activation of G proteins in human endothelial cells.* Biochem Biophys Res Commun, 2002. **299**(2): p. 258-62.

76. Sumpio, B.E., A.J. Banes, L.G. Levin, and G. Johnson, Jr., *Mechanical stress stimulates aortic endothelial cells to proliferate.* J Vasc Surg, 1987. **6**(3): p. 252-6.

77. Aitken, K. and D.J. Bagl, *Stretch-induced bladder smooth muscle cell (SMC) proliferation is mediated by RHAMM-dependent extracellular-regulated kinase (erk) signaling.* Urology, 2001. **57**(6 Suppl 1): p. 109.

78. Li, Q., Y. Muragaki, H. Ueno, and A. Ooshima, *Stretch-induced proliferation of cultured vascular smooth muscle cells and a possible involvement of local renin-angiotensin system and platelet-derived growth factor (PDGF).* Hypertens Res, 1997. **20**(3): p. 217-23.

79. Wernig, F., M. Mayr, and Q. Xu, *Mechanical stretch-induced apoptosis in smooth muscle cells is mediated by beta1-integrin signaling pathways.* Hypertension, 2003. **41**(4): p. 903-11.

80. Li, Q., Y. Muragaki, I. Hatamura, H. Ueno, and A. Ooshima, *Stretch-induced collagen synthesis in cultured smooth muscle cells from rabbit aortic media and a possible involvement of angiotensin II and transforming growth factor-beta.* J Vasc Res, 1998. **35**(2): p. 93-103.

81. Ko, K.S., P.D. Arora, and C.A. McCulloch, *Cadherins mediate intercellular mechanical signaling in fibroblasts by activation of stretch-sensitive calcium-permeable channels.* J Biol Chem, 2001. **276**(38): p. 35967-77.

82. Banes, A.J., P. Weinhold, X. Yang, M. Tsuzaki, D. Bynum, M. Bottlang, and T. Brown, *Gap junctions regulate responses of tendon cells ex vivo to mechanical loading.* Clin Orthop, 1999(367 Suppl): p. S356-70.

83. Taber, L.A., *Biomechanics of cardiovascular development.* Annu Rev Biomed Eng, 2001. **3**: p. 1-25.

84. Glowacki, J., E. Trepman, and J. Folkman, *Cell shape and phenotypic expression in chondrocytes.* Proc Soc Exp Biol Med, 1983. **172**(1): p. 93-8.

85. Nikolovski, J. and D.J. Mooney, *Smooth muscle cell adhesion to tissue engineering scaffolds.* Biomaterials, 2000. **21**(20): p. 2025-32.

86. Moiseeva, E.P., *Adhesion receptors of vascular smooth muscle cells and their functions.* Cardiovasc Res, 2001. **52**(3): p. 372-86.

87. Ralphs, J.R., A.D. Waggett, and M. Benjamin, *Actin stress fibres and cell-cell adhesion molecules in tendons: organisation in vivo and response to mechanical loading of tendon cells in vitro.* Matrix Biol, 2002. **21**(1): p. 67-74.

88. Rodriguez, E.K., A. Hoger, and A.D. McCulloch, *Stress-dependent finite growth in soft elastic tissues.* J Biomech, 1994. **27**(4): p. 455-67.

89. Taber, L.A. and D.W. Eggers, *Theoretical study of stress-modulated growth in the aorta.* J Theor Biol, 1996. **180**(4): p. 343-57.

90. Taber, L.A., *Biomechanical growth laws for muscle tissue.* J Theor Biol, 1998. **193**(2): p. 201-13.

91. Humphrey, J.D., *Remodeling of a collagenous tissue at fixed lengths.* J Biomech Eng, 1999. **121**(6): p. 591-7.

92. Zahalak, G.I., J.E. Wagenseil, T. Wakatsuki, and E.L. Elson, *A cell-based constitutive relation for bio-artificial tissues.* Biophys J, 2000. **79**(5): p. 2369-81.

93. Gibson, R.F., *Principles of composite material mechanics*. McGraw-Hill series in mechanical engineering. 1994, New York: McGraw-Hill. xvii, 425.

94. Agarwal, B.D. and L.J. Broutman, *Analysis and performance of fiber composites*. 2nd ed. SPE monographs. 1990, New York: Wiley. xviii, 449.

95. Kouznetsova, V., W.A.M. Brekelmans, and F.P.T. Baaijens, *An approach to micro-macro modeling of heterogeneous materials.* Computational Mechanics, 2001. **27**(1): p. 37-48.

96. Sutherland, F.W. and J.E. Mayer, Jr., *Ethical and regulatory issues concerning engineered tissues for congenital heart repair.* Semin Thorac Cardiovasc Surg Pediatr Card Surg Annu, 2003. **6**: p. 152-63.

97. Hearle, J.W.S. and A.T. Purdy, *The structure of needle punched fabric.* Fibre Science and Technology, 1971. **4**: p. 81-100.

98. Hearle, J.W.S. and A.T. Purdy, *On the nature of deformation of needled fabrics.* Fibre Science and Technology, 1972. **5**(2): p. 113-128.

99. Hearle, J.W.S. and A.T. Purdy, *On resistance to slippage in needled fabrics.* Fibre Science and Technology, 1978. **11**(2): p. 127-144.

100. Gloeckner, D.C., K.L. Billiar, and M.S. Sacks, *Effects of mechanical fatigue on the bending properties of the porcine bioprosthetic heart valve.* Asaio J, 1999. **45**(1): p. 59-63.

101. Frisch-Fay, R., *Flexible bars*. 1962, Washington,DC: Butterworths. 220.

102. Agrawal, C.M., J.S. McKinney, D. Lanctot, and K.A. Athanasiou, *Effects of fluid flow on the in vitro degradation kinetics of biodegradable scaffolds for tissue engineering.* Biomaterials, 2000. **21**(23): p. 2443-52.

103. Thompson, D.E., C.M. Agrawal, and K.A. Athanasiou, *The Effects of Dynamic Compressive Loading on Biodegradable Implants of 50-50% Polylactic Acid-Polyglycolic Acid.* Tissue Eng, 1996. **2**(1): p. 61-74.

104. Weng, Y., Y. Cao, C.A. Silva, M.P. Vacanti, and C.A. Vacanti, *Tissue-engineered composites of bone and cartilage for mandible condylar reconstruction.* J Oral Maxillofac Surg, 2001. **59**(2): p. 185-90.

105. Brown, A.N., B.S. Kim, E. Alsberg, and D.J. Mooney, *Combining chondrocytes and smooth muscle cells to engineer hybrid soft tissue constructs.* Tissue Eng, 2000. **6**(4): p. 297-305.

106. Ameer, G.A., T.A. Mahmood, and R. Langer, *A biodegradable composite scaffold for cell transplantation.* J Orthop Res, 2002. **20**(1): p. 16-9.

107. Gao, J., L. Niklason, and R. Langer, *Surface hydrolysis of poly(glycolic acid) meshes increases the seeding density of vascular smooth muscle cells.* J Biomed Mater Res, 1998. **42**(3): p. 417-24.

108. Sutherland, F.W., T.E. Perry, B.A. Nasseri, J. Wang, S. Kaushal, K.J. Guleserian, D.P. Martin, J.P. Vacant, and J.E. Mayer, Jr., *Advances in the mechanisms of cell delivery to cardiovascular scaffolds: comparison of two rotating cell culture systems.* Asaio J, 2002. **48**(4): p. 346-9.

109. Nasseri, B.A., I. Pomerantseva, M.R. Kaazempur-Mofrad, F.W. Sutherland, T. Perry, E. Ochoa, C.A. Thompson, J.E. Mayer, Jr., S.N. Oesterle, and J.P. Vacanti, *Dynamic rotational seeding and cell culture system for vascular tube formation.* Tissue Eng, 2003. **9**(2): p. 291-9.

110. Kim, Y.J., R.L. Sah, J.Y. Doong, and A.J. Grodzinsky, *Fluorometric assay of DNA in cartilage explants using Hoechst 33258.* Anal Biochem, 1988. **174**(1): p. 168-76.

111. Kim, B.S., A.J. Putnam, T.J. Kulik, and D.J. Mooney, *Optimizing seeding and culture methods to engineer smooth muscle tissue on biodegradable polymer matrices.* Biotechnol Bioeng, 1998. **57**(1): p. 46-54.

112. Simon, P., M.T. Kasimir, G. Seebacher, G. Weigel, R. Ullrich, U. Salzer-Muhar, E. Rieder, and E. Wolner, *Early failure of the tissue engineered porcine heart valve SYNERGRAFT in pediatric patients.* Eur J Cardiothorac Surg, 2003. **23**(6): p. 1002-6; discussion 1006.

113. Sacks, M.S., *The biomechanical effects of fatigue on the porcine bioprosthetic heart valve.* Journal of long-term effects of medical implants, 2001. **11**(3&4): p. 231-247.

114. Kim, B.S. and D.J. Mooney, *Scaffolds for engineering smooth muscle under cyclic mechanical strain conditions.* J Biomech Eng, 2000. **122**(3): p. 210-5.

115. Kim, B.S., J. Nikolovski, J. Bonadio, and D.J. Mooney, *Cyclic mechanical strain regulates the development of engineered smooth muscle tissue.* Nat Biotechnol, 1999. **17**(10): p. 979-83.

116. Schroeder, J.A., L.F. Jackson, D.C. Lee, and T.D. Camenisch, *Form and function of developing heart valves: coordination by extracellular matrix and growth factor signaling.* J Mol Med, 2003. **81**(7): p. 392-403.

117. Perry, T.E., S. Kaushal, F.W. Sutherland, K.J. Guleserian, J. Bischoff, M. Sacks, and J.E. Mayer, *Thoracic Surgery Directors Association Award. Bone marrow as a cell source for tissue engineering heart valves.* Ann Thorac Surg, 2003. **75**(3): p. 761-7; discussion 767.

118. Schnittler, H.J., T. Schmandra, and D. Drenckhahn, *Correlation of endothelial vimentin content with hemodynamic parameters.* Histochem Cell Biol, 1998. **110**(2): p. 161-7.

119. Durrant, L.A., C.W. Archer, M. Benjamin, and J.R. Ralphs, *Organisation of the chondrocyte cytoskeleton and its response to changing mechanical conditions in organ culture.* J Anat, 1999. **194 (Pt 3)**: p. 343-53.

120. Powell, D.W., R.C. Mifflin, J.D. Valentich, S.E. Crowe, J.I. Saada, and A.B. West, *Myofibroblasts. I. Paracrine cells important in health and disease.* Am J Physiol, 1999. **277**(1 Pt 1): p. C1-9.

121. Akhyari, P., P.W. Fedak, R.D. Weisel, T.Y. Lee, S. Verma, D.A. Mickle, and R.K. Li, *Mechanical stretch regimen enhances the formation of bioengineered autologous cardiac muscle grafts.* Circulation, 2002. **106**(12 Suppl 1): p. I137-42.

122. Fu, P., R. Sodian, C. Luders, T. Lemke, L. Kraemer, M. Hubler, Y. Weng, S.P. Hoerstrup, R. Meyer, and R. Hetzer, *Effects of basic fibroblast growth factor and transforming growth factor-beta on maturation of human pediatric aortic cell culture for tissue engineering of cardiovascular structures.* Asaio J, 2004. **50**(1): p. 9-14.

123. Costa, K.D., E.J. Lee, and J.W. Holmes, *Creating alignment and anisotropy in engineered heart tissue: role of boundary conditions in a model three-dimensional culture system.* Tissue Eng, 2003. **9**(4): p. 567-77.

124. Driessen, N.J., C.V. Bouten, and F.P. Baaijens, *Improved prediction of the collagen fiber architecture in the aortic heart valve.* J Biomech Eng, 2005. **127**(2): p. 329-36.

125. Hildebrand, D.K., Z.J. Wu, J.E. Mayer, Jr., and M.S. Sacks, *Design and hydrodynamic evaluation of a novel pulsatile bioreactor for biologically active heart valves.* Ann Biomed Eng, 2004. **32**(8): p. 1039-49.

126. Budilarto, S.G., B.J. Frankowski, B.G. Hattler, and W.J. Federspiel, *Flow visualization study of a pusating respiratory assist catheter.* Asaio J, 2005. **in-press**.

127. Weston, M.W., D.V. LaBorde, and A.P. Yoganathan, *Estimation of the shear stress on the surface of an aortic valve leaflet.* Ann Biomed Eng, 1999. **27**(4): p. 572-9.

128. Lee, A.A., D.A. Graham, S. Dela Cruz, A. Ratcliffe, and W.J. Karlon, *Fluid shear stress-induced alignment of cultured vascular smooth muscle cells.* J Biomech Eng, 2002. **124**(1): p. 37-43.

129. Wu, X., E. Rabkin-Aikawa, K.J. Guleserian, T.E. Perry, Y. Masuda, F.W. Sutherland, F.J. Schoen, J.E. Mayer, Jr., and J. Bischoff, *Tissue-engineered microvessels on three-dimensional biodegradable scaffolds using human endothelial progenitor cells.* Am J Physiol Heart Circ Physiol, 2004. **287**(2): p. H480-7.

130. Kadner, A., S.P. Hoerstrup, G. Zund, K. Eid, C. Maurus, S. Melnitchouk, J. Grunenfelder, and M.I. Turina, *A new source for cardiovascular tissue engineering: human bone marrow stromal cells.* Eur J Cardiothorac Surg, 2002. **21**(6): p. 1055-60.

131. Wang, H., G.M. Riha, S. Yan, M. Li, H. Chai, H. Yang, Q. Yao, and C. Chen, *Shear stress induces endothelial differentiation from a murine embryonic mesenchymal progenitor cell line.* Arterioscler Thromb Vasc Biol, 2005. **25**(9): p. 1817-23.

132. Oswald, J., S. Boxberger, B. Jorgensen, S. Feldmann, G. Ehninger, M. Bornhauser, and C. Werner, *Mesenchymal stem cells can be differentiated into endothelial cells in vitro.* Stem Cells, 2004. **22**(3): p. 377-84.

133. Pittenger, M.F., A.M. Mackay, S.C. Beck, R.K. Jaiswal, R. Douglas, J.D. Mosca, M.A. Moorman, D.W. Simonetti, S. Craig, and D.R. Marshak, *Multilineage potential of adult human mesenchymal stem cells.* Science, 1999. **284**(5411): p. 143-7.

134. Bi, Y., C.H. Stuelten, T. Kilts, S. Wadhwa, R.V. Iozzo, P.G. Robey, X.D. Chen, and M.F. Young, *Extracellular matrix proteoglycans control the fate of bone marrow stromal cells.* J Biol Chem, 2005. **280**(34): p. 30481-9.

135. Freed, L.E., G. Vunjak-Novakovic, R.J. Biron, D.B. Eagles, D.C. Lesnoy, S.K. Barlow, and R. Langer, *Biodegradable Polymer Scaffolds for Tissue Engineering.* Bio/technology, 1994. **12**: p. 689-693.

136. Oberpenning, F., J. Meng, J.J. Yoo, and A. Atala, *De novo reconstitution of a functional mammalian urinary bladder by tissue engineering [see comments].* Nat Biotechnol, 1999. **17**(2): p. 149-55.

137. Gooch, K.J., T. Blunk, D.L. Courter, A.L. Sieminski, G. Vunjak-Novakovic, and L.E. Freed, *Bone morphogenetic proteins-2, -12, and -13 modulate in vitro development of engineered cartilage.* Tissue Eng, 2002. **8**(4): p. 591-601.

138. Sacks, M.S., *Incorporation of experimentally-derived fiber orientation into a structural constitutive model for planar collagenous tissues.* J Biomech Eng, 2003. **125**(2): p. 280-7.

139. Sun, W., M.J. Scott, and M.S. Sacks, *Finite element implementation of a generalized Fung-elastic constitutive model for planar tissues.* Biomechanics and Modeling in Mechanobiology, in-press.

140. Backer, S. and D.R. Petterson, *Some principles of nonwoven fabrics.* Textile Research Journal, 1960. **30**(9): p. 704-711.

141. Cox, H.L., *The elasticity and strength of paper and other fibrous materials.* British Journal of Applied Physics, 1952. **3**(3): p. 72-79.

142. Hearle, J.W.S. and A. Newton, *Nonwoven fabric studies; part XIII: the influence of the binder on the tensile properties of nonwovens.* Textile Research Journal, 1967. **37**(6): p. 495-503.

143. Hearle, J.W.S. and P.J. Stevenson, *Nonwoven fabric studies; part III: the anisotropy of nonwoven fabrics.* Textile Research Journal, 1963. **33**(11): p. 877-888.

144. Hearle, J.W.S. and M.A.I. Sultan, *A study of needled fabrics; part V: the approach to theoretical understanding.* Journal of the Textile Institute, 1968. **59**: p. 183-201.

145. Hearle, J.W.S. and M.A.I. Sultan, *A study of needled fabrics; part I: experimental methods and properties.* Journal of the Textile Institute, 1967. **58**: p. 251-265.

146. Freeston, W.D., Jr. and M.M. Platt, *Mechanics of elastic performance of textile materials; part XVI: bending rigidity of nonwoven fabrics.* Textile Research Journal, 1965. **35**(1): p. 48-57.

147. Lee, S.M. and A.S. Argon, *The mechanics of the bending of non-woven fabrics part II: spunbonded fabric with spot bonds (fibretex).* Journal of the Textile Institute, 1983. **74**(1): p. 12-18.

148. Freeston, W.D., Jr. and M.M. Platt, *Bending rigidity of random webs.* Textile Research Journal, 1965. **35**(5): p. 480-481.

149. Termonia, Y., *Lattice model for the drape and bending properties of nonwoven fabrics.* Textile Research Journal, 2003. **73**(1): p. 74-78.

150. Sacks, M.S., D.B. Smith, and E.D. Hiester, *A small angle light scattering device for planar connective tissue microstructural analysis.* Ann Biomed Eng, 1997. **25**(4): p. 678-89.

151. Sacks, M.S., C.J. Chuong, W.M. Petroll, M. Kwan, and C. Halberstadt, *Collagen fiber architecture of a cultured dermal tissue.* J Biomech Eng, 1997. **119**(1): p. 124-7.

152. Chen, V.J. and P.X. Ma, *Nano-fibrous poly(L-lactic acid) scaffolds with interconnected spherical macropores.* Biomaterials, 2004. **25**(11): p. 2065-73.

153. Slivka, M.A., C.C. Chu, and I.A. Adisaputro, *Fiber-matrix interface studies on bioabsorbable composite materials for internal fixation of bone fractures. I. Raw material evaluation and measurement of fiber-matrix interfacial adhesion.* J Biomed Mater Res, 1997. **36**(4): p. 469-77.

154. Stankus, J.J., J. Guan, K. Fujimoto, and W.R. Wagner, *Microintegrating smooth muscle cells into a biodegradable, elastomeric fiber matrix.* Biomaterials, in-press.

155. Eberhardt, C.N. and A.R. Clarke, *Automated reconstruction of curvilinear fibres from 3D datasets acquired by X-ray microtomography.* Journal of Microscopy-Oxford, 2002. **206**: p. 41-53.

156. Prabhakar, V., M.W. Grinstaff, J. Alarcon, C. Knors, A.K. Solan, and L.E. Niklason, *Engineering porcine arteries: effects of scaffold modification.* J Biomed Mater Res, 2003. **67A**(1): p. 303-11.

157. Mirnajafi, A., J. Raymer, M.J. Scott, and M.S. Sacks, *The effects of collagen fiber orientation on the flexural properties of pericardial heterograft biomaterials.* Biomaterials, 2005. **26**(7): p. 795-804.

158. Cusick, G.E., J.W.S. Hearle, R.I.C. Michie, R.H. Peters, and P.J. Stevenson, *Physical properties of some commerical non-woven fabrics.* Journal of the Textile Institute, 1963. **54**: p. P52-P74.

159. Kim, B.S. and D.J. Mooney, *Engineering smooth muscle tissue with a predefined structure.* J Biomed Mater Res, 1998. **41**(2): p. 322-32.

160. Hearle, J.W.S., M.A.I. Sultan, and T.N. Choudhari, *A study of needled fabrics; part II: effects of the needling process.* Journal of the Textile Institute, 1968. **59**: p. 103-116.

161. Akbarov, S.D. and A.N. Guz§, *Mechanics of curved composites*. Solid mechanics and its applications; v. 78. 2000, Dordrecht; Boston: Kluwer Academic Publishers. xvi, 441.

162. Engelmayr, G.C., E. Rabkin, F.W. Sutherland, F.J. Schoen, J.E. Mayer Jr, and M.S. Sacks, *The independent role of cyclic flexure in the early in vitro development of an engineered heart valve tissue.* Biomaterials, 2005. **26**(2): p. 175-187.

163. Niskanen, K., *Paper Physics*. Papermaking Science and Technology; bk. 16. 1998, Helsinki; Atlanta: Published in cooperation with the Finnish Paper Engineers' Association and TAPPI. 324.

164. Junqueira, L.C., G. Bignolas, and R.R. Brentani, *Picrosirius staining plus polarization microscopy, a specific method for collagen detection in tissue sections.* Histochem J, 1979. **11**(4): p. 447-55.

165. Dolber, P.C. and M.S. Spach, *Conventional and confocal fluorescence microscopy of collagen fibers in the heart.* J Histochem Cytochem, 1993. **41**(3): p. 465-9.

166. Brotchie, D., M. Birch, N. Roberts, C.V. Howard, V.A. Smith, and I. Grierson, *Localisation of connective tissue and inhibition of autofluorescence in the human optic nerve and nerve head using a modified picrosirius red technique and confocal microscopy.* J Neurosci Methods, 1999. **87**(1): p. 77-85.

167. Akbarov, S.D. and A.N. Guz, *Mechanics of curved composites*. Solid mechanics and its applications; v. 78. 2000, Dordrecht; Boston: Kluwer Academic Publishers. xvi, 441.

168. Martin, I., B. Obradovic, L.E. Freed, and G. Vunjak-Novakovic, *Method for quantitative analysis of glycosaminoglycan distribution in cultured natural and engineered cartilage.* Ann Biomed Eng, 1999. **27**(5): p. 656-62.

169. Junquiera, L.C., L.C. Junqueira, and R.R. Brentani, *A simple and sensitive method for the quantitative estimation of collagen.* Anal Biochem, 1979. **94**(1): p. 96-9.

170. Starr, A., C.L. Fessler, G. Grunkemeier, and G.W. He, *Heart valve replacement surgery: past, present and future.* Clin Exp Pharmacol Physiol, 2002. **29**(8): p. 735-8.

171. Billiar, K.L. and M.S. Sacks, *Biaxial mechanical properties of the native and glutaraldehyde-treated aortic valve cusp: Part II--A structural constitutive model.* Journal of Biomechanical Engineering, 2000. **122**(4): p. 327-35.

172. Sacks, M.S., *Biomechanics of native and engineered heart valve tissues*, in *Functional Tissue Engineering*, F. Guilak, et al., Editors. 2003, Spring-Verlag: New York.

173. Hildebrand, D., Z.J. Wu, J.E. Mayer Jr, and M.S. Sacks, *Design and hydrodynamic evaluation of a novel pulsatile bioreactor for biologically active heart valves.* Annals of Biomedical Engineering, 2004. **32**(8): p. pp. 1039-1049.

174. Walboomers, X.F. and J.A. Jansen, *Cell and tissue behavior on micro-grooved surfaces.* Odontology, 2001. **89**(1): p. 2-11.

175. Massia, S.P. and J. Stark, *Immobilized RGD peptides on surface-grafted dextran promote biospecific cell attachment.* J Biomed Mater Res, 2001. **56**(3): p. 390-9.

176. Sacks, M.S., M.S. Chuong, W.M. Petroll, M. Kwan, and C. Halberstatd, *Collagen Fiber Architecture of a Cultured Dermal Tissue.* Journal of Biomechanical Engineering, 1997.

177. Billiar, K.L. and M.S. Sacks, *Biaxial mechanical properties of the natural and glutaraldehyde treated aortic valve cusp--Part I: Experimental results.* Journal of Biomechanical Engineering, 2000. **122**(1): p. 23-30.

178. Tranquillo, R.T., T.S. Girton, B.A. Bromberek, T.G. Triebes, and D.L. Mooradian, *Magnetically orientated tissue-equivalent tubes: application to a circumferentially orientated media-equivalent.* Biomaterials, 1996. **17**(3): p. 349-57.

179. Glass-Brudzinski, J., D. Perizzolo, and D.M. Brunette, *Effects of substratum surface topography on the organization of cells and collagen fibers in collagen gel cultures.* J Biomed Mater Res, 2002. **61**(4): p. 608-18.

180. Mudera, V.C., R. Pleass, M. Eastwood, R. Tarnuzzer, G. Schultz, P. Khaw, D.A. McGrouther, and R.A. Brown, *Molecular responses of human dermal fibroblasts to dual cues: contact guidance and mechanical load.* Cell Motil Cytoskeleton, 2000. **45**(1): p. 1-9.

181. Engelmayr, G.C. and M.S. Sacks, *A structural model for the flexural mechanics of nonwoven tissue engineering scaffolds.* J Biomech Eng, accepted.

182. Hutmacher, D.W., *Scaffold design and fabrication technologies for engineering tissues--state of the art and future perspectives.* J Biomater Sci Polym Ed, 2001. **12**(1): p. 107-24.

183. Tsang, V.L. and S.N. Bhatia, *Three-dimensional tissue fabrication.* Adv Drug Deliv Rev, 2004. **56**(11): p. 1635-47.

184. Boateng, S.Y., S.S. Lateef, W. Mosley, T.J. Hartman, L. Hanley, and B. Russell, *RGD and YIGSR synthetic peptides facilitate cellular adhesion identical to that of laminin and fibronectin but alter the physiology of neonatal cardiac myocytes.* Am J Physiol Cell Physiol, 2005. **288**(1): p. C30-8.

185. Vozzi, G., C. Flaim, A. Ahluwalia, and S. Bhatia, *Fabrication of PLGA scaffolds using soft lithography and microsyringe deposition.* Biomaterials, 2003. **24**(14): p. 2533-40.

186. Wang, J.H., F. Jia, T.W. Gilbert, and S.L. Woo, *Cell orientation determines the alignment of cell-produced collagenous matrix.* J Biomech, 2003. **36**(1): p. 97-102.

187. Yoshinari, M., K. Matsuzaka, T. Inoue, Y. Oda, and M. Shimono, *Effects of multigrooved surfaces on fibroblast behavior.* J Biomed Mater Res, 2003. **65A**(3): p. 359-68.

188. Wang, J.H., G. Yang, Z. Li, and W. Shen, *Fibroblast responses to cyclic mechanical stretching depend on cell orientation to the stretching direction.* J Biomech, 2004. **37**(4): p. 573-6.

189. Stankus, J.J., J. Guan, and W.R. Wagner, *Fabrication of biodegradable elastomeric scaffolds with sub-micron morphologies.* J Biomed Mater Res, 2004. **70A**(4): p. 603-14.

190. Yang, F., R. Murugan, S. Wang, and S. Ramakrishna, *Electrospinning of nano/micro scale poly(l-lactic acid) aligned fibers and their potential in neural tissue engineering.* Biomaterials, 2005. **26**(15): p. 2603-10.

191. Guan, J., K.L. Fujimoto, M.S. Sacks, and W.R. Wagner, *Preparation and characterization of highly porous, biodegradable polyurethane scaffolds for soft tissue applications.* Biomaterials, 2005. **26**(18): p. 3961-71.

192. Shum, A. and A. Mak, *Morphological and biomechanical characterization of poly(glycolic acid) scaffolds after in vitro degradation.* Polymer Degradation and Stability, 2003. **81**(1): p. 141-149.